ADVANCED REAL-TIME IMAGE RECONSTRUCTION ALGORITHMS

ADVANCED REAL-TIME IMAGE RECONSTRUCTION ALGORITHMS FOR MICROWAVE AND MILLIMETER-WAVE IMAGING

BY

ROMINA KAZEMIVALA, B.Sc., M.A.Sc.

A THESIS
SUBMITTED TO THE DEPARTMENT OF ELECTRICAL & COMPUTER ENGINEERING
AND THE SCHOOL OF GRADUATE STUDIES
OF MCMASTER UNIVERSITY
IN PARTIAL FULFILMENT OF THE REQUIREMENTS
FOR THE DEGREE OF
DOCTOR OF PHILOSOPHY

Doctor of Philosophy (2024)
(Electrical & Computer Engineering)

McMaster University
Hamilton, Ontario, Canada

TITLE:	Advanced Real-time Image Reconstruction Algorithms for Microwave and Millimeter-wave Imaging
AUTHOR:	Romina Kazemivala B.Sc. Shahid Beheshti University, Tehran, Iran M.A.Sc. Amirkabir University of Technology (Tehran Polytechnic), Tehran, Iran
SUPERVISORS:	Dr. Natalia K. Nikolova Ph.D (University of Electro-Communications) P. Eng. (Ontario)
	Dr. Micheal D. Noseworthy Ph.D (University of Guelph) P. Eng. (Ontario)
NUMBER OF PAGES:	xxi, 258

To my parents

ABSTRACT

Microwave/millimeter-wave imaging technology, distinguished by its ability to detect and visualize objects obscured by non-transparent materials, finds diverse applications in fields such as security, medical diagnostics, and industrial nondestructive testing. These applications often require rapid, accurate imaging capabilities that can operate effectively even in non-ideal conditions. This work's principal contribution is the advanced applications of Fourier-space scattered power mapping (F-SPM), which facilitates significant improvements in image reconstruction quality. Firstly, we introduce a novel integration of F-SPM with dual simultaneous utilization of the Born and Rytov approximations. This synergy enhances both the structural and quantitative accuracy of the imaging results by leveraging the unique strengths of each approximation. Secondly, we adapted Fourier-space scattered power mapping (F-SPM) for time-domain data, achieving the same performance as the original frequency-domain method. Simulation and experimental validations are conducted along with the concept of linear frequency-modulated radar (LFM), with performance compared to the rapid microwave holography method. Additionally, we present a broader application of the F-SPM method, which processes data from randomly placed spatial positions. This approach allows for real-time image updates concurrent with ongoing measurements, progressively refining and converging in quality as additional data is acquired. The innovative applications of F-SPM demonstrated in this study enable the achievement of high-quality images with fewer samples than typically required by the Nyquist criterion.

ACKNOWLEDGEMENTS

First and foremost, I must express my profound gratitude to my supervisor, Dr. Natalia K. Nikolova. Over the past five years, her extraordinary mentorship has significantly shaped my academic and personal growth. Dr. Nikolova is not only a remarkable scientist but also a compassionate individual whose influence extends beyond the laboratory. Her unwavering support and guidance were pivotal as I navigated the challenges of immigrating to Canada while pursuing my Ph.D. As an Iranian woman, I owe her my freedom of living, independency, and opportunity to grow. I am forever in her debt. Dr. Nikolova is a rare gem in academia—passionate about her work and deeply committed to her students. She invested countless hours in mentoring me, from exploring and developing new concepts to implementing and testing our ideas, and rigorously refining our manuscripts. As I move forward in my career, my ultimate aspiration is to become an engineer and a researcher who would make Dr. Nikolova proud. Her legacy of excellence and humanity is a beacon for all aspiring scientists, particularly women in engineering, and I am immensely fortunate to have had her as my mentor.

I extend my heartfelt thanks to my supervisory committee members, Dr. Michael D. Noseworthy and Dr. James Chen. Both are exemplary professors whose passion for research and teaching continually inspires me. Their invaluable support and guidance throughout my Ph.D. studies have been instrumental in driving my success. I am deeply appreciative of all their significant contributions to my research.

I must also express my profound gratitude to Dr. John W. Bandler (may he rest

in peace). Throughout my Ph.D. studies, I had the privilege of enhancing my communication skills through the Three Minute Thesis (3MT) program. Even during the challenges of lockdown, his support never wavered, albeit through virtual meetings. Thanks to his guidance, I am confident in my ability to communicate effectively at both technical and non-technical levels—a skill I will carry forward throughout my career.

I also extend my sincerest gratitude to my colleagues, whose support has been indispensable throughout my journey. Dr. Daniel Tajik, in particular, has been a pivotal figure in my academic success. I am deeply grateful for his mentorship and ongoing support, which have been crucial to my achievements. I owe a tremendous thank you to Aaron Pitcher, Jimmy Nguyen, and Mihail Georgiev for their steadfast assistance in the lab. Their companionship was invaluable, making the long hours more bearable and less lonely. Nooshin Valizadeh Shahmirzadi deserves a special mention for her unwavering support and countless hours spent perfecting the nuances of imaging. Her presence was a constant reassurance in times of failure and a joy in moments of success. I am profoundly grateful to Vartika Tiyagi, Arooj Qureshi, and Yang Meng, who were my initial pillars of support when I first arrived in Canada during the challenging times of lockdowns. Finally, my heartfelt thanks go to Sepideh Hassani, Roxana Nikoukar, Samarth Mehta, Golap Kanti Dey, Guanchen Li, and all my past and present colleagues. Without you, this journey would have been very difficult to complete.

Last, but certainly not least, I owe immense gratitude to my parents, Soudabeh and Bahram Kazemivala in Iran, and to my aunt and uncle, Azita and Sam Kazemi, in Canada. Your endless patience and unconditional love have been the bedrock of my strength. I am convinced that without your steadfast support and belief in me, completing this thesis would not have been possible. Thank you!

NOTATION AND ABBREVIATIONS

2D	Two Dimensional
3D	Three Dimensional
BA	Born's Approximation
BI-RADS	Breast Imaging Reporting and Data System
BPA	Back-projection Algorithm
CO	Calibration Object
CS	Compressed Sensing
CT	Computed Tomography
CNN	Convolutional Neural Network
CSI	Contrast Source Inversion
DAS	Delay And Sum
DFT	Discrete Fourier Transform
DL	Deep Learning
EM	Electromagnetic
FFT	Fast Fourier Transform
F-SPM	Fourier-space Scattered Power Mapping
FSPM-TD	Fourier-space Scattered Power Mapping Time Domain
FT	Fourier Transform
IFFT	Inverse Fast Fourier Transform
Im	Imaginary
IPSF	Image Point Spread Function
LFM	Linear Frequency Modulated
MHA	Microwave Holography Algorithm
MLP	Multilevel Perceptron
mmW	Millimeter-wave

MOM	Method Of Moments
MRI	Magnetic Resonance Imaging
OUT	Object Under Test
PSF	Point Spread Function
QMH	Quantitative Microwave Holography
RA	Rytov's Approximation
Re	Real
RMA	Range Migration Algorithm
RMSE	Root Mean Square Error
RO	Reference Object
ROI	Region of Interest
Rx	Receiving
SAR	Specific Absorption Rate **OR**
	Synthetic Aperture Radar
SFCW	Stepped-frequency Continuous Wave
SNCR	Signal to Noise/Clutter Ratio
SNR	Signal to Noise Ratio
SSIM	Structural Similarity Index
SP	Scattering Probe
SPA	Stationary Phase Approximation
SPM	Scattered Power Mapping
TEM	Transverse Electromagnetic
TR	Time Reversal
Tx	Transmitting
UWB	Ultra-wideband
VNA	Vector Network Analyzer

CONTENTS

LIST OF FIGURES

CHAPTER 1

INTRODUCTION

1.1 Background

Microwave and millimeter-wave (mmW) imaging technologies have significantly evolved over the past few decades, driven by substantial advancements in both theoretical frameworks and practical applications. These technologies, which operate in the electromagnetic spectrum from 300 MHz to 300 GHz, have become pivotal in a range of fields such as security, healthcare, and industrial processes due to their ability to perform non-invasive and high-resolution imaging. Unlike optical imaging, microwave imaging has the penetrating ability allowing to image through various materials, including non-metallic objects, fog, smoke, and clothing. This capability makes it highly valuable in diverse fields, such as medical diagnostics, industrial non-destructive testing, and security.

Electromagnetic (EM) imaging involves both forward scattering problems and inverse scattering problems [1, 2]. In the forward model, such as thos in computational electromagnetics, the properties of the object (e.g. dielectric properties) are known and we aim to obtain the scattered-field responses. The calculation of the measured $S-$parameters in an imaging setup is an example of a forward scattering problem. Commercial EM full-wave simulators solve forward scattering problems using numerical techniques, such as the method of moments (MOM) [3], finite difference methods [4] and finite element methods [5]. In the EM inverse problems, the output responses of the system are known, provided by measurements or simulations. In this case, we wish to infer the unknown properties or the object. Examples of inverse scattering problem include remote sensing and microwave/mmW imaging where the obtained reflectivity or permittivity profile can provide valuable diagnostic information. Solving the inverse scattering problem is a difficult task as the scattered field is nonlinearly related to the scatterer due to multiple scattering and mutual coupling effects. Additionally, the inverse scattering problem is generally non-unique and ill-posed.

The objective of microwave/mmW imaging is to localize, shape, and reconstruct an unknown target located in the imaged domain by means of interrogating electromagnetic waves. It is classified into two categories: qualitative and quantitative. Although qualitative imaging methods retrieve the shape and location of unknown objects within the imaged domain, they are incapable of providing the quantitative estimates of the material properties of unknown targets. Quantitative imaging methods, in contrast, reconstruct the values of electromagnetic parameters (e.g., permittivity and conductivity) of unknown scatterers but require higher computational resources (CPU time, memory, etc.).

There are two major approaches in solving the inverse scattering problem: direct inversion algorithms and iterative algorithms. On one hand, direct inversion algorithms use the linearized model of scattering that approximates the total internal field with the incident field using the 0th-order Born approximation. These algorithms have relatively low computational burden. However, they may exhibit structural inaccuracies, especially in near-field imaging of heterogeneous targets. Common qualitative imaging algorithms are back-projection [6,7], delay and sum (DAS), time-reversal (TR) [8,9] and holography methods. On the other hand, iterative algorithms account for non-linear scattering effects and can provide accurate quantitative imaging at the cost of heavy computational burden due to the use of electromagnetic simulations. Examples of such methods include the Born iterative and distorted Born iterative methods [10, 11], Newton-type inversion methods [12], contrast source inversion (CSI) [13, 14], and the model-based optimization methods [15, 16].

Another recent advancement in solving the inverse problems is utilizing deep learning methods [17–20]. Deep learning, particularly convolutional neural networks (CNNs) and multilayer perceptrons (MLPs), offers an efficient alternative by learning the mapping from the scattered-field measurements to scatterer properties [21]. These methods can be broadly categorized into direct learning approaches, learning-assisted objective-function approaches, and physics-assisted learning approaches [22]. Despite their potential, deep learning methods for inverse scattering problems face challenges such as the need for large and diverse training datasets, and generalization to unseen data [22, 23].

Another research development in this area focuses on signal processing algorithms rather than distinct image-reconstruction algorithms. These methods include compressed sensing (CS) and regularization approaches [24–27]. The CS methods are particularly useful for processing random and sparsely sampled data. However, they do have limitations, i.e. they cannot compensate for the lack of data. They operate under the assumption that the information content of the data in some domain is much lower than that found in the actual measurement space. These methods utilize mathematical representations of signals that can be expressed with only a few basis functions in a specific space [28].

In the past, linear (direct inversion) methods have been able to produce only qualitative images. However, recent developments have shown that these methods are in fact capable of generating quantitative images. A notable advancement is the development of a calibration method that enables the extraction of the resolvent kernel (i.e., the transfer function of the linearized scattering model) from the measured system point spread function (PSF). In the context of inverse scattering, the PSF describes the system's response to a point scatterer. In qualitative imaging, usually an analytical representation of the PSF is utilized, whereas in quantitative image reconstruction a small scattering probe (SP) is utilized to acquire the PSF through measurements. The measured PSF describes the hardware performance well as it encompasses the antenna field distribution (or pattern) and other factors that affect the measurement of the actual object under test (OUT). Using measured PSFs, quantitative imaging of dielectric objects has been demonstrated by algorithms such as quantitative microwave holography (QMH) [29–33].

1.2 Research Objective

Recently, a novel method has been proposed that combines the advantages of quantitative reconstruction with fast performance, avoiding the complexities of nonlinearity and iteration. This research is distinguished by two main features. First, it focuses on real-time imaging techniques, which enable rapid image reconstruction with minimal delay following the acquisition of measurements. Second, the research explores the application of the PSF in real-time image reconstruction, enhancing the precision and efficiency of the imaging process.

The primary objective of this research is to enhance the capabilities of the previously proposed scattered power mapping (SPM) method in [34,35]. The ultimate goal is to achieve rapid, high-fidelity reconstructions that can effectively support imaging technologies.

This study specifically introduces and evaluates an innovative imaging technique known as Fourier-space scattered power mapping (F-SPM). F-SPM is a versatile method capable of processing various signal types, including stepped-frequency continuous waves (SFCW), linear frequency modulated (LFM) signals, and ultra-wideband (UWB) radar pulses. It employs a direct inversion algorithm that leverages the Born approximation of the total internal field. This approach linearizes the forward scattering model, thereby facilitating real-time image reconstruction. Additionally, it allows for the quantitative estimation of an object's permittivity.

To validate the effectiveness of the F-SPM technique, extensive testing has been conducted in both simulated and experimental environments. These rigorous tests have led to significant enhancements in the method's performance. The improvements derived from these tests have been meticulously documented and are published in peer-reviewed journal papers. These findings are also elaborated upon extensively in this thesis, highlighting the method's efficacy and potential applications.

1.3 Contributions

The author has contributed to the development of microwave/millimeter-wave imaging in the following ways:

1. Implemented a novel hybrid Born/Rytov reconstruction technique that simultaneously employs both Born's and Rytov's approximations to significantly improve image quality [36]. Each approximation inherently possesses distinct limitations; however, their concurrent use effectively mitigates approximation-specific artifacts, therefore, enhancing the overall fidelity of the reconstructed images.
2. Addressed the need to expand the F-SPM algorithm application to time-domain LFM radar signals utilizing affordable off-the-shelf 77-81 GHz LFM radar sensors, reducing operational expenses and broadening radar technology utilization [37].
3. An in-house time-domain radar simulator is developed, which generates synthetic linear frequency-modulated data much faster than full-wave simulators at high-frequencies, reducing simulation time dramatically [37].
4. Developed and validated a novel image reconstruction method using SPM, designed for mobile platforms, that effectively processes data acquired at random spatial positions. The method demonstrates that it can achieve image quality comparable to that obtained with uniformly sampled data, meeting the Nyquist limit, but without the necessity for such regular sampling [38].

1.4 Outline of the Thesis

This thesis presents the results of an ongoing development of an EM imaging method. The thesis particularly considers the novel image reconstruction algorithms and data processing. Special attention is paid to such aspects of the EM inverse scattering theory as the forward model formulation, the resolvent kernel (i.e. the PSF) in the integral equation of scattering as well as the Born and Rytov scalar models of scattering.

Chapter 2 derives the combined Born/Rytov implementation of F-SPM algorithm, highlighting the benefits of using both approximations in tandem. It presents both simulated and experimental results which demonstrate its ability. This chapter is duplicated from a published journal paper in the IEEE Transactions on Microwave Theory and Techniques [36].

Chapter 3 introduces a novel image reconstruction method for real-time millimeter-wave imaging utilizing linear frequency modulation (LFM) radar and its time-domain responses, called Fourier-space scattered power mapping in the time domain (FSPM-TD). Employing synthetic data from an in-house developed radar simulator and real-world data acquired with a commercial LFM radar system, our method demonstrates significant improvements in image reconstruction speed and accuracy compared to existing techniques like microwave holography. This chapter is also duplicated directly from a first-authored manuscript [37].

Chapter 4 demonstrates a novel random sampling F-SPM method on non-uniform 3D trajectories, a common scenario in mobile and handheld devices, e.g. drones. The images are reconstructed and updated in real time concurrently with the measurements to produce an evolving image, the quality of which is continuously improving and converging as the number of data points increases with the stream of additional measurements This chapter is duplicated from a manuscript published in the MDPI Sensors journal [38].

Chapter 5 concludes the discussion on the advancements in the real-time SPM imaging method. It also provides suggestions for future work to further enhance the F-SPM method.

BIBLIOGRAPHY

[1] W. C. Chew, H. Gan, J. H. Lin, C. C. Lu, G. P. Otto, J. Song, R. L. Wagner, and W. H. Weedon, “Forward and inverse scattering problems in electromagnetic waves,” in *National Science Foundation (NSF) Forum on Optical Science and Engineering*, W. H. Carter, Ed., vol. 2524, International Society for Optics and Photonics. SPIE, 1995, pp. 189 – 200. [Online]. Available: https://doi.org/10.1117/12.219573

[2] M. Phaneuf, M. Kelly, and P. Mojabi, “Experimental evaluation of forward and inverse solvers for metasurface design,” in *2023 XXXVth General Assembly and Scientific Symposium of the International Union of Radio Science (URSI GASS)*, 2023, pp. 1–4.

[3] R. Harington, *Field Computation by Moment Method.* Krieger Publication, 1982.

[4] A. Taflove and K. Umashankar, “The finite-difference time-domain (fd-td) method for electromagnetic scattering and interaction problems,” *Journal of Electromagnetic Waves and Applications*, vol. 1, no. 3, pp. 243–267, 1987. [Online]. Available: https://doi.org/10.1163/156939387X00045

[5] M. Schweiger, S. R. Arridge, M. Hiraoka, and D. T. Delpy, “The finite element method for the propagation of light in scattering media: Boundary and source conditions,” *Medical Physics*, vol. 22, no. 11, pp. 1779–1792, 1995. [Online]. Available: https://aapm.onlinelibrary.wiley.com/doi/abs/10.1118/1.597634

[6] S. Hu, A. M. Molaei, O. Yurduseven, H. Meng, R. Nilavalan, L. Gan, and X. Chen, “Multistatic mimo sparse imaging based on fft and low-rank matrix recovery techniques,” *IEEE Transactions on Microwave Theory and Techniques*, vol. 71, no. 3, pp. 1285–1295, 2023.

[7] Z. Chen, Z. Zeng, D. Fu, Y. Huang, Q. Li, X. Zhang, and J. Wan, “Back-projection imaging for synthetic aperture radar with topography occlusion,” *Remote Sensing*, vol. 15, no. 3, 2023. [Online]. Available: https://www.mdpi.com/2072-4292/15/3/726

[8] M. E. Yavuz and F. L. Teixeira, “Ultrawideband microwave sensing and imaging using time-reversal techniques: A review,” *Remote Sensing*, vol. 1, no. 3, pp. 466–495, 2009. [Online]. Available: https://www.mdpi.com/2072-4292/1/3/466

[9] M. Yousefnia, A. Ebrahimzadeh, M. Dehmollaian, and A. Madannejad, “A time-reversal imaging system for breast screening: Theory and initial phantom results,” *IEEE Transactions on Biomedical Engineering*, vol. 65, no. 11, pp. 2542–2551, 2018.

[10] Y. M. Wang and W. C. Chew, “An iterative solution of the two-dimensional electromagnetic inverse scattering problem,” *International Journal of Imaging Systems and Technology*, vol. 1, no. 1, pp. 100–108, 1989. [Online]. Available: https://onlinelibrary.wiley.com/doi/abs/10.1002/ima.1850010111

[11] W. Chew and Y. Wang, “Reconstruction of two-dimensional permittivity distribution using the distorted born iterative method,” *IEEE Transactions on Medical Imaging*, vol. 9, no. 2, pp. 218–225, 1990.

[12] P. Mojabi and J. LoVetri, "Overview and classification of some regularization techniques for the gauss-newton inversion method applied to inverse scattering problems," *IEEE Transactions on Antennas and Propagation*, vol. 57, no. 9, pp. 2658–2665, 2009.

[13] P. M. van den Berg and R. E. Kleinman, "A contrast source inversion method," *Inverse Problems*, vol. 13, no. 6, p. 1607, dec 1997. [Online]. Available: https://dx.doi.org/10.1088/0266-5611/13/6/013

[14] P. M. van den Berg, A. Abubakar, and J. T. Fokkema, "Multiplicative regularization for contrast profile inversion," *Radio Science*, vol. 38, no. 2, pp. 23–1–23–10, 2003.

[15] P. Meaney, K. Paulsen, B. Pogue, and M. Miga, "Microwave image reconstruction utilizing log-magnitude and unwrapped phase to improve high-contrast object recovery," *IEEE Transactions on Medical Imaging*, vol. 20, no. 2, pp. 104–116, 2001.

[16] S. Hosseinzadegan, A. Fhager, M. Persson, S. D. Geimer, and P. M. Meaney, "Discrete dipole approximation-based microwave tomography for fast breast cancer imaging," *IEEE Transactions on Microwave Theory and Techniques*, vol. 69, no. 5, pp. 2741–2752, 2021.

[17] P. Mojabi, V. Khoshdel, and J. Lovetri, "Tissue-type classification with uncertainty quantification of microwave and ultrasound breast imaging: A deep learning approach," *IEEE Access*, vol. 8, pp. 182 092–182 104, 2020.

[18] M. Salucci, M. Arrebola, T. Shan, and M. Li, “Artificial intelligence: New frontiers in real-time inverse scattering and electromagnetic imaging,” *IEEE Transactions on Antennas and Propagation*, vol. 70, no. 8, pp. 6349–6364, 2022.

[19] H. M. Yao, W. E. I. Sha, and L. Jiang, “Two-step enhanced deep learning approach for electromagnetic inverse scattering problems,” *IEEE Antennas and Wireless Propagation Letters*, vol. 18, no. 11, pp. 2254–2258, 2019.

[20] H. H. Zhang, H. M. Yao, L. Jiang, and M. Ng, “Enhanced two-step deep-learning approach for electromagnetic-inverse-scattering problems: Frequency extrapolation and scatterer reconstruction,” *IEEE Transactions on Antennas and Propagation*, vol. 71, no. 2, pp. 1662–1672, 2023.

[21] Z. Wei and X. Chen, “Deep-learning schemes for full-wave nonlinear inverse scattering problems,” *IEEE Transactions on Geoscience and Remote Sensing*, vol. 57, no. 4, pp. 1849–1860, 2019.

[22] “A review of deep learning approaches for inverse scattering problems (invited review),” *Progress In Electromagnetics Research*, vol. 167, pp. 67–81, 2020.

[23] Z. Wu, Y. Peng, P. Wang, W. Wang, and W. Xiang, “A physics-induced deep learning scheme for electromagnetic inverse scattering,” *IEEE Transactions on Microwave Theory and Techniques*, vol. 72, no. 2, pp. 927–947, 2024.

[24] G. Zhang, C. Li, Z. Wang, J. Hu, S. Zheng, X. Liu, and G. Fang, “An efficient spectrum reconstruction algorithm for non-uniformly sampled signals and its application in terahertz sar,” *Remote Sensing*, vol. 15, no. 18, 2023. [Online]. Available: https://www.mdpi.com/2072-4292/15/18/4427

[25] S. Hu, A. M. Molaei, O. Yurduseven, H. Meng, R. Nilavalan, L. Gan, and X. Chen, “Multistatic mimo sparse imaging based on fft and low-rank matrix recovery techniques,” *IEEE Transactions on Microwave Theory and Techniques*, vol. 71, no. 3, pp. 1285–1295, 2023.

[26] M. Liu, J. Pan, J. Zhu, Z. Chen, B. Zhang, and Y. Wu, “A sparse sar imaging method for low-oversampled staggered mode via compound regularization,” *Remote Sensing*, vol. 16, no. 8, 2024. [Online]. Available: https://www.mdpi.com/2072-4292/16/8/1459

[27] Z. Xu, M. Liu, G. Zhou, Z. Wei, B. Zhang, and Y. Wu, “An accurate sparse sar imaging method for enhancing region-based features via nonconvex and tv regularization,” *IEEE Journal of Selected Topics in Applied Earth Observations and Remote Sensing*, vol. 14, pp. 350–363, 2021.

[28] S. Bernhardt, R. Boyer, S. Marcos, and P. Larzabal, “Compressed sensing with basis mismatch: Performance bounds and sparse-based estimator,” *IEEE Transactions on Signal Processing*, vol. 64, no. 13, pp. 3483–3494, 2016.

[29] D. Tajik, R. Kazemivala, and N. K. Nikolova, “Real-time imaging with simultaneous use of Born and Rytov approximations in quantitative microwave holography,” *IEEE Trans. Microw. Theory Tech.*, vol. 70, no. 3, pp. 1896–1909, 2022.

[30] D. Tajik, R. Kazemivala, J. Nguyen, and N. K. Nikolova, “Accurate range migration for fast quantitative Fourier-based image reconstruction with monostatic radar,” *IEEE Trans. Microw. Theory Tech.*, vol. 70, no. 9, pp. 4273–4283, 2022.

[31] D. Tajik, F. Foroutan, D. S. Shumakov, A. D. Pitcher, and N. K. Nikolova, "Real-time microwave imaging of a compressed breast phantom with planar scanning," *IEEE J. Electromagn. RF Microw. Med. Biol.*, vol. 2, no. 3, pp. 154–162, 2018.

[32] S. Doğu, D. Tajik, M. N. Akıncı, and N. K. Nikolova, "Improving the accuracy of range migration in 3-D near-field microwave imaging," *IEEE Trans. Microw. Theory Tech.*, vol. 71, no. 8, pp. 3540–3551, 2023.

[33] D. Tajik, A. D. Pitcher, and N. K. Nikolova, "Comparative study of the Rytov and Born approximations in quantitative microwave holography," *Prog. Electromagn. Res. B*, vol. 79, pp. 1–19, 2017.

[34] D. S. Shumakov and N. K. Nikolova, "Fast quantitative microwave imaging with scattered-power maps," *IEEE Transactions on Microwave Theory and Techniques*, vol. 66, no. 1, pp. 439–449, 2018.

[35] D. Shumakov, "Development of a near-field microwave imaging system," Ph.D. dissertation, McMaster University, 2017. [Online]. Available: http://hdl.handle.net/11375/22099

[36] R. Kazemivala, D. Tajik, and N. K. Nikolova, "Simultaneous use of the Born and Rytov approximations in real-time imaging with Fourier-space scattered power mapping," *IEEE Trans. Microw. Theory Tech.*, vol. 70, no. 5, pp. 2904–2920, 2022.

[37] R. Kazemivala, A. D. Pitcher, J. Nguyen, and N. K. Nikolova, "Real-time millimeter-wave imaging with linear frequency modulation radar and scattered

power mapping," *IEEE Transactions on Microwave Theory and Techniques*, pp. 1–14, 2024.

[38] R. Kazemivala and N. K. Nikolova, "Real-time synthetic aperture radar imaging with random sampling employing scattered power mapping," *Sensors*, vol. submitted and under revision, 2024.

CHAPTER 2

SIMULTANEOUS USE OF THE BORN AND RYTOV APPROXIMATIONS IN REAL-TIME IMAGING WITH FOURIER-SPACE SCATTERED POWER MAPPING AND RYTOV APPROXIMATIONS IN QUANTITATIVE MICROWAVE HOLOGRAPHY

Preface

This chapter is a reproduction of the following published article:

R. Kazemivala, D. Tajik and N. K. Nikolova, "Simultaneous Use of the Born and Rytov Approximations in Real-Time Imaging With Fourier-Space Scattered Power Mapping," in *IEEE Transactions on Microwave Theory and Techniques*, vol. 70, no. 5, pp. 2904-2920, May 2022, doi: 10.1109/TMTT.2022.3157728.

This article is open access under the Creative Commons 4.0 licensing agreement.

I designed and performed the measurements with the simulated data, implemented the quantitative Fourier-space scattered power mapping (F-SPM) algorithm using the Born and Rytov combination in code, performed the image reconstruction, and wrote/edited the manuscript. Daniel Tajik designed and performed the breast phantom experiment and assisted in the development and testing of the combined Born/Rytov technique and reviewed the manuscript. Natalia K. Nikolova assisted in the development of the combined Born/Rytov technique and edited the manuscript.

2.1 Introduction

Microwave and millimeter-wave imaging methods offer powerful means to detect defects and abnormalities in optically opaque objects. They are widely used in remote sensing, security screening, through-the-wall imaging, ground-penetrating radar, and non-destructive testing [1–9].

Major research efforts also focus on medical diagnostics, e.g., for breast and skin cancer early detection, bone-disease diagnostics and monitoring, and brain-stroke detection [10–16]. The advantages of the microwave modality in medical imaging stem from the relatively low cost and small size of the equipment along with the non-ionizing nature of the radiation [17, 18]. In these applications, high signal loss, near-field effects and strong dielectric heterogeneity present significant challenges for both measurement hardware and reconstruction methods. Nonetheless, especially in the case of breast imaging, clinical evaluations are underway [19–21], and are expected to demonstrate a beneficial alternative to the already well-established medical imaging modalities.

Nonlinear iterative methods for image reconstruction [22–35] constitute a large class in microwave imaging. Their main advantage is that they can account for multiple scattering and mutual coupling in highly heterogeneous media, where faster direct (or linear) inversion methods often fail. Another important advantage is the quantitative reconstruction of the object's permittivity. In contrast, conventional direct inversion methods offer only qualitative images. Quantitative imaging is beneficial when prior property information is available for inclusions of interest (e.g., identifying breast cancer based on its higher permittivity). The trade-off is computational effort, which may be many orders of magnitude larger than that in direct inversion [36]. However, the use of two-dimensional (2D) forward solvers along with tomographic measurement systems, which are designed to observe the limitations of the 2D model, provide a successful strategy to reduce the computational cost of nonlinear inversion and to minimize the modeling errors [37, 38].

The significant computational effort of nonlinear reconstruction has motivated alternative research on direct reconstruction methods for near-field imaging. The advantage of these method is the low computational complexity, leading to very fast (real-time) image reconstruction. Examples include the well-known time-domain algorithms of synthetic aperture radar (SAR) such as delay-and-sum (DAS) and matched filtering [36, 39, 40] as well as the frequency-domain algorithms exploiting inversion in Fourier space (also known as k-space or wavenumber space) [41]. Microwave holography is arguably the most common k-space algorithm [42–46] due its simplicity and computational efficiency.

Importantly, the above direct reconstruction methods are incapable of quantitative imaging. However, methods for direct inversion with quantitative property reconstruction have been proposed recently, namely, quantitative microwave holography (QMH) [47–50] and scattered power mapping (SPM) [50–52]. This breakthrough has become possible due to a measured system point-spread function (PSF), which captures the response of the measurement system to a point scatterer of known contrast [50]. The kernel of the system-specific linearized scattering model is derived from the measured PSF.

The inversion strategies of QMH and SPM are fundamentally different. QMH is a highly efficient computationally. It performs model-to-data matching at each point in (k_x, k_y, z) space, where k_x and k_y span the data k-space. In contrast, SPM minimizes the l_2 norm of the data error over the real (x, y, z) space [36]. The original SPM [51] performs the inversion in the (x, y, z) space, which makes it time-consuming for large objects.

In [52], an improvement to the original SPM is proposed, where the inversion is still carried out in (x, y, z) but the system matrix in the quantitative step is cast in the form of a block circulant with circulant blocks (BCCB) matrix. The BCCB solution leads to significant reduction in the solution time compared to the general approach in [51]. Yet the computational complexity remains higher than that of QMH. In [50], it is suggested that the BCCB quantitative-inversion stage be replaced by a faster solution in k-space. Here, we show that further significant acceleration can be achieved if the SPM qualitative-inversion stage, too, is performed in k-space using the Fourier-transformed data sets. Hereafter, this SPM approach, where both the qualitative and quantitative inversion stages are carried out in Fourier (or k) space, is referred to as Fourier-space SPM (F-SPM). The advantage of F-SPM over the previous SPM methods [50–52] is the reduced running time. As illustrated later, orders of magnitude reduction is achieved compared to the BCCB-SPM algorithm [52]. The larger the object is, the greater the time savings.

The second new development is the strategy to combine the Born and Rytov data approximations within a common F-SPM inversion procedure. As previously shown, the SPM method can be formulated with either Born's approximation (BA) or Rytov's approximation (RA) of the scattered-field data when extracted from the total-field and incident-field measurements [52, 53]. Each of these approximations has distinct limitations. The accuracy of the BA is limited by the product of the size and the permittivity contrast of the scattering object [36,54–58]. On the other hand, the RA is limited to low-contrast objects but it is insensitive to their size as long as the contrast is very low [36, 55, 56, 59]. In a number of applications, such as tissue imaging and non-destructive testing, the background permittivity is often high and this expands the region of applicability of the RA [60]. Also, it has been shown that the BA leads to better reconstruction of the object boundaries but not their interior, whereas the RA is more successful in reconstructing the interior [56, 60]. This observation is particularly reinforced with transmission measurements (as opposed to reflection or back-scattering measurements) when the RA exhibits improved accuracy compared to BA [60].

A well-known practical drawback of the RA-based image reconstruction is that it requires spatial phase unwrapping of the data, which is problematic with strongly heterogeneous high-contrast targets [50]. The problem has been successfully navigated by imposing continuity constraints from one frequency to the next for each transmit-receive antenna pair [37, 61]. Various approaches have also been proposed in the context of magnetic resonance imaging (MRI) [62]. Nonetheless, phase wrapping remains a challenge especially in the case of very wide frequency bandwidths and a large number sampling positions or transmit-receive pairs [63–66]. In the method proposed here, the phase unwrapping step is eliminated altogether in a modified RA-based model, which is then combined with the BA-based model in the new reconstruction algorithm. We demonstrate that this approach improves the image accuracy in the case of heterogeneous objects with electrically large structural components.

In summary, the proposed F-SPM algorithm is a fast quantitative image-reconstruction method, which can applied with far- and near-field measurements. It reduces the running time by orders of magnitude in comparison with the most recent BCCB SPM implementation. Moreover, it combines the Born and Rytov data-extraction strategies in a single inversion procedure, which improves the image quality in comparison with the SPM algorithms employing these strategies separately. Notably, the Rytov-based data extraction employed by F-SPM eliminates the need for spatial phase unwrapping of the data.

The idea of combining the Born and Rytov data approximations in a common reconstruction has been recently explored with QMH [49], [60]. However, up until now it remained unclear how this can be implemented with the SPM method.

The proposed F-SPM method is validated through a challenging near-field imaging experiment with a flattened breast phantom. It is also tested in a close-range millimeter-wave experiment for concealed object detection.

Next, we briefly introduce the SPM reconstruction method. The new F-SPM is presented in Section 2.3 and a comparison between F-SPM, BCCB-SPM and the original SPM is carried out in terms of computational time. In Section 2.4, the combined Born-Rytov F-SPM inversion method is presented, followed by an algorithm summary in Section 2.5. The simulation-based and measurement-based examples are presented and discussed in Sections 2.6 and 2.7, respectively.

2.2 Background

2.2.1 Forward Model of Scattering

The exact forward model of scattering in terms of the S-parameters (the data equation) has been derived in [67]. For real-time reconstruction, this exact model is linearized using the zero-order Born approximation of the total internal field [36], leading to the approximate model:

$$S_{jk}^{\mathrm{sc}}(\mathbf{r}_{\mathrm{Rx}}, \mathbf{r}_{\mathrm{Tx}}; \omega) \approx \frac{-\mathrm{i}\omega\epsilon_0}{2a_j a_k} \cdot \iiint_{V'} \Delta\epsilon_{\mathrm{r}}(\mathbf{r}')\, \mathbf{E}_j^{\mathrm{inc}}(\mathbf{r}_{\mathrm{Rx}}, \mathbf{r}'; \omega) \cdot \mathbf{E}_k^{\mathrm{inc}}(\mathbf{r}', \mathbf{r}_{\mathrm{Tx}}; \omega) dv' \,. \tag{2.1}$$

Here, $S_{jk}^{\mathrm{sc}}(\mathbf{r}_{\mathrm{Rx}}, \mathbf{r}_{\mathrm{Tx}}; \omega)$ is the scattered-field portion of the S-parameter measured with the transmitting (Tx) antenna at position $\mathbf{r}_{\mathrm{Tx}}$ and the receiving (Rx) antenna at $\mathbf{r}_{\mathrm{Rx}}$, and ω is the angular frequency. The subscripts j and k denote the Rx and Tx antenna ports, respectively. Also, a_k is the root-power wave [68] at the Tx antenna port whereas a_j is the root-power wave at the Rx antenna port if this antenna were to transmit, generating the incident field $\mathbf{E}_j^{\mathrm{inc}}(\mathbf{r}_{\mathrm{Rx}}, \mathbf{r}'; \omega)$ at position $\mathbf{r}' \in V'$. This field distribution is the vector Green's function of the system [67]. $\mathbf{E}_k^{\mathrm{inc}}(\mathbf{r}', \mathbf{r}_{\mathrm{Tx}}; \omega)$ is the incident field of the Tx antenna, which replaces the total internal field through Born's zero-order approximation. Further, ϵ_0 is the free-space permittivity, and $\Delta\epsilon_{\mathrm{r}}(\mathbf{r}')$ is the object's complex relative permittivity contrast,

$$\Delta\epsilon_{\mathrm{r}}(\mathbf{r}') = \epsilon_{\mathrm{r}}(\mathbf{r}') - \epsilon_{\mathrm{r,b}}(\mathbf{r}'), \quad \mathbf{r}' \in V' \,, \tag{2.2}$$

with ϵ_{r} and $\epsilon_{\mathrm{r,b}}$ being the complex relative permittivity values of the object and the background, respectively.

The linearized scattering model (2.1) can be expressed in terms of the system PSF as [50, 52, 53]:

$$S_{jk}^{\mathrm{sc}}(\mathbf{r}_{\mathrm{Rx}},\mathbf{r}_{\mathrm{Tx}};\omega) \approx \frac{1}{\Delta\epsilon_{\mathrm{r,sp}}\Omega_{\mathrm{sp}}} \cdot \iiint_{V'} \Delta\epsilon_{\mathrm{r}}(\mathbf{r}') \cdot H_{jk}^{\mathrm{sc}}(\mathbf{r}_{\mathrm{Rx}},\mathbf{r}_{\mathrm{Tx}};\mathbf{r}';\omega)\,dv'\,, \tag{2.3}$$

where the PSF $H_{jk}^{\mathrm{sc}}(\mathbf{r}_{\mathrm{Rx}},\mathbf{r}_{\mathrm{Tx}};\mathbf{r}';\omega)$ is the system response to an electrically small (point-like) scatterer at $\mathbf{r}'$ of contrast $\Delta\epsilon_{\mathrm{r,sp}} = \epsilon_{\mathrm{r,sp}} - \epsilon_{\mathrm{r,b}}$ and volume Ω_{sp}. The PSF is proportional to the field product $\mathbf{E}_j^{\mathrm{inc}} \cdot \mathbf{E}_k^{\mathrm{inc}}$, i.e., the kernel of the model in (2.1), as well as the contrast and volume of the small scatterer. In a uniform background, the far-zone PSF can be approximated with analytical expressions [36], whereas near-zone PSFs can be approximated using simulated incident-field distributions [43, 44, 69]. In either of these cases, the images are only qualitative since the PSF does not capture the system's quantitative aspects such as the actual transmitted power, the impact of the various components of the imaging setup and its contrast sensitivity. To enable quantitative imaging, the system-specific PSF must be measured with a scattering probe (SP) of known volume Ω_{sp} and contrast $\Delta\epsilon_{\mathrm{r,sp}}$.

To illustrate the meaning of the PSF as the measured response to a point scatterer, Fig. 1 shows the extracted scattered portion of the S_{11} parameter in a planar scan in a simulated scattering from a small probe with $\epsilon_{\mathrm{r,sp}} = 1.1$ and $\Omega_{\mathrm{sp}} = 1$ cm^3, where the background is air ($\epsilon_{\mathrm{r,b}} = 1$). The lateral position of the SP is at the center of the scanned plane ($x' = y' = 0$) whereas its distance from the plane (along z) is 3 cm. The PSF shows a near-circular pattern altered slightly by the radiation pattern of the dipole antenna measuring it.

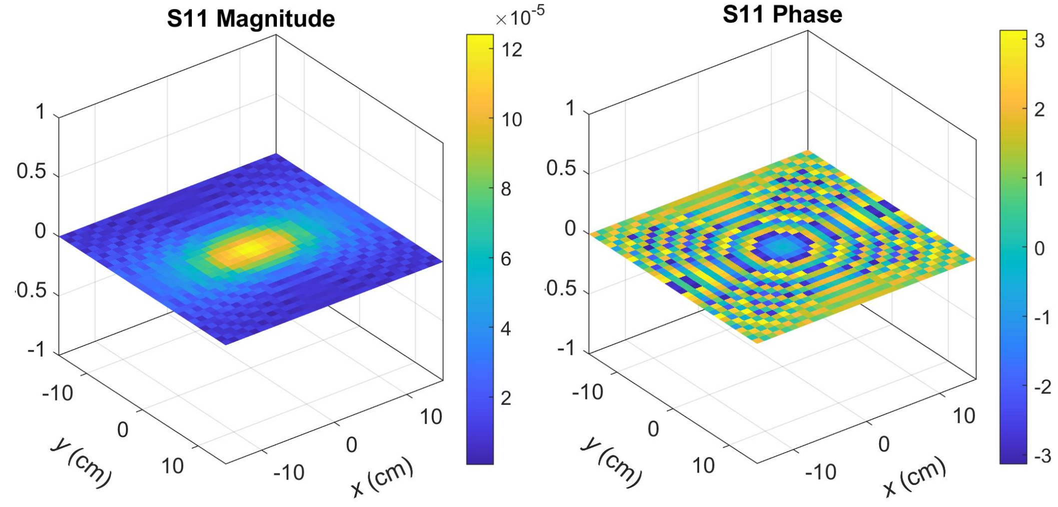

(a) (b)

Figure 2.1: System PSF for S_{11}^{sc} at 8 GHz for a cubical scattering probe (1 cm^3, $\epsilon_{\mathrm{r,sp}} = 1.1$) in air: (a) magnitude and (b) phase. The Tx/Rx antenna is a half-wavelength dipole scanning along x and y. The SP is at a distance $z = 3$ cm from the scanned plane. Data is obtained from simulations using the full-wave electromagnetic solver FEKO [70].

In the case of a uniform or layered background, the PSF is translationally invariant in the two lateral directions, which allows for casting (2.3) in the form of convolution integrals [36, 71]. In particular, in planar scanning along x and y (in the plane $\bar{z} =$ *const.*), with the background being uniform or with layers extending along x and y, (2.3) is written as:

$$S_{\zeta}^{\mathrm{sc}}(x, y, \bar{z}; \omega) = \frac{1}{\Delta\epsilon_{\mathrm{r,sp}}\Omega_{\mathrm{sp}}} \iiint\limits_{z'y'x'} \Delta\epsilon_{\mathrm{r}}(x', y', z') \cdot H_{\zeta}^{\mathrm{sc}}(x - x', y - y', \bar{z}; z'; \omega) dx' dy' dz', \; \zeta = 1, ..., N_{\mathrm{T}} \,. \quad (2.4)$$

Here, the subscript $\zeta \equiv (j,k)$ has been introduced for brevity, indicating the *response type*, i.e., reflection or transmission coefficient, co-polarized or cross-polarized response, etc. The number of response types is denoted with $N_{\rm T}$. $H_{\zeta}^{\rm sc}(x,y,\bar{z};z';\omega)$ is the ζ-type PSF obtained with the SP positioned at $x' = y' = 0$ in the plane $z' = const$. It is evident that (2.4) is a 2D convolution in of the object's contrast function and the system PSF $H_{\zeta}^{\rm sc}$ along x and y. Note that $H_{\zeta}^{\rm sc}$ requires only one measurement with the SP at the center of the plane $z' = const$. In near-zone measurements, for best accuracy, it is desirable to measure multiple PSFs with the SP located at each plane where an image slice is needed.

2.2.2 Extraction of Scattered Data

The measured S-parameters, in both the PSF and the object under test (OUT) measurements are total-field responses, which combine the incident and scattered field contributions. In order to extract the scattered-field contribution, a background calibration measurement is necessary where no scattering objects are present in the setup. This is referred to as the *reference object* (RO).

The first and most common approach to extracting scattered-field responses employs the first-order Born external-field (or data) approximation [36, 55]. The total-field response $S_{\zeta}^{\rm tot}$ is viewed as the superposition of the incident-field (or RO) response $S_{\zeta}^{\rm inc}$ and the scattered-field response $S_{\zeta}^{\rm sc}$, which is represented by the linearized scattering model in (2.1). It then follows that the scattered portions of the S-parameter can be extracted as [36, 55]:

$$S_{\zeta,{\rm B}}^{\rm sc}(\cdot) \approx S_{\zeta}^{\rm tot}(\cdot) - S_{\zeta}^{\rm inc}(\cdot)\,. \tag{2.5}$$

Here, the subscript B indicates Born's approximation.

Another extraction formula employs the first-order Rytov data approximation [36, 55]:

$$S^{\text{sc}}_{\zeta,\text{R}}(\cdot) \approx S^{\text{inc}}_{\zeta}(\cdot) \cdot \ln\left[\frac{S^{\text{tot}}_{\zeta}(\cdot)}{S^{\text{inc}}_{\zeta}(\cdot)}\right] . \tag{2.6}$$

In (2.6), $S^{\text{sc}}_{\zeta,\text{R}}$, too, must be represented by the linearized scattering model (2.1). It is worth noting that the logarithmic Rytov-based formula (2.6) can be also interpreted in the framework of the fundamental work of Box and Cox [72] on data transformation into optimal sets for regression analysis.

2.2.3 SPM Image Reconstruction in Real Space

SPM is a two-stage reconstruction procedure. The first stage computes the qualitative image of the OUT as [36, 51, 52]:

$$M(\mathbf{r}') = \sum_{m=1}^{N_\omega}\sum_{\zeta=1}^{N_\text{T}}\sum_{p=1}^{N_\text{Rx}}\sum_{q=1}^{N_\text{Tx}} \left[S^{\text{sc}}_{\zeta}(\mathbf{r}_p,\mathbf{r}_q;\omega_m)\right] \cdot \left[H^{\text{sc}}_{\zeta}(\mathbf{r}_p,\mathbf{r}_q;\mathbf{r}';\omega_m)\right]^* . \tag{2.7}$$

Here, $\mathbf{r}_p, p = 1, ..., N_\text{Rx}$, and $\mathbf{r}_q, q = 1, ..., N_\text{Tx}$, denote the observation and excitation points, respectively, N_ω is the number of frequency samples, and $\mathbf{r}'$ is the imaged point. Note that $\mathbf{r}'$ also corresponds to the location of the point scatterer in H^{sc}_{ζ}. $M(\mathbf{r}')$ is termed scattered-power map (or simply power map) since it scales with the scattered power emanating from $\mathbf{r}'$. The power map is complex-valued but its absolute value $|M(\mathbf{r}')|$ is a qualitative image of the OUT reflectivity.

In order to carry out the second stage of quantitative reconstruction, the power maps of the point scatterer (the SP) at all locations $\mathbf{r}' \in V'$ are required. These SP power maps are computed in a manner analogous to (2.7):

$$\mathcal{M}(\mathbf{r}';\mathbf{r'}) = \sum_{m=1}^{N_\omega}\sum_{\zeta=1}^{N_\mathrm{T}}\sum_{p=1}^{N_\mathrm{Rx}}\sum_{q=1}^{N_\mathrm{Tx}} \left[H_\zeta^\mathrm{sc}(\mathbf{r}_p,\mathbf{r}_q;\mathbf{r'};\omega_m)\right]\cdot\left[H_\zeta^\mathrm{sc}(\mathbf{r}_p,\mathbf{r}_q;\mathbf{r}';\omega_m)\right]^* \,. \tag{2.8}$$

Here, $\mathbf{r}'$ is again the imaged point whereas $\mathbf{r'}$ is the location of the SP. Note that $\mathcal{M}$ is rarely a 3D δ-function, i.e., it contains nonzero values at $\mathbf{r}' \neq \mathbf{r}''$. This is because it is the qualitative image point-spread function (IPSF) of the system.

The second (quantitative) stage of the SPM reconstruction is based on a proof that the OUT power map $M(\mathbf{r}')$ in (2.7) relates to the SP power maps $\mathcal{M}(\mathbf{r}';\mathbf{r'})$ through [36, 51]:

$$M(\mathbf{r}') = \frac{1}{\Delta\epsilon_{\mathrm{r,sp}}\Omega_\mathrm{sp}} \iiint_{V'} \Delta\epsilon_\mathrm{r}(\mathbf{r'})\mathcal{M}(\mathbf{r}';\mathbf{r'})d\mathbf{r'}\,. \tag{2.9}$$

The discretization of (2.9) over the imaged volume results in a square linear system of equations [36, 51]:

$$\boldsymbol{M}\boldsymbol{x} = \boldsymbol{m}\,, \tag{2.10}$$

where the q-th column of the system matrix $\boldsymbol{M}$ is the vectorized SP power map $\mathcal{M}(\mathbf{r}'_p;\mathbf{r'}_q)$, $p = 1,\ldots,N_\mathrm{v}$ (the SP is at $\mathbf{r'}_q$). The vector $\boldsymbol{m}$ is the vectorized M_OUT power map, and $\boldsymbol{x}$ contains the unknown values of the voxel complex reflectivity function $\Delta\epsilon_\mathrm{r}(\mathbf{r'}_q)\cdot\Omega_\mathrm{v}/(\Delta\epsilon_{\mathrm{r,sp}}\Omega_\mathrm{sp})$, $q = 1,\ldots,N_\mathrm{v}$, where $\Omega_\mathrm{v} = \Delta x'\Delta y'\Delta z'$ is the voxel's volume. By far, the most time consuming task in real-space SPM is solving (2.10) since the size of the system matrix is $N_\mathrm{v}\times N_\mathrm{v}$, where $N_\mathrm{v} = N_xN_yN_z$ is the number of image voxels in V'.

In [52], the translational invariance of the PSF in a uniform or layered background is exploited to accelerate SPM in the case when N_v is large. Specifically, the PSF for an SP, which is laterally shifted off-center by $(\Delta x', \Delta y')$, is approximated by the PSF for an SP at the center $x' = y' = 0$ through a coordinate shift $(x - \Delta x', y - \Delta y')$. Here, (x, y) is the position where the PSF is measured. This shift is then efficiently implemented in k-space using the shifting property of the Fourier transform (FT). As a result, the system matrix $\boldsymbol{M}$ in (2.10) becomes block circulant with circulant blocks (BCCB). The circulant matrices become diagonalized using a discrete Fourier transform. Hence, the respective BCCB method leads to significant reduction in the quantitative solution time compared to the more general approach in [51]. Its computational complexity $N_{\mathrm{v}} \log(N_{\mathrm{v}})$ as opposed to that of N_{v}^3 in [51]. Orders of magnitude reduction in the reconstruction time is reported in [52] compared to the least-squares method in [51] when N_{v} exceeds 10^4. Although the computational complexity has not been explicitly reported for the BCCB-SPM method in [52], it has a slightly higher cost compared to the SPM that has been discussed in [50]. Here, we show that further acceleration is achievable if both stages of the SPM inversion (qualitative and quantitative) are performed in Fourier space.

2.3 Fast SPM Inversion in Fourier Space

In [50], it is shown that the BCCB solution of (2.10) can be performed directly in 2D Fourier space. This is computationally advantageous since the need to cast the Fourier-transformed system PSFs back into real space is eliminated. Thus, the speed of the SPM algorithm so far has been limited mainly by its first stage that builds the OUT and SP scattered-power maps; see (2.7) and (2.8).

Here, we propose a method to compute the OUT and SP scattered-power maps directly in 2D Fourier space, where the quantitative inversion is done. This leads to orders of magnitude reduction of the computational time. The acceleration is particularly beneficial in view of the proposed simultaneous use of the Born and Rytov approximations, which doubles the amount of scattered-power maps.

The real-space computation of the power maps with (2.7) and (2.8) has the important advantage of accommodating arbitrary Tx and Rx positions ($\mathbf{r}_j$ and $\mathbf{r}_k$). However, if $\mathbf{r}_j$ and $\mathbf{r}_k$ describe a monostatic or a bi-static scenario with scanning on a uniform grid, these maps can be cast in the form of 2D cross-correlations, which are most efficiently computed in Fourier space. In these scenarios, the Tx and Rx antennas are in a fixed configuration, moving together relative to the imaged object. Thus, the Tx antenna position can be expressed in terms of the Rx one, i.e., $\mathbf{r}_k = \mathbf{r}_j + \bar{\mathbf{r}}$, where $\bar{\mathbf{r}}$ is a constant vector. The sum over the Tx positions $\sum_{k=1}^{N_{\text{Tx}}}$ in (2.7) and (2.8) now has only one term per Rx position and is omitted. Further, the summation over the Rx locations $\mathbf{r}_j \equiv (x_j, y_j, \bar{z})$ can be represented as an integral over the acquisition plane $\bar{z} = const.$ (assuming sufficiently dense sampling). Thus, (2.7) is cast as:

$$M(x', y', z') = \sum_{m=1}^{N_\omega} \sum_{\zeta=1}^{N_{\text{T}}} \iint_{yx} \left[S_\zeta^{\text{sc}}(x, y; \omega_m)\right] \cdot \left[H_\zeta^{\text{sc}}(x, y; x', y', z'; \omega_m)\right]^* dxdy\,. \tag{2.11}$$

Here, we have omitted $\bar{z}$ from the arguments of S_ζ^{sc} and H_ζ^{sc} for brevity. If the background is uniform or layered (layers extending along x and y), (2.11) can be expressed as:

$$M(x', y', z') = \sum_{m=1}^{N_\omega} \sum_{\zeta=1}^{N_{\text{T}}} \iint_{yx} \left[S_\zeta^{\text{sc}}(x, y; \omega_m)\right] \cdot \left[H_\zeta^{\text{sc}}(x - x', y - y', z'; \omega_m)\right]^* dxdy\,, \tag{2.12}$$

where $H_\zeta^{\text{sc}}(x, y; z'; \omega_m)$ is the PSF of a scattering probe at $(0, 0, z')$, $z' = const.$ Since the OUT power map (2.12) is a 2D cross-correlation of the OUT data and the respective PSFs, it can be efficiently computed at each point (k_x, k_y) in the 2D Fourier space as:

$$\tilde{M}(k_x, k_y, z') = \sum_{m=1}^{N_\omega} \sum_{\zeta=1}^{N_{\mathrm{T}}} \left[\tilde{S}_\zeta^{\mathrm{sc}}(k_x, k_y; \omega_m)\right] \cdot \left[\tilde{H}_\zeta^{\mathrm{sc}}(k_x, k_y; z'; \omega_m)\right]^* , \tag{2.13}$$

where *tilde* indicates the 2D FTs of the respective distributions.

The second SPM inversion stage, when performed in Fourier space [50], also requires the 2D FTs of the SP power maps. These can be obtained directly in k-space analogously to (C.29):

$$\tilde{\mathcal{M}}(k_x, k_y, z'; \boldsymbol{z}') = \sum_{m=1}^{N_\omega} \sum_{\zeta=1}^{N_{\mathrm{T}}} \left[\tilde{H}_\zeta^{\mathrm{sc}}(k_x, k_y; \boldsymbol{z}'; \omega_m)\right] \cdot \left[\tilde{H}_\zeta^{\mathrm{sc}}(k_x, k_y; z'; \omega_m)\right]^* . \tag{2.14}$$

Here, z' indicates the image slice in the SP power map whereas $\boldsymbol{z}'$ indicates the slice in which the SP actually resides; $z', \boldsymbol{z}' \in [z_1, z_2, \ldots, z_{N_z}]$. Finally, the 2D FT of the complex permittivity contrast $\Delta\tilde{\epsilon}_{\mathrm{r}}$ is extracted using the relation [50]:

$$\tilde{M}(k_x, k_y, z_p) = \frac{\Omega_{\mathrm{v}}}{\Delta\epsilon_{\mathrm{r,sp}}\Omega_{\mathrm{sp}}} \cdot \sum_{q=1}^{N_z} \Delta\tilde{\epsilon}_{\mathrm{r}}(k_x, k_y, z_q) \cdot \tilde{\mathcal{M}}(k_x, k_y, z_p; z_q), \quad p = 1, ..., N_z \, . \tag{2.15}$$

Note that (C.31) defines a square linear system of N_z equations for the N_z unknowns $\Delta\tilde{\epsilon}_{\mathrm{r}}(k_x, k_y, z_q), q = 1, \ldots, N_z$, solved at each point in Fourier space (k_x, k_y). The permittivity contrast in real space $\Delta\epsilon_{\mathrm{r}}(\boldsymbol{x}', \boldsymbol{y}', z_q)$, $q = 1, \ldots, N_z$, is recovered with the 2D inverse fast Fourier transform (IFFT) of $\Delta\tilde{\epsilon}_{\mathrm{r}}(k_x, k_y, z_q)$ at each image slice z_q, $q = 1, \ldots, N_z$.

The time savings realized by performing the first SPM stage in the Fourier space stems from the 2D cross-correlation in (2.11) being transformed into k-space multiplications. The overall cost of computing $M(x', y', z')$ and $\mathcal{M}(x', y', z'; z'')$ in real space in terms of floating-point operations (FLOPs) is

$$\begin{aligned} \text{FLOP}_{xyz} = & \underbrace{N_\omega N_\text{T} N_z (N_x N_y)^2}_{\text{cross-correlation}} + \underbrace{N_\omega N_\text{T} N_z}_{\text{summation}} + \\ & \underbrace{(N_z + N_z^2)(N_x N_y \log_2(N_x N_y))}_{\text{slice by slice 2D FFT on OUT \& SP power maps}} \quad . \end{aligned} \tag{2.16}$$

On the other hand, the computational cost of obtaining the OUT and SP power maps, $\tilde{M}(k_x, k_y, z')$ and $\tilde{\mathcal{M}}(k_x, k_y, z'; z'')$, directly in Fourier space is

$$\begin{aligned} \text{FLOP}_{k_x k_y z} = & \underbrace{N_\omega N_\text{T} (N_z + 1)(N_x N_y \log_2(N_x N_y))}_{\text{2D FFT on OUT and PSF data}} + \\ & \underbrace{N_\omega N_\text{T} N_x N_y N_z}_{\text{multiplications in } k\text{-space}} + \underbrace{N_\omega N_\text{T} N_z}_{\text{summation}} . \end{aligned} \tag{2.17}$$

The time reduction realized with (2.17) *versus* (2.16) is illustrated in Fig. 2.2. Here, the number of frequency samples and range samples are equal and set to $N_\omega = N_z = 12$. The number of response types is $N_\text{T} = 4$, and the number of spatial samples in the lateral directions $N_x = N_y = N$ varies from 1 to 128. It is observed that the FLOP count for the first SPM stage in Fourier space is always lower than the FLOP count in the real-space approach, with significant gains when $N > 4$. For practical cases where $N > 40$, the time reduction is more than three orders of magnitude.

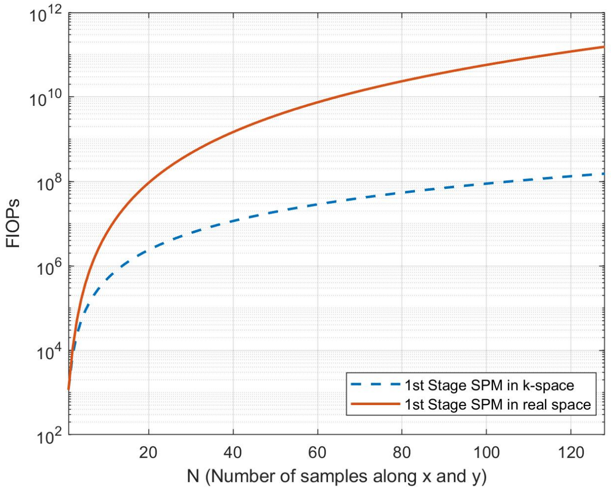

Figure 2.2: Comparison of the computational complexity in terms of FLOPs between the real-space computation of the OUT and SP power maps *versus* their computation in Fourier space. Here, $N_\omega = N_z = 12$, $N_\mathrm{T} = 4$, and $N_x = N_y = N$ varies between 1 and 128.

2.4 Simultaneous Use of Born's and Rytov's Approximations in the F-SPM Algorithm

2.4.1 Motivation

The Born and Rytov approximations of the data equation of scattering, (2.5) and (2.6), apply to the external field. Their limitations have been extensively studied and compared; see, e.g., [36,55,56,73] and the references therein. Here, we only state their mathematical formulations and discuss the advantages of using both approximations simultaneously.

Born's approximation is limited to scatterers satisfying [56]:

$$a \max\{|k(\mathbf{r}') - k_\mathrm{b}|\} < \pi/2 \, , \tag{2.18}$$

where k and k_{b} are the wavenumbers of the scatterer and the background, respectively, and a is the radius of the sphere circumscribing the scatterer. Notably, both the size and the contrast affect the approximation's accuracy. In contrast, Rytov's approximation is limited mostly by the object's contrast as dictated by the limit [36]:

$$|k^2(\mathbf{r}') - k_{\mathrm{b}}^2|/k_{\mathrm{b}}^2 << 1\,. \tag{2.19}$$

Thus, it is expected that Born's approximation would yield better imaging results for small high-contrast objects, whereas Rytov's approximation is better for large low-contrast objects. Slaney *et al.* [56] have compared the two approximations through 2D diffraction-tomography imaging of cylinders of various contrasts and diameters. It has been observed that indeed Rytov's approximation outperforms Born's approximation in the case of diameters larger than a wavelength, particularly in the reconstruction of the cylinders' interiors.

Another complementarity of the two approximations is rooted in their mathematical models of the total-field response in terms of its incident and scattered components. It is shown in [73] that Rytov's approximation, unlike Born's approximation, captures multiple scattering effects as long as (2.19) holds. While Born's approximation may perform better with far-zone measurements, where the mutual coupling and multiple scattering between the OUT and the antennas are negligible, Rytov's approximation is likely to be advantageous in near-field measurements, where such interactions are not negligible.

Yet another complementarity arises from the fact that Rytov's model relies on incident-field responses sufficiently strong to rise above the measurement noise and uncertainty – see the division by S_{ζ}^{inc} in (2.6). In contrast, Born's approximation (2.6) can, in principle, handle well both strong and weak incident-field responses.

Finally, there are scenarios where the two approximations yield very similar extracted scattered-field responses and reconstructed images. Consider Rytov's approximation of the total-field response:

$$S^{\text{tot}}_{\zeta,\text{R}}(\cdot) = S^{\text{inc}}_{\zeta}(\cdot) \exp\left\{ \left[S^{\text{inc}}_{\zeta}(\cdot) \right]^{-1} S^{\text{sc}}_{\zeta}(\cdot) \right\} , \tag{2.20}$$

and its Taylor's expansion:

$$S^{\text{tot}}_{\zeta,\text{R}}(\cdot) = S^{\text{inc}}_{\zeta}(\cdot) \left[1 + \frac{S^{\text{sc}}_{\zeta}(\cdot)}{S^{\text{inc}}_{\zeta}(\cdot)} + \left(\frac{S^{\text{sc}}_{\zeta}(\cdot)}{S^{\text{inc}}_{\zeta}(\cdot)} \right)^2 \frac{1}{2!} + \cdots \right] . \tag{2.21}$$

When the scattered response is much weaker that the incident one, the third and subsequent terms in the expansion can be neglected, and the Rytov approximation converges to Born's superposition of incident and scattered response components.

In summary, the complementarity of Born's and Rytov's data approximations suggests benefits in their simultaneous use in a new inversion strategy. The goal is image reconstruction quality, which is equivalent or better compared to that obtained with either of these approximations when used alone.

2.4.2 Rytov Approximation without Data Phase Unwrapping

In frequency-sweep measurements, the phase of the S-parameters (denoted here as $\angle S$) is wrapped between $-\pi$ and π. Rytov's data approximation (2.6) requires phase unwrapping with respect to the scan position x and y because the discontinuities are detrimental to the processing in Fourier space. To understand the impact of the phase discontinuities, the logarithm in (2.6) is written out explicitly in real and imaginary parts (see the Appendix, section A):

$$S^{\mathrm{sc}}_{\zeta,\mathrm{R}}(\cdot) \approx S^{\mathrm{inc}}_{\zeta}(\cdot) \left\{ \ln \frac{|S^{\mathrm{tot}}_{\zeta}(\cdot)|}{|S^{\mathrm{inc}}_{\zeta}(\cdot)|} + \mathrm{i} \left[\angle S^{\mathrm{tot}}_{\zeta}(\cdot) - \angle S^{\mathrm{inc}}_{\zeta}(\cdot) \right] \right\} . \tag{2.22}$$

It is evident that abrupt changes in the phases $\angle S^{\mathrm{inc}}_{\zeta}$ and $\angle S^{\mathrm{tot}}_{\zeta}$ as functions of $\mathbf{r} = (x, y, \bar{z})$ lead to a discontinuous imaginary part of $S^{\mathrm{sc}}_{\zeta,\mathrm{R}}$. The 2D FT then leads to strong rippling artifacts (Gibb's effect) in k-space. Therefore, 2D phase unwrapping in the (x, y) domain is necessary when using Rytov's approximation.

In [47,49], Rytov's approximation was studied in image reconstruction with quantitative microwave holography, which, too, employs 2D FTs of the data. It is found that unwrapping the response phases with respect to ω does not help with the phase unwrapping in (x, y) and it is recommended that the unwrapping is performed directly in (x, y). Unfortunately, the 2D phase unwrapping is prone to errors with measured signals due to [74–79]: (i) noise, (ii) under-sampling (relative to the phase gradient in (x, y), and (iii) abrupt phase changes from one sample point to the next in excess of π that are not a result of wrapping but are due to actual high-contrast interfaces in the OUT. Yet, in [49], an important observation is made: while 2D phase unwrapping may fail with the measured total-field phase $\angle S^{\mathrm{tot}}_{\zeta}$, it is always successful when applied to the incident-field phase $\angle S^{\mathrm{inc}}_{\zeta}$ and the PSF phase $\angle H^{\mathrm{tot}}_{\zeta}$. This is expected since the incident-field data are acquired in a homogeneous medium whereas the PSF data are acquired with a weakly scattering probe immersed in the homogeneous medium. The 2D phase unwrapping therein is performed with Itoh's method [80]. It unwraps the phase along x first and then the result is unwrapped along y.

In summary, while the Rytov-based PSF $H^{\text{sc}}_{\zeta,\text{R}}$ can be reliably extracted as a smooth function of x and y (by successfully unwrapping $\angle S^{\text{inc}}_{\zeta}$ and $\angle H^{\text{tot}}_{\zeta}$), the OUT data $S^{\text{sc}}_{\zeta,\text{R}}$ may suffer from unwrapping errors in $\angle S^{\text{tot}}_{\zeta}$. As suggested in [49], this problem can be avoided by using only the real part of (2.22). To this end, the forward model (2.4) is modified by multiplying both sides by $|S^{\text{inc}}_{\zeta}(\cdot)|/S^{\text{inc}}_{\zeta}(\cdot)$ and taking the real part of the equation. With (2.22) in mind, this leads to

$$\text{Re}S^{\text{sc}}_{\zeta,\text{R}}(x,y;\omega) = \iiint\limits_{z''y''x''} \text{Re}\Big[\rho(x',y',z') \cdot H^{\text{sc}}_{\zeta,\text{R}}(x-x',y-y',z';\omega)\Big] dx'dy'dz' \,, \quad (2.23)$$

where

$$\text{Re}S^{\text{sc}}_{\zeta,\text{R}}(\cdot) = |S^{\text{inc}}_{\zeta}(\cdot)| \cdot \ln\left(\frac{|S^{\text{tot}}_{\zeta}(\cdot)|}{|S^{\text{inc}}_{\zeta}(\cdot)|}\right) \,, \quad (2.24)$$

is the modified real-valued Rytov data;

$$\rho(x',y',z') = \frac{\Delta\epsilon_{\text{r}}(x',y',z')}{\Delta\epsilon_{\text{r,sp}}\Omega_{\text{sp}}} \,, \quad (2.25)$$

is the complex (relative) reflectivity function to be found, and

$$H^{\text{sc}}_{\zeta,\text{R}}(\cdot) = \big|S^{\text{inc}}_{\zeta}(\cdot)\big| \cdot \ln\left(\frac{H^{\text{tot}}_{\zeta}(\cdot)}{S^{\text{inc}}_{\zeta}(\cdot)}\right) \,, \quad (2.26)$$

is the modified complex Rytov PSF. Note that (2.23) provides a relation to the *complex* unknown reflectivity despite the fact that the data (2.24) is only real-valued. This is due to the availability of the complex-valued PSF (2.26).

According to the SPM theory, the scattered-power map of an OUT must be constructed using a PSF response, which is formulated in exactly the same manner as the OUT response [36]. Therefore, the Rytov-based OUT map is computed as

$$M_{\mathrm{R}}(x', y', z') = \sum_{m=1}^{N_\omega} \sum_{\zeta=1}^{N_{\mathrm{T}}} \iint\limits_{yx} \mathrm{Re}S^{\mathrm{sc}}_{\zeta\mathrm{R}}(x, y; \omega_m) \cdot \left[\mathrm{Re}H^{\mathrm{sc}}_{\zeta,\mathrm{R}}(x - x', y - y'; z'; \omega_m)\right]^* dxdy\,, \tag{2.27}$$

where the conjugation of the second term is superfluous but added for consistency with the general complex-response formulation (2.12).

The substitution of (2.23) into (2.27) leads to the quantitative equation for the reflectivity function ρ in terms of its real and imaginary parts:

$$\begin{aligned} M_{\mathrm{R}}(x', y', z') = \iiint\limits_{z''y''x''} &\left[\mathrm{Re}\rho(x'', y'', z'') \cdot \mathcal{M}^{\mathrm{Re}}_{\mathrm{R}}(x' - x'', y' - y'', z'; z'') - \right. \\ &\left. \mathrm{Im}\rho(x'', y'', z'') \cdot \mathcal{M}^{\mathrm{Im}}_{\mathrm{R}}(x' - x'', y' - y'', z'; z'')\right] dx''dy''dz'', \end{aligned} \tag{2.28}$$

where

$$\begin{aligned} \mathcal{M}^{\mathrm{Re}}_{\mathrm{R}}(x', y', z'; z'') = \sum_{m=1}^{N_\omega} \sum_{\zeta=1}^{N_{\mathrm{T}}} \iint\limits_{yx} &\mathrm{Re}H^{\mathrm{sc}}_{\zeta,\mathrm{R}}(x, y; z''; \omega_m) \\ &\cdot \left[\mathrm{Re}H^{\mathrm{sc}}_{\zeta,\mathrm{R}}(x - x', y - y'; z'; \omega_m)\right]^* dxdy\,, \end{aligned} \tag{2.29}$$

$$\begin{aligned} \mathcal{M}^{\mathrm{Im}}_{\mathrm{R}}(x', y', z'; z'') = \sum_{m=1}^{N_\omega} \sum_{\zeta=1}^{N_{\mathrm{T}}} \iint\limits_{yx} &\mathrm{Im}H^{\mathrm{sc}}_{\zeta,\mathrm{R}}(x, y; z''; \omega_m) \\ &\cdot \left[\mathrm{Re}H^{\mathrm{sc}}_{\zeta,\mathrm{R}}(x - x', y - y'; z'; \omega_m)\right]^* dxdy\,. \end{aligned} \tag{2.30}$$

The double integrals in (2.29) and (2.30) are in the form of cross-correlations, allowing for efficient computation of these PSF power maps in Fourier space as:

$$\tilde{\mathcal{M}}^{\mathrm{Re}}_{\mathrm{R}}(\boldsymbol{\kappa}, z'; z'') = \sum_{m=1}^{N_\omega} \sum_{\zeta=1}^{N_{\mathrm{T}}} \left[\tilde{H}^{\mathrm{Re}}_{\zeta,\mathrm{R}}(\boldsymbol{\kappa}; z''; \omega_m)\right] \left[\tilde{H}^{\mathrm{Re}}_{\zeta,\mathrm{R}}(\boldsymbol{\kappa}; z'; \omega_m)\right]^*, \tag{2.31}$$

$$\tilde{\mathcal{M}}_{\mathrm{R}}^{\mathrm{Im}}(\boldsymbol{\kappa}, z'; z'') = \sum_{m=1}^{N_\omega} \sum_{\zeta=1}^{N_{\mathrm{T}}} \left[\tilde{H}_{\zeta,\mathrm{R}}^{\mathrm{Im}}(\boldsymbol{\kappa}; z'; \omega_m)\right] \left[\tilde{H}_{\zeta,\mathrm{R}}^{\mathrm{Re}}(\boldsymbol{\kappa}; z'; \omega_m)\right]^*, \tag{2.32}$$

where

$$\tilde{H}_{\zeta,\mathrm{R}}^{\mathrm{Re}}(\boldsymbol{\kappa}; z'; \omega_m) = \mathrm{FT}_{\mathrm{2D}} \left\{\mathrm{Re} H_{\zeta,\mathrm{R}}^{\mathrm{sc}}(x, y; z'; \omega_m)\right\}, \tag{2.33}$$

$$\tilde{H}_{\zeta,\mathrm{R}}^{\mathrm{Im}}(\boldsymbol{\kappa}; z'; \omega_m) = \mathrm{FT}_{\mathrm{2D}} \left\{\mathrm{Im} H_{\zeta,\mathrm{R}}^{\mathrm{sc}}(x, y; z'; \omega_m)\right\}. \tag{2.34}$$

Note that the 2D FTs in (2.33) and (2.34) are calculated separately for the real and imaginary parts of the PSF. They are complex and their conjugation in (2.31) and (2.32) is *not* superfluous.

Similarly, the OUT power map in (2.27) is cast in Fourier space as

$$\tilde{M}_{\mathrm{R}}(\boldsymbol{\kappa}, z') = \sum_{m=1}^{N_\omega} \sum_{\zeta=1}^{N_{\mathrm{T}}} \left[\tilde{S}_{\zeta,\mathrm{R}}^{\mathrm{Re}}(\boldsymbol{\kappa}; \omega_m)\right] \left[\tilde{H}_{\zeta,\mathrm{R}}^{\mathrm{Re}}(\boldsymbol{\kappa}; z'; \omega_m)\right]^*, \tag{2.35}$$

where

$$\tilde{S}_{\zeta,\mathrm{R}}^{\mathrm{Re}}(\boldsymbol{\kappa}; z'; \omega_m) = \mathrm{FT}_{\mathrm{2D}} \left\{\mathrm{Re} S_{\zeta,\mathrm{R}}^{\mathrm{sc}}(x, y; z'; \omega_m)\right\}. \tag{2.36}$$

With the power maps in (2.31), (2.32) and (2.35) available, the quantitative equation (2.28) can be efficiently solved in Fourier space since the integration over x' and y' is a 2D convolution:

$$\tilde{M}_{\mathrm{R}}(\boldsymbol{\kappa}, z') = \int_{z''} \left[\tilde{\rho}^{\mathrm{Re}}(\boldsymbol{\kappa}, z') \cdot \tilde{\mathcal{M}}_{\mathrm{R}}^{\mathrm{Re}}(\boldsymbol{\kappa}, z'; z'') - \tilde{\rho}^{\mathrm{Im}}(\boldsymbol{\kappa}, z') \cdot \tilde{\mathcal{M}}_{\mathrm{R}}^{\mathrm{Im}}(\boldsymbol{\kappa}, z'; z')\right] dz''. \tag{2.37}$$

Here,

$$\tilde{\rho}^{\mathrm{Re}}(\boldsymbol{\kappa}, z') = \mathrm{FT}_{\mathrm{2D}} \left\{\mathrm{Re}\rho(x', y', z')\right\}_{(\boldsymbol{\kappa})}, \tag{2.38}$$

$$\tilde{\rho}^{\mathrm{Im}}(\boldsymbol{\kappa}, z') = \mathrm{FT}_{2\mathrm{D}} \left\{ \mathrm{Im}\rho(x', y', z') \right\}_{(\boldsymbol{\kappa})} . \tag{2.39}$$

Let us consider the slices of $\tilde{M}_{\mathrm{R}}(\boldsymbol{\kappa}, z')$ at a discrete set of z positions $z' = z_p$, $p = 1, \ldots, N_z$. At each z_p, an equation can be written by discretizing the integral in (2.37) over z'. With a uniform step of Δz, this equations is:

$$\begin{aligned} \tilde{M}_{\mathrm{R}}(\boldsymbol{\kappa}, z_p) = \Delta z \sum_{q=1}^{N_z} & \left[\tilde{\rho}^{\mathrm{Re}}(\boldsymbol{\kappa}, z_q) \cdot \tilde{\mathcal{M}}_{\mathrm{R}}^{\mathrm{Re}}(\boldsymbol{\kappa}, z_p; z_q) \right. \\ & \left. - -\tilde{\rho}^{\mathrm{Im}}(\boldsymbol{\kappa}, z_q) \cdot \tilde{\mathcal{M}}_{\mathrm{R}}^{\mathrm{Im}}(\boldsymbol{\kappa}, z_p; z_q) \right], p = 1, \ldots, N_z . \end{aligned} \tag{2.40}$$

The quantitative relations in (2.40) provide N_z equations at each point $\boldsymbol{\kappa}$ in k-space for the $2N_z$ unknown values of $\tilde{\rho}^{\mathrm{Re}}(\boldsymbol{\kappa}, z_q)$ and $\tilde{\rho}^{\mathrm{Im}}(\boldsymbol{\kappa}, z_q)$, $z_q = 1, \ldots, N_z$. This system must be combined with the system obtained with Born's approximation (2.5).

When Born's or Rytov's data are used separately, the quantitative system of equations (C.31) is solved using the respective OUT and SP power maps as shown in [50]. However, there, the unknown quantity is in the form of the 2D FT of the complex contrast function. In contrast, in (2.40), the unknown quantity is broken into two 2D FTs, that of the real part of the contrast and that of its imaginary part. This necessitates the re-formulation of (C.31) to match the unknown quantities in (2.40). This re-formulation is detailed in section B of the Appendix along with the composition of the system of equations, which combines (2.40) with the Born-based quantitative equations.

The combined system of equations resulting from the Born-based and Rytov-based quantitative equations at each point in k-space is obtained as:

$$\boldsymbol{M}_{\mathrm{C}}(\boldsymbol{\kappa}) \boldsymbol{\rho}_{\mathrm{C}}(\boldsymbol{\kappa}) = \boldsymbol{m}_{\mathrm{C}}(\boldsymbol{\kappa}) , \tag{2.41}$$

where

$$\begin{aligned}\boldsymbol{\rho}_{\mathrm{C}}(\boldsymbol{\kappa}) = \Big[&\tilde{\rho}^{\mathrm{Re}}(\boldsymbol{\kappa}, z_1), \ldots, \tilde{\rho}^{\mathrm{Re}}(\boldsymbol{\kappa}, z_{N_z}),\\ &\tilde{\rho}^{\mathrm{Im}}(\boldsymbol{\kappa}, z_1), \ldots, \tilde{\rho}^{\mathrm{Im}}(\boldsymbol{\kappa}, z_{N_z})\Big]^T,\end{aligned} \tag{2.42}$$

$$\begin{aligned}\boldsymbol{m}_{\mathrm{C}}(\boldsymbol{\kappa}) = \Big[&\tilde{M}_{\mathrm{B}}^{\mathrm{Re}}(\boldsymbol{\kappa}, z_1), \ldots, \tilde{M}_{\mathrm{B}}^{\mathrm{Re}}(\boldsymbol{\kappa}, z_{N_z}),\\ &\tilde{M}_{\mathrm{B}}^{\mathrm{Im}}(\boldsymbol{\kappa}, z_1), \ldots, \tilde{M}_{\mathrm{B}}^{\mathrm{Im}}(\boldsymbol{\kappa}, z_{N_z}),\\ &\tilde{M}_{\mathrm{R}}(\boldsymbol{\kappa}, z_1), \ldots, \tilde{M}_{\mathrm{R}}(\boldsymbol{\kappa}, z_{N_z})\Big]^T,\end{aligned} \tag{2.43}$$

$$\boldsymbol{M}_{\mathrm{C}}(\boldsymbol{\kappa}) = \begin{bmatrix} \tilde{\mathcal{M}}_{\mathrm{B}}^{\mathrm{Re}}(\boldsymbol{\kappa}) & -\tilde{\mathcal{M}}_{\mathrm{B}}^{\mathrm{Im}}(\boldsymbol{\kappa}) \\ \tilde{\mathcal{M}}_{\mathrm{B}}^{\mathrm{Im}}(\boldsymbol{\kappa}) & \tilde{\mathcal{M}}_{\mathrm{B}}^{\mathrm{Re}}(\boldsymbol{\kappa}) \\ \tilde{\mathcal{M}}_{\mathrm{R}}^{\mathrm{Re}}(\boldsymbol{\kappa}) & -\tilde{\mathcal{M}}_{\mathrm{R}}^{\mathrm{Im}}(\boldsymbol{\kappa}) \end{bmatrix}_{3N_z \times 2N_z} . \tag{2.44}$$

The OUT k-space power map $\tilde{M}_{\mathrm{R}}(\boldsymbol{\kappa}, z_p)$, $p = 1, \ldots, N_z$, is defined in (2.35) whereas the composition of the sub-matrices in the system matrix (2.44) can be found in the Appendix.

The system (C.32) is solved at each point in k-space. Here, a pseudoinverse solver is used. The real and imaginary parts of the k-space contrast, $\tilde{\rho}^{\mathrm{Re}}(\boldsymbol{\kappa}, z_q)$ and $\tilde{\rho}^{\mathrm{Im}}(\boldsymbol{\kappa}, z_q)$, are cast back into real space using 2D IFFT to obtain $\rho^{\mathrm{Re}}(x', y', z_q)$ and $\rho^{\mathrm{Im}}(x', y', z_q)$, $z_q = 1, \ldots, N_z$. Then the complex relative permittivity of the OUT is obtained as:

$$\epsilon_r(x', y', z_q) = \epsilon_{\mathrm{b}} + \Omega_{\mathrm{v}} \cdot \rho(x', y', z_q),\ q = 1, \ldots, N_z\ . \tag{2.45}$$

Since (C.34) and (2.44) use the FTs of the real and imaginary parts of the Born and the Rytov power maps, the computational complexity of the combined approach is expected to be approximately two times that of the SPM approach when only one of the approximations is used.

2.5 Summary of the F-SPM Algorithms

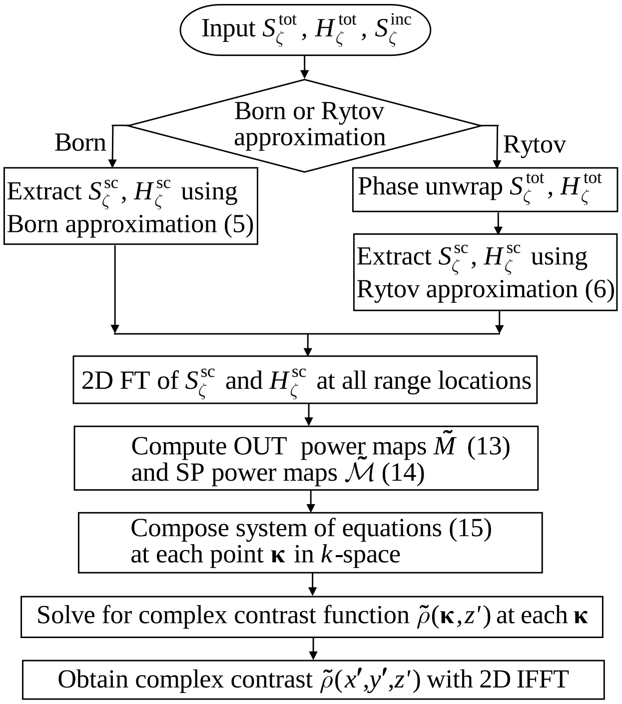

Figure 2.3: Flowchart of the F-SPM algorithm when using either Born's or Rytov's approximation.

The proposed F-SPM algorithm is summarized by the flowchart in Fig. 2.3 for the cases where it employs either the Born or the Rytov approximation. The two cases differ only in the data-extraction formula and the phase unwrapping required by Rytov's approximation.

The newly proposed approach that exploits both approximations in a common inversion process is summarized by the flowchart in Fig. 2.4. The left branch of the flowchart describes the Rytov-based processing whereas the Born-based processing is

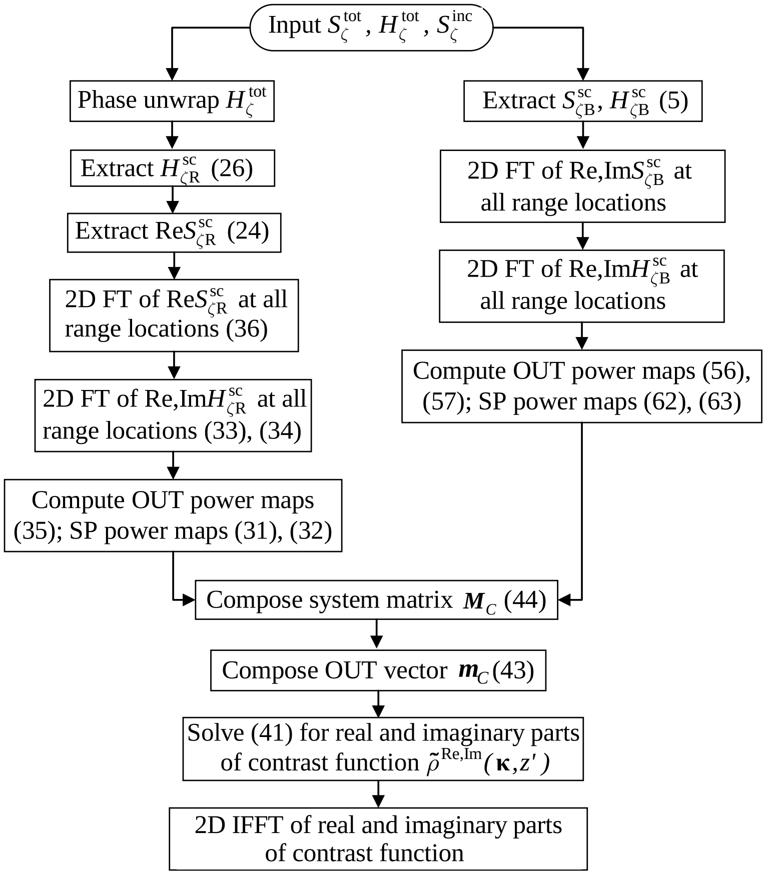

Figure 2.4: Flowchart of the F-SPM algorithm with the combined Born-Rytov approximation.

shown in the right-hand branch. Note the differences in the Rytov-based processing in Fig. 2.3 and the Rytov-based processing in the combined Born-Rytov approximation in Fig. 2.4. First, in the combined approach (Fig. 2.4) there is no need for phase unwrapping of the OUT data sets $S_\zeta^{\rm tot}$; only the total-field responses of the scattering probe $H_\zeta^{\rm tot}$ are phase-unwrapped. Second, the solution for the unknown contrast function in k-space is found for the FTs of its real and imaginary parts (separately) as opposed to the Rytov-based algorithm in Fig. 2.3, where the k-space contrast solution is the FT of the complex contrast function.

Finally, it is important to point out that the presented algorithms are directly applicable to far-zone qualitative imaging scenarios where the data PSFs are approximated by analytical expressions, e.g., $H^{\rm sc} \sim \exp[-{\rm i}k(r_{\rm Rx}+r_{\rm Tx})]/(r_{\rm Rx}r_{\rm Tx})$, where $r_{\rm Rx}$ and $r_{\rm Tx}$ are the distances from the Rx and Tx antennas to the scattering point, respectively. In such cases, the system calibration step that involves the measurements of a scattering probe is omitted but the image has no quantitative value and it is best represented by a plot of the normalized magnitude of the retrieved contrast function.

2.6 Imaging Based on Simulated Near-field Data

The F-SPM algorithms are first demonstrated through an example where S-parameter near-field measurements of the OUT, the scattering probe (SP) and the reference object (RO) are simulated using the full-wave simulator FEKO [70]. The example compares the F-SPM performance in the three implementations discussed here: (i) with Born's data approximation, (ii) with Rytov's data approximation, and (iii) the new combined Born-Rytov method. The example is designed to represent the imaging of a heterogeneous object consisting of high-permittivity lossy targets, some of which are embedded within larger ones. This is a scenario which challenges the structural and quantitative accuracy of the F-SPM algorithm since it solves the linearized model of scattering without any attempt to update the total internal field.

Six dipole antennas are employed in a raster scan on both sides of the imaged object as shown in Fig. 2.5. The dipole at $z = 45\,$mm and the central dipole at $z = -5\,$mm transmit and receive whereas the other four antennas only receive. This results in the following types of responses at each scan position (x, y): S_{11}, S_{22}, S_{31}, S_{41}, S_{51}, S_{61}, S_{32}, S_{42}, S_{52}, and S_{62}, i.e., $N_\zeta = 10$. The distance between the two

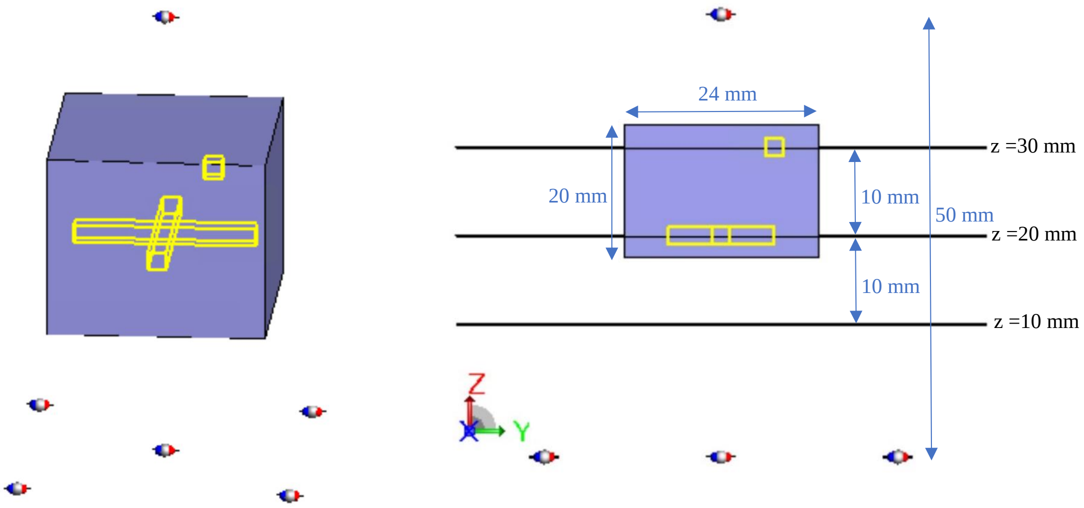

(a) (b)

Figure 2.5: The setup of the simulation example in FEKO when measuring the OUT. The background medium has a relative permittivity of $\epsilon_{\mathrm{r,b}} = 16$. The X-shape object ($\epsilon_{\mathrm{r}} = 32 - \mathrm{i}16$) is aligned along the $z = 20$ mm. The length of the arm of the X-shape is 20 mm whereas the height and width of each arm are 2 mm. The small cube of side 2 mm ($\epsilon_{\mathrm{r}} = 50 - \mathrm{i}5$) is at $z = 30$ mm. The position of the encompassing prism ($\epsilon_{\mathrm{r}} = 24 - \mathrm{i}3$) is indicated in (b). The prism has a thickness of 20 mm, and its width and length along x and y is 24 mm.

acquisition planes is 50 mm. The offset between the center dipole in the five-antenna arrangement and its neighbors is 20 mm. The bandwidth is from 3 GHz to 13 GHz with a frequency step of 500 MHz. The scanned area is 80 mm×80 mm with a sampling step of 2 mm along both x and y. This sampling step is approximately $\lambda_{\mathrm{min}}/3$ where λ_{min} is the shortest wavelength in the background medium with $\epsilon_{\mathrm{r,b}} = 16$. The lateral voxel size is set equal to the sampling step, i.e., $\Delta x = \Delta y = 2$ mm.

The best achievable range resolution is estimated to be approximately 4 mm using the well-known fundamental limit of $\delta_z = v_{\mathrm{b}}/(2B)$ (for the far-zone monostatic case) [36], where v_{b} is the speed of light in the background and B is the bandwidth. In view of the limited aperture extent, it is expected that the actual achievable range resolution in this experiment is approximately twice larger than the fundamental limit. Thus, the distance between the imaged planes along z is set to $\Delta z = 10\,\text{mm}$, which is the image-voxel size along range. Note that Δx, Δy, and Δz determine the volume over which the OUT contrast is averaged in the quantitative reconstruction.

Fig. 2.5 shows the OUT simulation setup when the antennas are at the centers of the top and bottom apertures, $(x, y) = (0, 0)$. The positions of the three imaged slices, relative to antennas and objects are indicated in Fig. 2.5b. A lossy X-shaped object with relative permittivity of $\epsilon_\text{r} = 32 - \text{i}16$ and a small cube of $\epsilon_\text{r} = 50 - \text{i}5$ are embedded inside a lossy rectangular prism of $\epsilon_\text{r} = 24 - \text{i}3$. The X-shape's arm length is 20 mm whereas the height and width of each arm are 2 mm. The side of the small cube is 2 mm. The thickness of the prism (along z) is 20 mm and its lateral sides along x and y are both 24 mm.

The PSFs are acquired with the scattering-probe (SP) simulation setup, where the antenna arrangement, the scan aperture and sampling, and the background medium are identical to those in the OUT simulation. The SP is a cubicle with relative permittivity of $\epsilon_\text{r} = 30$ and a size of $2 \times 2 \times 2\,\text{mm}^3$. With three separate simulations, the PSFs are obtained for three SP range positions: $z' = 10$, 20, and 30 mm, where the SP is at the center $x' = y' = 0$.

The incident-field (RO) S-parameters are obtained through a single frequency-sweep simulation with the antenna setup and the background medium being the same as in the OUT and SP simulations. Scanning along x and y is unnecessary since the background is uniform and infinite.

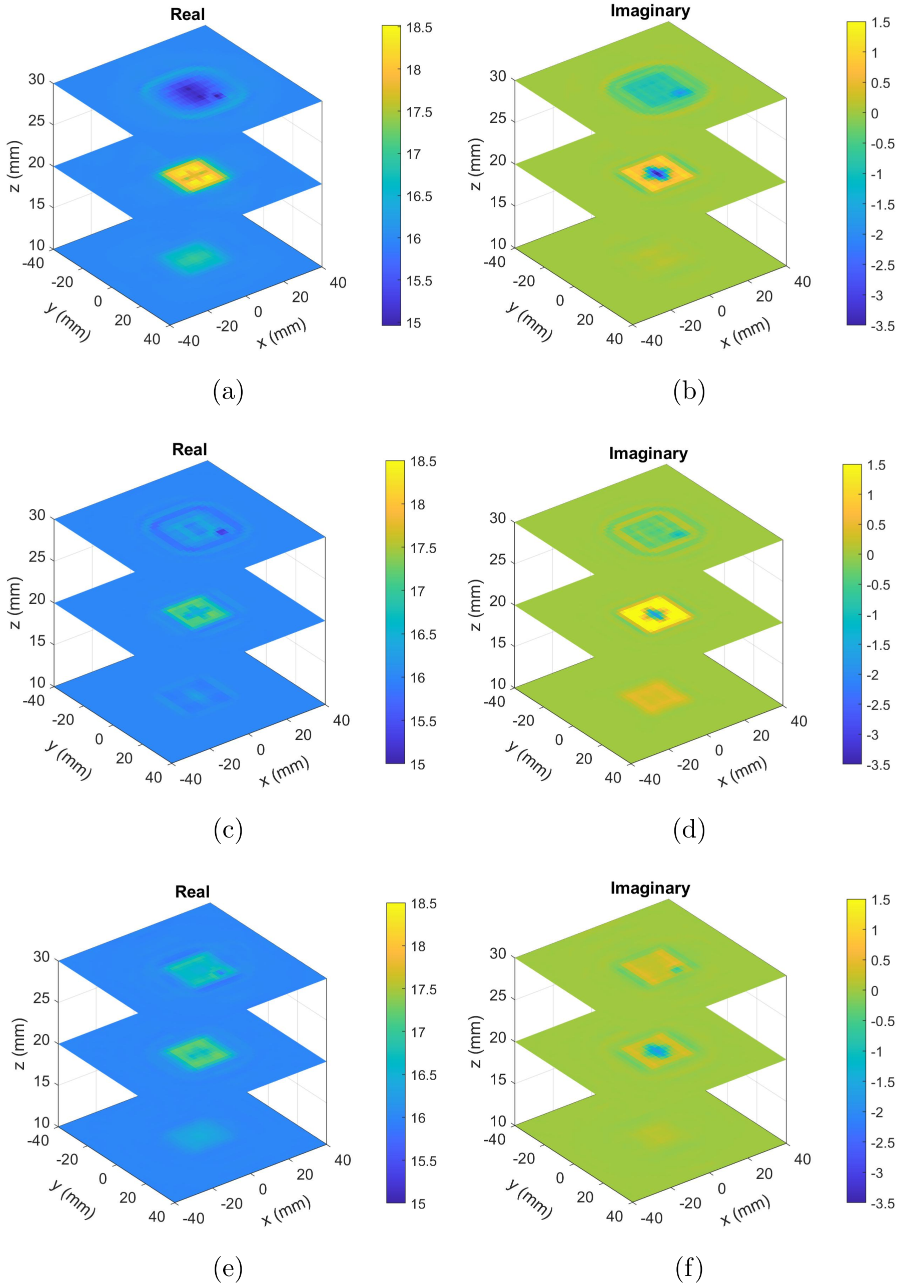

(a) (b)

(c) (d)

(e) (f)

Figure 2.6: 3D reconstructions of the permittivity in the simulation example, where an X-shaped object and a cubicle are embedded in a larger lossy prism: (a), (b) using Born's approximation, (c), (d) using Rytov's approximation, and (e), (f) using the combined Born-Rytov method.

Fig. 2.6 presents the quantitative images of the OUT of Fig. 2.5 in terms of the three range slices where the PSFs are available. The images are obtained with the three F-SPM algorithms summarized in the previous section. All three image sets (for the real and imaginary OUT permittivity functions) can locate the lossy X-shape embedded inside the middle layer of the larger prism as well as the small cube in the top layer. However, the best structural accuracy is achieved in the combined Born-Rytov reconstruction shown in Fig. 2.6e (real permittivity) and Fig. 2.6f (imaginary permittivity). First, this reconstruction shows the best lateral spatial resolution, judging from the size of the reconstructed small cube in the top slice ($z' = 30\,\mathrm{mm}$). Second, it also captures best the square shape of the large prism in this slice with very little ripple artifacts or range artifacts from the X-shape. In contrast, the Born-based (Fig. 2.6a and Fig. 2.6b) and the Rytov-based (Fig. 2.6c and Fig. 2.6d) reconstructions show faint artifacts of the X-shape in the real-permittivity image in the top slice ($z' = 30\,\mathrm{mm}$). Additionally, the Rytov-based reconstruction in Fig. 2.6c also shows an artifact of the X-shape in the real-permittivity image in the bottom slice ($z' = 10\,\mathrm{mm}$). The likely reason for the more significant range artifacts in the Rytov-based reconstruction is that the phase unwrapping of the OUT data fails at several frequencies. Phase unwrapping failures lead to “ripple” artifacts in both range and cross-range.

The combined Born-Rytov reconstruction also proves to be superior in terms of the quantitative permittivity estimates, especially for the imaginary part of permittivity shown in Fig. 2.6f. We emphasize that the estimated contrast is averaged over a range distance of $\Delta z = 10\,\mathrm{mm}$. It also correctly identifies in the real-permittivity image in Fig. 2.6f that the slice at $z' = 30\,\mathrm{mm}$ has a higher averaged permittivity compared to the slice at $z' = 10\,\text{mm}$, which lies in the background medium. In contrast, the Born-based reconstruction in Fig. 2.6a incorrectly indicates that the slice at $z' = 30\,\text{mm}$ has a lower averaged permittivity than the slice at $z' = 10\,\text{mm}$.

We also observe that in all images the estimated real permittivity values of the X-shape and the cube embedded in the large prism are incorrect, i.e., lower than that of the prism whereas in reality they are higher. This is attributed to the linearizing approximation of the nonlinear model of scattering in all three reconstructions. In this example, a large portion of the background is replaced by the high-loss high-contrast prism, which violates the limits of both approximations; see (2.18) and (2.19). This leads to large differences between the total internal field and the incident field which replaces it in the linear model of scattering. Thus, the example elucidates the limitations of real-time quantitative reconstruction. These limitations cannot be overcome by the combined use of Born's and Rytov's approximations.

To evaluate the precision of the reconstructed permittivities of objects, the root mean square error (RMSE) is used [36]:

$$RMSE = \sqrt{\frac{1}{N_{\text{v}}} \sum_{n=1}^{N_{\text{v}}} |\epsilon_{\text{r}}(\mathbf{r}'_n) - \overline{\epsilon_{\text{r}}}(\mathbf{r}'_n)|^2}\,, \tag{2.46}$$

where $\overline{\epsilon_{\text{r}}}(\mathbf{r}'_n)$ is the true distribution of the complex permittivity. The corresponding errors of the reconstructed complex relative permittivity with Born's, Rytov's, and the combined Born-Rytov approaches are obtained as 0.0995, 0.1008, and 0.0869, respectively. Although the errors are not that different, they verify that the combined Born-Rytov reconstruction provides better quantitative estimates compared to the other two methods.

Further analysis of the quantitative accuracy is carried out in terms of the root mean square (RMS) residual errors. Here, the residual error [37, 81] refers to the difference between the measured OUT scattered-field data and the data obtained from the model (2.3) when the reconstructed permittivity is substituted. The RMS residuals of the Born-based, Rytov-based, and Born-Rytov solutions are 0.081, 0.0891, and 0.0568, respectively, indicating best quantitative accuracy for the combined approach. All three residuals are relatively low, which shows that the unwanted errors introduced by the inversion in Fourier space are small.

The computational costs of the Born-based, Rytov-based and combined Born-Rytov F-SPM reconstructions are approximately 1.82 s, 1.88 s, and 2.84 s, respectively. These execution times are obtained on an Intel Core i7-8750H @ 2.20 GHz system, using MATLAB [82], without parallel computing or code optimization. On the other hand, the BCCB-SPM reconstruction is approximately 11 times slower than the proposed method (about 31 s).

2.7 Image Reconstruction with Measured Data

In this experiment, near-field measurements are performed with a heterogeneous compressed breast phantom, which includes four tumor simulants immersed in various healthy-tissue simulants. The imaging setup and the phantom are identical to those presented in [49]. Note that this is not a clinical prototype. The scanning setup is used here to verify the imaging algorithm.

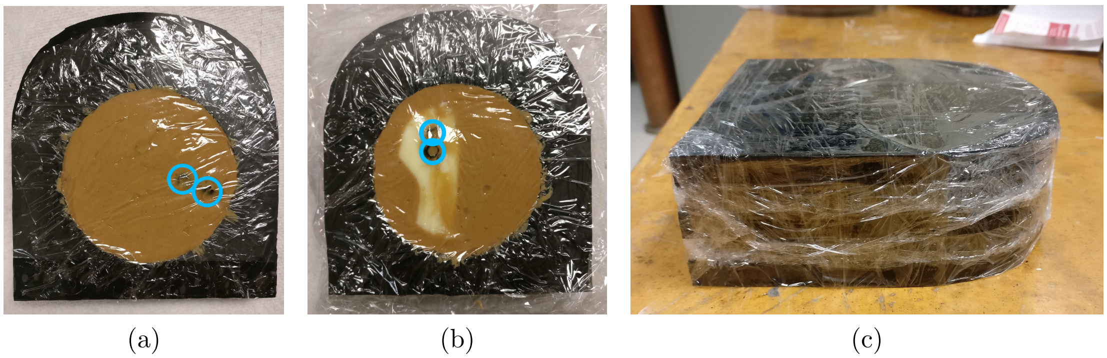
(a) (b) (c)

Figure 2.7: Photos of the breast phantom: (a) Layer 2 which contains two tumor simulants surrounded by the matching material; (b) Layer 4 which contains two tumor simulants surrounded by the fibroglandular simulant and matching material; and (c) the assembled phantom. The phantom is enclosed in plastic wrap to hold it together and protect it from the embedding medium. Photos taken from [49].

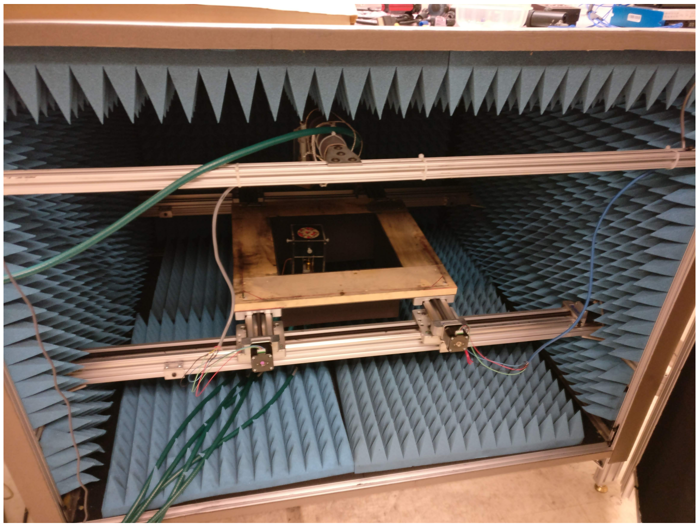

Figure 2.8: Photo of the measurement setup used to scan the breast phantom and its respective RO and CO. Photo taken from [48].

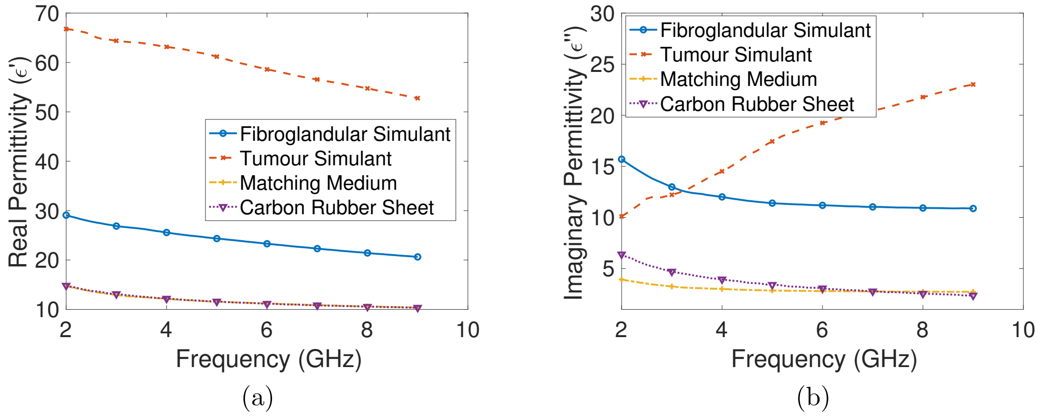

(a) (b)

Figure 2.9: Dielectric properties of phantom materials from 3 GHz to 9 GHz [49].

The breast phantom (the OUT) comprises a number of dispersive materials as shown in Fig. 2.9. Note that there is no skin-like material in this experiment. A compressed breast phantom of thickness 55 mm is constructed from five carbon-rubber sheets (each 11 mm thick) with an averaged complex permittivity selected to mimic a BIRADS Type II density of the breast (scattered fibroglandular tissue). Each sheet defines a layer where additional tissue simulants can be inserted. Layers 1, 3, and 5 are left intact; they are homogeneous. In Layers 2 and 4, circular sections (80 mm diameter) are removed. In Layer 2 (second from the bottom), two 1-cm diameter spherical tumor simulants are inserted in the embedding medium touching each other as indicated in Fig. 2.7a by the black circles. This placement of the tumor simulants is used to evaluate the image resolution of the system in the case of a high contrast between malignant and healthy tissue. In Layer 4 (fourth from the bottom), a material mimicking healthy fibroglandular tissue is used to make an irregularly shaped inclusion; see white-colored inclusion in Fig. 2.7b. Two more tumor simulants are inserted within this fibroglandular object. Again, the two tumor simulants are placed so that they touch each other in order to evaluate the spatial image resolution in the case of low contrast between malignant and healthy tissue. All inserts are carefully surrounded by the matching medium to remove the air pockets; see the brown substance in Fig. 2.7a and Fig. 2.7b. Layers 2 and 4 are wrapped with plastic wrap to contain all inclusions. After stacking all five layers, the whole phantom is also wrapped by plastic wrap to hold it together.

To measure the data PSF of the system, the calibration object (CO) is made of five sheets of the same carbon-rubber material. A cylindrical microwave-ceramics probe ($\epsilon_{\mathrm{r}} = 50 - \mathrm{i}0.05$) with a height of 10 mm and a radius of 5 mm is inserted at the center of the middle sheet (Layer 3). The axis of the cylindrical probe is aligned with the vertical z axis. Only one SP measurement is performed with the probe in Layer 3. As a result, the OUT images are only 2D with the permittivity contrasts being averaged along range (the z axis).

The phantom is placed in a *Plexiglas* tray filled with a matching medium identical to the embedding medium within the tissue phantom. The tray's bottom is 4.5 mm thick. A *Plexiglas* lid of thickness 1.5 mm is placed on top of the phantom to protect the antennas. The matching medium surrounds the side walls of the phantom to reduce the reflections from these walls. The top and bottom surfaces of the phantom are exposed to the antennas through the tray's bottom and lid. The antennas scan at a distance of about 1 mm.

To extract the scattered portion of the responses within the breast phantom (the OUT), an RO is first measured to obtain the incident-field responses. The RO comprises the tray filled with embedding medium, the thickness of which matches that of the phantom (about 55 mm).

The acquisition setup as shown in Fig. 2.8 comprises one transverse electromagnetic (TEM) horn antenna [83] as a transmitter at the top and an array of five Rx bow-tie antennas at the bottom [44]. The five Rx antennas receive one at a time and they are switched using an RF switching network (R3970 16-port adapter/switch) connected to a vector network analyzer (Advantest R3770). All antennas are designed for optimal impedance match when being in direct contact with the breast tissue. The antennas are fixed whereas the *Plexiglas* platform moves the measured object along a raster-scanning path. A frequency sweep from 3 GHz to 8 GHz in 100 MHz intervals is performed.

The VNA dynamic range is from about 118 dB at 3 GHz to about 112 dB at 8 GHz. However, the dynamic range of the actual measurement is much lower. The RO measurement indicates that the maximum transmission coefficient value through the nearly 60-mm thick lossy object, which includes the tissue phantom and the *Plexiglas* plates, is about -60 dB at 3 GHz and -90 dB at 8 GHz. Thus the measurement dynamic range is about 58 dB at 3 GHz and about 22 dB at 8 GHz. Further, the dynamic range of the scattered-field data supplied to the reconstruction algorithms is even lower. The maximum scattered-field transmission value as measured with the SP is about -84 dB at 3 GHz and -107 dB at 8 GHz. This yields very limited data dynamic range of about 35 dB at 3 GHz and 5 dB at 8 GHz. In order to improve the data dynamic range, we use a power amplifier at the transmitting antenna, the gain of which is approximately 50 dB across the frequency band. The estimated power transmitted by the TEM horn, after taking its efficiency into account [83], is about 2.6 W (averaged over the frequency band). The experimental setup with the power amplifier has been evaluated for data quality control [48] to ensure sufficient signal-to-noise ratio of the measured PSFs. It is important to note that this experiment has not been evaluated in terms of the specific absorption rate (SAR) in the tissue since this is not a clinical prototype. However, with careful design of the antenna arrays and the acquisition setup, the transmitted-power requirements can be significantly reduced in order to operate within the SAR limits for the medical imaging systems; see, e.g., [84]. Examples of such clinically viable systems can be found in [85, 86].

The system scans across a 141 mm by 141 mm aperture in 3-mm sampling steps along x and y. The system allows for the measurement of the five transmission coefficients. Since reflection coefficients are not available and the offset distance between the antennas in the bow-tie receiving array is small (20 mm), the imaging system lacks range resolution. This is why only one PSF is measured with the SP at the center of the background medium and the reconstruction is 2D.

In experiments, especially with near-field measurements, filtering is important for successful reconstruction. Fourier-space methods, F-SPM included, are prone to ringing artifacts if the data are not continuous across the aperture edges [47]. Data apodization in (x, y) space mitigates such artifacts. Further, post-inversion low-pass filtering of the reconstructed contrast in k-space ensures the suppression of high spatial-frequency noise and errors. These are due to the very weak signal components of spatial frequencies at or beyond the limit of $k_{\max} \approx 2\pi/\lambda_{\min}$, where $\lambda_{\min}$ is the shortest wavelength in the background medium [47]. Such k-space components correspond to evanescent waves or waves propagating at near-grazing angles at the acquisition plane. Since the background medium in this example is very lossy, such modes are below the noise and uncertainty of the measurement.

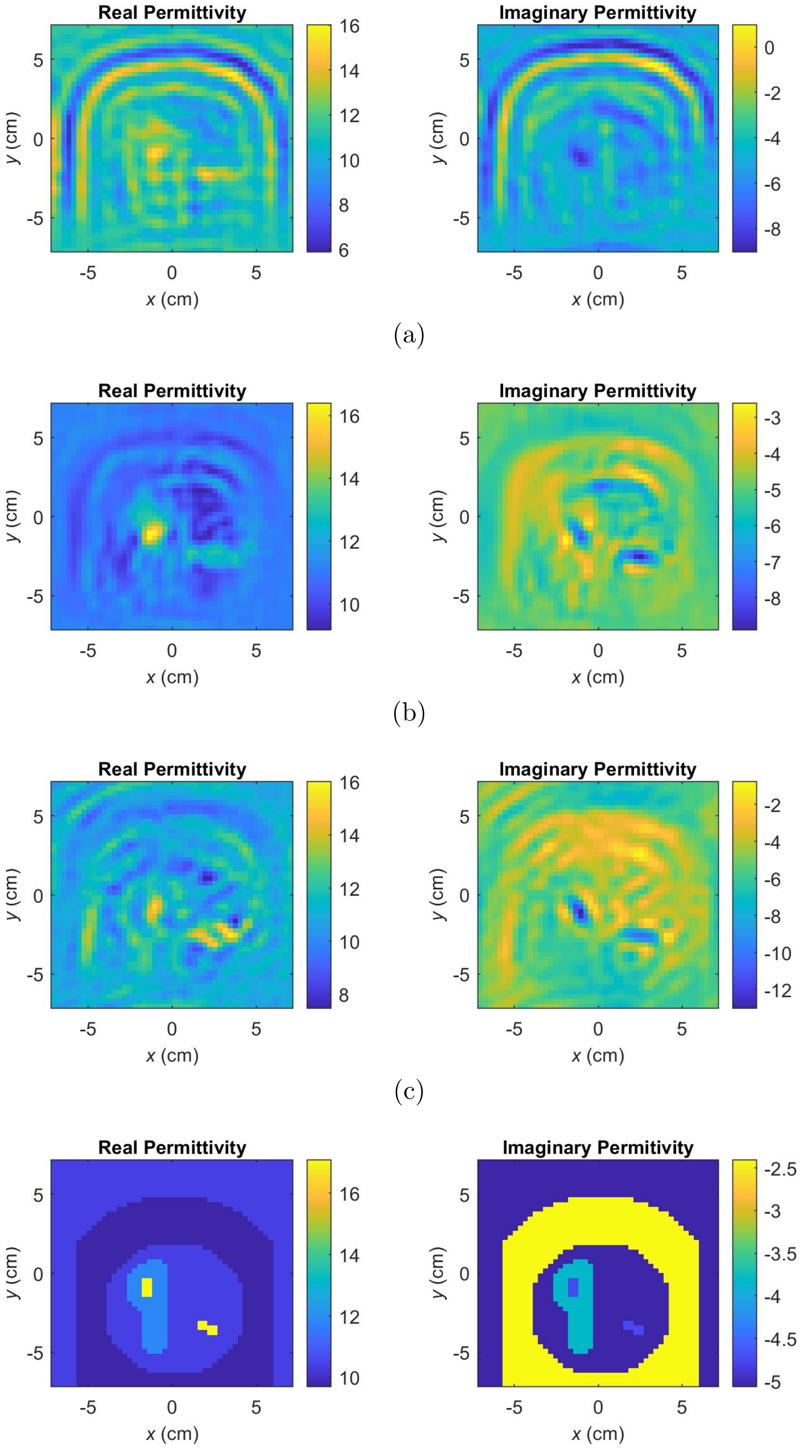

Figure 2.10: 2D reconstructions of the real and imaginary parts of the permittivity of the breast phantom with the F-SPM method using: (a) Born's data approximation, (b) Rytov's data approximation, and (c) the combined Born-Rytov approach. (d) The averaged 2D permttivity map of the breast phantom [60]. The averaging is performed over all frequencies and along depth.

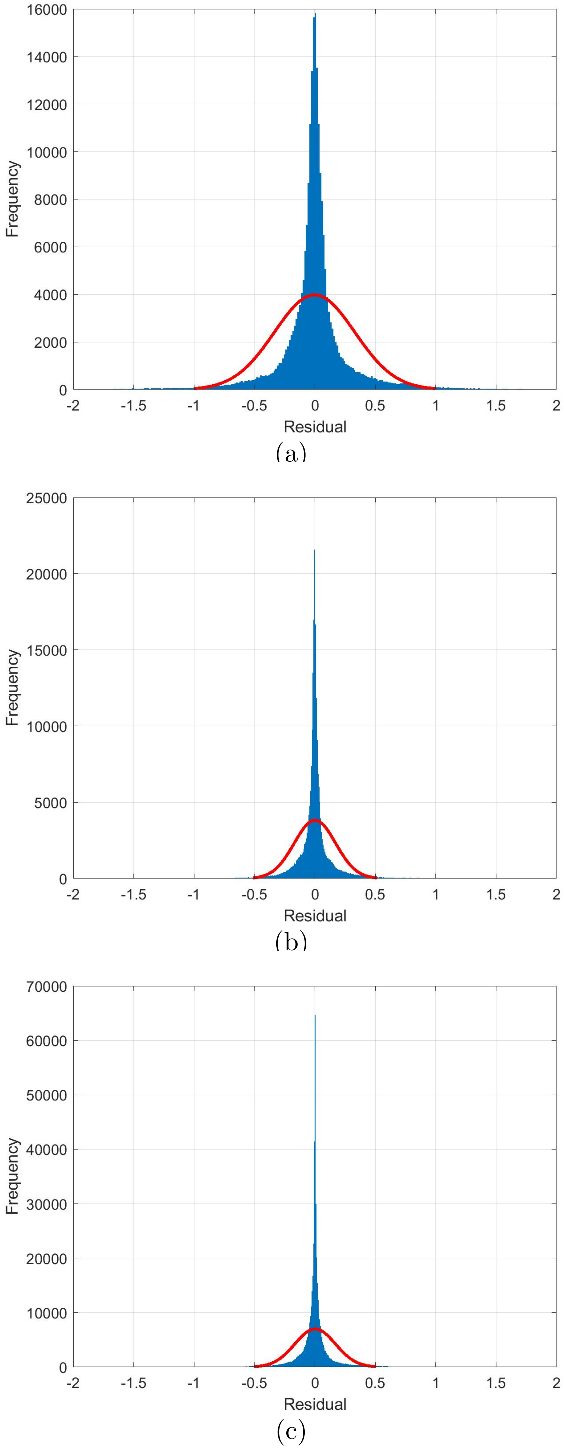

(a)

(b)

(c)

Figure 2.11: Histograms of the residuals for the F-SPM inverse solution in the breast-phantom example in the case of: (a) Born-based method, (b) Rytov-based method, and (c) combined Born-Rytov method.

The F-SPM 2D reconstructions for the heterogeneous breast phantom are shown in Fig. 2.10a (Born-based), Fig. 2.10b (Rytov-based), and Fig. 2.10c (combined Born-Rytov). The ringing artifacts in the Born-based reconstruction are strong. They are due to the abrupt permittivity change at the edges of the phantom where the plastic wrap introduces a gap of very low permittvity compared to the phantom and the embedding medium. Although very thin, this gap runs throughout the depth of the measured object and its impact on the measured responses is significant. These artifacts are considerably reduced in the Rytov-based reconstruction; see Fig. 2.10b.

It is observed that, unlike in the simulation-based example, here, Born's and Rytov's data approximations lead to significantly different images. This is due to the significant difference between the scattered data extracted with the two approximations. This situation arises when the scattered responses are strong relative to the incident ones. It is expected that the combined Born-Rytov reconstruction is the most beneficial in such cases. Fig. 2.10c shows the images resulting from this reconstruction. Similarly to the simulation-based example, these images exhibit the best structural and quantitative accuracy. Specifically, the ringing artifacts are suppressed, the shape of the healthy fibroglandular inclusion in Layer 4 is well captured, especially in the real-permittivity image, and the spatial resolution is marginally sufficient to distinguish the two tumor simulants in Layer 2 (high contrast with the embedding medium). Both the real and imaginary permittivity images display remarkable contrast at the location of the tumor simulants. We also observe that the spatial resolution is insufficient to differentiate the two spherical tumor simulants in Layer 4 where they are embedded in the high-permittivity healthy fibroglandular tissue. Overall, the proposed combined Born-Rytov F-SPM algorithm is beneficial in the near-field imaging of strongly heterogeneous objects when compared to the Born or the Rytov approximations alone.

In order to obtain the RMSE of the breast phantom reconstructions, the permittivity distribution displayed in Fig. 2.10d is used as a reference. The RMSE values for the Born-based, Rytov-based, and Born-Rytov reconstruction approaches are 2.75, 2.109, and 2.405, respectively. It is interesting to observe that the Rytov-based reconstruction appears to provide the best quantitative accuracy. Note that in this example the OUT data phase unwrapping is successful, which is a prerequisite for artifact-free reconstruction.

Fig. 2.11 shows the histograms of the the residual errors for the breast phantom experiment. The residual errors represent the differences between the scattered-field responses extracted from the measurements and the respective responses computed with the forward model where the reconstructed complex permittivity is substituted. The number of residual errors in the Born-only and Rytov-only reconstructions (1 175 040) corresponds to 5 scattered responses (real and imaginary parts), 48×48 spatial samples, and 51 frequency samples. Since the combined Born-Rytov method utilizes both approximations to form the forward model, the samples are twice that number. A normal distribution is fitted to the histograms using *histfit* command of MATLAB; see Fig. 2.11. All three residual error distributions demonstrate that there is no significant bias introduced into the problem [37, 81]. The standard deviation of the residual errors for the Born, Rytov, and Born-Rytov are found to be 0.333, 0.171, and 0.168, respectively, indicating the best accuracy in the proposed combined approach. Finally, the RMS residual errors for the Born, Rytov, and Born-Rytov reconstructions, are 0.5096, 0.1363, and 0.1405, respectively. These values are in agreement with the image RMSE results. Note that although the RMSE and RMS-residual values are somewhat higher for the combined Born-Rytov approach compared to the Rytov-based one, they still provide better quantitative estimates compared to the Born-based F-SPM.

The execution times in this example are approximately 1.5 s, 2.4 s, and 1.99 s for the Born, Rytov, and the combined Born-Rytov methods, respectively. Since there is no need for phase unwrapping of the OUT data, the combined Born-Rytov algorithm tends to have lower computation cost compared to Rytov alone. In comparison, the computational cost of the BCCB-SPM algorithm is about 20.2 seconds.

To further validate the benefits of the proposed combined Born-Rytov F-SPM algorithm, a far-field experiment is conducted at millimeter-wave frequencies. The data acquisition involves only the transmission-coefficient (S_{21}) measurements with planar scanning using two WR-28 horn antennas aligned along each other's boresight at a distance of 20 cm. The measurements are from 26 GHz to 40 GHz with 200 MHz intervals. This frequency sampling sets the maximum range to about 37 cm, using the standard expression that can be found in [36]. Since the imaged volume has a range extent of 20 cm, the frequency interval is sufficiently small to satisfy the Nyquist criterion and prevent range aliasing. The antennas operate in air. The scanned area is 20 cm × 20 cm and the sampling step along x and y is 2 mm.

The inspected object is a plush teddy bear toy. As shown in Fig. 2.12a, it is laid flat on the positioning platform, where it occupies an area of approximately 23 cm in width (across the arms) and 25 cm in length. The size of the toy in the vertical direction (along range), as measured from the back of the head to the tip of the nose, is approximately 13 cm. A cross-shape inclusion (shown in Fig. 2.12b) is embedded in the teddy bear's tummy. Its overall arm length is 3 cm and its height is 1 cm. Its relative permittivity is $\epsilon_{\rm r} = 18 - {\rm i}0.006$.

A cylindrical SP of radius 5 mm and height 10 mm is used to acquire the S_{21} PSF. It is made of microwave ceramics with relative permittivity $\epsilon_{\rm r,sp} = 12$. The probe is placed directly on the tray at the center of the scanned area.

(a) (b)

Figure 2.12: Photos of the setup of the millimeter-wave imaging experiment: (a) a teddy bear toy as an inspected object lying flat on the *Plexiglas* platform; (b) the cross-shape inclusion which is inside the teddy bear's tummy.

The 2D projection images produced by the F-SPM reconstructions are shown in Fig. 2.13. The shape of the teddy bear and the item inside are well identified in the Born-based results in Fig. 2.13a. The high-permittivity regions at the teddy bear's underarms are likely a result of its T-shirt sleeves rolled up and clumped in the underarms. In fact, the T-shirt, which partially covers the torso of the teddy bear, is also visible. The cross-shape item is very apparent in the imaginary-permittivity image and less so in the real-permittivity image.

The Rytov-based reconstruction in Fig. 2.13b is distorted by strong artifacts.

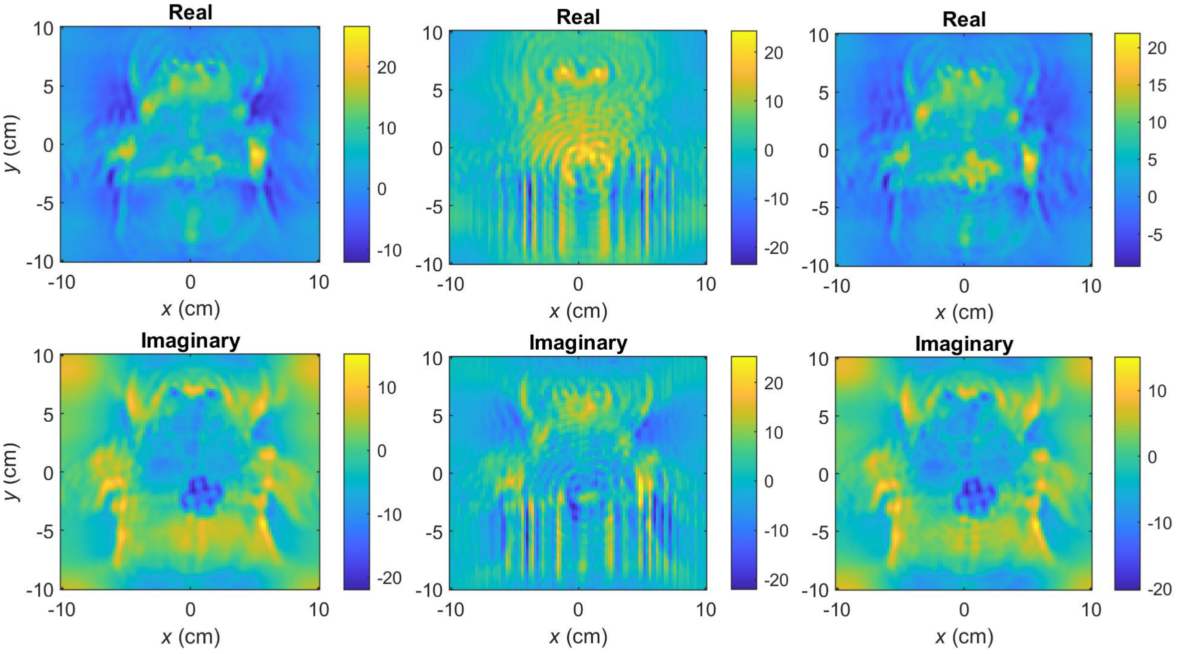

(a) (b) (c)

Figure 2.13: 2D reconstructions of the real and imaginary parts of the permittivity of the teddy bear object with the F-SPM algorithms using: (a) Born's approximation, (b) Rytov's approximation, and (c) the combined Born-Rytov approach.

These are due to the failure of the phase unwrapping at most frequencies. The high-permittivity cross-shape inclusion leads to sharp discontinuities in the phase of S_{21}^{tot} as a function of x and y, including jumps by $\pm\pi$, which are due to the inclusion and not phase wrapping. Such discontinuities cannot be handled by the 2D phase unwrapping algorithm [80].

The combined Born-Rytov approach does not suffer from artifacts (see Fig. 2.13c) since the phase unwrapping is avoided altogether. The image reconstruction is structurally very similar to that in the Born-based reconstruction. On the other hand, the real-permittivity image provides a better quantitative estimate compared to the Born-based result, with the inclusion being of higher contrast relative to the teddy bear itself. Overall, the combined Born-Rytov approach provides an improvement over the Born-based and the Rytov-based approaches, which agrees with the results in the previous simulation-based and experimental examples. In this real-life experiment, calculating the RMSE of the reconstructions is not possible since the permittivity of all the materials in the teddy bear toy are not known. These materials include the filling, the torso fabric, the T-shirt fabric, the plastics used for the eyes and the nose. The images also suggest that the increased fabric density at the stitches and the clumps of material affect significantly the millimeter-wave scattering and the quantitative reconstruction.

Finally, we note that both the Born-based and the combined Born-Rytov approaches overestimate significantly the imaginary part of the inclusion's permittivity. This is likely due to the large electrical size of the SP. In order the SP to properly emulate a point scatterer, it has to be of size not exceeding $\lambda_{\min}/8$ ($\approx 1\,\text{mm}$ at 40 GHz) whereas the SP size here is 1 cm in the lateral and depth directions. This choice of SP is dictated by the need to obtain good signal-to-noise ratio (SNR) in the measurements used to extract the system PSF. While the so extracted PSF ensures high-fidelity structural reconstruction, it leads to significant errors in the quantitative reconstruction. Thus, this example illustrates the limitations of real-time quantitative reconstruction with the linearized model of scattering, even if it employs a measured system-specific PSF. While in near-field imaging, high SNR PSFs can be measured with electrically small SPs, in far-field experiments this may be difficult to achieve.

The execution times for the Born, Rytov, and the combined Born-Rytov methods are approximately 1.24 s, 3.07 s, and 2.48 s, respectively. An acceleration factor of 36 is observed compared to the BCCB-SPM algorithm which has an execution time of 97 seconds.

2.8 Conclusion

We have proposed an efficient real-time image-reconstruction algorithm which dramatically improves the speed of the scattered-power mapping (SPM) imaging method by performing the computation of the scattered power maps in Fourier space. It is shown that significant time savings are realized compared to the previously proposed BCCB-SPM algorithm. The execution times reported here are achieved on a personal laptop with implementation in MATLAB. These execution times can be further reduced significantly with code optimization and parallel computing since large portions of the computations are independent, e.g., the 2D FTs of the OUT and PSF data sets of the various response types and at the various frequencies as well as the solutions of the quantitative systems of equations at each point in k-space.

Furthermore, we have proposed a combined Born-Rytov F-SPM image-reconstruction method that benefits from using Rytov's approximation in addition to the Born approximation while avoiding altogether the need to perform phase unwrapping on the OUT data. It has been shown through simulation-based and experimental examples that this combined approach consistently enhances the image quality in terms of structural and quantitative accuracy.

Future work aims at improving the quantitative accuracy in the reconstructed images. The quantitative inaccuracy in real-time imaging, the F-SPM method included, is rooted in the linearization of the inherently nonlinear model of scattering. Therefore, this problem needs to be addressed through the use of higher-order Born or Rytov approximations of the total internal field that can account for multiple-scattering and mutual-coupling effects.

BIBLIOGRAPHY

[1] D. M. Sheen, D. L. McMakin, and T. E. Hall, "Three-dimensional millimeter-wave imaging for concealed weapon detection," *IEEE Trans. Microw. Theory Techn.*, vol. 49, no. 9, pp. 1581–1592, Sep. 2001.

[2] S. Lambot, E. C. Slob, I. van den Bosch, B. Stockbroeckx, and M. Vanclooster, "Modeling of ground-penetrating radar for accurate characterization of subsurface electric properties," *IEEE Trans. Geosci. Remote Sens.*, vol. 42, no. 11, pp. 2555–2568, Nov. 2004.

[3] M. Dehmollaian and K. Sarabandi, "Refocusing through building walls using synthetic aperture radar," *IEEE Trans. Geosci. Remote Sens.*, vol. 46, no. 6, pp. 1589–1599, Jun. 2008.

[4] M. Benedetti, M. Donelli, and A. Massa, "Multicrack detection in two-dimensional structures by means of GA-based strategies," *IEEE Trans. Antennas Propag.*, vol. 55, no. 1, pp. 205–215, Jan. 2007.

[5] Y. Meng, C. Lin, J. Zang, A. Qing, and N. K. Nikolova, "General theory of holographic inversion with linear frequency modulation radar and its application to whole-body security scanning," *IEEE Trans. Microw. Theory Techn.*, vol. 68, no. 11, pp. 4694–4705, Nov. 2020.

[6] J. R. Gallion and R. Zoughi, "Millimeter-wave imaging of surface-breaking cracks in steel with severe surface corrosion," *IEEE Trans. Instrum. Meas.*, vol. 66, no. 10, pp. 2789–2791, Oct. 2017.

[7] M. Zoofaghari, A. Tavakoli, and M. Dehmollaian, "Reconstruction of concealed objects in a corrugated wall with a smoothly varying roughness using the linear sampling method," *IEEE Trans. Geosci. Remote Sens.*, vol. 54, no. 6, pp. 3589–3598, Jun. 2016.

[8] M. Moallem and K. Sarabandi, "Polarimetric study of MMW imaging radars for indoor navigation and mapping," *IEEE Trans. Antennas Propag.*, vol. 62, no. 1, pp. 500–504, Jan. 2014.

[9] C. A. Schuetz, C. Harrity, G. J. Schneider, J. Murakowski, S. Shi, J. Deroba, and D. W. Prather, "A promising outlook for imaging radar: Imaging flash radar realized using photonic spatial beam processing," *IEEE Microw. Mag.*, vol. 19, no. 3, pp. 91–101, May 2018.

[10] F. Topfer and J. Oberhammer, "Millimeter-wave tissue diagnosis: The most promising fields for medical applications," *IEEE Microw. Mag.*, vol. 16, no. 4, pp. 97–113, May 2015.

[11] P. M. Meaney, D. Goodwin, A. H. Golnabi, T. Zhou, M. Pallone, S. D. Geimer, G. Burke, and K. D. Paulsen, "Clinical microwave tomographic imaging of the calcaneus: A first-in-human case study of two subjects," *IEEE Trans. Biomed. Eng.*, vol. 59, no. 12, pp. 3304–3313, Dec. 2012.

[12] R. Scapaticci, L. Di Donato, I. Catapano, and L. Crocco, "A feasibility study on microwave imaging for brain stroke monitoring," *Prog. Electromagn. Res. B*, vol. 40, Jan. 2012.

[13] A. Fhager, S. Candefjord, M. Elam, and M. Persson, “Microwave diagnostics ahead: Saving time and the lives of trauma and stroke patients,” *IEEE Microw. Mag.*, vol. 19, no. 3, pp. 78–90, May 2018.

[14] D. Ireland, K. Bialkowski, and A. Abbosh, “Microwave imaging for brain stroke detection using Born iterative method,” *IET Microw. Antennas Propag.*, vol. 7, pp. 909–915, Aug. 2013.

[15] D. O’Loughlin, M. O’Halloran, B. M. Moloney, M. Glavin, E. Jones, and M. A. Elahi, “Microwave breast imaging: Clinical advances and remaining challenges,” *IEEE Trans. Biomed. Eng.*, vol. 65, no. 11, pp. 2580–2590, Nov. 2018.

[16] A. Mirbeik-Sabzevari and N. Tavassolian, “Tumor detection using millimeter-wave technology: Differentiating between benign lesions and cancer tissues,” *IEEE Microw. Mag.*, vol. 20, no. 8, pp. 30–43, Aug. 2019.

[17] E. C. Fear, X. Li, S. C. Hagness, and M. A. Stuchly, “Confocal microwave imaging for breast cancer detection: localization of tumors in three dimensions,” *IEEE Trans. Biomed. Eng.*, vol. 49, no. 8, pp. 812–822, Aug. 2002.

[18] N. K. Nikolova, *Microwave Biomedical Imaging.* American Cancer Society, 2014, pp. 1–22. [Online]. Available: https://onlinelibrary.wiley.com/doi/abs/10.1002/047134608X.W8214

[19] A. W. Preece, I. Craddock, M. Shere, L. Jones, and H. L. Winton, “MARIA M4: clinical evaluation of a prototype ultrawideband radar scanner for breast cancer detection,” *J. Med. Imaging*, vol. 3, no. 3, pp. 1 – 7, Jul. 2016.

[20] A. Fasoula, S. Anwar, Y. Toutain, and L. Duchesne, "Microwave vision: From RF safety to medical imaging," in *2017 11th Eur. Conf. Antennas Propag. EUCAP*, Mar. 2017, pp. 2746–2750.

[21] D. O'Loughlin, M. O'Halloran, B. M. Moloney, M. Glavin, E. Jones, and M. A. Elahi, "Microwave breast imaging: Clinical advances and remaining challenges," *IEEE Trans. Biomed. Eng.*, vol. 65, no. 11, pp. 2580–2590, Nov. 2018.

[22] M. Pastorino, *Microwave Imaging.* John Wiley & Sons, 2010.

[23] C. Xudong, *Computational Methods for Electromagnetic Inverse Scattering.* Wiley-IEEE, 2018.

[24] D. W. Winters, B. D. Van Veen, and S. C. Hagness, "A sparsity regularization approach to the electromagnetic inverse scattering problem," *IEEE Trans. Antennas Propag.*, vol. 58, no. 1, pp. 145–154, Jan. 2010.

[25] T. Rubaek, P. M. Meaney, P. Meincke, and K. D. Paulsen, "Nonlinear microwave imaging for breast-cancer screening using Gauss–Newton's method and the CGLS inversion algorithm," *IEEE Trans. Antennas Propag.*, vol. 55, no. 8, pp. 2320–2331, Aug. 2007.

[26] Q. Fang, P. M. Meaney, and K. D. Paulsen, "Viable three-dimensional medical microwave tomography: Theory and numerical experiments," *IEEE Trans. Antennas Propag.*, vol. 58, no. 2, pp. 449–458, Feb. 2010.

[27] M. Ostadrahimi, P. Mojabi, A. Zakaria, J. LoVetri, and L. Shafai, "Enhancement of Gauss–Newton inversion method for biological tissue imaging," *IEEE Trans. Microw. Theory Techn.*, vol. 61, no. 9, pp. 3424–3434, Sep. 2013.

[28] P. Tournier, M. Bonazzoli, V. Dolean, F. Rapetti, F. Hecht, F. Nataf, I. Aliferis, I. El Kanfoud, C. Migliaccio, M. de Buhan, M. Darbas, S. Semenov, and C. Pichot, "Numerical modeling and high-speed parallel computing: New perspectives on tomographic microwave imaging for brain stroke detection and monitoring." *IEEE Antennas Propag. Mag.*, vol. 59, no. 5, pp. 98–110, Oct. 2017.

[29] C. Estatico, A. Fedeli, M. Pastorino, and A. Randazzo, "Quantitative microwave imaging method in Lebesgue spaces with nonconstant exponents," *IEEE Trans. Antennas Propag.*, vol. 66, no. 12, pp. 7282–7294, Dec. 2018.

[30] I. Bisio, C. Estatico, A. Fedeli, F. Lavagetto, M. Pastorino, A. Randazzo, and A. Sciarrone, "Brain stroke microwave imaging by means of a Newton-Conjugate-Gradient method in l^p banach spaces," *IEEE Trans. Microw. Theory Techn.*, vol. 66, no. 8, pp. 3668–3682, Aug. 2018.

[31] V. L. Coli, P. Tournier, V. Dolean, I. E. Kanfoud, C. Pichot, C. Migliaccio, and L. Blanc-Féraud, "Detection of simulated brain strokes using microwave tomography," *IEEE J. Electromagn. RF Microw. Med. Biol.*, vol. 3, no. 4, pp. 254–260, Dec. 2019.

[32] M. Asefi and J. LoVetri, "Use of field-perturbing elements to increase nonredundant data for microwave imaging systems," *IEEE Trans. Microw. Theory Techn.*, vol. 65, no. 9, pp. 3172–3179, Sep. 2017.

[33] M. Asefi, A. Baran, and J. LoVetri, "An experimental phantom study for air-based quasi-resonant microwave breast imaging," *IEEE Trans. Microw. Theory Techn.*, vol. 67, no. 9, pp. 3946–3954, Sep. 2019.

[34] N. Abdollahi, I. Jeffrey, and J. LoVetri, “Improved tumor detection via quantitative microwave breast imaging using eigenfunction-based prior,” *IEEE Trans. Comput. Imag.*, vol. 6, pp. 1194–1202, Jul. 2020.

[35] M. Hopfer, R. Planas, A. Hamidipour, T. Henriksson, and S. Semenov, “Electromagnetic tomography for detection, differentiation, and monitoring of brain stroke: A virtual data and human head phantom study.” *IEEE Antennas Propag. Mag.*, vol. 59, no. 5, pp. 86–97, Oct. 2017.

[36] N. K. Nikolova, *Introduction to Microwave Imaging*, ser. EuMA High Frequency Technologies Series. Cambridge University Press, 2017.

[37] P. M. Meaney, S. D. Geimer, and K. D. Paulsen, “Two-step inversion with a logarithmic transformation for microwave breast imaging,” *Med. Phys.*, vol. 44, p. 4239–4251, Jul. 2017.

[38] S. Hosseinzadegan, A. Fhager, M. Persson, S. D. Geimer, and P. M. Meaney, “Discrete dipole approximation-based microwave tomography for fast breast cancer imaging,” *IEEE Transactions on Microwave Theory and Techniques*, vol. 69, no. 5, pp. 2741–2752, 2021.

[39] D. Byrne, M. Halloran, M. Glavin, and E. Jones, “Data independent radar beamforming algorithms for breast cancer detection,” *Prog. Electromagn. Res.*, vol. 107, 2010.

[40] M. O’Halloran, M. Glavin, and E. Jones, “Performance and robustness of a multistatic MIST beamforming algorithm for breast cancer detection,” *Prog. Electromagn. Res.*, vol. 105, pp. 403–424, Jan. 2010.

[41] M. Soumekh, *Synthetic Aperture Radar Signal Processing with MATLAB Algorithms.* Wiley, 1999.

[42] D. Smith, O. Yurduseven, B. Livingstone, and V. Schejbal, "Microwave imaging using indirect holographic techniques," *Antennas Propag. Mag.*, vol. 56, no. 1, pp. 104–117, Feb. 2014.

[43] R. K. Amineh, A. Khalatpour, and N. K. Nikolova, "Three-dimensional microwave holographic imaging using co- and cross-polarized data," *IEEE Trans. Antennas Propag.*, vol. 60, no. 7, pp. 3526–3531, Jul. 2012.

[44] R. K. Amineh, J. J. McCombe, A. Khalatpour, and N. K. Nikolova, "Microwave holography using point-spread functions measured with calibration objects," *IEEE Trans. Instrum. Meas.*, vol. 64, no. 2, pp. 403–417, 2015.

[45] L. Wang, A. Al-Jumaily, and R. Simpkin, "Investigation of antenna array configurations using far-field holographic microwave imaging technique," *Prog. Electromagn. Res. M*, vol. 42, pp. 1–11, Apr. 2015.

[46] M. Elsdon, D. Smith, M. Leach, and S. J. Foti, "Experimental investigation of breast tumor imaging using indirect microwave holography," *Microw. Opt. Technol. Lett.*, vol. 48, no. 3, pp. 480–482, Mar. 2006. [Online]. Available: https://onlinelibrary.wiley.com/doi/abs/10.1002/mop.21384

[47] D. Tajik, A. Pitcher, and N. Nikolova, "Comparative study of the Rytov and Born approximations in quantitative microwave holography," *Prog. Electromagn. Res. B*, vol. 79, pp. 1–19, Jan. 2017.

[48] D. Tajik, J. Trac, and N. K. Nikolova, "Quality control of microwave equipment for tissue imaging," *IEEE J. Electromagn. RF Microw. Med. Biol.*, vol. 4, no. 1, pp. 52–60, Mar. 2020.

[49] D. Tajik, N. K. Nikolova, and M. D. Noseworthy, "Improving quantitative microwave holography through simultaneous use of the Born and Rytov approximations," in *2019 16th Eur. Radar Conf.*, Oct. 2019, pp. 281–284.

[50] D. Tajik, F. Foroutan, D. S. Shumakov, A. D. Pitcher, and N. K. Nikolova, "Real-time microwave imaging of a compressed breast phantom with planar scanning," *IEEE J. Electromagn. RF Microw. Med. Biol.*, vol. 2, no. 3, pp. 154–162, May 2018.

[51] S. Tu, J. J. McCombe, D. S. Shumakov, and N. K. Nikolova, "Fast quantitative microwave imaging with resolvent kernel extracted from measurements," *Inverse Problems*, vol. 31, no. 4, p. 045007, Apr. 2015. [Online]. Available: https://doi.org/10.1088/0266-5611/31/4/045007

[52] D. S. Shumakov and N. K. Nikolova, "Fast quantitative microwave imaging with scattered-power maps," *IEEE Trans. Microw. Theory Techn.*, vol. 66, no. 1, pp. 439–449, May 2018.

[53] D. S. Shumakov, D. Tajik, A. S. Beaverstone, and N. K. Nikolova, *Real-Time Quantitative Reconstruction Methods in Microwave Imaging.* Springer International Publishing, 2018, pp. 415–442.

[54] T. Habashy, R. Groom, and B. Spies, “Beyond the Born and Rytov approximations: A nonlinear approach to electromagnetic scattering,” *J. Geophys. Res.*, vol. 98, pp. 1759–1775, Feb. 1993.

[55] W. C. Chew, *Waves and Fields in Inhomogeneous Media.* Wiley-IEEE Press, 1995.

[56] M. Slaney, A. C. Kak, and L. E. Larsen, “Limitations of imaging with first-order diffraction tomography,” *IEEE Trans. Microw. Theory Techn.*, vol. 32, no. 8, pp. 860–874, Aug. 1984.

[57] F. C. Lin and M. A. Fiddy, “The Born–Rytov controversy: I. comparing analytical and approximate expressions for the one-dimensional deterministic case,” *J. Opt. Soc. Am. A*, vol. 9, no. 7, pp. 1102–1110, Jul. 1992.

[58] D. Marks, “A family of approximations spanning the Born and Rytov scattering series,” *Opt. Express*, vol. 14, pp. 8837–48, Sep. 2006.

[59] G. Tsihrintzis and A. Devaney, “Higher order (nonlinear) diffraction tomography: Inversion of the Rytov series,” *IEEE Trans. Inf. Theory*, vol. 46, pp. 1748 – 1761, Aug. 2000.

[60] D. Tajik, R. Kazemivala, and N. K. Nikolova, “Real-time imaging with simultaneous use of born and rytov approximations in quantitative microwave holography,” *IEEE Trans. Microw. Theory Techn.*, p. available through early access, Dec. 2021.

[61] T. Grzegorczyk, P. Meaney, S. Jeon, S. Geimer, and K. Paulsen, “Importance of phase unwrapping for the reconstruction of microwave tomographic images,” *Biomed. Opt. Express*, vol. 2, pp. 315–30, Feb. 2011.

[62] J. Szumowski, W. R. Coshow, F. Li, and S. F. Quinn, “Phase unwrapping in the three-point dixon method for fat suppression mr imaging,” *Radiology*, vol. 192, no. 2, pp. 555–561, Aug. 1994, pMID: 8029431.

[63] D. C. Ghiglia and L. A. Romero, “Robust two-dimensional weighted and unweighted phase unwrapping that uses fast transforms and iterative methods,” *J. Opt. Soc. Am. A*, vol. 11, no. 1, pp. 107–117, Jan. 1994. [Online]. Available: http://opg.optica.org/josaa/abstract.cfm?URI=josaa-11-1-107

[64] J. W. Goodman, *Speckle Phenomena in Optics: Theory and Applications*, 2nd ed. SPIE, 2020.

[65] M. Arevalillo-Herráez, D. Burton, M. Lalor, and M. Gdeisat, “Fast two-dimensional phase-unwrapping algorithm based on sorting by reliability following a noncontinuous path,” *Appl. Opt.*, vol. 41, pp. 7437–44, Jan. 2003.

[66] Q. Zhang, Y. Han, and Y. Wu, “Comparison and combination of three spatial phase unwrapping algorithms,” *Opt. Rev.*, vol. 26, pp. 380—-390, Aug. 2019.

[67] A. S. Beaverstone, D. S. Shumakov, and N. K. Nikolova, “Frequency-domain integral equations of scattering for complex scalar responses,” *IEEE Trans. Microw. Theory Techn.*, vol. 65, no. 4, pp. 1120–1132, Jan. 2017.

[68] D. M. Pozar, *Microwave Engineering*, 4th ed. John Wiley & Sons, 2012.

[69] R. K. Amineh, J. McCombe, and N. K. Nikolova, “Microwave holographic imaging using the antenna phaseless radiation pattern,” *IEEE Antennas Wireless Propag. Lett.*, vol. 11, pp. 1529–1532, Dec. 2012.

[70] Altiar FEKO, Electromagnetic Simulation Software. [Online]. Available: https://altairhyperworks.com/product/FEKO

[71] R. K Amineh, N. Nikolova, and M. Ravan, *Real-Time Three-Dimensional Imaging of Dielectric Bodies Using Microwave/Millimeter-Wave Holography.* Wiley-IEEE Press, 2019.

[72] G. E. P. Box and D. R. Cox, “An analysis of transformations,” *J. R. Stat. Soc. Series B Stat. Methodol.*, vol. 26, no. 2, pp. 211–252, Apr. 1964.

[73] G. R. Heidbreder, “Multiple scattering and the method of Rytov,” *J. Opt. Soc. Am.*, vol. 57, no. 12, pp. 1477–1479, Dec. 1967.

[74] W. Xu and I. Cumming, “A region-growing algorithm for InSAR phase unwrapping,” *IEEE Trans. Geosci. Remote Sens.*, vol. 37, no. 1, pp. 124–134, Jan. 1999.

[75] M. Arevalillo-Herráez, F. R. Villatoro, and M. Gdeisat, “A robust and simple measure for quality-guided 2D phase unwrapping algorithms,” *IEEE Trans. Image Process.*, vol. 25, pp. 1–1, Apr. 2016.

[76] D. Kitahara and I. Yamada, “Algebraic phase unwrapping based on two-dimensional spline smoothing over triangles,” *IEEE Trans. Signal Process.*, vol. 64, no. 8, pp. 2103–2118, Apr. 2016.

[77] J. Strand, T. Taxt, and A. Jain, "Two-dimensional phase unwrapping using a block least-squares method," *IEEE Trans. Image Process.*, vol. 8, no. 3, pp. 375–386, Mar. 1999.

[78] R. G. McKilliam, B. G. Quinn, I. V. L. Clarkson, B. Moran, and B. N. Vellambi, "Polynomial phase estimation by least squares phase unwrapping," *IEEE Trans. Signal Process.*, vol. 62, no. 8, pp. 1962–1975, Feb. 2014.

[79] D. Tajik, D. S. Shumakov, and N. K. Nikolova, "An experimental comparison between the Born and Rytov approximations in microwave tissue imaging," in *2017 IEEE MTT-S Int. Microw. Symp.*, Oct. 2017, pp. 1391–1393.

[80] K. Itoh, "Analysis of the phase unwrapping problem," *Appl. Opt.*, vol. 21, p. 2470, Jul. 1982.

[81] *NIST/SEMATECH e-Handbook of Statistical Methods*, Apr. 2012. [Online]. Available: http://www.itl.nist.gov/div898/handbook/

[82] MATLAB, *version R2019b*. Natick, Massachusetts: The MathWorks Inc., 2019.

[83] R. K. Amineh, A. Trehan, and N. K. Nikolova, "TEM horn antenna for ultra-wide band microwave breast imaging," *Prog. Electromagn. Res. B*, vol. 13, pp. 59–74, Jul. 2009.

[84] *Limits of human exposure to radiofrequency electromagnetic energy in the frequency range from 3 KHz to 300 GHz*. Health Canada, 2015. [Online]. Available: https://www.canada.ca/en/health-canada/services/publications/health-risks-safety/

limits-human-exposure-radiofrequency-electromagnetic-energy-range-3-300.html

[85] P. Meaney, A. Hartov, S. Bulumulla, T. Raynolds, C. Davis, F. Schoenberger, S. Richter, and K. Paulsen, "A 4-channel, vector network analyzer microwave imaging prototype based on software defined radio technology," *Rev. Sci. Instrum.*, vol. 90, p. 044708, Apr. 2019.

[86] S. Poltschak, M. Freilinger, R. Feger, A. Stelzer, A. Hamidipour, T. Henriksson, M. Hopfer, R. Planas, and S. Semenov, "High precision realtime RF-measurement system for imaging of stroke," in *2017 47th Eur. Microw. Conf. EuMC*, Oct. 2017, pp. 864–867.

content...

CHAPTER 3

REAL-TIME MILLIMETER-WAVE IMAGING WITH LINEAR FREQUENCY MODULATION RADAR AND SCATTERED POWER MAPPING

Preface

This chapter is a reproduction of the following published article:

R. Kazemivala, A. D. Pitcher, J. Nguyen and N. K. Nikolova, "Real-Time Millimeter-Wave Imaging With Linear Frequency Modulation Radar and Scattered Power Mapping," in *IEEE Transactions on Microwave Theory and Techniques*, 2024, doi:10.1109/TMTT.2024.3378680.

I designed and performed both the measurements of simulated and experimental data, implemented the Fourier-space scattered power mapping time-domain(FSPM-TD) algorithm. implemented a simple in-house radar simulator, performed the image reconstruction, and wrote/edited the manuscript. Aaron Pitcher and Jimmy Nguyen automated the scanning system using the off-the-shelf LFM radar and reviewed the manuscript. Natalia K. Nikolova assisted in the development of the FSPM-TD algorithm and edited the manuscript.

3.1 Introduction

The emerging applications of radar imaging are manifold [1–6], including search and rescue, through-wall imaging [7–10], nondestructive testing (NDT) [11–16], concealed object detection [17–20], and medical diagnostics [21–26]. Most radars currently used for imaging and sensing operate in the microwave regime. However, the pursuit of better image quality drives the interest in the emerging millimeter-wave (mm-wave) and terahertz (THz) radars. Although the mm-wave/THz radiation suffers from significant attenuation compared to the microwave signals, it offers advantages such as improvement in the image spatial resolution (due to wider bandwidths and shorter wavelengths) and smaller size of the antennas. Therefore, mm-wave/THz radars offer a promising technology for short-range imaging and sensing.

Imaging radars produce a two-dimensional (2D) or a three-dimensional (3D) image of a target (or scene). Qualitative images depict the target's reflectivity, i.e., the intensity of the scattering within its volume, whereas quantitative images depict the target's permittivity composition. The image-reconstruction algorithms depend on the type of data the radars provide. The frequency-modulated continuous-wave [27–29] and the ultrawide-band (UWB) pulsed radars [30] provide time-domain data, and both are common in the microwave (low-GHz) frequency ranges. Their advantage is faster measurement compared to the wide-band frequency-sweep (or stepped-frequency) systems. However, at mm-wave frequencies, pulsed radar is currently impractical due to the limitations of the direct time-sampling technology and its excessive cost. On the other hand, the linear frequency modulated (LFM) radar down-converts the received signal to the beat-frequency (kHz to MHz) range [31], where real-time sampling is performed by low-cost analog-to-digital converters. For this reason, LFM radars are currently the most common low-cost option in the mm-wave frequency range.

Most of the image-reconstruction algorithms developed for microwave imaging rely on coherent stepped-frequency continuous wave (SFCW) measurements, which can be time-consuming when taking many frequency samples across a wide frequency range. Also, at mm-wave frequencies, the equipment is costly. Since LFM radars offer faster and more cost-effective option [32], there is great interest in developing fast image-reconstruction methods to process the LFM data.

Back-projection is a classic synthetic aperture radar image-reconstruction approach, and back-projection algorithms (BPAs) have been developed for LFM mm-wave imaging [33–37], where they operate directly on the time-domain data. They compute the round-trip delays in the background medium between each imaged pixel and the receiving/transmitting antenna pairs in order to obtain a coherent sum of all measured signals specific to a pixel. The image depicts the energy of these pixel-specific sums, indicating the scattering intensity (or reflectivity) within the imaged scene.

Fourier-based imaging is a computationally efficient alternative to back-projection. The approach is often referred to as microwave holography [19, 38].[1] The hallmark of the microwave holography algorithms (MHAs) is the image reconstruction in the spatial-frequency domain (k-space). This requires the 2D Fourier transform (FT) of the data. The MHAs, originally developed for frequency-domain data, are also

---

[1] In instrumentation, holography is defined as an interferometric technique for recording the amplitude and the phase of monochromatic waves [39]. In imaging, holography refers to a class of image-reconstruction methods, which process amplitude and phase data using 2D and/or 3D direct and inverse Fourier transforms to produce 3D images, i.e., images with depth [40].

applicable with LFM data. However, the latter application requires an approximation of the down-converted (de-chirped) signal that neglects the second-order time-delay term [41].

To achieve 3D image reconstruction in k-space, most MHAs (see, e.g., [20,41,42]) rely on an analytical range-migration model, which provides the link between the frequency (ω) dependence of the data and the range (or depth) dependence of the image, along with Stolt's interpolation. The k-space result is then cast back to 3D real space via the 3D inverse Fourier transform (IFT). This approach is known as the range-migration algorithm (RMA). Stolt's interpolation is by far the most computationally intensive task but this drawback has been overcome by recent MHAs, which avoid this interpolation, e.g., the range-stacking algorithms [43,44] and the near-field MHAs [21,40,45,46]. They perform the inversion in the mixed (k_x, k_y, z) space, where k_x and k_y are the Fourier variables corresponding to the lateral coordinates x and y, whereas z is range.

Stolt's interpolation and the FTs introduce numerical errors, which may lead to image artifacts in MHA reconstructions, unless filtering is applied [46]. BPAs do not suffer from such artifacts. It is shown in [47] that the RMA yields 2D images with better cross-range resolution compared to the BPA, but offset errors due to Stolt's interpolation may occur. In 3D imaging, however, the BPA seems to offer better resolution. Overall, the BPAs are significantly slower than the MHAs [44, 47] but they are less prone to image artifacts [48–51].

To improve the image accuracy and to enable quantitative reconstruction in near-field imaging, the measured system (or data) point-spread function (PSF) is used [40, 45,52–54] in place of the analytical PSFs used in far-field imaging. The measured PSF provides the system-specific quantitatively accurate resolvent kernel of the linearized scattering model. Using measured PSFs, quantitative imaging of dielectric objects has been demonstrated by algorithms such as quantitative microwave holography (QMH) [21, 55, 56] and Fourier-space scattered power mapping (F-SPM) [57, 58].

Here, we propose a novel image-reconstruction method for processing LFM signals, which we refer to as FSPM-TD (Fourier-space scattered power mapping with time-domain responses). It is based on the F-SPM method, originally developed for SFCW data [57, 58], and it operates directly on time-domain data. The data spatial dependence is treated in k-space, leading to superior computational speed, shown to be better than that of the existing k-space algorithms. At the same time, unlike these algorithms, the FSPM-TD algorithm does not neglect the second-order time-delay term in the LFM signal. The algorithm is validated through simulated data (generated by an in-house radar simulator) as well as measured data obtained with an off-the-shelf LFM platform [59]. Its speed and accuracy are compared with the fast QMH algorithm [21, 55], which does not employ Stolt's interpolation.

Next, Section II introduces the FSPM-TD method and its implementation with LFM data. Sections 3.3 and 3.4 present validation examples with synthetic and measured data, respectively. Conclusions are drawn in Section 3.5.

3.2 Theory

3.2.1 Fourier-space Scattered Power Mapping with Time-Domain Responses (FSPM-TD)

Scattered power mapping (SPM) is a well established method for fast (real-time) microwave imaging [57, 58, 60]. It is a direct reconstruction method since it relies on a linearized model of scattering. With quantitatively accurate (measured) system PSFs, it can also reconstruct images of the real and imaginary parts of the object's complex permittivity (quantitative images). The method operates on frequency-domain signals. The most computationally efficient SPM algorithm is F-SPM [58], which performs the inversion in k-space. Since this algorithm serves as the basis for the current development, it is summarized in Appendix C.

The SPM is a two-stage inversion procedure. To understand its new implementation with time-domain signals, we start with its formulation in real (x, y, z) space.

With frequency-domain responses, the first SPM stage constructs a complex-valued qualitative image $M_\omega(\mathbf{r}')$ (scattered-power map, or simply, map) of an object as [52, 57]

$$M_\omega(\mathbf{r}') = \sum_{\zeta=1}^{N_\mathrm{T}} \int_\omega \iint_{S_\mathrm{a}} S_\zeta^{\mathrm{sc}}(\mathbf{r}, \omega) \left[H_\zeta^{\mathrm{sc}}(\mathbf{r}, \omega, \mathbf{r}')\right]^* d\mathbf{r}\, d\omega \tag{3.1}$$

where ω is frequency, ζ indicates an antenna pair associated with a response, N_T is the number of responses acquired at each observation (receiver) position $\mathbf{r}$ on the aperture S_a, $\mathbf{r}'$ is a position in the imaged domain, $S_\zeta^{\mathrm{sc}}(\mathbf{r}, \omega)$ is the scattered portion of the response measured with the object in place, $H_\zeta^{\mathrm{sc}}(\mathbf{r}, \omega, \mathbf{r}')$ is the scattering response measured with a point scatterer at $\mathbf{r}'$ in the background medium (the system PSF), and * indicates conjugation. It is clear from (3.1) that the object's map $M_\omega(\mathbf{r}')$ is an inner product of the measured responses and the system PSFs in the data space spanned by $\mathbf{r}$, ω and ζ.

In the time domain, (3.1) can be written as

$$M_\omega(\mathbf{r}') = \sum_{\zeta=1}^{N_\mathrm{T}} \int_\omega \iint_{S_\mathrm{a}} \mathcal{F}_\tau \underbrace{\left\{ S_\zeta^\mathrm{sc}(\mathbf{r},t) \otimes H_\zeta^\mathrm{sc}(\mathbf{r},t,\mathbf{r}') \right\}}_{\text{cross-correlation } X_\zeta(\mathbf{r},\tau,\mathbf{r}')} d\mathbf{r}d\omega \tag{3.2}$$

where $X_\zeta(\mathbf{r},\tau,\mathbf{r}')$ is the temporal cross-correlation of $S_\zeta^\mathrm{sc}(\mathbf{r},t)$ and $H_\zeta^\mathrm{sc}(\mathbf{r},t,\mathbf{r}')$ with the time shift τ, and $\mathcal{F}_\tau$ is the FT with respect to time. We next consider the integral over ω in conjunction with the FT of $X_\zeta(\mathbf{r},\tau,\mathbf{r}')$. Assuming infinite frequency bandwidth, at any $\mathbf{r}$ and $\mathbf{r}'$, we obtain

$$\int_{-\infty}^{\infty}\int_\tau X_\zeta(\tau) e^{-\mathrm{i}\omega\tau} d\tau d\omega = \int_\tau X(\tau) \left(\int_{-\infty}^{\infty} e^{-\mathrm{i}\omega\tau} d\omega \right) d\tau \tag{3.3}$$

where $\mathrm{i} = \sqrt{-1}$. The improper integral in the brackets equals $2\pi\delta(\tau)$, where δ denotes Dirac's *delta* function. Therefore,

$$\int_{-\infty}^{\infty}\int_\tau X_\zeta(\tau) e^{-\mathrm{i}\omega\tau} d\tau d\omega = 2\pi X(0)\,. \tag{3.4}$$

The substitution of (3.4) into (3.2) results in the map of the object expressed in terms of time-domain responses:

$$M(\mathbf{r}') = \sum_{\zeta=1}^{N_\mathrm{T}} \iint_{S_\mathrm{a}} \int_t S_\zeta^\mathrm{sc}(\mathbf{r},t)\, [H_\zeta^\mathrm{sc}(\mathbf{r},t,\mathbf{r}')]^* dt d\mathbf{r}\,. \tag{3.5}$$

Here, the scaling factor 2π has been omitted since it has no impact on the final image. In conclusion, the first stage of the SPM image reconstruction can employ time-domain instead of frequency-domain data to obtain the object under test (OUT) map. The comparison of (3.5) and (3.1) shows that the integration over ω is replaced by that over time t. Note that with UWB radar, the temporal sequences are real, but with LFM radar systems, they are complex, i.e., at each $\mathbf{r}$, $S_{\zeta}^{\text{sc}}(t) = I(t) + \mathrm{i}Q(t)$, where I and Q denote the in-phase and quadrature receiver outputs. With complex time-domain signals, the conjugation in (3.5) matters.

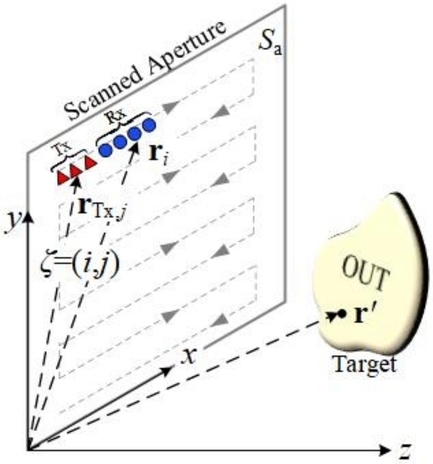

Figure 3.1: Illustration of the single-sided multi-static measurement setup with a planar aperture denoted as S_{a}. The red triangles and the blue points represent Tx and Rx positions, respectively. The response acquired with the j-th Tx antenna ($j = 1, 2, 3$) and the i-th Rx antenna ($i = 1, \ldots, 4$) is denoted by $\zeta \equiv (i, j)$. The array of 3 Tx and 4 Rx antennas moves along a raster-scan path indicated by the grey dash line. Thus, the positions of the Tx antennas, $\mathbf{r}_{\text{Tx},j}$, and the Rx antennas, $\mathbf{r}_i$, are all incremented with a common sampling step along x and y during the scan. The imaged position is denoted as $\mathbf{r}'$.

The direct computation of the OUT map $M(\mathbf{r}')$ with (3.5) is slow. It can be carried out much faster in the 2D k-space under the assumption of a homogeneous background, where the dependence of the PSF on $\mathbf{r}$ and $\mathbf{r}'$ reduces to a subtraction,

$H_\zeta^{\mathrm{sc}}(\mathbf{r}-\mathbf{r}',t)$. Note that the time variable t is also a function of $(\mathbf{r}-\mathbf{r}')$ through its dependence on the distance $R_{\mathrm{Rx}} = |\mathbf{r}-\mathbf{r}'|$ between the imaged point $\mathbf{r}'$ and the measurement (receiver) point $\mathbf{r}$. Thus, the integration over $\mathbf{r} \in S_{\mathrm{a}}$ in (3.5) becomes a 2D cross-correlation of the OUT response and the system PSF in the lateral (cross-range) coordinates. In 2D k-space, this cross-correlation is a point-wise multiplication of the respective 2D FTs. The computation is most efficient in the case of uniform sampling on canonical surfaces (planar, cylindrical) since this allows for the use of the 2D fast Fourier transform (FFT).

Fig. 3.1 illustrates a single-sided multistatic measurement setup, where the scan is over a planar surface. This setup reflects all examples presented later. The measurement LFM-radar platform features 3 transmitting (Tx) and four receiving (Rx) antennas, all moving together over the acquisition plane S_{a} at regular intervals along x and y.

Appendix C describes the process of casting the OUT scattered-power map (3.1) for frequency-dependent data into 2D k-space in the case of planar scanning, where the cross-range variables are x and y. The same process can be applied to the time-domain formulation of the OUT scattered-power map in (3.5), leading to its 2D FT form:

$$\tilde{M}(\boldsymbol{\kappa}, z') = \sum_{\zeta=1}^{N_{\mathrm{T}}} \sum_{k=0}^{N_t} \tilde{S}_\zeta^{\mathrm{sc}}(\boldsymbol{\kappa}, t_k) \left[\tilde{H}_\zeta^{\mathrm{sc}}(\boldsymbol{\kappa}, t_k, z') \right]^* \tag{3.6}$$

where $\boldsymbol{\kappa} = (k_x, k_y)$ is a point in k-space with k_x and k_y being the Fourier variables corresponding to x and y, respectively, z' is the range position of an imaged slice, $t_k = k\Delta t$ is the k-th time sample as determined by the time-sampling step Δt, and N_t is the number of time samples. $\tilde{S}_\zeta^{\mathrm{sc}}(\boldsymbol{\kappa}, t)$ and $\tilde{H}_\zeta^{\mathrm{sc}}(\boldsymbol{\kappa}, t, z')$ are the 2D FTs of $S_\zeta^{\mathrm{sc}}(x,y,t)$ and $H_\zeta^{\mathrm{sc}}(x,y,t,z')$, respectively, where H_ζ^{sc} is the system response acquired with a scattering probe (point scatterer) at position $(x', y', z') = (0, 0, z')$. It should also be pointed out that the range variable z' belongs to a discrete set of range slices, $z'_n = n\Delta z$, $n = 1, 2, \ldots, N_z$, where Δz is the range step size. The implementation of (3.6) in the case of LFM radar is detailed later in Section 3.2.2.

Once the 2D FT of the OUT map is computed with (3.6), it can be cast back in real space using 2D inverse FT:

$$M(x', y', z') = \mathcal{F}_{\text{2D}}^{-1}\left\{\tilde{M}(\boldsymbol{\kappa}, z')\right\} . \tag{3.7}$$

The absolute value of the so obtained OUT map $|M(x', y', z')|$ (usually normalized) provides a qualitative image of the object's reflectivity. However, a significant image improvement is achieved with the second SPM stage. As explained next, this stage operates directly on the k-space OUT map $\tilde{M}(\boldsymbol{\kappa}, z')$, thus bypassing the inverse FT operation in (3.7).

It is shown in [57, 58, 60] (for the case of frequency-domain responses) that the second SPM step provides an image with significantly improved spatial resolution compared to the OUT qualitative image (the map) obtained with (3.1) (real-space processing) or with the IFT of (C.29) (Fourier-space processing; see Appendix C). It also enables the quantitative estimate of the complex permittivity of dielectric objects, provided the system PSFs are quantitatively accurate.[2] Similarly to the first stage, for best computational efficiency, the second SPM stage is performed in

---

[2] A quantitatively accurate PSF predicts accurately the measured response to a scattering probe of known volume and contrast. Such PSFs are usually acquired through calibration measurements [45,46,52] since they depend on specific system parameters such as transmitted power, antenna gain or near-field patterns, the background medium, etc.

k-space. Since the processing is essentially the same as in the second stage of the F-SPM algorithm for frequency-domain data (see Appendix C), only the computations relevant to time-domain responses are presented below, followed by a summary of the algorithm.

The second SPM stage operates on the OUT k-space map $\tilde{M}(\boldsymbol{\kappa}, z'_n)$, $n = 1, \ldots, N_z$, computed with (3.6). It also requires the computation of N_z k-space maps, $\tilde{\mathcal{M}}(\boldsymbol{\kappa}, z'_n; \boldsymbol{z'}_m)$, $n, m = 1, \ldots, N_z$, of the scattering probe, when this probe resides at $\mathbf{r'}_m = (0, 0, \boldsymbol{z'}_m)$, $m = 1, \ldots, N_z$. This computation mirrors that of the OUT map; see (3.6). Specifically,

$$\tilde{\mathcal{M}}(\boldsymbol{\kappa}, z'_n; \boldsymbol{z'}_m) = \sum_{\zeta=1}^{N_{\mathrm{T}}} \sum_{k=0}^{N_t} \tilde{H}^{\mathrm{sc}}_{\zeta}(\boldsymbol{\kappa}, t_k, \boldsymbol{z'}_m) \left[\tilde{H}^{\mathrm{sc}}_{\zeta}(\boldsymbol{\kappa}, t_k, z'_n) \right]^* , n, m = 1, \ldots, N_z \, . \tag{3.8}$$

Note that the real-space maps of the point scatterers, $\mathcal{M}(x', y', z'_n; \boldsymbol{z'}_m)$, corresponding to the k-space maps computed with (3.8), are the image PSFs (IPSFs) resulting from the first SPM stage.[3] The scattering-probe maps in (3.8) are independent of the imaged object and can be pre-computed for faster execution of the image reconstruction.

As shown in Appendix C, with the OUT and scattering-probe maps available in k-space, the second SPM stage solves a small $N_z \times N_z$ system of equations at each point $\boldsymbol{\kappa}$ to obtain the 2D FT of the reflectivity function $\tilde{\rho}(\boldsymbol{\kappa}, z'_n)$, $n = 1, \ldots, N_z$. The real-space reflectivity function $\rho(x', y', z'_n)$ is then recovered via 2D IFT of $\tilde{\rho}(\boldsymbol{\kappa}, z_n)$; see (C.36). The plot of $|\rho(x', y', z'_n)|$ provides a qualitative image of the object's

---

[3] The image PSF (IPSF) is the image a reconstruction algorithm produces from the data acquired with a point scatterer. The IPSF is not to be confused with the system PSF, which is the data set acquired with a point scatterer. The IPSF characterizes the image-reconstruction algorithm whereas the system PSF characterizes the measurement system.

reflectivity. A quantitative estimate of the OUT complex permittivity is possible, provided the system PSFs, $H_\zeta^{\mathrm{sc}}(x, y, t; z'_n)$, scale properly with the probe's volume Ω_{sp} and relative-permittivity contrast $\Delta\varepsilon_{\mathrm{r,sp}}$. Then, the object's relative-permittivity contrast is computed with (C.37).

The proposed FSPM-TD algorithm is summarized in Fig. 4.2. It takes as inputs the measured OUT responses $S_\zeta^{\mathrm{sc}}(x, y, t)$, $\zeta = 1, \ldots, N_{\mathrm{T}}$, and the system PSFs, $H_\zeta^{\mathrm{sc}}(x, y, t, z'_n)$, $n = 1, \ldots, N_z$, the latter being obtained either through measurements, or simulations, or analytical models. Note that, in a multi-static system, each Tx/Rx antenna pair, indicated by $\zeta \equiv (i, j)$, has a dedicated system PSF H_ζ^{sc}.

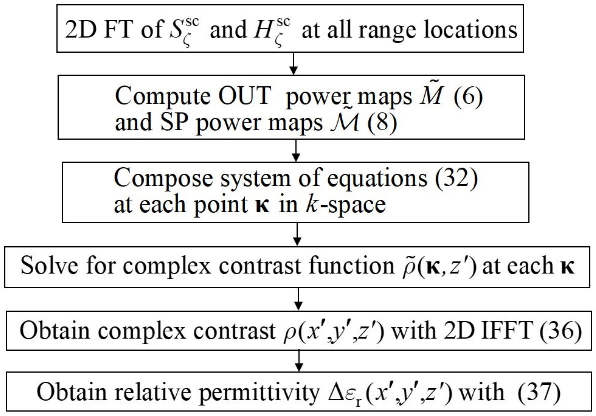

Figure 3.2: Flowchart of the FSPM-TD algorithm.

3.2.2 Forward Model of Scattering with LFM Signals

The LFM radar signal is a "chirp" waveform – a sine wave of frequency which increases or decreases linearly with time. A transmitted LFM chirp is expressed as [61, 62]

$$s_{\mathrm{Tx}}(t) = A_{\mathrm{Tx}} P\left(t/T_{\mathrm{p}}\right) \cos\left[2\pi(f_{\mathrm{c}} t + 0.5\gamma t^2)\right] \tag{3.9}$$

where A_{Tx} is amplitude, f_{c} is the center frequency, t is the *fast time* (the time within a single chirp), T_{p} is the chirp duration (pulse width), $\gamma = \frac{B}{T_{\mathrm{p}}}$ is the frequency-modulation slope (chirp rate), B is the chirp's frequency bandwidth, and

$$P(x) = \begin{cases} 1, & |x| \leq 0.5 \\ 0, & \text{otherwise.} \end{cases} \tag{3.10}$$

The spatial impulse response $h^{\mathrm{sc}}(\mathbf{r}, t, \mathbf{r}')$ of the LFM radar describes the scattered signal from a differential scatterer (scattering probe), $dh^{\mathrm{sc}}(\mathbf{r}, t, \mathbf{r}') = \rho d\Omega h^{\mathrm{sc}}(\mathbf{r}, t, \mathbf{r}')$, where ρ and $d\Omega$ are the reflectivity and volume of the probe, respectively. For static objects in a homogeneous unbounded background, the LFM-radar impulse response (i.e., its analytical PSF) is modeled as a scaled and time-delayed version of $s_{\mathrm{Tx}}(t)$:

$$\begin{aligned} h^{\mathrm{sc}}(\mathbf{r}, t, \mathbf{r}') = A_{\mathrm{Tx}}(R_{\mathrm{Tx}}R_{\mathrm{Rx}})^{-1} P\big((t-\tau_{\mathrm{d}})/T_{\mathrm{p}}\big) \\ \cos\left[2\pi(f_{\mathrm{c}}(t-\tau_{\mathrm{d}}) + 0.5\gamma(t-\tau_{\mathrm{d}})^2)\right] \end{aligned} \tag{3.11}$$

where $\mathbf{r}$ is the Rx position, $\mathbf{r}'$ is the probe's position, and

$$\tau_{\mathrm{d}} = (R_{\mathrm{Tx}} + R_{\mathrm{Rx}})/c \tag{3.12}$$

is the time delay corresponding to the distance travelled by the signal. Here, c is the speed of light whereas $R_{\mathrm{Tx}} = |\mathbf{r} - \mathbf{r}_{\mathrm{Tx}}|$ and $R_{\mathrm{Rx}} = |\mathbf{r} - \mathbf{r}'|$ are the distances from the Tx antenna at $\mathbf{r}_{\mathrm{Tx}}$ to the probe and from the probe to the Rx antenna, respectively. The model in (3.11) accounts for the signal decay due to the spherical spread of the transmitted and scattered waves through the factor $(R_{\mathrm{Tx}}R_{\mathrm{Rx}})^{-1}$. On the other hand, it is a greatly simplified approximation of reality since it ignores the vector nature of the electromagnetic waves, the depolarization that may occur upon scattering, the gain and dispersion of the employed antennas, etc. Note that, at each scan position, R_{Rx} and R_{Tx} differ, depending on which antenna pair $\zeta \equiv (i.j)$ in the multi-static system the PSF describes.

Upon reception, the scattered signal is dechirped by quadrature down-conversion to produce the *beat* or baseband signal, which is used for the image reconstruction. The baseband output corresponding to $h^{\mathrm{sc}}(\mathbf{r}, t, \mathbf{r}')$ in (3.11) is the analytical system PSF [41, 61]:

$$H^{\mathrm{sc}}(\mathbf{r}, t, \mathbf{r}') = \frac{A_{\mathrm{Tx}}}{R_{\mathrm{Tx}} R_{\mathrm{Rx}}} P\left(\frac{t - \tau_{\mathrm{d}}}{T_{\mathrm{p}}}\right) \exp\left[-\mathrm{i}2\pi\left(f_{\mathrm{c}}\tau_{\mathrm{d}} + \gamma t \tau_{\mathrm{d}} - 0.5\gamma\tau_{\mathrm{d}}^2\right)\right] . \tag{3.13}$$

Note that the signal in (3.13) is complex, where its real and imaginary parts represent the I and Q Rx outputs, respectively.

The investigation of the LFM forward model in [41] points out that the spatial resolution of the images obtained with MHAs is negatively affected if the third term of the exponent in (3.13) is not negligible. This is due to the MHAs treating the LFM time-domain signals as frequency-domain signals of equivalent frequency $f' = f_{\mathrm{c}} + \gamma t$ and wavenumber $k' = 2\pi f'/c$ [41]. The proposed FSPM-TD algorithm does not suffer from this limitation since it takes the system PSFs in any form and it does not need an equivalent frequency. Nonetheless, if the phase contribution of the term $\pi\gamma\tau_{\mathrm{d}}^2$ is kept below 2.5°, as suggested in [41], then the LFM system PSF can be approximated as:

$$H^{\mathrm{sc}}(\mathbf{r}, t, \mathbf{r}') \approx H_{\mathrm{a}}^{\mathrm{sc}}(\mathbf{r}, t, \mathbf{r}') = \frac{A_{\mathrm{Tx}}}{R_{\mathrm{Tx}} R_{\mathrm{Rx}}} P\left(\frac{t - \tau_{\mathrm{d}}}{T_{\mathrm{p}}}\right) \exp\left[-\mathrm{i}2\pi(f_{\mathrm{c}} + \gamma t)\tau_{\mathrm{d}}\right] . \tag{3.14}$$

Note that the phase of $H_{\mathrm{a}}^{\mathrm{sc}}$ is now proportional to τ_{d}, leading to an exponential term of the form $e^{-\mathrm{i}k'(R_{\mathrm{Tx}}+R_{\mathrm{Rx}})}$, which matches that in a frequency-domain response. The PSF $H_{\mathrm{a}}^{\mathrm{sc}}$ is employed by the QMH algorithm in the examples presented later, where the FSPM-TD algorithm is compared with QMH.

The linearized forward model of scattering views the signal from an object as a superposition of the scattering emanating from all differential scatterers that make up this object. Thus, using (3.13), the cumulative OUT signal is modelled as:

$$S(\mathbf{r},t) = A_{\mathrm{Tx}} \iiint\limits_{V'} \rho(\mathbf{r}')H^{\mathrm{sc}}(\mathbf{r},t,\mathbf{r}')d\mathbf{r}' \tag{3.15}$$

where $\rho(\mathbf{r}')$ is reflectivity, and

$$-0.5T_{\mathrm{p}} + \tau_{\mathrm{d}} \leq t \leq 0.5T_{\mathrm{p}} + \tau_{\mathrm{d}}\,. \tag{3.16}$$

The forward model in (3.15) is the basis of the LFM radar simulator used in the synthetic experiments presented next. The FSPM-TD image reconstruction employs the analytical system PSF (3.13) with both synthetic and measured data.

3.3 Validation with Synthetic Data

An LFM simulator is implemented in MATLAB [63] using the scalar scattering model (3.15) for the case of planar scanning with multi-static measurements. The PSF employs (3.13). Note that this PSF, along with (3.15), inherently assume scattering in an unbounded medium. The multi-static scenario allows for using any number of Rx and Tx antennas, which remain in a fixed configuration during the scan. Thus,

Table 3.1: System Parameters in the Imaging Experiments with Synthetic mm-Wave LFM Data

Parameters	Values
Center frequency f_c	79 GHz
Bandwidth B	4 GHz
Frequency sweep time T_p	51.1 μs
Frequency sampling rate F_s	10000 kS/s
Frequency-modulation slope γ	72.42 MHz/μs
Sample points in time/frequency	512
Sampling step along x, y	2 mm
Aperture width	15 cm×15 cm
Number of spatial samples	76×76
Number of transmitters	3
Number of receivers	4

at each scan position $\mathbf{r}$, the number of acquired responses is $N_\mathrm{T} = N_\mathrm{Tx}N_\mathrm{Rx}$, where N_Tx and N_Rx are the number of Tx and Rx antennas, respectively. To match our experimental setup employing a single LFM board [59], the scans are single-sided.

In each synthetic experiment, the LFM imaging-system parameters are first set. For a list of these parameters, refer to Table 3.1. Then the system-calibration simulations are performed using (3.13). These emulate the PSF measurements with a scattering probe (SP) located at the center of each imaged slice $(0, 0, z'_n)$, $n = 1, \ldots, N_z$. The SP volume $\Omega_\mathrm{sp} = d\Omega$ is set equal to that of the imaged voxel. This process provides the system PSFs, $H^\mathrm{sc}_\zeta(x, y, t; z'_n)$, $\zeta = 1, \ldots, N_\mathrm{T}$. This is followed by the computation of the OUT data $S^\mathrm{sc}_\zeta(x, y, t)$ using (3.15).

Table 3.1 summarizes the system parameters employed in all presented examples, except for the sampling step along x and y, which is 1 mm for the IPSF study in section 3.3.1. The first six system parameters describe the radar itself. These have been chosen to match the settings of the LFM radar [59] used in the experiments. The spatial sampling step $\Delta x = \Delta y = \Delta_\perp$ (2 mm in Table 3.1) is always chosen to be somewhat smaller than the expected cross-range resolution limit $\delta_\perp$. This limit is given by $\delta_\perp = \frac{\lambda_\mathrm{c}}{4\sin\alpha}$ [52, 64] where $\lambda_\mathrm{c} = c/f_\mathrm{c}$ and α is the maximum viewing angle of the scan, $\alpha = \min\big[\theta_\mathrm{a}, \mathrm{avg}(0.5\theta_\mathrm{h}, 0.5\theta_\mathrm{e})\big]$. Here, $\theta_\mathrm{a} = \arctan(0.5A/R)$ is the viewing angle provided by the aperture, with A and R being the aperture width and the range distance to the object's center, respectively. $\theta_\mathrm{h,e}$ denote the antenna half-power beamwidths in two principal planes. For example, in the simulations, the antennas are isotropic, thus α is determined by the aperture. Provided that $A = 15$ cm and the target is 22.5 cm away, $\alpha \approx 18.4°$, leading to $\delta_\perp \approx 3$ mm.

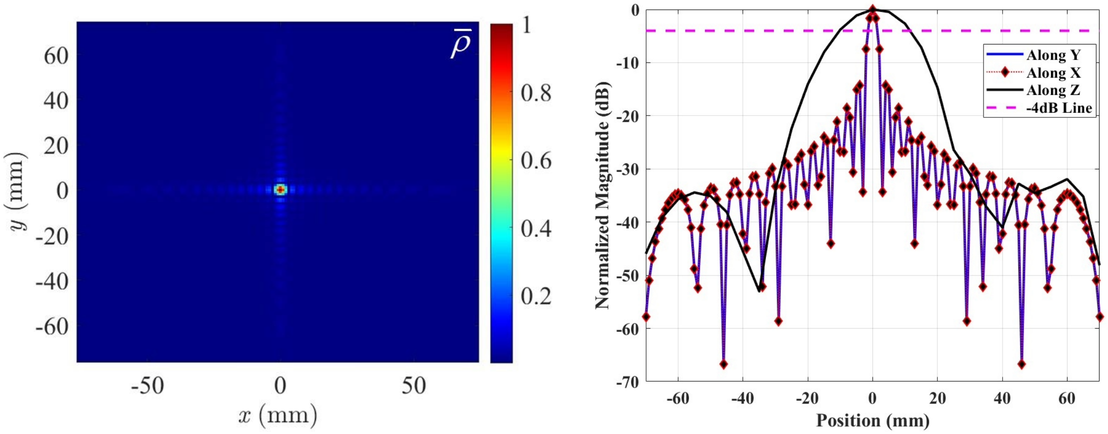

(a) (b)

Figure 3.3: FSPM-TD reconstructed image of a cubical probe 1 mm on a side, at the range distance 22.5 cm: (a) 2D IPSF at the $z = 22.5$ cm in terms of normalized reflectivity $\bar{\rho}$, (b) range and cross-range profiles of the IPSF.

It is worth commenting that obtaining synthetic LFM-radar data with full-wave simulators is prohibitive slow due to: (i) the extremely long chirp signals, and (ii) the need to simulate a large amount of of illumination (Tx) positions associated with scanning a multi-static radar system over a large aperture.[4]

---

[4] Consider the F-shape/bar-shape example, which requires about 102 million mesh cells to comply

3.3.1 Image Point Spread Function and Spatial Resolution

In the first experiment, we image a single-voxel scatterer at 22.5 cm from the acquisition plane, and obtain the IPSF of the FSPM-TD algorithm. From the IPSF, the cross-range and range resolution values are estimated and compared to the theoretical limits. Here, the scanning step is $\Delta_\perp = 1$ mm, and $\Omega_{\text{sp}} = d\Omega = 1$ mm^3. The IPSF contains 29 range slices separated by $\Delta z = 5$ mm and centered on the $z = 22.5$ cm plane. Fig. 3.3a shows the IPSF slice at $z = 22.5$ cm. The IPSF width at -4 dB indicates the spatial resolution in the respective direction [52]. Fig. 3.3b shows the line cuts of the IPSF along x and y at $z = 22.5$ cm, and along the line cut along z at $x = y = 0$. The results indicate cross-range resolution of 3 mm, which agrees with the theoretical limit $\delta_\perp \approx 3$ mm. The range resolution is obtained as 22 mm whereas the theoretical limit is [64] $\delta_z = \frac{c}{2B} \approx 37$ mm.

3.3.2 3D Imaging with Synthetic Data

A 3D object is implemented in the LFM radar simulator as shown in Fig. 4.7. All structural components are built of cubical scatterers 1 mm on a side. Fig. 3.4a shows the tilted bar shape of length 50 mm and width 3 mm in the plane $z = -120$ mm. Its relative permittivity is set to $\varepsilon_{\text{r}} = 3$. An F-shape of $\varepsilon_{\text{r}} = 1.8$ is located at $z = 0$ mm (see Fig. 3.4b). The background is vacuum ($\varepsilon_{\text{r,b}} = 1$). The F-shape has vertical and horizontal arms of length 50 mm whereas the middle arm measures 25 mm. All arms are 3 mm wide. The third slice at $z = 120$ mm has no inclusions. The sampling

---

with a cell size equal to one-tenth of the shortest wavelength. With a time step satisfying the Courant–Friedrichs–Lewy (CFL) condition, it is estimated that the transmitted LFM chirp requires $N_{t,\text{pulse}} = 68\,133\,333$ time samples, and at least double this number of time steps to complete the simulation for a single Tx position. The multi-static scanning imaging experiment requires a total of $3 \times 76 \times 76 = 17\,328$ simulations.

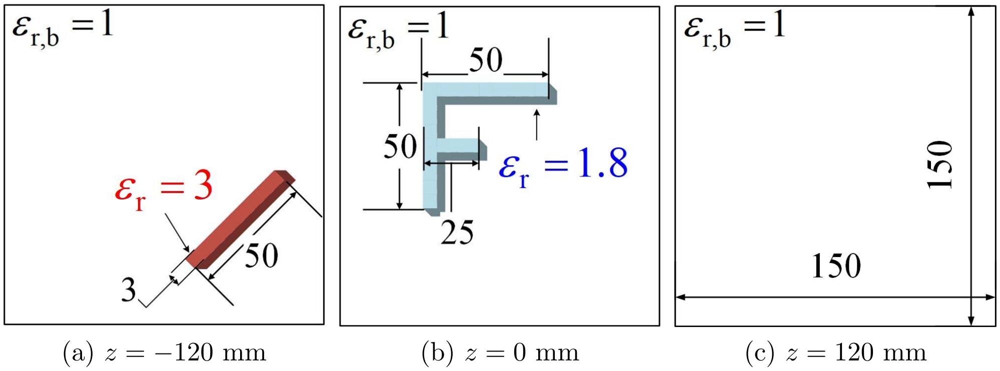

(a) $z = -120$ mm (b) $z = 0$ mm (c) $z = 120$ mm

Figure 3.4: The 3D structure imaged in a synthetic example: (a) bar shape of relative permittivity $\varepsilon_r = 3$ at $z = -120$ mm, (b) F-shape of $\varepsilon_r = 1.8$ at $z = 0$, and (c) a slice without any targets at $z = 120$ mm. Background is vacuum, $\varepsilon_{r,b} = 1$. All dimensions are in mm.

step is $\Delta_\perp = 2$ mm.

The PSFs are acquired with a cubical SP of size 0.5 mm^3 and $\varepsilon_{r,sp} = 1.5$, placed at $z = -120, 0, 120$ mm. This results in 3D image reconstruction at these three slices. Once the OUT responses are computed with (3.15), the FSPM-TD algorithm reconstructs the images of the real and imaginary parts of the object's relative permittivity shown in Fig. 3.5. The results indicate that the algorithm retrieves well the permittivity values of the bar and F shapes (see Fig. 3.5a and Fig. 3.5b). This quantitatively accurate result is expected since both the PSFs and the OUT data are generated by the same "measurement system" emulated by the LFM radar simulator. Also, the radar simulator employs the simple superposition scattering model in (3.15), i.e., it does not model the mutual coupling and multiple scattering, which occurs in reality, and which is the main reason for image degradation in quantitative imaging. This example highlights the advantage of measuring the PSFs with the same system used to measure the OUT. Unfortunately, measuring the PSFs is not always possible, especially in far-zone measurements, where the SP signal may be too weak to detect

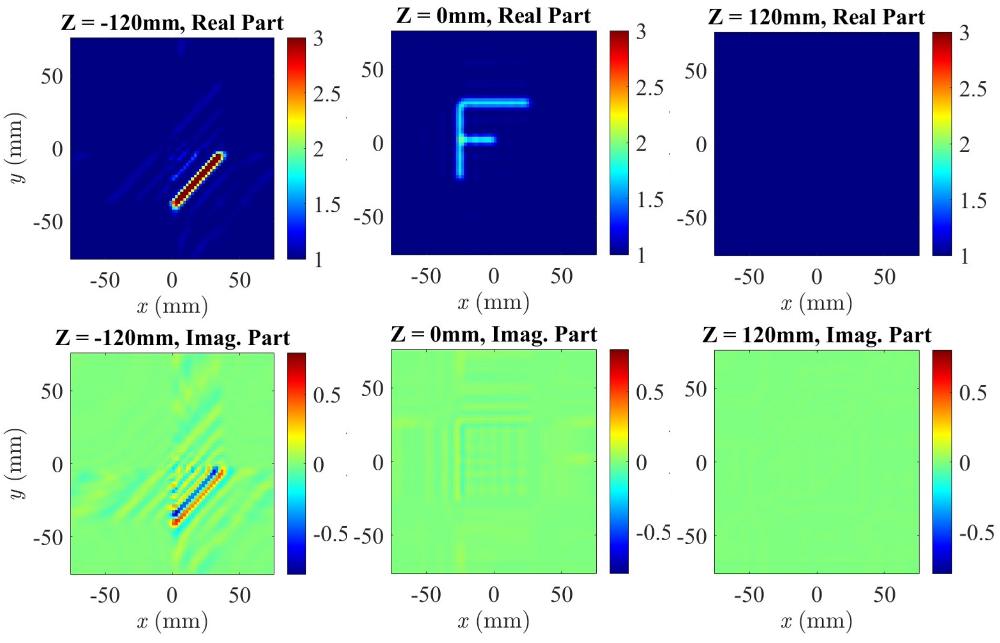

(a) (b) (c)

Figure 3.5: Reconstructed images of the real and imaginary parts of the relative permittivity of the object in Fig. 4.7 using synthetic data: (a) the bar shape in the $z = -120$ mm slice (true permittivity $\varepsilon_{\mathrm{r}} = 3$); (b) the F-shape in the $z = 0$ slice (true permittivity $\varepsilon_{\mathrm{r}} = 1.8$), and (c) the slice at $z = 120$ mm where there are no embedded targets.

with sufficient signal-to-noise ratio.

To quantify the image quality in Fig. 3.5, the structural similarity (SSIM) index is computed [65]. The SSIM index ranges from 0 to 1, where 1 indicates perfect similarity and 0 indicates no similarity. Here, the SSIM is 0.9515 in the F-shape slice and 0.9104 in the bar-shape slice. Additionally, to evaluate the precision of the reconstructed permittivities, the root-mean-square error (RMSE) is calculated as [52]:

$$\mathrm{RMSE} = \sqrt{\frac{1}{N_{\mathrm{v}}}\sum_{n=1}^{N_{\mathrm{v}}} |\varepsilon_{\mathrm{r}}(\mathbf{r}'_n) - \overline{\varepsilon}_{\mathrm{r}}(\mathbf{r}'_n)|^2}\,, \tag{3.17}$$

where $\overline{\varepsilon}_{\mathrm{r}}(\mathbf{r}'_n)$ is the true distribution, $\varepsilon_{\mathrm{r}}(\mathbf{r}'_n)$ is the reconstructed distribution, and N_{v} is the number of voxels. Here, the image RMSE is 0.0219.

The accuracy of the FSPM-TD reconstruction is compared with that of the quantitative microwave holography (QMH) method. The QMH method is a fast MHA, which does not employ Stolt's interpolation. The QMH images are not shown here since there is no visible difference with those in Fig. 3.5. To compare better the two reconstructions, an RMSE is computed where the FSPM-TD result provides the reconstructed distribution $\varepsilon_{\mathrm{r}}(\mathbf{r}'_n)$ whereas the QMH result is the true distribution $\overline{\varepsilon}_{\mathrm{r}}(\mathbf{r}'_n)$. The resulting RMSE is very small: 3.12×10^{-16}.

The two algorithms are also compared in terms of running time. The FSPM-TD algorithm takes about 2.9 s whereas the QMH algorithms takes about 5 s. Note that both algorithms are implemented in MATLAB without any code optimization and using the same direct and inverse fast FT (FFT) function calls. To understand the reason for the faster performance of FSPM-TD, we first point out that both methods share common initial steps, which involve the 2D FFT of the PSFs and the OUT data. Also, both of them employ 2D inverse FFT (slice by slice) on the reconstructed k-space reflectivity function. However, they differ in solving their respective linear systems of equations in k-space. FSPM-TD solves square $N_z \times N_z$ systems (C.32) whereas QMH solves tall $(N_\omega N_{\mathrm{T}}) \times N_z$ systems [46, 55]. The number of slices N_z rarely exceed 10, and the number of response types N_{T} is also on the order of 1 to 10. However, in the image reconstruction with QMH, the number of equivalent frequencies N_ω equals that of the time samples N_t, and that is on the order of $\sim 10^2$ to $\sim 10^3$, depending on the length of the employed chirp sequence. In this example, which spans a single chirp, $N_t = 512$. To solve the tall system of equations, QMH uses MATLAB's pseudo-inverse (pinv) function, which employs a singular value decomposition approach [66], the computational complexity of which is $O((N_t N_{\mathrm{T}})^2 N_z + N_z^3)$. FSPM-TD, on the other hand, can employ either LU decomposition or pseudo-inverse solvers. In either case, its computational complexity is about $O(N_z^3)$. It is now clear that the computational advantage of the FSPM-TD algorithm arises when $N_z < N_t N_{\mathrm{T}}$.

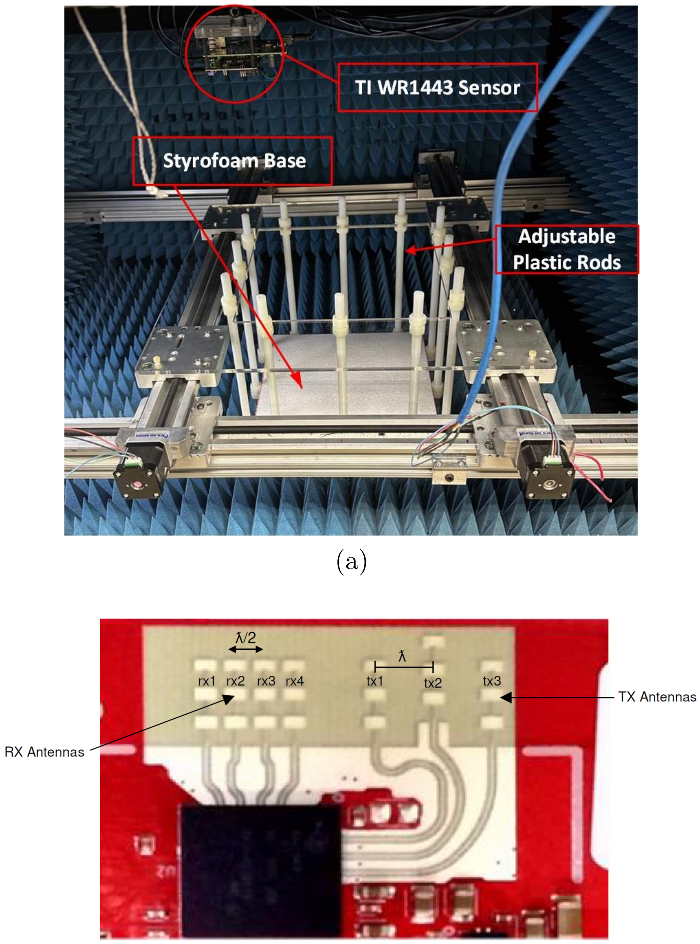

(a)

(b)

Figure 3.6: Photos of: (a) acquisition chamber, and (b) on-board antenna array of the IWR1443 sensor (from [59]).

3.4 Verification with Measurements

The experiments are carried out in a planar raster-scanning chamber shown in Fig. 4.13a. With the advent of system-on-chip mm-wave sensing technology, the market now offers various off-the-shelf radar modules. Here, we use the IWR1443Boost evaluation module [59] along with the real-time data-capture adapter board DCA1000EVM [67]. The mm-wave sensor is equipped with three Tx and four Rx antennas as shown in Fig. 3.6b (from [59]). The LFM transceivers can accommodate up to 4 GHz bandwidth from 77 GHz to 81 GHz. The configuration of the radar system is done via the *TI mmWave Studio* software suite. This includes activating/deactivating Tx and Rx channels, the choice of the chirp sequence, and the chirp settings. The chosen system parameters match those in Table 3.1. All twelve radar channels, formed by the three Tx and four Rx on-board antennas, are used in the experiments. The OUT data $S(\mathbf{r}, t)$ are captured through measurements employing all available radar channels.

The radar module is mounted at the top of the chamber (see Fig. 4.13a) and it is stationary while the platform carrying the imaged object moves laterally along a raster-scan path with increments $\Delta x = \Delta y = 2$ mm. At each grid point, the radar takes measurements for about 2 s, during which time the platform does not move.

The relative positions of the Tx and Rx antennas are needed to calculate the time delay τ_{d} associated with an imaged point and each Tx/Rx antenna pair. The center-to-center spacing between the Rx elements is 1.9 mm whereas between the Tx elements it is 3.8 mm. The center-to-center spacing from rx4 to tx1 is 4.75 mm (see Fig. 3.6b). The coordinate system is aligned so that Rx antenna #4 (rx4 in Fig. 3.6b) is at $(0, 0, \bar{z})$ at the start of the scan, where $\bar{z}$ is the distance from the radar printed circuit board (PCB) to the center of the imaged object.

In all experiments presented next, background subtraction is not used to extract the scattered portion of a response from the total measured response. This subtraction is mandatory in near-field imaging and especially when forward-scattering signals are employed because the incident-field portion of the total object response is strong. Here, background de-embedding is unnecessary since the background signals are negligible compared to the back-scattering from the objects.

3.4.1 System Calibration

The measurements are susceptible to various types of uncertainties, of which the internal system delay t_{sys} is the most detrimental to the ranging information carried by the scattered signal. Aside from ignoring signal dispersion due to the antennas, the PSF models in (3.13) or (4.16) assume that: (i) the signals at the Rx antenna terminals arrive at the input of the down-converting mixer without delays, and (ii) the signals transmitted by the Tx antennas are the same as those submitted to the mixer. The first assumption is not true due to the coplanar-waveguide (CPW) transmission lines connecting the Rx antennas to the radar chip (see Fig. 3.6b) along with signal pathways inside the chip. Similarly, the second assumption is not true due to the CPW and on-chip interconnects to the Tx antennas. The cumulative effect of the delays along interconnects is represented by a constant t_{sys}, which must be added to the signal-delay time variable τ_{d} in the PSF model. The calibration method aims at extracting t_{sys}.

The calibration measurement setup is illustrated in Fig. 3.7. It employs a 5×5 cm^2 copper plate serving as an ideal reflector, which lies parallel to the radar PCB

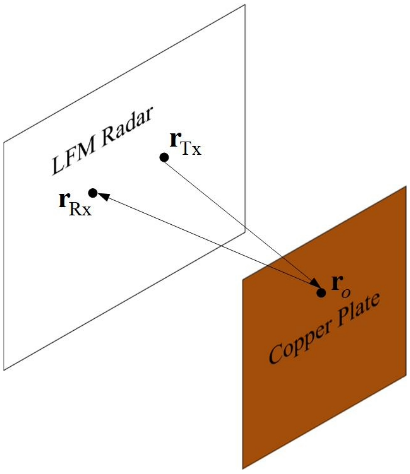

Figure 3.7: Schematic of system calibration setup.

and centered on the boresight of the Tx/Rx antenna set. The system delay does not depend on the distance between the radar and the plate but measurements at various distances should be carried out to verify the extracted τ_{sys}. Here, distances anywhere between 20 cm and 40 cm have been employed, which are within the possible ranges in the chamber.

The echo signal $S_\zeta^{\text{m}}(t)$ is captured by every (ζ) Tx/Rx antenna pair. The goal is to align the measured signals $S_\zeta^{\text{m}}(t)$ with an analytical model $S_\zeta^{\text{a}}(t)$ based on (3.13), namely,

$$S_\zeta^{\text{a}}(t) = -H_\zeta^{\text{sc}}(t)\,. \tag{3.18}$$

The response in (3.18) accounts for the phase reversal (the minus sign) upon reflection from the copper plate. The integration over the plate's surface is ignored since the plate's lateral size is much smaller than the range distance. The time delay $\tau_{\text{d},\zeta}$, needed to compute $H_\zeta^{\text{sc}}(t)$, is obtained from $R_{\text{Tx}\zeta}$ and $R_{\text{Rx}\zeta}$ using (3.12), where $R_{\text{Tx}\zeta} = |\mathbf{r}_{\text{Tx}\zeta} - \mathbf{r}_0|$ and $R_{\text{Rx}\zeta} = |\mathbf{r}_\zeta - \mathbf{r}_0|$ are the distances from the plate's center (at $\mathbf{r}_0$) to the Tx and Rx antennas, respectively.

The alignment is done in the frequency (f) domain. The FT of $S^{\rm a}_{\zeta}(t)$, $\tilde{S}^{\rm a}_{\zeta}(f)$, has a magnitude spectrum which peaks at the frequency $f_{\rm p} = -\gamma\tau_{{\rm d},\zeta}$ since [61, 68]:

$$\tilde{S}^{\rm a}_{\zeta}(f) = -T_{\rm p}{\rm sinc}\left[T_{\rm p}(\gamma\tau_{{\rm d},\zeta} + f)\right] e^{-{\rm i}2\pi f_c\tau_{{\rm d},\zeta}+{\rm i}\pi\gamma\tau^2_{{\rm d},\zeta}}\, e^{-{\rm i}2\pi(f+\gamma\tau_{{\rm d},\zeta})\tau_{{\rm d},\zeta}}\,. \tag{3.19}$$

Here, ${\rm sinc}(x) \equiv \frac{\sin(x)}{x}$. The peak frequency $f_{\rm p}$ is a crucial marker for the target's range. If the target motion is negligible (zero Doppler shift), $f_{\rm p}$ is proportional to $\tau_{{\rm d},\zeta}$ [61, 68], and, therefore, to the distance to the target; see (3.12). We exploit this LFM signal feature to find $t_{\rm sys}$.

First, we generate the time sequence of $S^{\rm a}_{\zeta}(t)$ with the same sampling step and length as that of $S^{\rm m}_{\zeta}(t)$. FFT is then applied to both $S^{\rm a}_{\zeta}(t)$ and $S^{\rm m}_{\zeta}(t)$. An example plot (for the rx4/tx1 antenna pair) of the magnitude spectra of the copper-plate measured and analytical responses is shown in Fig. 3.8, when the plate is 355 mm away from the radar. It is clear that the peak frequencies of $|\tilde{S}^{\rm a}_{\zeta}(f)|$ and $|\tilde{S}^{\rm m}_{\zeta}(f)|$ are not aligned, which necessitates a correction of the analytical model through $t_{\rm sys}$. The delay $t_{\rm sys}$ is calculated from the peak frequency of the measured signal $f^{\rm m}_{\rm p}$ and that of the analytical signal $f^{\rm a}_{\rm p}$ as

$$t_{\rm sys} = (f^{\rm m}_{\rm p} - f^{\rm a}_{\rm p})/\gamma\,. \tag{3.20}$$

The internal system delays for the LFM radar employed here have been determined for all Tx/Rx channels first with the copper plate placed 355 mm away from the radar. The values are the same across all radar channels: $\tau_{\rm sys} = 0.26969$ ns. The calibration has been repeated for various range positions of the copper plate and $t_{\rm sys}$ has been confirmed to be the same.

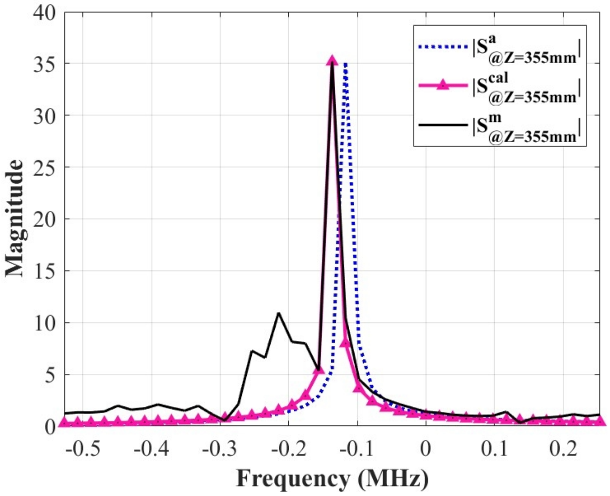

Figure 3.8: Comparison between the magnitude spectra of a measured calibration response $\tilde{S}^{\mathrm{m}}_{\zeta}(f)$ and the respective analytical response $\tilde{S}^{\mathrm{a}}_{\zeta}(f)$ for a copper plate placed 355 mm away from the radar. $\tilde{S}^{\mathrm{a}}_{\zeta}(f)$ is the analytical result before calibration whereas $\tilde{S}^{\mathrm{cal}}_{\zeta}(f)$ is the result after calibration.

To verify the calibration, the so obtained t_{sys} is applied to the analytical response $S^{\mathrm{a}}_{\zeta}(t)$ in (3.18) by replacing τ_{d} with $\tau_{\mathrm{d}} + t_{\mathrm{sys}}$. The magnitude spectrum of the calibrated analytical response $|\tilde{S}^{\mathrm{cal}}_{\zeta}(f)|$ is plotted in Fig. 3.8 for comparison with the measurement $|\tilde{S}^{\mathrm{m}}_{\zeta}(f)|$, showing the peak-frequency alignment. It is worth noting that although the peak-frequency misalignment between the uncalibrated analytical response and the measured response may appear small, it actually corresponds to about 4 cm difference in distance. Without calibration, this difference results in extremely unfocused images with the measured data.

Similarly, t_{sys} is used to calibrate the analytical system PSFs in (3.13) and obtain $H^{\mathrm{sc}}_{\mathrm{cal},\zeta}(\mathbf{r}, t, \mathbf{r}')$ by replacing $\tau_{\mathrm{d},\zeta}$ with $\tau_{\mathrm{d},\zeta} + t_{\mathrm{sys}}$ for each Tx/Rx antenna pair. These calibrated PSFs are used in the image reconstruction with the measured data.

3.4.2 Imaging Experiments

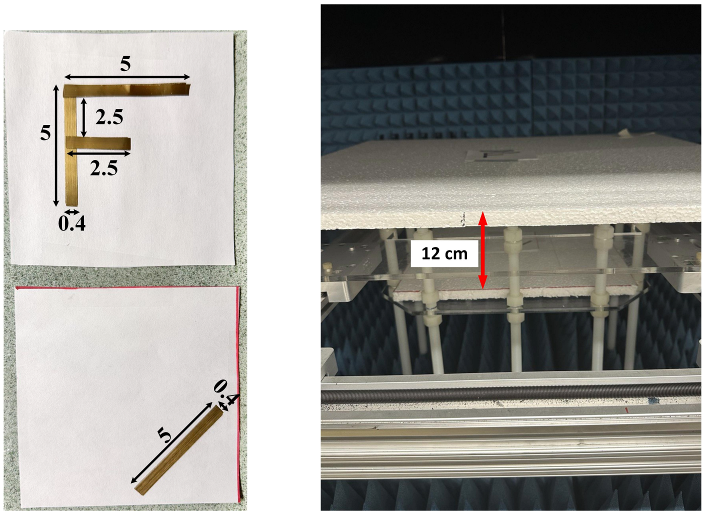

(a) (b)

Figure 3.9: Imaging setup for the 3D reconstruction of two copper-tape objects depicted in (a). Both shapes consist of four layers of copper tape carefully applied to a paper surface. The F-shape is positioned at the uppermost layer, while the tilted bar shape resides at the bottom layer, as illustrated in (b). The F-shape plane is situated 22.5 cm away from the radar, whereas the plane of the bar shape extends an additional 12 cm. All dimensions are in cm

The initial validation is conducted using the same 3D F-shape/bar-shape object described in Section 3.3.2. However, in this experiment, copper tapes of thickness 1 oz (34.8 μm) and width 4 mm are used in crafting the shapes, as shown in Fig. 3.9a. Each arm of the F and bar shapes comprises 4 stacked layers of copper tape to ensure large reflectivity. The F-shape contains arms of lengths 5 cm and 2.5 cm. The bar shape is 5 cm long. The shapes are affixed to paper sheets (see Fig. 3.9a). The imaging setup is shown in Fig. 3.9b. The F-shape is placed at the reference plane $z = 0$, which is 22.5 cm away from the radar. The bar shape is at $z = -12$ cm (34.5 cm away from the radar). The paper sheets holding the shapes are placed on *Styrofoam* ($\varepsilon_r \approx 1.175$) slabs of thickness 12.7 mm. The system and sampling parameters are listed in Table 3.1.

In the image reconstruction, we employ the calibrated analytical PSFs computed for a cubical scattering probe of volume $d\Omega = 1$ mm^3 positioned at the three slices of interest: $z = -120, 0, 120$ mm. Therefore, in this and all subsequent experiments, the images are qualitative.

We briefly mention that we have attempted the measurement of the PSFs using probes of size $\frac{\lambda_c}{4} \approx 1$ mm. Unfortunately, at the employed ranges, the scattering from such probes is too weak to rise above the uncertainty of our measurement system.

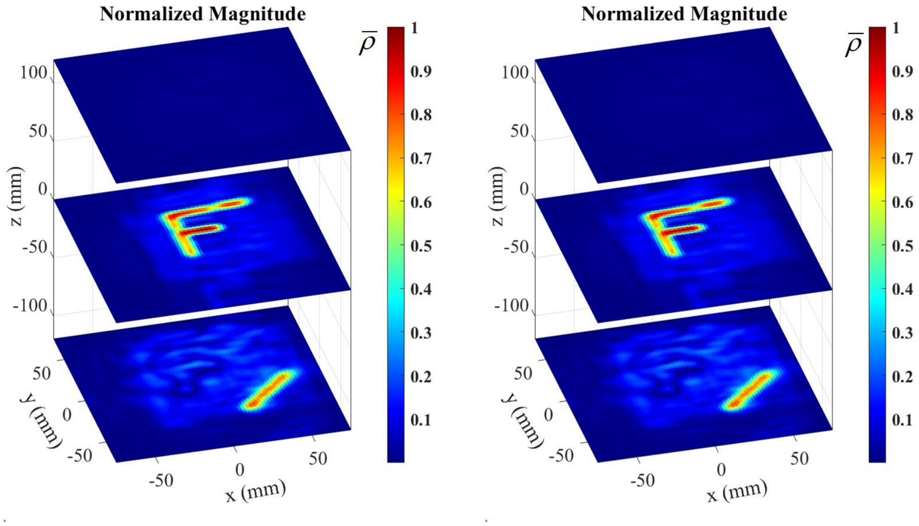

(a) FSPM-TD (b) QMH

Figure 3.10: Reconstructed 3D images in terms of normalized reflectivity $\bar{\rho}$ enabling: (a) FSPM-TD method, and (b) QMH method using measured data with the F-shape/bar-shape object. The bar-shape and the F-shape are correctly located at $z = -120$ mm and $z = 0$ mm, respectively. The top layer at $z = 120$ mm correctly shows a slice without any targets.

The FSPM-TD reconstructed image of the normalized reflectivity is presented in Fig. 3.10a. The F and bar shapes are reconstructed with good structural accuracy.

Even a small air-gap in the top horizontal arm of the F-shape (see Fig. 3.9a) is reconstructed well in the middle layer ($z = 0$) of Fig. 3.10a. The top layer at $z = 120$ mm (air in the setup shown in Fig. 3.9b) accurately shows the absence of objects.

Regarding the image quality, the image slices are well resolved along range, i.e., there is no "range bleeding". This is expected since the slice separation is well beyond the range resolution limit of $\delta_z \approx 37$ mm. However, artifacts are present in the bottom layer where the bar shape is. These are due to reflections coming from the plastic rods as well as the scanning platform itself. Note that, as shown in Fig. 3.9b, the F-shape at the top is far from any structural components of the scanner and its image in the slice $z = 0$ shows practically no artifacts.

To compare the accuracy of FSPM-TD images with an MHA algorithm, the QMH image is provided in Fig. 3.10b. The two images are almost identical, validating the accuracy of the FSPM-TD algorithm. We note that the QMH algorithm, although using the approximate PSF in (4.16), provides focused images since (4.16) is accurate in this example. With a frequency-modulation slope of $\gamma = 72.42 \times 10^{12}$ Hz/s and distance to target of about 35 cm, the phase contribution of the $\pi\gamma\tau_{\mathrm{d}}^2$ term does not exceed 0.09°, which is well below the limit of 2.5° recommended in [41]. As in the example with the synthetic data, since all sampling rates are similar, the FSPM-TD algorithm is faster than QMH (2.9 s versus 5.0 s).

The second imaging experiment addresses a scenario featuring realistic items. The object includes a metallic key, a penny, and a liquid lipstick, see Fig. 3.11a. In an initial experiment, all three objects are lying on a *Styrofoam* sheet, which is 22.5 cm away from the radar. In a second experiment, the same objects are enclosed within a toy bag shown in Fig. 3.11b and the bag is placed on the same *Styrofoam* sheet. The radar and sampling parameters remain the same as those in Table 3.1.

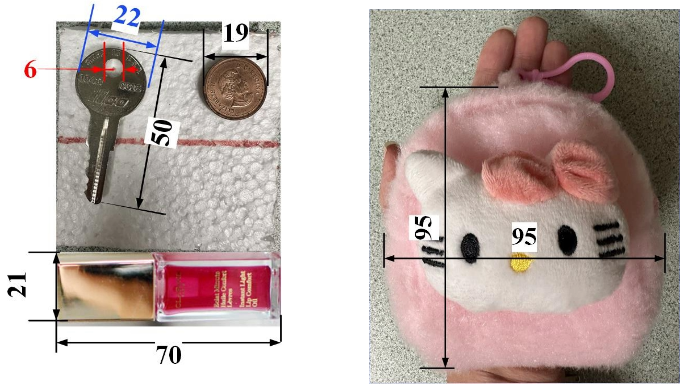

(a) (b)

Figure 3.11: Photos of: (a) key, penny, and liquid lipstick lying on a *Styrofoam* sheet, (b) small toy bag used to “conceal” the key, the penny, and the lipstick. Dimensions are in mm.

Fig. 3.12a shows a 2D image of the unobstructed key, penny, and lipstick experiment. The image is obtained by a maximum value projection of 6 slices within a volume of 2.5 cm range thickness, i.e., confined between the planes $z = 19$ cm and $z = 21.5$ cm. The reason for presenting the 2D projection images is that the objects have different thicknesses and their reflectivity is best represented in a projection. The image in Fig. 3.12a shows all items with excellent resolution and no visible artifacts. The 2D projection image of the same objects concealed in the bag is shown in Fig. 4.13c, following the same procedure. It is clear that the bag has a negative impact on the structural accuracy of the reconstructed objects, likely due to the fact that the materials from which the bag is made are not entirely transparent to the mm-wave radiation. In fact, the outline of the bag is visible in Fig. 4.13c. Moreover, the *hello-kitty* plush toy attached to the bag is relatively large and thick (see Fig. 3.11b).

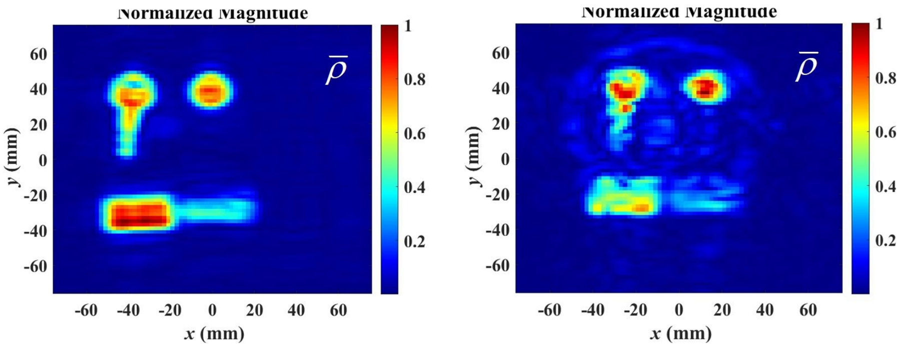

(a) (b)

Figure 3.12: FSPM-TD image of the normalized 2D projection of the reflectivity $\bar{\rho}$ of: (a) key, penny, and lipstick on the scanning platform, (b) the same objects inside the bag.

The last experiment reported here addresses the realized cross-range resolution of the experimental setup. To this end, two benchmark targets are fabricated in PCB technology, each consisting of five copper strips of thickness 2 oz (69.6 μm) and length 2.5 cm; see Fig. 3.13. The PCBs employ FR-4 substrates ($\varepsilon_\mathrm{r} \approx 4.3$) of size 8×8 cm^2. The strip width in Benchmark #1 is 3 mm whereas in Benchmark #2 it is 2 mm. In both benchmark targets, the strip edge-to-edge spacing varies from 2 mm to 5 mm at 1 mm increment. The reconstructed 2D image of Benchmark #1 is shown in Fig. 3.14a. All strips are resolved well, even the two strips with a 2 mm spacing. On the other hand, the image of Benchmark #2, shown in Fig. 3.14b, fails in resolving the 2 mm-width strips which are separated by a 2 mm gap. The results suggest a cross-range resolution of about 3 mm. This agrees well with the theoretical cross-range resolution $\delta_\perp = \frac{\lambda_\mathrm{c}}{4\sin\alpha} \approx 2.95$ mm. Here, $\lambda_\mathrm{c} \approx 3.8$ mm, and the viewing angle is limited by the half-power beamwidths of the on-board antennas, $\alpha = \mathrm{avg}(0.5\theta_\mathrm{h}, 0.5\theta_\mathrm{e})$, where $\theta_\mathrm{h} \approx 56°$ and $\theta_\mathrm{e} \approx 28°$ [59]. Thus $\alpha \approx 21°$.

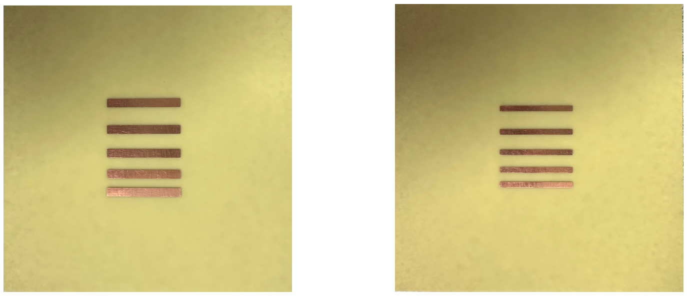

(a) (b)

Figure 3.13: Photos of benchmark PCB targets composed of copper strips of 2 oz (69.6 μm) thickness and length of 2.5 cm: (a) Benchmark #1 with strip width of 3 mm, (b) Benchmark #2 with strip width of 2 mm. In both benchmark targets, the strip edge-to-edge spacing varies from 2 mm to 5 mm at 1 mm increment. The PCBs employ FR-4 ($\varepsilon_{\mathrm{r}} \approx 4.3$) substrates of size 8×8 cm^2.

3.5 Discussion and Conclusions

We have introduced the new Fourier-space scattered power mapping in the time domain (FSPM-TD) method for the fast processing of time-domain signals in microwave and mm-wave image reconstruction. The method's application with mm-wave LFM radar signals is presented and validated with synthetic and measured data.

The proposed inversion algorithm employs a linearized integral scattering model whose kernel (the radar's spatial impulse response) is the PSF. For fast k-space inversion, the assumption of a uniform unbounded background medium is made, which renders the scattering model a 2D convolution in the lateral coordinates. Unlike conventional direct-inversion methods, which rely on analytical PSFs, the FSPM-TD algorithm can operate with analytical, simulated, or measured PSFs without any modifications and with no impact on its speed. Since measured PSFs enable near-field and quantitative imaging, this capability is an important advantage.

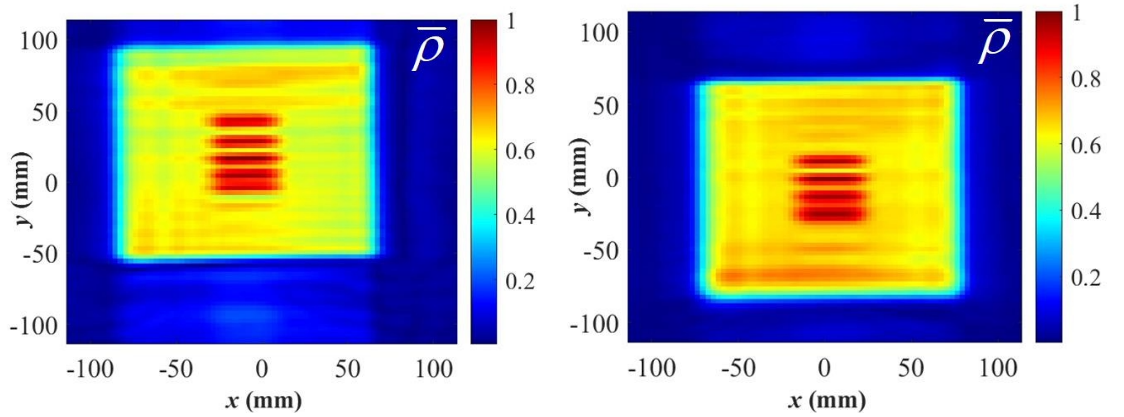

(a) (b)

Figure 3.14: Reconstructed images of benchmark targets with strips of width (a) 3 mm and (b) 2 mm, in terms of normalized permittivity $\bar{\rho}$

.

In its first inversion stage, the FSPM-TD algorithm is a projection algorithm, since it employs the inner product of the measured responses with the system PSFs to produce a reflectivity image. In its second inversion stage, it performs image enhancement (and quantitative imaging, if the PSFs are measured) by deconvolving the object's reflectivity image with that of the scattering probe. This approach of projection forming an inner product, followed by image deconvolution, is the hallmark of the proposed algorithm.

The computational efficiency of the FSPM-TD algorithm stems from performing both inversion stages in the mixed (k_x, k_y, z) space. In contrast, prior k-space algorithms, perform deconvolution in the (k_x, k_y, k_z) space or the (k_x, k_y, k) space, where the number of samples along k_z or k equals the equivalent-frequency samples. LFM signals feature a large number of time samples, or, equivalent-frequency samples. This number is usually much larger than the number of image slices along z. This is why the FSPM-TD algorithm is computationally more efficient than the QMH k-space algorithm, which does not employ Stolt's interpolation. At the same time, the image quality is the same. The comparison with the fast QMH algorithm shows an acceleration factor of $\sim (N_t N_{\mathrm{T}})^2/N_z^2$, where N_t is the number of time samples, N_{T} is the number of Tx/Rx pairs, and N_z is the number of image slices. The typical running time of the FSPM-TD reconstruction is 1 s to 2 s with an unoptimized MATLAB code on a conventional laptop in examples where the imaged volume consists of $\sim 10^4$ voxels.

Also, a radar simulator based on a linearized model of scattering has been developed for the rapid generation of synthetic LFM data. The extremely long time scale of the LFM signal renders the full-wave time-domain simulations prohibitively slow, especially for multi-static imaging experiments involving tens of thousands of scanned positions. The radar simulator provides the synthetic data within several minutes for objects consisting of thousands of sub-wavelength voxels as opposed to weeks of simulation time with full-wave simulations. The synthetic data has allowed for the assessment of the FSPM-TD reconstruction in terms of its IPSF and its spatial resolution. It is shown that the algorithm achieves the theoretical spatial-resolution limits of far-zone imaging.

Validation using experiments is also carried out with an off-the-shelf mm-wave radar (77 GHz to 81 GHz), where the FSPM-TD algorithm achieves spatial resolution consistent with the theoretical estimates. It is shown that calibration of the employed analytical PSF is critically important since there is temporal misalignment with the measured responses. Here, a simple calibration approach is used based on a measurement of a copper plate. It extracts the system internal delay t_{sys}, which is used to correct the time-delay variable in the PSF.

Finally, we note that, unlike the synthetic data that are noise-free, the measured data contain significant noise and radar clutter. The noise figure of the mm-wave LFM receiver used in the experiments is 15 dB. But it is the radar clutter (reflections from the structural components of the imaging setup) that is more detrimental to the signal-to-noise/clutter (SNCR) ratio of the data. The calibration IF signal depicted in Fig. 3.8 indicates an SNCR of about 9.3 dB, when measuring the $5 \times 5\,\mathrm{cm}^2$ metallic plate at a distance of 355 mm from the radar. However, the SNCR is much poorer when we measure a scattering probe. For example, with a 2-mm probe at a distance of 274 mm from the radar, the SNCR is about 3 dB, whereas at 355 mm the probe's signal cannot be detected. Despite the low SNCR values in the experiments, the proposed FSPM-TD algorithm yields images, which are structurally correct and with spatial resolution close to the theoretical limits.

Future work will focus on enhanced calibration methods to enable the quantitative imaging of targets with far-zone measurements as well as the development of an FSPM-TD algorithm for the real-time processing of randomly and sparsely sampled data. The latter development will target applications in imaging with mobile and handheld platforms.

Acknowledgment

This research is partially supported by the IEEE Antennas and Propagation Society (AP-S) Fellowship Program for the academic year 2023-2024. We express our sincere gratitude to the AP-S for their commitment to fostering excellence in the field of antennas and propagation.

BIBLIOGRAPHY

[1] C. Feng, X. Jiang, M.-G. Jeong, H. Hong, C.-H. Fu, X. Yang, E. Wang, X. Zhu, and X. Liu, “Multitarget vital signs measurement with chest motion imaging based on mimo radar,” *IEEE Trans. Microw. Theory Tech.*, vol. 69, no. 11, pp. 4735–4747, 2021.

[2] F. Gumbmann and A. Schiessl, “Short-range imaging system with a nonuniform SFCW approach,” *IEEE Trans. Microw. Theory Tech.*, vol. 65, no. 4, pp. 1345–1354, 2017.

[3] C. Li, Z. Peng, T.-Y. Huang, T. Fan, F.-K. Wang, T.-S. Horng, J.-M. Muñoz-Ferreras, R. Gómez-García, L. Ran, and J. Lin, “A review on recent progress of portable short-range noncontact microwave radar systems,” *IEEE Trans. Microw. Theory Tech.*, vol. 65, no. 5, pp. 1692–1706, 2017.

[4] C. J. Li, S.-T. Yang, and H. Ling, “In-situ ISAR imaging of wind turbines,” *IEEE Trans. Antennas Propag.*, vol. 64, no. 8, pp. 3587–3596, 2016.

[5] L. Pang, H. Liu, Y. Chen, and J. Miao, “Real-time concealed object detection from passive millimeter wave images based on the YOLOv3 algorithm,” *Sensors*, vol. 20, no. 6, 2020. [Online]. Available: https://www.mdpi.com/1424-8220/20/6/1678

[6] C. Q. Mayoral, C. García González, J. C. I. Galarregui, D. Marín, D. Gastón,

C. Miranda, R. Gonzalo, I. Maestrojuán, L. G. Santesteban, and I. Ederra, "Water content continuous monitoring of grapevine xylem tissue using a portable low-power cost-effective FMCW radar," *IEEE Trans. Geosci. Remote Sens.*, vol. 57, no. 8, pp. 5595–5605, 2019.

[7] Y. Song, T. Jin, Y. Dai, and X. Zhou, "Efficient through-wall human pose reconstruction using UWB MIMO radar," *IEEE Antennas Wirel. Propag. Lett.*, vol. 21, no. 3, pp. 571–575, 2022.

[8] J. Chen, Y. Zhang, S. Guo, G. Cui, P. Wu, C. Jia, and L. Kong, "Joint estimation of NLOS building layout and targets via sparsity-driven approach," *IEEE Trans. Geosci. Remote Sens.*, vol. 60, pp. 1–13, 2022.

[9] B. Yektakhah and K. Sarabandi, "All-directions through-the-wall imaging using a small number of moving omnidirectional bi-static FMCW transceivers," *IEEE Trans. Geosci. Remote Sens.*, vol. 57, no. 5, pp. 2618–2627, 2019.

[10] A. Randazzo, C. Ponti, A. Fedeli, C. Estatico, P. D'Atanasio, M. Pastorino, and G. Schettini, "A two-step inverse-scattering technique in variable-exponent Lebesgue spaces for through-the-wall microwave imaging: Experimental results," *IEEE Trans. Geosci. Remote Sens.*, vol. 59, no. 9, pp. 7189–7200, 2021.

[11] S. Kharkovsky and R. Zoughi, "Microwave and millimeter wave nondestructive testing and evaluation - overview and recent advances," *IEEE Instrum. Meas. Mag.*, vol. 10, no. 2, pp. 26–38, 2007.

[12] J. Jebramcik, I. Rolfes, N. Pohl, and J. Barowski, “Millimeterwave radar systems for in-line thickness monitoring in pipe extrusion production lines,” *IEEE Sens. Lett.*, vol. 4, no. 5, pp. 1–4, 2020.

[13] H. Rahbarimagham, H. K. Porzani, M. S. A. Hejazi, M. S. Naderi, and G. B. Gharehpetian, “Determination of transformer winding radial deformation using UWB system and hyperboloid method,” *IEEE Sens. J.*, vol. 15, no. 8, pp. 4194–4202, 2015.

[14] H. Karami, H. Tabarsa, G. B. Gharehpetian, Y. Norouzi, and M. A. Hejazi, “Feasibility study on simultaneous detection of partial discharge and axial displacement of HV transformer winding using electromagnetic waves,” *IEEE Trans. Ind. Inform.*, vol. 16, no. 1, pp. 67–76, 2020.

[15] R. K. Amineh, M. Ravan, and R. Sharma, “Nondestructive testing of nonmetallic pipes using wideband microwave measurements,” *IEEE Trans. Microw. Theory Tech.*, vol. 68, no. 5, pp. 1763–1772, 2020.

[16] M. B. Shah, Y. Gao, M. Ravan, and R. K. Amineh, “Quantitative defect size evaluation in fluid-carrying nonmetallic pipes,” *IEEE Trans. Microw. Theory Tech.*, vol. 70, no. 8, pp. 4071–4081, 2022.

[17] Z. Briqech, S. Gupta, A.-A. Beltay, A. Elboushi, A.-R. Sebak, and T. A. Denidni, “57–64 GHz imaging/detection sensor—part II: Experiments on concealed weapons and threatening materials detection,” *IEEE Sens. J.*, vol. 20, no. 18, pp. 10 833–10 840, 2020.

[18] D. M. Sheen, D. L. McMakin, and T. E. Hall, “Cylindrical millimeter-wave imaging technique for concealed weapon detection,” in *26th AIPR Workshop: Exploiting New Image Sources and Sensors*, J. M. Selander, Ed., vol. 3240, International Society for Optics and Photonics. SPIE, 1998, pp. 242 – 250. [Online]. Available: https://doi.org/10.1117/12.300061

[19] D. Sheen, D. McMakin, and T. Hall, “Three-dimensional millimeter-wave imaging for concealed weapon detection,” *IEEE Trans. Microw. Theory Tech.*, vol. 49, no. 9, pp. 1581–1592, 2001.

[20] ——, “Near-field three-dimensional radar imaging techniques and applications,” *Appl. Opt.*, vol. 49, no. 19, pp. E83–E93, July 2010. [Online]. Available: https://opg.optica.org/ao/abstract.cfm?URI=ao-49-19-E83

[21] D. Tajik, F. Foroutan, D. S. Shumakov, A. D. Pitcher, and N. K. Nikolova, “Real-time microwave imaging of a compressed breast phantom with planar scanning,” *IEEE J. Electromagn. RF Microw. Med. Biol.*, vol. 2, no. 3, pp. 154–162, 2018.

[22] D. J. Kurrant, M. Omer, and E. C. Fear, “Automated workflow for evaluating microwave and multi-modality breast images,” *IEEE J. Electromagn. RF Microw. Med. Biol.*, vol. 7, no. 3, pp. 290–300, 2023.

[23] M. Ghamati, M. Taherzadeh, F. Nabki, and M. Popović, “Integrated fast UWB time-domain microwave breast screening,” *IEEE Trans. Instrum. Meas.*, vol. 72, pp. 1–12, 2023.

[24] S. Hosseinzadegan, A. Fhager, M. Persson, S. D. Geimer, and P. M. Meaney, "Discrete dipole approximation-based microwave tomography for fast breast cancer imaging," *IEEE Trans. Microw. Theory Tech.*, vol. 69, no. 5, pp. 2741–2752, 2021.

[25] D. O. Rodriguez-Duarte, J. A. T. Vasquez, R. Scapaticci, L. Crocco, and F. Vipiana, "Assessing a microwave imaging system for brain stroke monitoring via high fidelity numerical modelling," *IEEE J. Electromagn. RF Microw. Med. Biol.*, vol. 5, no. 3, pp. 238–245, 2021.

[26] Y. Fang, K. Bakian-Dogaheh, and M. Moghaddam, "Real-time 3D microwave medical imaging with enhanced variational Born iterative method," *IEEE Trans. Med. Imaging*, vol. 42, no. 1, pp. 268–280, 2023.

[27] J.-W. Ting, D. Oloumi, and K. Rambabu, "FMCW SAR system for near-distance imaging applications—practical considerations and calibrations," *IEEE Trans. Microw. Theory Tech.*, vol. 66, no. 1, pp. 450–461, 2018.

[28] A. Mostajeran, A. Cathelin, and E. Afshari, "A 170-GHz fully integrated single-chip FMCW imaging radar with 3-D imaging capability," *IEEE J. Solid-State Circuits*, vol. 52, no. 10, pp. 2721–2734, 2017.

[29] Y. Nan, X. Huang, and Y. J. Guo, "A millimeter-wave GCW-SAR based on deramp-on-receive and piecewise constant Doppler imaging," *IEEE Trans. Geosci. Remote Sens.*, vol. 58, no. 1, pp. 680–690, 2020.

[30] M. M. Saurer, B. Hofmann, and T. F. Eibert, "A fully polarimetric multilevel fast spectral domain algorithm for 3-D imaging with irregular sample locations," *IEEE Trans. Microw. Theory Tech.*, vol. 70, no. 9, pp. 4231–4242, 2022.

[31] N. J. Kinzie, "Ultra-wideband pulse Doppler radar for short-range targets," Ph.D. dissertation, University of Colorado at Boulder, 2011.

[32] L. Junhui, W. Hong, W. Xuegang, Y. Yang, and H. Donglin, "Comparative study on stepped frequency, pulsed and continuous wave SARs," 2016. [Online]. Available: https://api.semanticscholar.org/CorpusID:117345140

[33] J. Moll, P. Schops, and V. Krozer, "Towards three-dimensional millimeter-wave radar with the bistatic fast-factorized back-projection algorithm—potential and limitations," *IEEE Trans. Terahertz Sci. Technol.*, vol. 2, no. 4, pp. 432–440, 2012.

[34] T. Kitamura and K. Suwa, "Doppler division multiplexed multiple-input–multiple-output imaging using cascaded millimeter-wave radars," *IEEE Trans. Microw. Theory Tech.*, vol. 70, no. 3, pp. 1571–1581, 2022.

[35] B. Zhang, G. Xu, R. Zhou, H. Zhang, and W. Hong, "Multi-channel back-projection algorithm for mmWave automotive MIMO SAR imaging with Doppler-division multiplexing," *IEEE J. Sel. Top. Signal Process.*, vol. 17, no. 2, pp. 445–457, 2023.

[36] Y. Song, J. Hu, N. Chu, T. Jin, J. Zhang, and Z. Zhou, "Building layout reconstruction in concealed human target sensing via UWB MIMO through-wall

imaging radar," *IEEE Geosci. Remote Sens. Lett.*, vol. 15, no. 8, pp. 1199–1203, 2018.

[37] D. Bleh, M. Rösch, M. Kuri, A. Dyck, A. Tessmann, A. Leuther, S. Wagner, B. Weismann-Thaden, H.-P. Stulz, M. Zink, M. Rießle, R. Sommer, J. Wilcke, M. Schlechtweg, B. Yang, and O. Ambacher, "W -band time-domain multiplexing FMCW MIMO radar for far-field 3-D imaging," *IEEE Trans. Microw. Theory Tech.*, vol. 65, no. 9, pp. 3474–3484, 2017.

[38] D. Smith, O. Yurduseven, B. Livingstone, and V. Schejbal, "Microwave imaging using indirect holographic techniques," *IEEE Antennas and Propagation Mag.*, vol. 56, no. 1, pp. 104–117, 2014.

[39] E. J. Feleppa, "Holography and medicine," *IEEE Trans. Biomed. Eng.*, no. 3, pp. 194–205, 1972.

[40] R. K. Amineh, N. K. Nikolova, and M. Ravan, *Real-Time Three-Dimensional Imaging of Dielectric Bodies Using Microwave/Millimeter Wave Holography.* John Wiley & Sons, 2019.

[41] Y. Meng, C. Lin, J. Zang, A. Qing, and N. K. Nikolova, "General theory of holographic inversion with linear frequency modulation radar and its application to whole-body security scanning," *IEEE Trans. Microw. Theory Tech.*, vol. 68, no. 11, pp. 4694–4705, 2020.

[42] X. Zhuge and A. G. Yarovoy, "Three-dimensional near-field MIMO array imaging using range migration techniques," *IEEE Trans. Image Process.*, vol. 21, no. 6, pp. 3026–3033, 2012.

[43] S. Li, G. Zhao, H. Sun, and M. Amin, "Compressive sensing imaging of 3-D object by a holographic algorithm," *IEEE Trans. Antennas Propag.*, vol. 66, no. 12, pp. 7295–7304, 2018.

[44] Y. Meng, C. Lin, A. Qing, and N. K. Nikolova, "Accelerated holographic imaging with range stacking for linear frequency modulation radar," *IEEE Trans. Microw. Theory Tech.*, vol. 70, no. 3, pp. 1630–1638, 2022.

[45] R. K. Amineh, J. J. McCombe, A. Khalatpour, and N. K. Nikolova, "Microwave holography using point-spread functions measured with calibration objects," *IEEE Trans. Instrum. Meas.*, vol. 64, no. 2, pp. 403–417, 2015.

[46] D. Tajik, A. D. Pitcher, and N. K. Nikolova, "Comparative study of the Rytov and Born approximations in quantitative microwave holography," *Prog. Electromagn. Res. B*, vol. 79, pp. 1–19, 2017.

[47] G. Wang, F. Qi, Z. Liu, C. Liu, C. Xing, and W. Ning, "Comparison between back projection algorithm and range migration algorithm in terahertz imaging," *IEEE Access*, vol. 8, pp. 18 772–18 777, 2020.

[48] A. Ribalta, "Time-domain reconstruction algorithms for FMCW-SAR," *IEEE Geosci. Remote. Sens. Lett.*, vol. 8, no. 3, pp. 396–400, 2011.

[49] B. Yektakhah and K. Sarabandi, "All-directions through-the-wall imaging using a small number of moving omnidirectional bi-static FMCW transceivers," *IEEE Trans. Geosci. Remote Sens.*, vol. 57, no. 5, pp. 2618–2627, 2019.

[50] Z. Chen, Z. Zeng, D. Fu, Y. Huang, Q. Li, X. Zhang, and J. Wan, "Back-projection imaging for synthetic aperture radar with topography

occlusion," *Remote Sens.*, vol. 15, no. 3, 2023. [Online]. Available: https://www.mdpi.com/2072-4292/15/3/726

[51] A. Zhuravlev, V. Razevig, A. Rogozin, and M. Chizh, "Microwave imaging of concealed objects with linear antenna array and optical tracking of the target for high-performance security screening systems," *IEEE Trans. Microw. Theory Tech.*, vol. 71, no. 3, pp. 1326–1336, 2023.

[52] N. K. Nikolova, *Introduction to Microwave Imaging*, ser. EuMA High Frequency Technologies Series. Cambridge University Press, 2017.

[53] M. Kazemi, Z. Kavehvash, and M. Shabany, "K-space aware multi-static millimeter-wave imaging," *IEEE Trans. Image Processing*, vol. 28, no. 7, pp. 3613–3623, 2019.

[54] Q. Mao, J. Liu, Y. Zhu, C. Lv, Y. Lu, D. Wei, S. Yan, S. Ding, and D. Ling, "Developing industry-level terahertz imaging resolution using mathematical model," *IEEE Trans. Terahertz Sci. Technol.*, vol. 11, no. 5, pp. 583–590, 2021.

[55] D. Tajik, R. Kazemivala, and N. K. Nikolova, "Real-time imaging with simultaneous use of Born and Rytov approximations in quantitative microwave holography," *IEEE Trans. Microw. Theory Tech.*, vol. 70, no. 3, pp. 1896–1909, 2022.

[56] D. Tajik, R. Kazemivala, J. Nguyen, and N. K. Nikolova, "Accurate range migration for fast quantitative Fourier-based image reconstruction with monostatic radar," *IEEE Trans. Microw. Theory Tech.*, vol. 70, no. 9, pp. 4273–4283, 2022.

[57] D. S. Shumakov and N. K. Nikolova, “Fast quantitative microwave imaging with scattered-power maps,” *IEEE Transactions on Microwave Theory and Techniques*, vol. 66, no. 1, pp. 439–449, 2018.

[58] R. Kazemivala, D. Tajik, and N. K. Nikolova, “Simultaneous use of the Born and Rytov approximations in real-time imaging with Fourier-space scattered power mapping,” *IEEE Trans. Microw. Theory Tech.*, vol. 70, no. 5, pp. 2904–2920, 2022.

[59] *IWR1443BOOST Evaluation Module mmWave Sensing Solution*, Texas Instruments, 2020. [Online]. Available: https://www.ti.com/lit/ug/swru518d/swru518d.pdf?ts=1703684594280

[60] S. Tu, J. McCombe, D. Shumakov, and N. Nikolova, “Fast quantitative microwave imaging with resolvent kernel extracted from measurements,” *Inverse Probl.*, vol. 31, no. 4, p. 045007, 2015.

[61] G. Wang, J.-M. Muñoz-Ferreras, C. Gu, C. Li, and R. Gómez-García, “Application of linear-frequency-modulated continuous-wave (LFMCW) radars for tracking of vital signs,” *IEEE Trans. Microw. Theory Tech.*, vol. 62, no. 6, pp. 1387–1399, 2014.

[62] E. D. Jansing, *Introduction to Synthetic Aperture Radar*. McGraw Hill, 2021.

[63] MATLAB, *ver. R2022b*. Natick, Massachusetts: The MathWorks Inc., 2022.

[64] Y. K. Chan and V. Koo, “An introduction to synthetic aperture radar (SAR),” *Prog. Electromagn. Res. B*, vol. 2, pp. 27–60, 2008.

[65] Z. Wang, A. Bovik, H. Sheikh, and E. Simoncelli, "Image quality assessment: from error visibility to structural similarity," *IEEE Trans. Image Processing*, vol. 13, no. 4, pp. 600–612, 2004.

[66] G. Golub and C. Van Loan, *Matrix Computations*, 3rd ed. Baltimore: John Hopkins University Press, 1996.

[67] *DCA1000EVM Real-time Data-capture Adapter for Radar Sensing Evaluation Module*, Texas Instruments, 2019.

[68] Z. Peng, J. M. Muñoz-Ferreras, Y. Tang, C. Liu, R. Gómez-García, L. Ran, and C. Li, "A portable FMCW interferometry radar with programmable low-IF architecture for localization, ISAR imaging, and vital sign tracking," *IEEE Trans. Microw. Theory Tech.*, vol. 65, no. 4, pp. 1334–1344, 2017.

CHAPTER 4

REAL-TIME SYNTHETIC APERTURE RADAR IMAGING WITH RANDOM SAMPLING EMPLOYING SCATTERED POWER MAPPING

Preface

This chapter is a reproduction of the following published article:

R. Kazemivala and N. K. Nikolova, “Real-time Synthetic Aperture Radar Imaging with Random Sampling Employing Scattered Power Mapping,” in *Sensors*, vol. 24, no. 12, June 2024, doi: 10.3390/s24123849.

The contribution of the authors are: Conceptualization, Natalia K. Nikolova methodology, Romina Kazemivala and Natalia K. Nikolova; validation, Romina Kazemivala and Natalia K. Nikolova; investigation, Romina Kazemivala and Natalia K. Nikolova; resources, Natalia K. Nikolova; writing original draft preparation, Romina Kazemivala; writing review and editing, Romina Kazemivala and Natalia K. Nikolova; supervision, Natalia K. Nikolova; project administration, Natalia K. Nikolova; funding acquisition,Natalia K. Nikolova

4.1 Introduction

In recent years, many microwave and millimeter-wave (mm-wave) imaging technologies have emerged to cater to a multitude of applications based on the principles of synthetic aperture radar (SAR). These innovative applications span various domains such as nondestructive testing and evaluation (NDT&E) [1–7], security inspection [8–13], and medical imaging [14–20]. Revolutionizing aerial surveillance, small unmanned aerial vehicles (UAVs) emerge as pivotal players in SAR imaging [21–26]. Their potential as platforms for SAR imaging is due to the remarkable progress of the positioning technology, which now provides accurate platform coordinates. The convergence of UAVs with ground-penetrating radars (GPRs) [27–34], operating at wavelengths as short as 73 mm, necessitates positional accuracy at the centimeter or millimeter scale for effective imaging. This accuracy, akin to trajectory accuracy in remote sensing, is of paramount importance since errors as small as a fraction of a wavelength lead to pronounced image distortions. Positional accuracy remains a challenge in handheld mm-wave imagers, where state-of-the-art systems rely on fast electronically switched antenna arrays forming the acquisition aperture [35–37]. Nonetheless, handheld imagers stand to benefit greatly from the addition of positioning technology since this can dramatically expand the realized synthetic aperture beyond the size of the switched antenna array. A common requirement for the image-reconstruction algorithms of such UAV-borne or handheld imaging systems is that they must be able to process randomly sampled datasets acquired in three-dimensional (3D) space with coordinates which do not conform to uniform grids.

In conventional close-range imaging, mechanical scanning is typically realized with

1D or 2D automated scanners (also known as translation stages), equipped with high-precision positioning mechanisms. The sampling is usually uniform, i.e., at regular spatial intervals, although advanced scanners also allow for random sampling. The scanning, however, is inherently constrained to canonical (planar, cylindrical, and spherical) surfaces. Most of the real-time image-reconstruction algorithms (e.g., microwave holography and the range migration) take advantage of such uniformly sampled data in order to employ fast Fourier transform (FFT) algorithms and to achieve remarkable reconstruction speeds [38–40]. However, this also renders them incapable of processing randomly sampled data. Nonuniform sampling on canonical acquisition surfaces can be handled by interpolation, but this entails significant computational overhead and may result in unfocused images [41–43]. On the other hand, nonuniform sampling on such surfaces has been shown to allow for sampling densities below the Nyquist limit [44–46].

In summary, innovative solutions are needed to address nonuniform and random sampling since they would benefit both the imaging systems sampling along unpredictable 3D trajectories (e.g., handheld and UAV-borne) and those scanning over canonical 2D surfaces.

To this end, a few image-reconstruction algorithms based on the back-projection (or back-propagation) algorithm (BPA) have been proposed [24, 27, 29, 47, 48]. The BPAs, when applied in real (x, y, z) space, can inherently handle any sampling position; thus, they are preferred in the case of nonuniform and random sampling. However, the computational resources required by the BPAs are significant as they rely on aggregating phase-conjugated scattered field data [49, 50]. This may preclude real-time image reconstruction. The accuracy of the sampling positions is critical in imaging reconstruction, and it is a major problem with moving SAR platforms. Various approaches to mitigate positional inaccuracies through hardware adjustments are employed [51–53] to make the data suitable for BPA processing. These methods employ an integrated navigation system to monitor the real-time motion velocity of the radar platform. Among the BPAs, some incorporate interpolation of the nonuniformly sampled signals [52, 54]. Other BPAs incorporate image fusion to increase the quality of the images by splitting the large synthetic aperture into multiple subapertures [24, 52]. Further, in order to accurately extract the velocity to obtain high-quality BPA images, the adaptive notch filtering (ANF) technique has been employed [47].

The ω-k algorithms, such as the range-migration algorithms (RMAs) and the microwave holography algorithms (MHAs), provide a compelling alternative to the BPAs [42, 49, 55–58]. These methods first transform the data sampled over the aperture into the Fourier spatial-frequency domain (the k-space) through FFT. These algorithms harness an analytical range-migration model, which links the frequency (ω) dependence of the data to the range (or depth) position of a scattering center within the imaged object. This is facilitated by Stolt's interpolation. The object's reflectivity is reconstructed in k-space, after which it is translated back into real space via the inverse Fourier transform (IFT). By operating mostly in k-space, the ω-k algorithms gain a significant speed advantage over the BPAs. However, they are limited to uniform sampling on canonical surfaces. This limitation is overcome with various methods referred to as spectral estimation [56]. The spectral estimation aims at recovering the spectrum of the data on a uniform grid in k-space while the data are acquired with nonuniform sampling on the synthetic aperture (in real space). Methods include natural neighbor interpolation, nonuniform FFT (NUFFT), nonuniform discrete Fourier transform (NDFT), and multilevel conjugate-gradient residual error minimization. The spectral estimation comes at a significant computational cost. Moreover, it remains limited by the requirement for a synthetic aperture of canonical shape.

Various recent studies focus on data preprocessing for randomly and nonuniformly sampled data rather than new image-reconstruction algorithms. The respective approaches can be categorized into regularization-based algorithms [59–64] and compressive-sensing (CS) algorithms [65–72]. The latter can address not only the random sampling but can also potentially deal with data sparsity, thus reducing the required amount of measurements [67]. As an example of a regularization-based algorithm, Zhang et al. [59] formulate a linear system of equations, where the system matrix comprises Fourier coefficients. Tikhonov regularization is employed to solve the system of equations, providing the 1D k-spectrum of the nonuniform spatially sampled data along the azimuth. The application is geared toward linear frequency-modulated (LFM) radar signals. In effect, the preprocessing performs spectral estimation before providing the k-space result to an image-reconstruction algorithm. Uniformly sampled k-space data can be processed with various k-space image-reconstruction algorithms such as the RMAs, the MHAs, or the range Doppler algorithm (RDA) [59,60]. On the other hand, the CS techniques are primarily focused on achieving high image resolution with sparse data, where the sampling rate is well below the Nyquist limit [65, 66]. The sparse data may be uniformly or randomly sampled, but there seems to be benefits in the latter case [67, 73]. The main limitation of CS is that the outcome strongly depends on the adequate choice of the *representation basis* [67], where the information content of the data is anticipated to be much lower than in the actual measurement space [73]. In imaging, the existence of such basis and the data sparsity in it are dictated by the complexity of the imaged object and some distinct shape or material features. Therefore, CS algorithms do not compensate for the lack of data; they leverage mathematical representations of signals known to be presentable in terms of only a few basis functions in some space [74].

Scattered power mapping (SPM) is a well-established method for rapid (real-time) SAR imaging, which has been applied with both frequency-domain (stepped frequency continuous wave, SFCW) and LFM data [38, 75–78]. This paper proposes a new SPM algorithm adapted to perform image reconstruction with nonuniformly sampled data acquired on random 3D trajectories—a scenario arising when imaging radars are mounted on mobile or handheld platforms. We emphasize that the proposed method is not a compressed sensing approach. The hallmark of SPM is a two-stage inversion, where the first stage is a projection that maps the data onto a 3D image of the target reflectivity, and the second stage is an image deconvolution which enhances the output of the first stage. The first (projection) stage of the algorithm can work either in real (x, y, z) space [75, 76] or in k-space [77, 78]. The k-space implementation is computationally very efficient, but this efficiency relies on the FFT of the data, which in turn requires uniform sampling on canonical synthetic apertures. In contrast, the real-space implementation can handle any sampling position while still producing a reflectivity image on a uniform 3D grid. Therefore, it is capable of utilizing data that are randomly sampled in 3D space. On the other hand, the second (image-deconvolution) stage is always performed in k-space since it operates on the reflectivity output of the first stage, which is already cast onto a uniform 3D grid. Thus, the second stage does not depend on whether the sampling is random or uniform, and it is very fast.

In summary, the proposed image reconstruction has the flexibility of BPAs to handle randomly sampled data, but it yields images of higher quality due to the image-deconvolution stage. In comparison with the ω-k algorithms, the proposed algorithm does not require synthetic apertures on canonical surfaces. The randomly sampled aperture is in fact a 3D volume. Neither NUFFT nor other spectral estimation methods are needed, which renders the reconstruction faster than that with the ω-k algorithms.

Finally, the algorithm processes the data on-the-run, i.e., the image reconstruction does not need to wait for the completion of a scan. In fact, utilizing a convergence criterion, it is the algorithm which decides when the amount of data is sufficient and its collection can be terminated.

4.2 Methodology

4.2.1 3D Scanning

Figure 4.1 illustrates a scan along a random 3D trajectory as opposed to a scan on a planar 2D synthetic aperture. The positions of the imaging platform along the trajectory, where measurements are taken, are assumed known and are denoted as $\mathbf{r}$. These positions are illustrated by the dots comprising the trajectory. Each measurement instance is associated with N_{Tx} transmitting (Tx) antennas and N_{Rx}

receiving (Rx) antenna positions to allow for the possibility of utilizing a multiple-input multiple-output (MIMO) radar. The Tx and Rx antennas are rigidly mounted on the platform; therefore, it is assumed that the Rx antenna positions $\mathbf{r}_i$ ($i = 1, \ldots, N_{\text{Rx}}$) and the Tx antenna positions $\mathbf{r}_j$ ($j = 1, \ldots, N_{\text{Tx}}$) can be determined from the platform's position $\mathbf{r}$. An imaged position is denoted by $\mathbf{r}'$. The measurement may be carried out using SFCW or LFM radars, examples of which are presented here. The SPM algorithm can also be applied with pulsed radar data. Using multiple antennas on a moving platform has several advantages. Firstly, multiple Tx and Rx antennas offer diversity in illumination and observation angles, respectively, which is beneficial in close-range measurements. Secondly, having more data from multiple antennas significantly reduces image noise and clutter [79]. Lastly, these benefits drive the development of MIMO radars, where the array element spacing is about half a wavelength or more, enhancing phase diversity in collected responses. Note that in our investigation, the tilt angle of the antenna relative to the range is constant. Thus, the platform's orientation does not vary. Furthermore, the antenna far-field patterns are not considered in the presented examples. The use of antenna patterns in SAR imaging is well-known, and its benefits have been investigated in [80,81]. While it can enhance accuracy, its use is often impractical due to the unavailability of 3D patterns or near-zone measurement conditions [3,6,40,44,63,77,82–85].

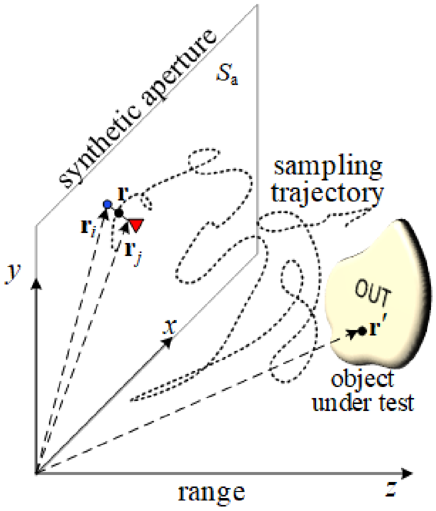

Figure 4.1: Illustration of a measurement on a random 3D trajectory (black dots) as opposed to a measurement on a planar aperture denoted as S_{a}. The trajectory may also be 2D, lying entirely within S_{a}. The red triangle and the blue point represent Tx and Rx positions, respectively. The response acquired with the i-th Rx antenna ($i = 1, \ldots, N_{\mathrm{Rx}}$) and the j-th Tx antenna ($j = 1, \ldots, N_{\mathrm{Tx}}$) is identified by a subscript $\zeta \equiv (i, j)$. The platform's position $\mathbf{r}$ is assumed known at each measurement instance, and the positions of the Rx and Tx antennas, $\mathbf{r}_i$ and $\mathbf{r}_j$, respectively, are determined from $\mathbf{r}$. An imaged position is denoted as $\mathbf{r}'$. Note that the bore–sight axis of the antennas is fixed along the range direction.

4.2.2 Image Reconstruction with Randomly Sampled Data Employing Scattered Power Mapping

The SPM is a two-stage inversion method for real-time SAR imaging [75–78, 86]. It has been originally applied with frequency-domain data, for which an exact forward model of scattering exists in terms of the S-parameters [87]. For real-time image reconstruction, this exact model is linearized using the zero-order Born approximation of the total internal field [38], leading to the approximate data equation for the scattered portion of the measured S-parameters:

$$S_{\zeta}^{\mathrm{sc}}(\mathbf{r},\omega) \approx c_{\zeta} \iiint_{V'} \Delta\varepsilon_{\mathrm{r}}(\mathbf{r}')\mathbf{E}_{\zeta,\mathrm{Rx}}^{\mathrm{inc}}(\mathbf{r}',\mathbf{r},\omega) \cdot \mathbf{E}_{\zeta,\mathrm{Tx}}^{\mathrm{inc}}(\mathbf{r}',\mathbf{r},\omega)d\mathbf{r}' \,. \tag{4.1}$$

Here, ω is frequency, $\mathbf{r}$ is the measurement position, $\mathbf{r}' \in V'$ is a position within the imaged volume V', and $\zeta \equiv (i,j)$ denotes the antenna pair determined by the Rx (i-th) and Tx (j-th) antennas. For instance, $\zeta = 1,2,3,\ldots,N_{\mathrm{Tx}}N_{\mathrm{Rx}}$ refers to S_{11}, S_{22}, S_{21}, etc. Here, $\mathbf{E}_{\zeta,\mathrm{Tx}}^{\mathrm{inc}}$ is the incident field due to the Tx antenna at $\mathbf{r}_j(\mathbf{r})$, which replaces the total internal field through Born's zero-order approximation, and $\mathbf{E}_{\zeta,\mathrm{Rx}}^{\mathrm{inc}}$ is the incident field due to the Rx antenna at $\mathbf{r}_i(\mathbf{r})$, if this antenna were to transmit. Mathematically, $\mathbf{E}_{\zeta,\mathrm{Rx}}^{\mathrm{inc}}$ represents the background vector Green function. Additionally, $\Delta\varepsilon_{\mathrm{r}}(\mathbf{r}')$ is the object's relative-permittivity contrast, which is assumed independent of the frequency and the field polarization. The object's contrast is in general complex, i.e., it can represent lossy materials. It is defined as $\Delta\varepsilon_{\mathrm{r}} = \varepsilon_{\mathrm{r}} - \varepsilon_{\mathrm{r,b}}$, where ε_{r} is the object's complex relative permittivity and $\varepsilon_{\mathrm{r,b}}$ is that of the background. The constant $c_{\zeta} = \frac{-\mathrm{i}\omega\varepsilon_0}{2a_{\mathrm{Rx}}a_{\mathrm{Tx}}}$ is determined by the root-power waves a_{Rx} and a_{Tx} (root-power waves, or power waves, are phasors that describe traveling electromagnetic waves in waveguides [38, 88]. The magnitude is the square root of the power carried by the wave, and the phase corresponds to the phase of the wave's electric field) and the incident on the ports of the antennas generating the respective fields. Here, ε_0 denotes the permittivity of the vacuum.

Here we assume that the objects are nonmagnetic and that the scattering is polarization-independent. Additionally, we assume that the permittivity is constant in the frequency band of interest (the object is nondispersive) [89–91] since dispersion effects are weak at microwave and millimeter-wave frequencies. However, the $\mathbf{E}$-fields and the S-parameters (the data) in (C.22) are frequency-dependent, as dictated by the wavenumbers of the background and the object as well as the signal phase delays to/from the object. This frequency dependence provides response diversity and is critical in achieving high image quality.

For the purposes of the discussion that follows, the forward model of scattering must be cast in terms of the system PSF, which plays a central role in the proposed SPM method. The system PSF represents the response (the measured signal) due to a point scatterer in the background medium [38]. It is clear that the PSF of the data Equation (C.22) is

$$H_{\zeta}^{\mathrm{sc}}(\mathbf{r}, \omega; \mathbf{r}_{\mathrm{sp}}) = c_{\zeta} \Omega_{\mathrm{sp}} \Delta\varepsilon_{\mathrm{r,sp}} \mathbf{E}_{\zeta,\mathrm{Rx}}^{\mathrm{inc}}(\mathbf{r}_{\mathrm{sp}}, \mathbf{r}, \omega) \cdot \mathbf{E}_{\zeta,\mathrm{Tx}}^{\mathrm{inc}}(\mathbf{r}_{\mathrm{sp}}, \mathbf{r}_{\mathrm{Tx}}, \omega)\,, \tag{4.2}$$

describing the scattering from an electrically small (point-like) scatterer of volume Ω_{sp} and contrast distribution represented by Dirac's δ-function, $\Delta\varepsilon_{\mathrm{r,sp}}\delta(\mathbf{r}' - \mathbf{r}_{\mathrm{sp}})$. Here, $\mathbf{r}_{\mathrm{sp}}$ is the position of the point scatterer (also referred to as the scattering probe). The system-specific kernel in (C.23) can be determined through a calibration measurement independently of the OUT. By measuring an electrically small scatterer of known Ω_{sp} and $\Delta\varepsilon_{\mathrm{r,sp}}$ embedded in the background medium, one can obtain the measured PSFs $H_{\zeta}^{\mathrm{sc}}(\mathbf{r}, \omega; \mathbf{r}_{\mathrm{sp}})$. In close-range radar imaging applications, measuring the PSF with a high SNR is feasible as long as the scattering probe can be embedded in the background medium. In long-range radar imaging, measuring the PSF is challenging since the scattering signal from a distant small probe is very weak, thus the preference for using analytical PSFs.

As suggested by (C.22), acquiring the incident fields distribution as represented by the dot product is complex. If the PSF is acquired as shown in (C.23), there is a simple linear relation between (C.22) and (C.23). The linearized scattering model (C.22) is then expressed as

$$S_{\zeta}^{\mathrm{sc}}(\mathbf{r},\omega) \approx \iiint_{V'} \rho(\mathbf{r}') H_{\zeta}^{\mathrm{sc}}(\mathbf{r},\omega;\mathbf{r}') d\mathbf{r}' \,, \tag{4.3}$$

where $\rho(\mathbf{r}') = \Delta\varepsilon_{\mathrm{r}}(\mathbf{r}')/(\Delta\varepsilon_{\mathrm{r,sp}}\Omega_{\mathrm{sp}})$ is termed the object's reflectivity function. Clearly, the model in (C.24) views the imaged object as a collection of point (or differential) scatterers and represents the measured signal as the superposition of the scattering emanating from all point scatterers making up the object. Note that the relation between the measured PSF and the incident fields due to the Tx and Rx antennas are determined by comparing (C.22) and (C.24). Further, (C.23) is crucial in computing quantitative estimations of permittivity. The advantage of the representation in (C.24) is that it allows for using a PSF, which is derived either analytically, or from simulations, or from measurements. The analytical PSFs typically employ far-field approximations of the incident fields in (C.23) (possibly enhanced by the antenna's far-field patterns [81]) whereas simulation-based PSFs utilize incident field distributions obtained by simulating the radiation from the Rx and Tx antennas in the background medium [92]. Measured PSFs are obtained by measuring an electrically small scattering probe of known volume Ω_{sp} and contrast $\Delta\varepsilon_{\mathrm{r,sp}}$ placed at the center of the imaged volume [75, 93].

With the data $S_{\zeta}^{\mathrm{sc}}(\mathbf{r},\omega)$ and the PSFs $H_{\zeta}^{\mathrm{sc}}(\mathbf{r},\omega;\mathbf{r}')$ available, the SPM reconstructs $\rho(\mathbf{r}')$ through a computationally efficient two-stage procedure. The first SPM stage is a projection that builds the 3D scattered power map $M(\mathbf{r}')$ of the object under test

(OUT) as the discrete inner product of the data and the system PSFs:

$$M(\mathbf{r}') = \sum_{\zeta=1}^{N_\mathrm{R}} \sum_{n=1}^{N_\omega} \sum_{m=1}^{N_m} S_\zeta^\mathrm{sc}(\mathbf{r}_m, \omega_n) \ \left[H_\zeta^\mathrm{sc}(\mathbf{r}_m, \omega_n; \mathbf{r}')\right]^* . \tag{4.4}$$

Here, N_m is the number of measurement positions, N_ω is the number of frequency points, and N_R is the total number of used antenna pairs (the number of responses) at each measurement position $\mathbf{r}$ and each frequency ω as determined by the available Tx/Rx antenna pairs in $\zeta = (i, j)$. The measurement positions $\mathbf{r}_m$, $m = 1, \ldots, N_m$ may belong to a synthetic 2D aperture, a 3D acquisition volume, or a random trajectory. We emphasize that we do not consider the variation in the platform orientation and it is fixed along the antennas' bore–sight axis. Note that the OUT power map $M(\mathbf{r}')$ has complex values. With a large number of responses, this map converges to a distribution, which is proportional to the OUT complex permittivity $\Delta\varepsilon_\mathrm{r}(\mathbf{r}')$ [38]. Therefore, $|M(\mathbf{r}')|$ is a representation of the OUT reflectivity $|\rho(\mathbf{r}')|$, and its normalized plot provides a qualitative OUT image.

Recently, it has been shown that the projection reconstruction stage described by (4.4) can also be applied with time-domain signals $S_\zeta^\mathrm{sc}(\mathbf{r}, t)$ [78], where the summation over ω is simply replaced by a summation over time t:

$$M(\mathbf{r}') = \sum_{\zeta=1}^{N_\mathrm{R}} \sum_{n=1}^{N_n} \sum_{m=1}^{N_m} S_\zeta^\mathrm{sc}(\mathbf{r}_m, t_n) \ \left[H_\zeta^\mathrm{sc}(\mathbf{r}_m, t_n; \mathbf{r}')\right]^* . \tag{4.5}$$

Note that the conjugation of $H_\zeta^\mathrm{sc}(\mathbf{r}, t; \mathbf{r}')$ matters in the case of LFM radar signals, which are complex, i.e., at each $\mathbf{r}$, the receiver output contains an in-phase (I) and a quadrature (Q) signal component so that the time-dependent signal is expressed as $S(t) = I(t) + iQ(t)$.

The first SPM stage carried out with (4.4) for frequency-domain signals or with (4.5) for time-domain signals allows for mapping the random spatial samples ($\mathbf{r}$) onto a uniform 3D image grid ($\mathbf{r}$'). Moreover, since the OUT map $M(\mathbf{r}')$ is computed as the sum of contributions $C_m(\mathbf{r}')$ from the measurement positions $\mathbf{r}_m$ ($m = 1, \ldots, N_m$),

$$M(\mathbf{r}') = \sum_{m=1}^{N_m} C_m(\mathbf{r}')\,,\ C_m(\mathbf{r}') = \sum_{\zeta=1}^{N_\mathrm{R}} \sum_{n=1}^{N_n} S_\zeta^{\mathrm{sc}}(\mathbf{r}_m, \nu_n)\ \left[H_\zeta^{\mathrm{sc}}(\mathbf{r}_m, \nu_n; \mathbf{r}')\right]^*\ ,\ \nu = \omega \text{ or } t\,, \tag{4.6}$$

it can be updated concurrently with the measurements by adding a measurement contribution when it becomes available, assuming that the PSF $H_\zeta^{\mathrm{sc}}(\mathbf{r}_m, \nu_n; \mathbf{r}')$ has been determined on a uniform grid $\mathbf{r}'$ in the OUT power map for random measurement positions $\mathbf{r}_m$. In (4.6), N_n is the number of frequency or temporal samples. We emphasize that the method is versatile and not limited to specific frequency bands, as the contribution of each frequency/time sample ν_n is being summed as shown in (4.6). As the number of data points increases with the stream of additional measurements, this map converges to a first-stage OUT image, which is further processed by the second SPM stage. We reiterate that the imaged positions $\mathbf{r}'$ belong to a uniformly sampled spatial grid whereas the measurement (or observation) positions $\mathbf{r}_m$, $m = 1, \ldots, N_m$ are random.

The second SPM stage performs image deconvolution, which greatly enhances the image quality. This deconvolution is performed efficiently in Fourier (k) space, taking advantage of the fact that the first-stage OUT map $M(\mathbf{r}')$ in (4.6) is already cast on a uniformly sampled grid. Assuming a homogeneous unbounded (an unbounded medium is a standard term in numerical electromagnetics indicating that the domain of interest is "open", i.e., without exterior reflecting boundaries. In EM simulations, this is achieved using open-space Green's functions or nonreflecting boundary conditions, e.g., perfectly matched layers) background, $M(\mathbf{r}')$, $\mathbf{r}' \equiv (x', y', z')$ can be expressed through the 2D convolution of the reflectivity function $\rho(x', y', z')$ and the point-scatterer maps $\mathcal{M}(x', y', z'; z'')$ [38, 75, 77]:

$$M(x', y', z') = \iiint\limits_{z''y''x''} \rho(x^{\boldsymbol{\prime}}, y^{\boldsymbol{\prime}}, z^{\boldsymbol{\prime}})\ \mathcal{M}(x' - x^{\boldsymbol{\prime}}, y' - y^{\boldsymbol{\prime}}, z', z^{\boldsymbol{\prime}}) dx^{\boldsymbol{\prime}} dy^{\boldsymbol{\prime}} dz^{\boldsymbol{\prime}} \,. \tag{4.7}$$

The second SPM stage aims at recovering the unknown reflectivity function $\rho(\mathbf{r}')$. The point-scatterer map $\mathcal{M}(x', y', z'; z^{\boldsymbol{\prime}})$ is the first-stage map of a point scatterer residing at the center ($x^{\boldsymbol{\prime}} = y^{\boldsymbol{\prime}} = 0$) of the image slice at $z^{\boldsymbol{\prime}}$ in the homogeneous background. Hereafter, we refer to this map as a PSF map. Note that for each image slice $z^{\boldsymbol{\prime}}$, there is a corresponding 3D PSF map. The PSF map $\mathcal{M}(x', y', z'; z^{\boldsymbol{\prime}})$ is defined analogously to the first-stage OUT projection (4.6), where the OUT response $S_{\zeta}^{\text{sc}}(\mathbf{r}_m, \nu_n)$, $\mathbf{r}_m = (x_m, y_m, z_m)$, is replaced by the PSF $H_{\zeta}^{\text{sc}}(\mathbf{r}_m, \nu_n; z^{\boldsymbol{\prime}})$ representing the response from a scattering probe at $\mathbf{r}^{\boldsymbol{\prime}} = (0, 0, z^{\boldsymbol{\prime}})$:

$$\mathcal{M}(x', y', z'; z^{\boldsymbol{\prime}}) = \sum_{m=1}^{N_m} \sum_{\zeta=1}^{N_{\text{R}}} \sum_{n=1}^{N_n} H_{\zeta}^{\text{sc}}(x_m, y_m, z_m, \nu_n; z^{\boldsymbol{\prime}}) \left[H_{\zeta}^{\text{sc}}(x_m, y_m, z_m, \nu_n; x', y', z')\right]^* \,, \ \nu = \omega \text{ or } t \,. \tag{4.8}$$

In contrast to the OUT map, however, the PSF maps do not need to be computed from spatially random samples. The PSFs H_{ζ}^{sc} are independent of the OUT and they can be obtained analytically, or via simulations, or via measurements, on any convenient grid of observation points $\mathbf{r}$. From a computational efficiency point of view, a PSF evaluation on a uniform grid is advantageous since it allows for the deconvolution of (4.7) to be performed in k-space, as explained next.

We assume that the PSFs are evaluated on a planar synthetic aperture S_a (see Figure 4.1), whose range position $\bar{z}$ relative to the OUT is chosen to be within the span of the range positions z_m, $m = 1, \ldots, N_m$ during the OUT random scan. The lateral rectangular extent of S_a is also determined by the minimum and maximum lateral (x and y) coordinates of the random samples. The sampling along x and y on this plane is coincident with the grid points along x' and y' of the OUT map. This sampling must be sufficiently dense so that it conforms to the Nyquist limit. For example, with monostatic radar measurements, the spatial sampling steps Δx and Δy should not exceed $\frac{\lambda_\mathrm{min}}{4\sin\alpha}$ [38], where α is the maximum viewing angle determined by the aperture size and the antenna beamwidths. The assumptions of a homogeneous background and uniform sampling along (x, y) allow for casting (4.8) in terms of a discrete 2D convolution:

$$\mathcal{M}(x', y', z'; z'') = \sum_{\chi=1}^{N_x} \sum_{\eta=1}^{N_y} \sum_{\zeta=1}^{N_\mathrm{R}} \sum_{n=1}^{N_n} H_\zeta^\mathrm{sc}(x_\chi, y_\eta, \bar{z}, \nu_n; z'') \left[H_\zeta^\mathrm{sc}(x_\chi - x', y_\eta - y', \bar{z}, \nu_n; z')\right]^* \,, \ \nu = \omega \text{ or } t \,. \quad (4.9)$$

In k-space, the 2D convolution in (4.9) is a multiplication of the 2D FTs of the PSF responses:

$$\tilde{\mathcal{M}}(k_x, k_y, z'; z'') = \sum_{\zeta=1}^{N_\mathrm{R}} \sum_{n=1}^{N_n} \tilde{H}_\zeta^\mathrm{sc}(k_x, k_y, \bar{z}, \nu_n; z'') \left[\tilde{H}_\zeta^\mathrm{sc}(k_x, k_y, \bar{z}, \nu_n; z')\right]^* \,, \ \nu = \omega \text{ or } t \,. \quad (4.10)$$

Here, $\tilde{\mathcal{M}}(k_x, k_y, z'; z'')$ is the 2D FT of the PSF map $\mathcal{M}(x', y', z'; z'')$; $\tilde{H}_\zeta^\mathrm{sc}(k_x, k_y, \bar{z}, \nu_n; z_\mathrm{sp})$ is the 2D FT of the PSF response $H_\zeta^\mathrm{sc}(x, y, \bar{z}, \nu; z_\mathrm{sp})$ when the scattering probe is at the center of the range slice $z_\mathrm{sp} = z', z''$; and k_x and k_y are the Fourier variables corresponding to x' and y', respectively. Although the computation in (4.10) requires the 2D FT of the PSFs, it is orders of magnitude faster than its real-space counterpart in (4.9) [77]. Moreover, it is the k-space PSF maps that are needed for the efficient deconvolution of (4.7) and the recovery of the reflectivity function $\rho(\mathbf{r}')$, as explained next.

Applying 2D FT to both sides of (4.7) and discretizing the integration over z' into a sum leads to

$$\tilde{M}(k_x, k_y, z'_p) = \Delta\Omega_{\text{v}} \sum_{k=1}^{N_z} \tilde{\rho}(k_x, k_y, z'_k)\tilde{\mathcal{M}}(k_x, k_y, z'_p; z'_k)\,, p = 1, \ldots, N_z\,, \tag{4.11}$$

where N_z is the number of image slices, $\Delta\Omega_{\text{v}} = \Delta x \Delta y \Delta z$ is the image voxel volume, $\tilde{M}(k_x, k_y, z'_p)$ is the 2D FT of $M(x', y', z'_p)$, and $\tilde{\rho}(k_x, k_y, z'_k)$ is the 2D FT of $\rho(x', y', z'_k)$. The relation in (C.31) defines a square linear system of N_z equations for the N_z unknowns $\tilde{\rho}(k_x, k_y, z'_k)$, $k = 1, \ldots, N_z$ solved at each point in Fourier space (k_x, k_y). With the k-space reflectivity function found, the real-space reflectivity $\rho(x', y', z'_k)$ is recovered slice by slice via the inverse 2D FT:

$$\rho(x', y', z'_n) = \mathcal{F}_{\text{2D}}^{-1}\left\{\tilde{\rho}(k_x, k_y, z'_k)\right\}\,, k = 1, \ldots, N_z\,. \tag{4.12}$$

The plot of $|\rho(x', y', z'_n)|$, usually normalized, provides a qualitative image of the object's reflectivity. A quantitative image is also possible, provided the system PSFs scale properly with the probe's volume Ω_{sp} and relative-permittivity contrast $\Delta\varepsilon_{\text{r,sp}}$. The quantitative estimate of the object's relative-permittivity contrast is obtained as

$$\Delta\varepsilon_{\text{r}}(x', y', z'_n) = \Omega_{\text{sp}}\Delta\varepsilon_{\text{r,sp}}\rho(x', y', z'_n)\,. \tag{4.13}$$

4.2.3 Image-Convergence Check

The computation of the OUT power map $M(x', y', z')$ (the first-stage SPM image) involves a summation over the contributions from all available measured positions $\mathbf{r}_m$, $m = 1, \ldots, N_m$; see (4.6). However, unlike measurements with mechanical or electronically switched scanners, the number of spatial samples N_m is not known a priori. Vehicle-borne or handheld imaging platforms usually cannot follow exactly a predetermined trajectory. In this case, the data collection must continue until a convergent image emerges such that the addition of more data points no longer contributes to its quality. Therefore, a criterion for image convergence is needed.

To assess the convergence of the evolving image, we utilize the structural similarity index measure (SSIM) between two consecutive OUT power maps after an incremental addition of random acquisition points. The SSIM varies between 0 (no similarity) and 1 (perfect match). Thus, an SSIM value above a certain threshold (0.97 or higher) indicates that adding more data points would no longer contribute to the image improvement and the scan can be terminated.

While the above concept is straightforward, it does not guarantee sufficient sampling by itself. The sampling must be distributed over a broad synthetic aperture to provide the widest possible range of viewing angles of the imaged object. This is critical for achieving the best possible image spatial resolution [38]. To this end, we first determine the lateral extent of the observation domain based on the size of the imaged object, the average stand-off distance, and the beamwidth of the used antennas. For example, the x axis extent of a planar synthetic aperture X_a for an object of size X_o is

$$X_\mathrm{a} = X_\mathrm{o} + 2\bar{z}\tan(0.5\theta^{xz}_{\mathrm{HPBW}})\,, \tag{4.14}$$

where $\bar{z}$ is the range distance between the aperture and the object's center and $\theta^{xz}_{\mathrm{HPBW}}$ is the antenna's half-power beamwidth in the xz plane. This lateral aperture is then divided into equal sub-areas of extent on the order of one to ten λ_{c}, where λ_{c} is the wavelength at the central frequency of the band of operation.

The random sampling strategy must provide coverage of the entire lateral domain. This is why we impose the requirement to collect at least one sample with lateral coordinates within each sub-area before performing the first image-convergence check. This ensures that each sub-area is adequately represented in the dataset, preventing regional bias. Similarly, each subsequent convergence check is performed only after at least one additional sample is acquired within each sub-area.

We emphasize that the convergence check is applied only to the OUT power map $M(x', y', z')$ in (4.6), which serves as an input to the second SPM reconstruction step. The second reconstruction step is not performed until a convergent OUT map emerges. The convergence check is implemented with an SSIM threshold of 0.97 as

$$\mathrm{SSIM}\left(|\bar{M}_p(\mathbf{r}')|, |\bar{M}_{p-1}(\mathbf{r}')|\right) \geq 0.97\,, p = N_p, N_p - 1, N_p - 2, N_p - 3\,, \qquad (4.15)$$

where $|\bar{M}_p(\mathbf{r}')|$ is the normalized absolute value OUT power map in the p-th convergence check and N_p is the total number of convergence checks reached. It is clear from (4.15) that we employ four consecutive SSIM image comparisons, all of which must exceed the threshold. This is necessary because, with random sampling, the image convergence is not smooth or monotonic. Once the SSIM check satisfies (4.15), the data acquisition is terminated and the algorithm proceeds to the second stage of the SPM method to perform image enhancement and quantitative image reconstruction (with measured PSFs).

We briefly note that with large sub-areas (a size of $3\lambda_c$ or more), it may be computationally prudent to impose a minimum number of collected samples to start the image-convergence checks. It is unlikely that image convergence will start unless there is at least one sample within an area of $\lambda_c \times \lambda_c$ on average.

The proposed random sampling algorithm is summarized in Figure 4.2. The green and blue blocks represent the implementation of the first stage of SPM, while the orange blocks correspond to the second stage. The flowchart is divided into two main sections: the blue arm and the green arm. Before initiating the random sampling procedure, the formation of the SP power maps is necessary, which is shown in the blue blocks of Figure 4.2. After both SP and OUT power maps are obtained in the Fourier domain, the algorithm proceeds to the second stage of SPM to acquire quantitative estimates of permittivity.

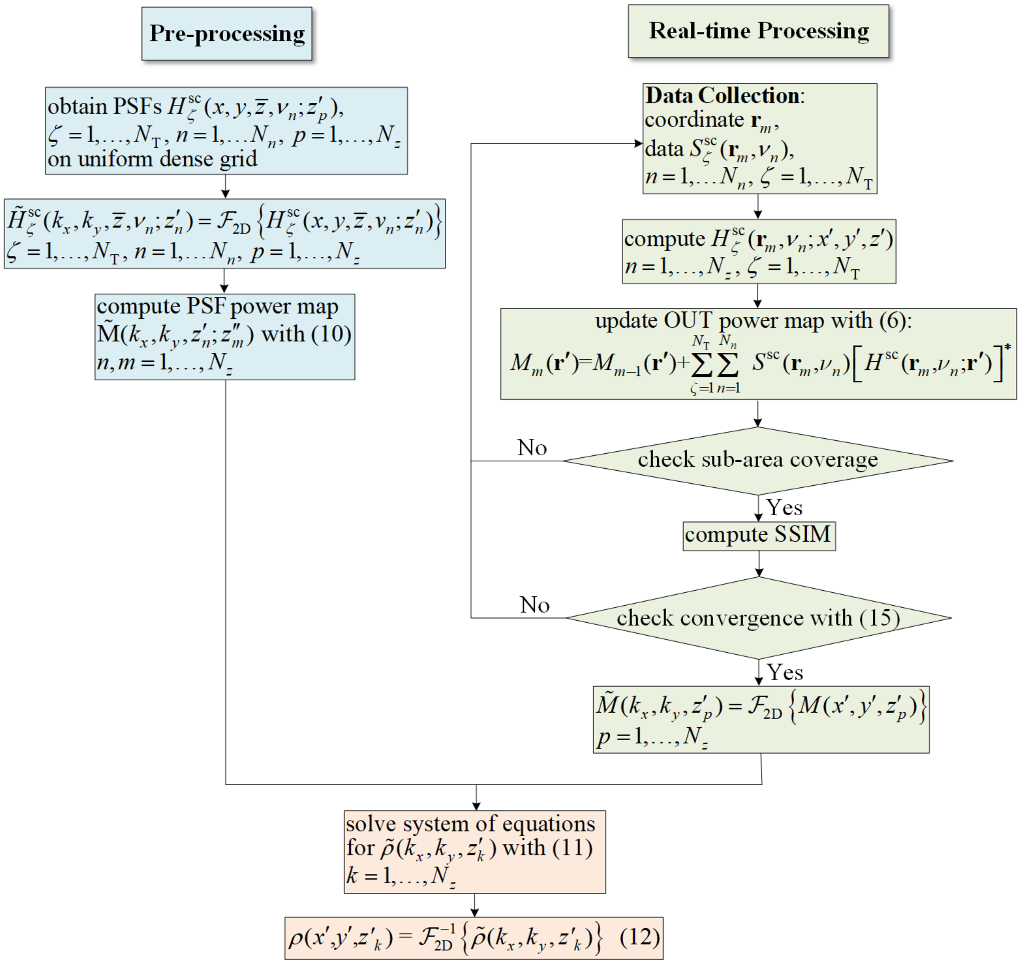

Figure 4.2: Flowchart of the SPM algorithm for random sampling.

4.3 Validation Examples with Simulated Data

To validate the efficacy of the SPM algorithm in reconstructing the permittivity of objects from random spatial samples, we carry out experiments with data obtained from simulations with Altair FEKO full-wave simulator [94] and an in-house LFM radar simulator [78] developed in MATLAB [95].

In general, the image reconstruction needs to de-embed the background radar responses from the total-field responses. The background responses are those acquired in the absence of an object under test (OUT) whereas the total-field responses are acquired in the presence of the OUT. The FEKO simulations employ realistic dipole antennas in both monostatic and bi-static measurement setups. Thus, the background responses (reflection and transmission S-parameters) are significant and need to be acquired and de-embedded. Since the background medium is assumed homogeneous, only one simulation is needed, where the antennas transmit/receive in the employed antenna-array configuration without an OUT. The de-embedding employs a simple subtraction of the background responses from their OUT counterparts to obtain the needed scattered-field responses. On the other hand, the LFM radar simulator generates the scattered-field responses directly employing an analytical scattering model [78]. Therefore, the LFM radar examples do not require a background response acquisition.

Further, the system PSFs $H_{\zeta}^{\text{sc}}(\mathbf{r}, \nu; \mathbf{r}')$, $\nu = \omega, t$, are needed in the first SPM reconstruction stage to compute the OUT power map (4.6) using the randomly sampled OUT data. The LFM simulator computes those analytically using the distances $R_{\text{Tx}}(\mathbf{r}, \mathbf{r}')$ and $R_{\text{Rx}}(\mathbf{r}, \mathbf{r}')$ between the scattering probe at $\mathbf{r}'$ and the Tx and Rx antennas, respectively [78]. In our notations, the Rx antenna position is $\mathbf{r}$ whereas the Tx antenna position is determined from $\mathbf{r}$ since the antennas are in a fixed array configuration. On the other hand, the PSF acquisition with FEKO simulations involves a simulated measurement scan of an electrically small scattering probe (SP) positioned at the center of an imaged slice $(0, 0, z')$. Each imaged slice (z'_p, $p = 1, 2, \ldots, N_z$) requires a simulated scan to acquire $H_{\zeta}^{\text{sc}}(x, y, \bar{z}, \omega; 0, 0, z'_p)$. Here, $\bar{z}$ is the range position of the synthetic aperture where the respective Rx antenna scans. The PSFs for any other lateral position of the SP (x', y', z'_p) are obtained by a coordinate shift, i.e., $H^{\mathrm{sc}}_{\zeta}(x, y, \bar{z}, \omega; x', y', z'_p) = H^{\mathrm{sc}}_{\zeta}(x - x', y - y', \bar{z}, \omega; 0, 0, z'_p)$.

Additionally, as explained in Section 4.2, the k-space PSFs $\tilde{H}^{\mathrm{sc}}_{\zeta}(k_x, k_y, \bar{z}, \nu; z'_p)$, $p = 1, 2, \ldots, N_z$, are needed to compute the k-space PSF power maps $\tilde{\mathcal{M}}(k_x, k_y, z'; \boldsymbol{z'})$ using (4.10). We reiterate that this computation employs the 2D FTs of the real-space PSFs $H^{\mathrm{sc}}_{\zeta}(x, y, \bar{z}, \nu; z'_p)$, $p = 1, 2, \ldots, N_z$, acquired on a uniformly sampled "dense" 2D grid on a planar synthetic aperture S_{a}, where the spatial sampling steps Δx and Δy conform to the Nyquist limit of $\frac{\lambda_{\min}}{4 \sin \alpha}$. These steps dictate the pixel size of the image. The PSF power maps are independent of the OUT and are pre-computed.

To emulate an OUT measurement with random spatial sampling, we first define a uniform dense-grid observation domain, where $\Delta x = \Delta y \approx \frac{\lambda_{\mathrm{c}}}{4}$. We perform simulations with the OUT and acquire the OUT responses at all observation points in this grid. Subsequently, an algorithm randomly selects the points whose responses are utilized to compute the OUT power map using (4.6). As detailed in Section 4.2.3, we divide the observation domain into equal sub-regions. In all examples, we employ 16 sub-regions, the lateral extent of which does not exceed $10\lambda_{\mathrm{c}}$.

After collecting the minimum required number of points (at least 1 point in each designated sub-region), the generation of the first OUT power map $M_1(\mathbf{r}')$ is complete and this map is stored to be compared with the subsequent updated power map $M_2(\mathbf{r}')$. The process continues until image convergence is observed as per (4.15). As an illustration, Figure 4.3 shows a plot of the SSIM value *versus* the amount of used spatial samples (in percentage) relative to the number of samples in the dense (Nyquist compliant) grid on the planar synthetic aperture S_{a}. It is observed that in both simulation examples, the OUT power maps converge with about 50% of the sample point, which would be required by a uniform sampling scan.

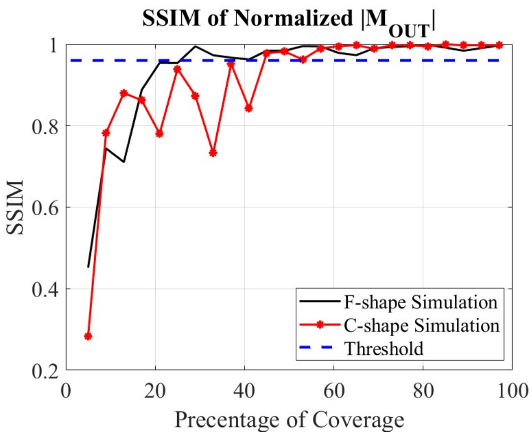

Figure 4.3: Image convergence in the F-shape and the C-shape simulated examples in terms of the SSIM between two subsequent OUT power maps *versus* the amount of used spatial samples (in percentage) relative to the number of samples in the dense (Nyquist compliant) grid on the planar synthetic aperture S_{a}.

4.3.1 C-shape Image Reconstruction with Simulated Data

In the FEKO simulation, a scenario similar to that in previous studies is replicated [96]. The OUT consists of a C-shaped dielectric object in the $z' = 0$ plane with a relative permittivity of $\epsilon_{\mathrm{r}} = 1.5$. Adjacent to it, three small cubes with a permittivity of $\epsilon_{\mathrm{r}} = 1.1$ reside at distances of 3 cm, 4 cm, and 5 cm along the z axis and with a slight offset (center-to-center distance of 2 cm) along the y axis. The background is vacuum ($\epsilon_{\mathrm{r}} = 1$). The setup is depicted in Figure 4.4.

The PSFs are acquired by simulating the scans of a scattering probe (SP) at the center ($x' = y' = 0$) of three imaged planes: $z' = 3, 4, 5$ cm. The SP is a small cube, 1 cm on a side, with a relative permittivity $\varepsilon_{\mathrm{r}} = 1.1$.

The measurement setup involves two half-wavelength (at the central frequency of 5 GHz) dipole antennas spaced 8 cm apart, with the OUT centrally located between

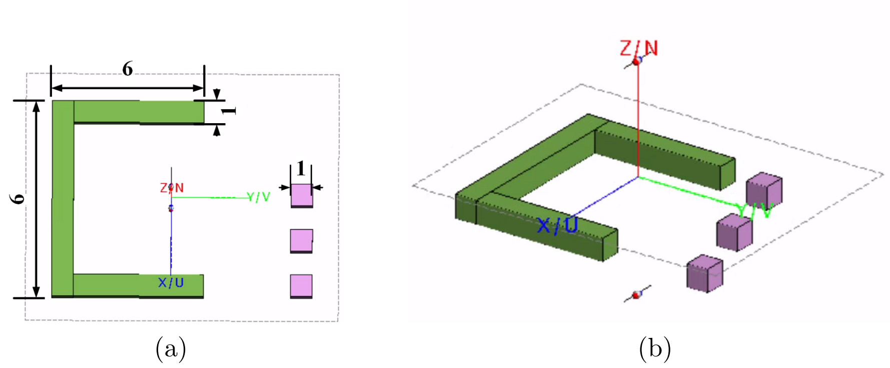

Figure 4.4: The full-wave FEKO simulation example of a 3D structure: (a) top view, and (b) isometric view. The C-shape and the three small cubes reside in three range slices ($z' = 3$ cm, $z' = 4$ cm, and $z' = 5$ cm). Two dipoles are positioned 8 cm apart so that the C-shape is centered between them. The C-shape is $7 \times 9 \times 1$ cm^3, and the cubes are all 1 cm^3. The C-shape and the cubes have relative permittivity of $\varepsilon_{\mathrm{r}} = 1.5$, and $\varepsilon_{\mathrm{r}} = 1.1$, respectively. Background is vacuum, $\varepsilon_{\mathrm{r,b}} = 1$. All dimensions are in cm.

them. The imaged domain contains slices that are as close as 3 cm from the antennas. Although we are at the object's close-range, this is still a borderline far-field scenario with respect to the antenna's lateral extent. The two antennas collect reflection, S_{11} and S_{22}, as well as transmission, S_{21}, data across a frequency range from 3 GHz to 8 GHz and over a 30 cm by 30 cm acquisition plane. We divide this aperture into 16 equal sub-regions, the lateral extent of which is about $1.4\lambda_{\mathrm{c}}$. On the other hand, the sampling interval employed in acquiring the dense uniform-grid PSFs is $0.18\lambda_{\mathrm{c}} = 1$ cm. Note that with monostatic measurements such as S_{11} and S_{22}, the Nyquist criterion dictates sampling interval from a quarter-wavelength to half-wavelength, depending on the maximum viewing angle of the antenna beam and the aperture size [38]. The dense uniform-grid sampling is also utilized in the OUT simulations, which provides a high-quality image, serving as a benchmark to assess the images reconstructed from the randomly sampled data.

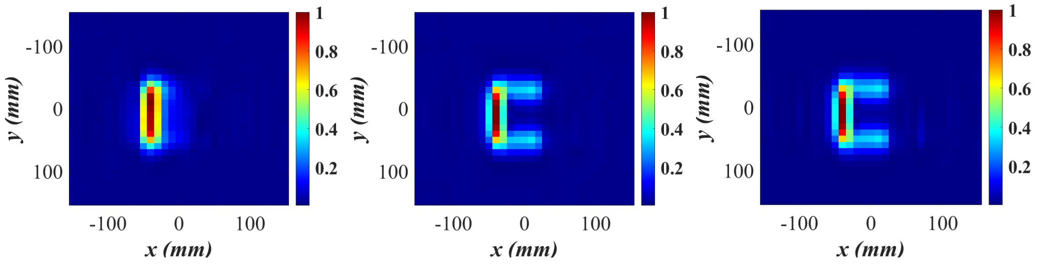

(a) (b) (c)

Figure 4.5: The slice at $z' = 0$ of the normalized magnitude OUT map $\bar{M}(\mathbf{r}')$ of the C-shape generated by the first SPM stage, for percentage of utilized spatial samples selected randomly: (a) 40%, (b) 70%, and (c) 100%. The total number of spatial samples in the dense uniform sampling grid is 961.

Figure 4.5 shows the slice at $z' = 0$ of the normalized magnitude OUT map $\bar{M}(\mathbf{r}')$ of the C-shape generated by the first SPM stage as the map evolves while the spatial samples are collected randomly. The reported percentages reflect the proportion of samples used relative to the total available samples (961) acquired on the dense uniform grid.

Figure 4.5a shows the image obtained with 40% of the entire data set, corresponding to only 385 randomly selected spatial samples. It captures only the vertical arm of the C-shape and the small cube in this slice is not visible due to the fact that the horizontal arms are not covered as well as the vertical arm at the early stages of the random acquisition. Consequently, their contribution to the formed image is less pronounced. As the scanning progresses, with additional samples collected in each sub-region, the complete C-shape starts to emerge. By the time 70% of the area sample points are utilized and the convergence is met according to Figure 4.3, the C-shape is clearly formed, although the small cube is still not visible as depicted in Figure 4.5b. The scattering from this low-contrast small cube is weak, and even with 100% of the dense-grid samples, the OUT power map does not depict well this detail;

see Figure 4.5c.

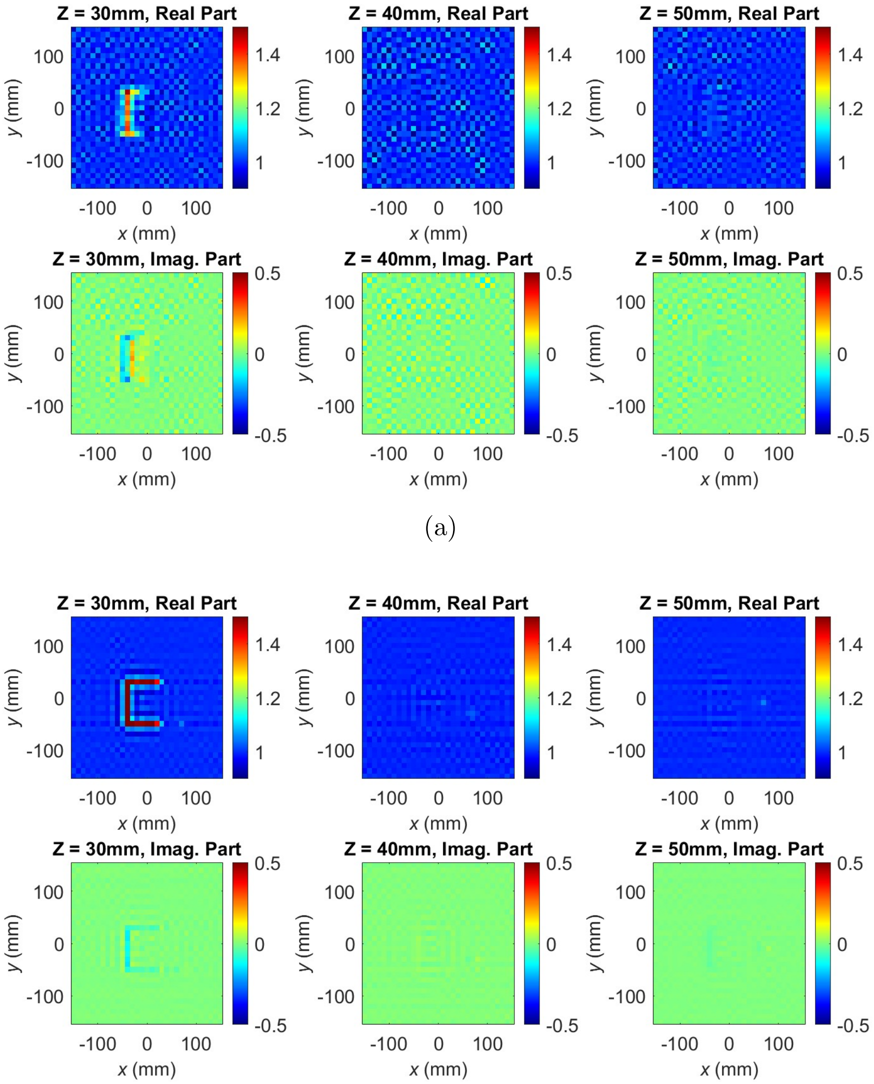

(a)

(b)

Figure 4.6: Quantitative SPM reconstructed images in terms of real and imaginary parts of the C-shape relative permittivity utilizing randomly sampled data of the object shown in Figure 4.4 with: (a) 40%, and (b) 70% of the dense-grid samples. The images in each column correspond to a range slice.

The small cubes in all three image slices become visible only after the second SPM stage. At 70% utilization of the dense-grid points, the SSIM value is 0.988, and the C-shape power map is already convergent; see also Figure 4.3. At this stage, the scan is terminated. The three slices of the OUT power map are subjected to 2D FT and the OUT reflectivity is recovered by the second SPM stage; see (C.31). The recovered quantitative complex-permittivity images are of much better structural and resolution quality than the OUT power map. Figure 4.6a illustrates the quantitative C-shape image slices formed using 40% of the dense data set for the OUT power map, resulting in an SSIM value of 0.86, indicating incomplete recovery of the C-shape. The converged result, shown in Figure 4.6b, utilizes 70% of the dense data set, demonstrating a marginal improvement post-convergence and a 30% reduction in required measurements compared to the Nyquist-compliant dense-grid scan (100% data). The SSIM value between the 100% and 70% reconstructed images is 0.999.

4.3.2 F-shape Image Reconstruction with LFM Radar Synthetic Data

The in-house LFM radar simulator employs a far-zone scalar scattering model, which assumes point-like sources (the term *point source* refers to a scalar-field source whose radiated field is represented by e^{-jkr}/r (a spherical wave). The spherical wave represents adequately the distance dependence of antennas' far-zone fields [97]). It accounts for the signal decay due to the spherical spread of the transmitted and scattered waves. However, it ignores the depolarization that may occur upon scattering. With these assumptions, the LFM system PSF is analytically expressed as [78]:

$$H^{\mathrm{sc}}(\mathbf{r}_m, t; \mathbf{r}') = \frac{A_{\mathrm{Tx}}}{R_{\mathrm{Tx},m} R_{\mathrm{Rx},m}} P\left(\frac{t - \tau_{\mathrm{d},m}}{T_{\mathrm{p}}}\right) \exp\left[-\mathrm{i}2\pi(f_{\mathrm{c}} + \gamma t)\tau_{\mathrm{d},m}\right] , \tag{4.16}$$

where A_{Tx} is amplitude, f_{c} is the center frequency, t is the *fast time* (the time within a single chirp), T_{p} is the chirp duration (pulse width), $\gamma = \frac{B}{T_{\mathrm{p}}}$ is the frequency-modulation slope (chirp rate), and B is the chirp's frequency bandwidth. $R_{\mathrm{Tx},m} = |\mathbf{r}_{\mathrm{Tx},m} - \mathbf{r}'|$ and $R_{\mathrm{Rx},m} = |\mathbf{r}_m - \mathbf{r}'|$ are the distances from the Tx antenna at $\mathbf{r}_{\mathrm{Tx},m}$ and the Rx antenna at $\mathbf{r}_m$ to the scattering point at $\mathbf{r}'$, respectively. Note that the range compression in LFM radar signals is already taken into account in the derivation of the analytical PSF in (4.16), where the correlation of the received signal with the reference (transmitted) signal, produces the down-converted (baseband) signal. We reiterate that the Tx and Rx antenna pairs are in a fixed configuration; therefore, $\mathbf{r}_{\mathrm{Tx},m}$ is determined from $\mathbf{r}_m$. Further, $\tau_{\mathrm{d},m}$ is the time delay corresponding to the distance traveled by the signal, i.e., $\tau_{\mathrm{d},m} = (R_{\mathrm{Tx},m} + R_{\mathrm{Rx},m})/c$, where c is the speed of light. Note that here we employ point sources and point sampling and the scenario is a far-field one. As shown in (C.24) the linearized forward model of scattering views the signal from an object as a superposition of the scattering emanating from all differential scatterers that make up this object. Thus, using (4.16), the cumulative OUT signal is synthesized using the time-domain counterpart of the superposition integral in (C.24).

In the synthetic experiment, the LFM imaging-system parameters are first set. Here, we present a monostatic case, i.e., the Tx and Rx positions are coincident. The central frequency f_{c} is 29.9 GHz, while covering frequencies from 27.0 GHz to 32.8 GHz. The chirp duration T_{p} is 20 μs and the chirp rate is $\gamma = 2.9 \times 10^{14}$ Hz/s. Overall, there are 201 time samples in a single chirp. The lateral spatial resolution is estimated from the wavelength at f_{c} as $\delta_{\perp} \approx \lambda_{\mathrm{c}}/4 \approx 2.5$ mm and the range resolution is $\delta_z \approx c/2B \approx 26$ mm.

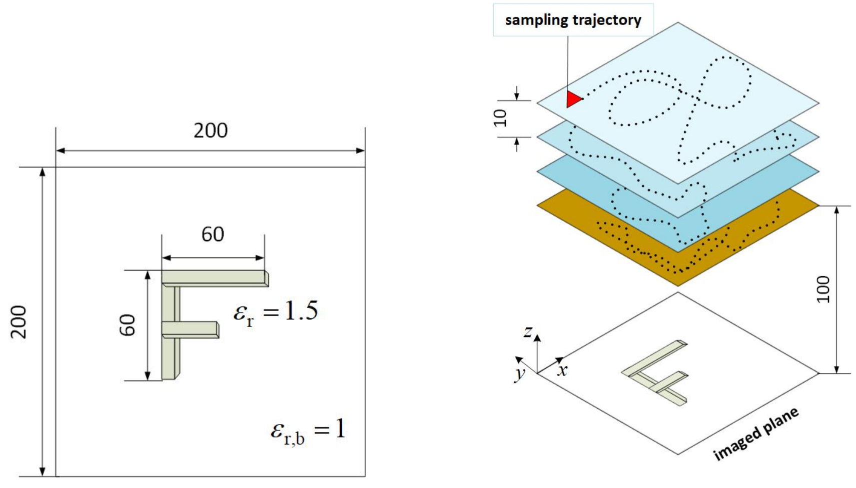

(a) (b)

Figure 4.7: Illustration of a monostatic LFM radar simulation example: (a) the F-shape object of relative permittivity $\varepsilon_{\mathrm{r}} = 1.5$ at $z' = 0$, and (b) 3D sampling trajectory in four planes at $\bar{z} = 100, 110, 120, 130$ mm. Background is vacuum, $\varepsilon_{\mathrm{r,b}} = 1$. All dimensions are in mm.

The reference SPM image is obtained from an OUT and PSF scans on a uniform grid over a planar aperture of size 200×200 mm^2, with spatial increments of 4 mm along x and y. The aperture is at $\bar{z} = 100$ mm. This results in a dense grid of 51×51 (2601) sampling points. The PSF is acquired with a cubical SP of size 1 mm^3 and $\varepsilon_{\mathrm{r}} = 1.5$. We reiterate that this PSF is needed not only to obtain the reference OUT power map but also to carry out the second SPM stage, regardless of whether the OUT data are acquired on a random trajectory or on the dense uniform-grid planar aperture.

The random scanning of an F-shape object is implemented in the LFM radar simulator as shown in Figure 4.7. The F-shape, of relative permittivity $\varepsilon_{\mathrm{r}} = 1.5$, is built of cubical scatterers 1 mm on a side, in the $z' = 0$ plane; see Figure 4.7a. The background is vacuum ($\varepsilon_{\mathrm{r,b}} = 1$). The F-shape has vertical and horizontal arms of length 60 mm whereas the middle arm measures 30 mm. To emulate 3D random sampling, four planes along z are set so that they are 10 mm apart ($\bar{z} = 100, 110, 120, 130$ mm). The sampling trajectory for the OUT measurement follows a random selection along x, y, and z as shown in Figure 4.7b.

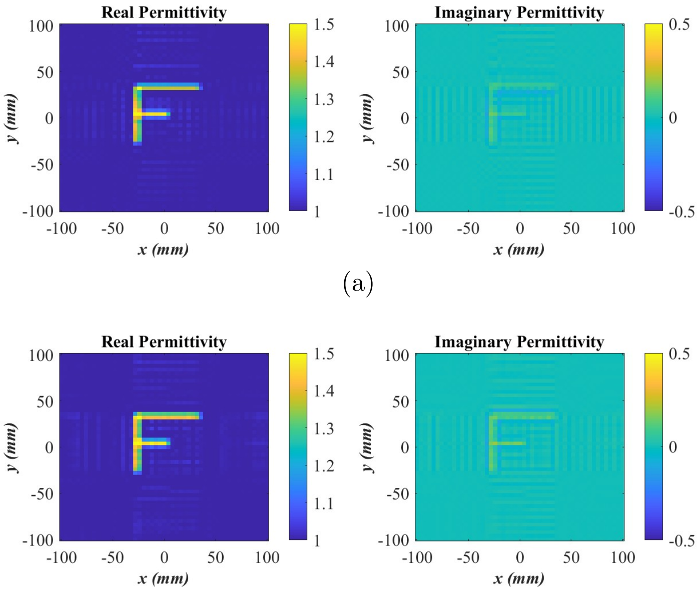

(a)

(b)

Figure 4.8: Quantitative reconstructed images in terms of real and imaginary parts of the relative permittivity of the F-shape object utilizing randomly sampled data: (a) using the convergent OUT map obtained from random samples, the number of which is only 40% of the number of samples on the dense uniformly sampled planar grid, (b) using all the samples on the dense uniformly sampled planar grid

.

The methodology is the same as in the C-shape example. The 3D (4-slice) sampling domain of overall lateral extent 200 × 200 mm^2 is divided into 16 equal 3D sub-regions of lateral extent 50 × 50 mm^2. As before, the convergence check on the OUT image is performed only if each additional data set provides at least one sample within each sub-region. Remarkably, the OUT map converges with a number of 3D random samples which constitutes only 40% of the total sample number on the dense planar grid (2601); see the SSIM plot in Figure 4.3.

For brevity, we only present the final quantitative (second-stage) image in Figure 4.8a obtained with a number of random samples amounting to 40% of the sample number of the dense planar synthetic aperture. As a reference, the quantitative image obtained with the full dataset acquired on the dense uniformly sampled planar aperture is shown in Figure 4.8b. We again observe only marginal improvement in comparison with the image obtained from the under-sampled random data while reducing the required measurements by 60%. This illustrates the importance of employing the image convergence of the OUT map to terminate the measurements with random sampling in a timely manner. In conjunction with the previous C-shape example, it also shows that the number of required random samples can vary significantly, depending on the employed radar system (continuous wave *versus* LFM) as well as the complexity of the imaged scene.

4.4 Validation Examples with Measured Data

The experiments discussed here are first carried out using a uniform grid in a planar raster-scanning chamber shown in Figure 4.13a. These measurements provide a full OUT data set, from which samples can be selected randomly.

The PSFs are acquired experimentally in the near-field imaging experiment (breast-phantom scan), presented in Section 4.4.1. Near-field measurements allow for capturing the scattered responses from an electrically small SP in the background medium. This is due to the short distance between the synthetic aperture and the SP. Since the SP is small, its scattering is weak; however, the antennas are very close and the captured signals provide sufficient signal-to-noise ratio (SNR). With measured PSFs, the SPM algorithm reconstructs quantitative images.

On the other hand, in the far-field experiments with mm-wave LFM radar, presented in Section 4.4.2, measuring the system PSF is not possible. The scattering from an electrically small SP is so weak that it does not provide sufficient SNR when the SP resides in the antenna's far zone. Thus, in the far-zone experiments, we employ the same analytical PSFs as in the simulation-based example presented in Section 4.3.2. In such far-field measurement scenarios, there is no significant difference between the OUT power map (SPM first-stage image) and the second-stage image. Importantly, since the analytical PSF is incapable of accounting for setup specifics such as antenna patterns, cable losses, and illumination strength, the second-stage SPM images are only qualitative. Consequently, the OUT permittivity distribution is simply presented in terms of the normalized reflectivity.

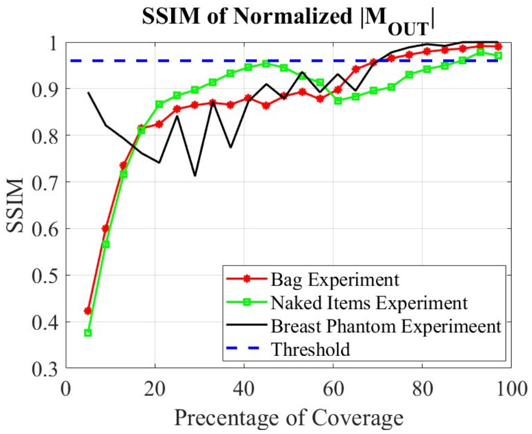

Figure 4.9: Convergence curves for the experimental examples in terms of SSIM between two subsequent OUT power maps versus number of randomly selected samples (in percentage) relative to the total number of samples on the dense uniform grid on the synthetic aperture.

Figure 4.9 illustrates the SSIM curves for each conducted experiment. As in the examples with simulated data, the scan-termination threshold is at SSIM = 0.97.

As demonstrated next, this rigorous convergence criterion ensures that satisfactory image quality is achieved before terminating the scan.

4.4.1 Compressed Breast Phantom Imaging

A near-field imaging experiment identical to the one presented in [98] is carried out to evaluate the effectiveness of SPM method with randomly sampled data. The scanned aperture measures 18×18 cm^2. The dense aperture scan utilizes an interval of 3 mm (approximately $0.05\lambda_c$) axis, creating a a grid of 61×61 spatial samples. Consistent with other examples, the domain is divided into 16 sub-regions, each measuring $4.5 \times 4.5\,\text{cm}^2$ (approximately $1.3\lambda_c$). The measurements are performed on a heterogeneous compressed breast phantom, which includes three tumor simulants immersed in various healthy-tissue simulants. The breast phantom (the OUT) is made of three layers of 11 mm-thick carbon-rubber slabs mimicking the electrical properties of healthy scattered-fibroglandular breast tissue and two 2 mm-thick silicone rubber sheets mimicking skin tissue (see Figure 4.10a). The 2 mm-thick silicone rubber sheets are placed on the top and the bottom of the three stacked 11 mm-thick carbon-rubber slabs. The average relative permittivity of the slabs (listed in Table 4.1) is chosen to match the averaged complex permittivity of BIRADS Type II density of the breast (scattered fibroglandular tissue). The breast phantom also comprises a number of dispersed materials, as shown in Figure 4.10b. Each slab defines a layer where additional tissue simulants can be inserted. In this phantom, Layers 1 and 3 are homogeneous. In Layer 2, a circular section (94 mm diameter) is removed to insert various tissue simulants. A kidney-shaped material mimicking the healthy fibroglandular tissue (see Figure 4.10a) is put inside the circular section. One tumor

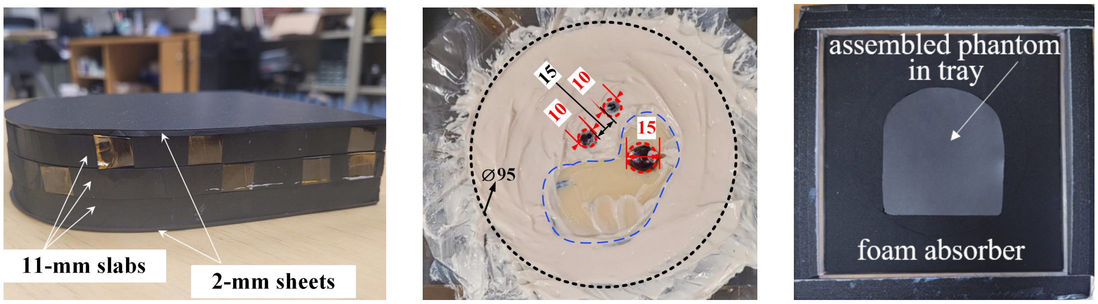

(a) (b) (c)

Figure 4.10: Photos of compressed breast phantom: (a) side-view showing the three carbon-rubber slabs with permittivity close to that healthy breast tissue and the two thin silicone-rubber sheets as skin simulant, (b) middle layer including two tumor simulants surrounded by the matching material and one surrounded by the fibroglandular simulant, and (c) assembled phantom surrounded by microwave absorbing foam. All dimensions are in mm.

simulant is inserted within this fibroglandular object and two tumor simulants are embedded in the circular section carefully surrounded by a matching medium with a relative permittivity reported in Table 4.1. The phantom is placed in a *Plexiglass* tray and surrounded by black foam microwave absorbers as shown in Figure 4.10c to minimize reflections and to reduce the image artifacts.

The setup for measuring the system PSF is the same as the OUT measurement setup except for the second layer where a small scattering probe (a cylinder of height 1 cm and diameter 4 mm) with the relative permittivity value given in Table 4.1 is positioned at the center of an otherwise homogeneous carbon–rubber slab. Finally, in order to extract the scattered field responses for both the OUT and the PSF measurements, a background measurement is necessary. The background object is composed of three homogeneous carbon–rubber slabs with the two silicone–rubber sheets at the top and the bottom, surrounded by microwave-absorbing foam. All these measurements inherently incorporate the properties of the actual antennas.

Table 4.1: Averaged Dielectric Properties of the Compressed Breast Phantom Materials Over the Frequency Band from 3 GHz to 8 GHz [98]

Material (Structure)	ε'	ε''
Carbon-rubber Sheet (Averaged Breast Tissue)	9.6	3.82
Silicon-rubber Sheet (Averaged Skin Tissue)	19.36	14
Embedding/Matching Medium	11.3	2.59
Tumour Simulant	64.11	22.32
Fibroglandular Tissue Simulant	17.61	7.89
Scattering Probe (PSF)	43.7	0

Figure 4.11 shows the normalized OUT power maps of the compressed breast phantom obtained from randomly sampled data at three percentage values of utilization of the available densely sampled data. The reconstructed relative permittivity distribution is represented as 2D projections since the imaging setup uses transmission coefficients only. Note that the Rx array elements are at the bore-sight (or only slightly off) of the Tx antenna, which results in the lack of range resolution. Figure 4.11a shows the result when processing only 50% of the points on the dense (Nyquist compliant) grid. At this stage, the SSIM is well below the threshold indicating insufficient image quality; see Figure 4.9. Indeed, the comparison of the image in Figure 4.11a with those in Figure 4.11b (70% utilization of the points on the dense grid) and Figure 4.11c (100% utilization) confirms incomplete OUT map reconstruction. The OUT maps in Figure 4.11b and Figure 4.11c are visually similar, but the third tumor simulant in the right side of the fibroglandular region is not discernible. Note that the SSIM value at the 70% stage reaches 0.97; see Figure 4.9. However, as discussed in (4.15), the convergence criterion requires the SSIM to be greater than the threshold in four consecutive iterations. For this reason, the scan continues for another three batches of sampled data. The data eventually converges when 80% of the reference

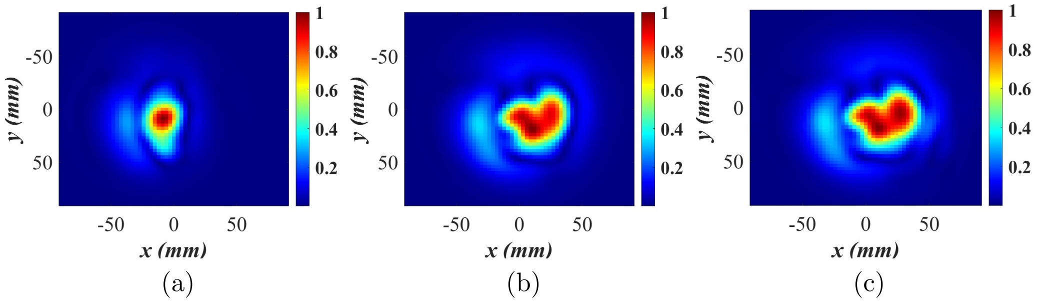

(a) (b) (c)

Figure 4.11: Normalized OUT power maps of the compressed breast phantom, when the number of randomly selected samples (in percentage) relative to the total number of samples on the planar synthetic aperture is: (a) 50%, (b) 70%, and (c) 100%. The total number of spatial samples is 3721.

data is utilized and it is then terminated to proceed to the second stage of SPM algorithm.

We briefly mention the importance of using an apodization filter [99] in this challenging experimental example. The challenges in the image reconstruction here arise from the significant reflections arising at the interface between the breast phantom and the microwave foam. The apodization filter is aligned with the boundary of the circular section in Layer 2; see black dash line in Figure 4.10b). Here, a 2D Butterworth apodization filter is used, which is applied radially over a circular region. The cut-off -3 dB level corresponds to a radial distance of about 4 cm from the center. The apodization filter suppresses the contribution of the samples outside the circular boundary, thus mitigating reflections due to imperfect absorption by the microwave foam.

The quantitative reconstruction of the breast-phantom relative permittivity by the SPM second stage is shown in Figure 4.12. Figure 4.12a shows the reconstruction result with the OUT power map based on 70% of all available samples, selected randomly, whereas Figure 4.12b shows the quantitative image when using the OUT

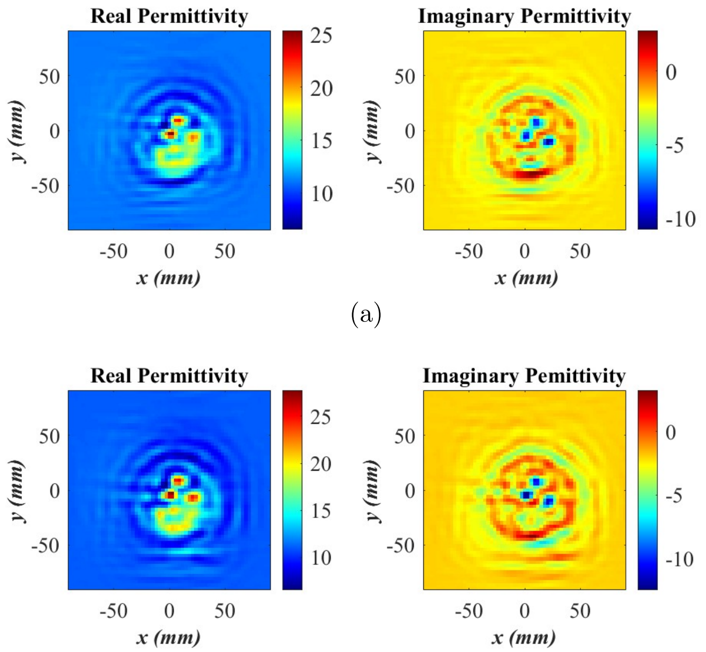

(a)

(b)

Figure 4.12: Quantitative SPM reconstructed images in terms of real and imaginary parts of the breast-phantom permittivity utilizing randomly sampled data in percentage proportion of all available samples: (a) 70%, (b) 80%.

power map which employs 80% of all available samples with the SSIM of 0.99 compared to the reference image (100% densely sampled), also selected randomly. In both image sets, the tumor simulants and the healthy fibroglandular tissue regions are reconstructed well, with the tumor simulants correctly identified by large permittivity values (both real and imaginary). As expected, the converged image utilizing the 80% set of available data features slightly better spatial resolution, which results in better structural outline of the phantom inclusions. The permittivity value distributions of 2D images in Figure 4.12 are effectively averaged over the thickness (3.7 cm) of the phantom. Thus, the values are lower than those provided in Table 4.1.

We briefly comment on the benefit from employing filtering at the second SPM stage. Low-pass filtering is applied to the reconstructed complex permittivity in k-space [99] before applying the inverse 2D FT. This is important in suppressing image artifacts when experimental data are used. High spatial (k-space) frequency components correspond to near-grazing angles of signal arrival and, in near-field imaging, evanescent-field scattering. These components suffer from very poor SNR, which may corrupt the final reconstruction.

Finally, it is noteworthy that the reconstruction algorithm operates with remarkable speed during the relative permittivity retrieval, typically completing in a few seconds on conventional laptops using MATLAB codes without code optimization, acceleration, or parallel computing. The enhanced imaging results after applying the second SPM stage, as evidenced by the comparison of the images in Figure 4.12 with those in Figure 4.11, underline the importance of this stage.

4.4.2 Imaging of Various Small Items with mm-Wave LFM Radar

The off-the-shelf radar module used for LFM radar measurement is the IWR1443Boost evaluation module [100] along with the real-time data-capture adapter board DCA1000EVM [101]. The mm-wave sensor is equipped with three Tx and four Rx antennas, however, in this experiment, only one Tx is activated while all four Rx elements receive. Here, too, we are at the far-field of the antennas. The LFM transceivers can accommodate up to 4 GHz bandwidth from 77 GHz to 81 GHz. The chirp duration is $T_{\mathrm{p}} = 51.1~\mu$s with 512 temporal samples. The frequency-modulation slope is $\gamma = 72.42$ MHz/μs. The off-the-shelf mm-wave radar performs the range compression on hardware (with mixing) and provides as an output only the baseband in-phase (I) and quadrature

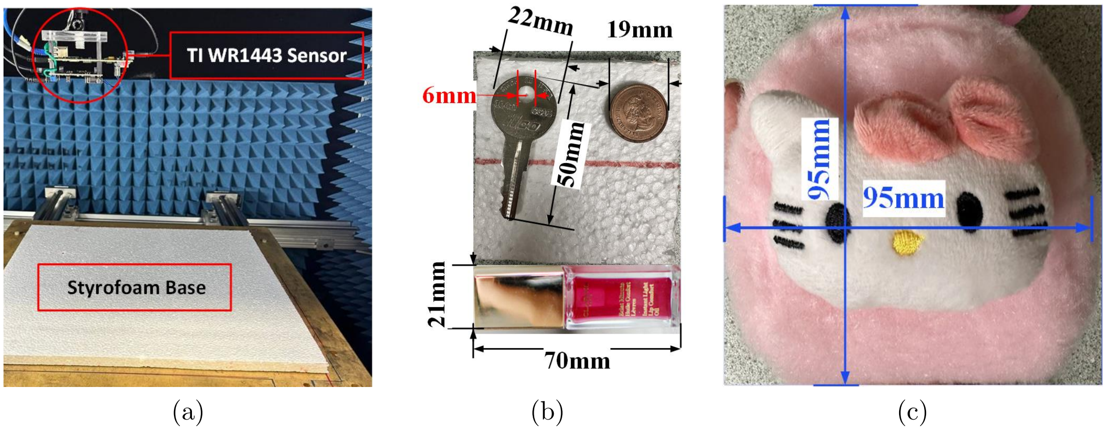

(a) (b) (c)

Figure 4.13: Photos of: (a) the acquisition chamber, (b) a key, a penny, and a liquid lipstick laid on a *Styrofoam* sheet, and (c) a toy bag where the key, penny and lipstick are inserted in the first imaging experiment.

(Q) outputs as a function of time.

The imaging setup and the measured objects repeat an experiment reported in [78] (see Figure 4.13a). The scanned aperture has a size of 15×15 cm^2. The dense aperture scan employs an interval of 2 mm (approximately $0.53\lambda_c$) along x and y, resulting in a grid of 76×76 spatial samples. As per other examples, the domain is divided into 16 sub-regions, each with a size of $3.75 \times 3.75\,\text{cm}^2$ (approximately $10\lambda_c$).

It is important to note that the LFM radar module suffers from internal system delays; therefore, the analytical PSF needs to be calibrated. Here, we use the calibration approach described in [78]. Further, in the LFM radar experiments presented here, background de-embedding is not necessary since the background signals are negligible compared to the back-scattering from the objects. Also, the system PSF is computed analytically using (4.16). Therefore, background and PSF measurements are unnecessary.

In the first imaging experiment, the OUT consists of a metallic key, a penny, and

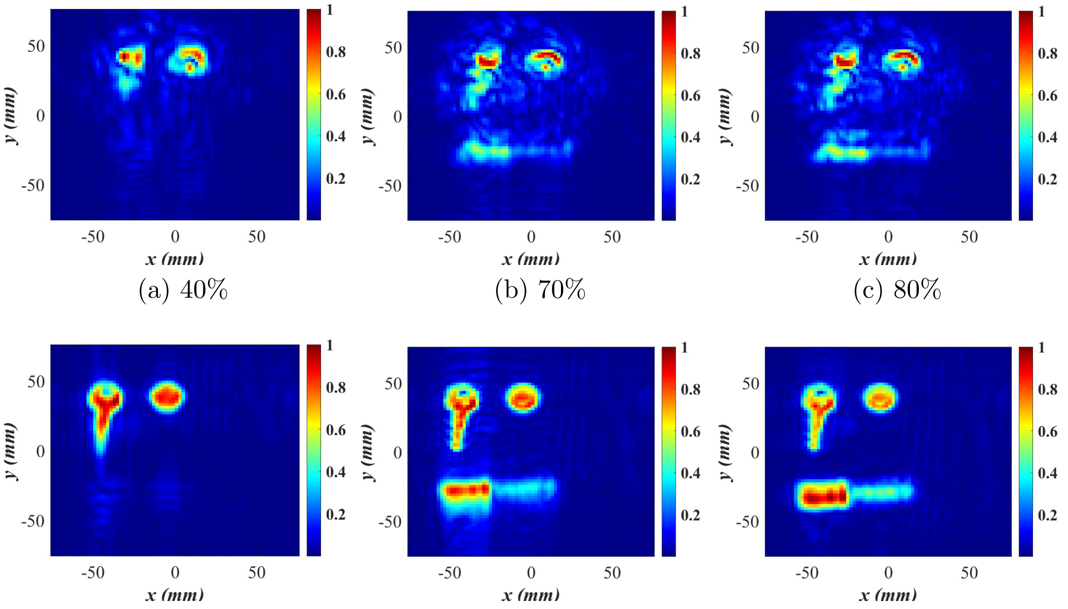

(a) 40% (b) 70% (c) 80%

(d) 40% (e) 70% (f) 90%

Figure 4.14: Qualitative results in terms of normalized magnitude of reflectivity $\bar{\rho}$ distribution for: (a)-(c) the embedded objects in the bag, and (d)-(f) naked objects. The percentage of random samples compared to the total available uniformly sampled data is 40%, 70%, 80% and 90% as denoted in the figure.

a liquid lipstick (see Figure 4.13b), enclosed within a toy bag, shown in Figure 4.13c. All three objects are laid on a *Styrofoam* sheet and then inserted in the bag. The OUT is 22.5 cm away from the radar. In the second experiment, the same objects are imaged without the bag and at the same range distance.

Figures 4.14a-4.14c show 2D images of the key, penny, and lipstick experiment, concealed in the bag, at various stages of completion of the random sampling and when the convergence is at SSIM of 0.98 when 80% of the referenced samples are utilized. The images are obtained at a single slice at $z = 21.5$ cm from the radar antenna array. The 2D images of the same objects, this time out of the bag, are depicted in Figures 4.14d-4.14f. Here, the convergence is when 90% of the densely sampled reference data is used and the scan is terminated at the SSIM 0.99. It is clear that the bag obscures the objects to some extent, which is expected since the materials from which the bag is made are not entirely transparent to the mm-wave radiation. Note that the images in 4.14a-4.14c indicate the presence of the bag by a low-reflectivity region surrounding the objects.

The adequacy of the selected points is demonstrated through the experiments depicted in Figures 4.14c and 4.14f, corresponding to the bagged and unobscured conditions, respectively, which indicates where the scan can be terminated. In both scenarios, the visual representation of the key and the penny closely matches those observed with 100% random sampling. Therefore, the 100% data is not presented for brevity. The impact of insufficient data (40%) is particularly evident in Figure 4.14d, where the lipstick is not detectable at all and the key's leg is also not recovered well. The SSIM value of 0.92 also indicates that more acquisition points are required to reach convergence.

In the bag experiment, utilizing 40% of the data results in an SSIM value of 0.88, which falls below the established threshold, as shown in Figure 4.9. When data coverage reaches approximately 70%, the SSIM value meets the 0.97 threshold. Subsequently, as the SSIM value remains above this threshold for the next three measurements, the scanning process is discontinued thereafter at 80% of coverage. Conversely, in the experiment with unbagged items, convergence is achieved only after nearly 90% of the data is utilized. Nonetheless, the image resolution at 70% coverage is deemed adequate, as illustrated in Figure 4.14e.

4.5 Discussion

To demonstrate the advantages of our SPM method in the context of nonuniform random sampling, we should consider multiple factors when comparing it with the conventional BPA and ω-k methods.

First, we analyze the overall computational complexity, which includes all N_m spatial samples acquired during the scan. According to (4.6), the first SPM stage involves $N_m N_\mathrm{R} N_n N_\mathrm{v}$ multiplications and the same number of summations, where $N_\mathrm{v} = N_x N_y N_z$ is the number of image voxels. Thus, its computational complexity can be expressed as $O(N_m N_\mathrm{R} N_n N_\mathrm{v})$, which is the same as that of the BPA. The second SPM stage computes the 2D FFT of the OUT power maps (slice by slice) as well as the 2D IFFT of the k-space reconstructed permittivity (also slice by slice), both of which have a complexity of $O(N_z N_x N_y \log_2(N_x N_y)) \equiv O(N_\mathrm{v} \log_2(N_x N_y))$. It also solves the system of equations in k-space, which has a complexity of $O(N_x N_y N_z^2) \equiv O(N_z N_\mathrm{v})$. It is clear that the computational complexity of the second SPM stage is much lower than its first stage. Since the number of range image slices N_z is much smaller than N_x and N_y, the computational complexity of the SPM algorithm is governed by the dominant term $O(N_m N_\mathrm{R} N_n N_\mathrm{v})$, which is the same as that of the BPA.

In comparison, the ω-k methods, which use NUFFT along with interpolation, have a computational complexity of $O(N_\mathrm{R} N_z N_x N_y \log_2(N_x N_y) + N_n N_\mathrm{R} N_m)$ [83, 102]. Therefore, if all data are processed after the completion of a scan, the computational complexity of the BPA and the proposed SPM method is higher than that of the ω-k algorithms.

Note, however, that the overall computational complexity is not the only factor determining the method's efficiency in the context of random sampling. The proposed random sampling SPM method ultimately offers significant acceleration over the BPA due to the incremental update of the object's power map (the first-stage image), performed concurrently with the measurements. It is this incremental image update (with a computational complexity of $O(N_{\mathrm{R}}N_nN_{\mathrm{v}})$) that also allows for employing the proposed image-convergence criterion, which results in a substantial reduction in the number of measurements compared to a Nyquist-compliant uniform densely sampled grid, as demonstrated in the examples. Thus, the proposed method not only leverages computations that run alongside the measurements but also reduces the measurement time. Note that the $\omega - k$ methods, just like the BPA, start the image reconstruction only after the scan is completed.

An important advantage of both the SPM and the BPA is their ability to process samples on arbitrary 3D trajectories, noncanonical surfaces, and 3D observation domains. In contrast, the ω-k approach for nonuniform sampling is limited to sampling on canonical surfaces (planar and cylindrical).

Regarding quantitative analysis, neither the BPA nor the ω-k methods can provide quantitative permittivity estimates as they are incapable of utilizing a measured PSF. To the best of our knowledge, the SPM algorithm is the only linear-inversion method that can reconstruct the permittivity distribution of the scanned object. The quantitative imaging is enabled by the second inversion stage of the SPM. Even with analytical PSFs, the second stage of SPM dramatically improves the image quality. Since this stage is absent in the BPA, the BPA image quality is always inferior to that of SPM, even if the SPM method employs analytical PSFs the way the BPA does. The image improvement in the second SPM stage is evidenced by the comparison of the images in Figures 4.5 and 4.6 or Figures 4.11 and 4.12.

Further, the SPM, just like the BPA, is very effective at suppressing measurement noise, errors, and radar clutter by using a large number of measurements (larger than the number that would be needed in noise-free clutter-free measurements). It is shown in [38] that the SPM first stage minimizes the ℓ_2 norm of the data error, i.e., the difference between the measured responses and the responses that are predicted by the linearized model of scattering with the extracted target permittivity (or reflectivity). ℓ_2 norm solutions are effective in reducing the impact of noise and measurement errors. This is not the case in the ω-k algorithms, where the Fourier transforms are sensitive to measurement noise and errors. Note that filtering strategies are also a powerful tool in suppressing radar clutter and rejecting poor SNR data. These have been applied in the example with the compressed breast phantom measurements.

The proposed random sampling SPM method does have limitations, which we address here. One limitation stems from the power map computation in real space, which is significantly slower than the k-space computation as shown in [77, 78]. However, the k-space computation employs 2D FFT, which needs uniformly sampled data and can start only after the scan is completed. The computational complexity of the power map updates with (4.6) scales with the number of image voxels N_{v}. When $N_{\text{v}}{\sim}10^6$ or more, the time required by a sequential computing algorithm may exceed a second, which is slower than the rate at which most imaging radars perform a measurement. For example, off-the-shelf ultra-wideband (UWB) radars can be as fast as 50 waveforms per second [103], but advanced research prototypes may reach rates of $\sim$1000 measurements per second [104]. To simplify the data-offload management and to reduce the data-storage demands, it is important to achieve a power map update, the speed of which is equal to or better than the speed at which the measurement system provides a spatial sample.

Another limitation in the current investigation is the assumption that the bore–sight axis of the antennas is fixed along the range direction (the z axis) and it does not consider a possible tilt of the imaging platform. The platform tilt has two implications: (i) the signal strength depends on the orientation of the antenna beams, and (ii) the signal paths from the Tx antenna to the target and then onto the Rx antenna will change. Both of these implications can be accounted for by the PSFs provided that the antenna-gain patterns and the tilt angle of the platform are known. However, the current implementation does not take these factors into account.

Finally, we emphasize that the proposed method does not employ compressive sensing (CS) strategies; therefore, it is not a solution to the problem of sparse sampling. The reported reduction in the number of spatial samples needed to reconstruct high-quality images is only due to the rigorous convergence criterion, which is automatically determined when the data are sufficient.

4.6 Conclusions and Future Work

This study introduces a novel SPM algorithm optimized for real-time SAR imaging with randomly sampled data on 3D trajectories, a common scenario in mobile and handheld radar platforms. Our approach differs from traditional methods by eliminating the need for uniform sampling across canonical surfaces and spectral estimation techniques, thereby simplifying the computational process and reducing the time requirements. The first stage of the SPM algorithm works concurrently with the measurements on the arbitrary trajectory. With each additional measurement, it updates an evolving scattered power map of the object (a projection image) cast on a uniform 3D grid. The advantage of this updating strategy is three-fold. First, the projection-image update is fast as it amounts to computing and adding $N_{\mathrm{R}} \times N_n$ terms to the already-existing power map voxel value; see (4.6). As a reminder, N_{R} is the number of responses measured at each observation position $\mathbf{r}$, and N_n is the number of frequency or temporal samples in each response. Second, once the contribution of a spatial sample is added, it is no longer needed, thus eliminating the need to store the entire measurement dataset. This is important in realizing compact mobile or handheld imaging platforms where the image processing is performed on-board and the amount of measurements is extensive. Third, each power map voxel is updated independently, thus allowing for parallel computations with significant acceleration.

The second SPM stage, which is fundamentally an image deconvolution performed in Fourier space, significantly enhances the image quality of the output from the first stage. This stage is computationally very efficient and is independent of the sampling strategy. It, too, is amenable to parallel computations since a small $N_z \times N_z$ system of Equation (4.7) is solved independently at each (k_x, k_y) point in Fourier space. Importantly, the second SPM stage allows for quantitative imaging. We reiterate that quantitative imaging is enabled by measured PSFs, i.e., data obtained by measuring the domain of interest in the presence of a point-like scatterer (not the OUT). When measuring the PSF is not feasible, it is obtained with (C.23), wherein the incident field distributions of the Tx and Rx antennas are expressed either through analytical formulas or simulated distributions.

A pivotal element of our methodology is the convergence check of the OUT power map update, eliminating the need for a predetermined scan completion. The convergence criterion employs the SSIM between two successive power map updates and an SSIM threshold of 0.97, which must be met by four consecutive SSIM evaluations. It has been observed that the OUT power map converges to a high-resolution image with a number of spatial samples, which is appreciably lower than the number of samples dictated by the Nyquist criterion for a uniformly sampled synthetic aperture. In the imaging of a simple F shape object with simulated data on a 3D trajectory, convergence is achieved with only 40% of the number of samples in the dense uniformly sampled grid on a planar aperture. In addition to the simplicity of the imaged object, the reduction in the spatial samples is likely due to the 3D nature of the observation trajectory, which provides responses at various range distances from the object. On the other hand, in the imaging of a more complex object (key, coin, and lipstick in a bag), measured with an LFM mm-wave radar module, the number of random samples reaches 90% of those on the dense uniform planar grid.

Validation through simulated and measured data confirms the robustness of the proposed approach when applied to both stepped-frequency continuous wave and LFM radar data. The ability to automatically determine the sufficiency of data and to terminate the data acquisition in a timely manner is beneficial in reducing operational costs and time in practical applications.

In order to overcome the limitations discussed in Section 4.5, upcoming work will focus on implementing the algorithm with parallel programming on multicore, multiprocessor platforms in order to accelerate the computation of the power maps and to achieve real-time processing that matches the speed of the measurements. The second task in the future algorithm enhancement is the ability to take into account the platform tilt by incorporating in the system PSFs the tilt angles and the antenna gain patterns. Third, we aim to enhance the SPM algorithm by integrating it with a compressed sensing (CS) preprocessing step. This integration will enable an OUT power map update directly in k-space, achieving convergence with fewer spatial samples, thus accelerating not only the computations but also the measurement process. Finally, we underscore the importance of having accurate measurement coordinates relative to the imaged object. This accuracy is critical for achieving focused images since the spatial resolution is limited to within the accuracy range of the coordinates. Much research and technical solutions are needed in this respect for applications with handheld and mobile platforms. Improving the tolerance of our image-reconstruction method to positioning errors is another focus of future research.

4.7 Acknowledgment

This research is partially supported by the IEEE Antennas and Propagation Society (AP-S) Fellowship Program for the academic year 2023-2024. We express our sincere gratitude to the AP-S for their commitment to fostering excellence in the field of antennas and propagation.

BIBLIOGRAPHY

[1] S. Kharkovsky, J. Case, M. Abou-Khousa, R. Zoughi, and F. Hepburn, "Millimeter-wave detection of localized anomalies in the space shuttle external fuel tank insulating foam," *IEEE Transactions on Instrumentation and Measurement*, vol. 55, no. 4, pp. 1250–1257, 2006.

[2] M. Dvorsky, S. Y. Sim, D. T. Motes, T. Watt, A. Shah, M. T. A. Qaseer, and R. Zoughi, "Multistatic ka-band (26.5–40 ghz) millimeter-wave 3-d imaging system," *IEEE Transactions on Instrumentation and Measurement*, vol. 72, pp. 1–14, 2023.

[3] M. J. Horst, M. T. Ghasr, and R. Zoughi, "A compact microwave camera based on chaotic excitation synthetic-aperture radar," *IEEE Transactions on Antennas and Propagation*, vol. 67, no. 6, pp. 4148–4161, 2019.

[4] T. Truong, A. Dinh, and K. Wahid, "An ultra-wideband frequency system for non-destructive root imaging," *Sensors*, vol. 18, no. 8, 2018. [Online]. Available: https://www.mdpi.com/1424-8220/18/8/2438

[5] M. A. Abou-Khousa, M. S. U. Rahman, K. M. Donnell, and M. T. A. Qaseer, "Detection of surface cracks in metals using microwave and millimeter-wave nondestructive testing techniques—a review," *IEEE Transactions on Instrumentation and Measurement*, vol. 72, pp. 1–18, 2023.

[6] C. Liu and R. Zoughi, "Adaptive synthetic aperture radar (sar) imaging for optimal cross-range resolution and image quality in nde applications," *IEEE Transactions on Instrumentation and Measurement*, vol. 70, pp. 1–7, 2021.

[7] M. Paun, "Through-wall imaging using low-cost frequency-modulated continuous wave radar sensors," *Remote Sensing*, vol. 16, no. 8, 2024. [Online]. Available: https://www.mdpi.com/2072-4292/16/8/1426

[8] A. Zhuravlev, V. Razevig, A. Rogozin, and M. Chizh, "Microwave imaging of concealed objects with linear antenna array and optical tracking of the target for high-performance security screening systems," *IEEE Trans. Microw. Theory Tech.*, vol. 71, no. 3, pp. 1326–1336, 2023.

[9] S. Gui, J. Li, Y. Yang, F. Zuo, and Y. Pi, "A sar imaging method for walking human based on mωka-FrFT-mmGLRT," *IEEE Transactions on Geoscience and Remote Sensing*, vol. 60, pp. 1–12, 2022.

[10] S. Gui, Y. Yang, J. Li, F. Zuo, and Y. Pi, "Thz radar security screening method for walking human torso with multi-angle synthetic aperture," *IEEE Sensors Journal*, vol. 21, no. 16, pp. 17 962–17 972, 2021.

[11] A. Zhuravlev, V. Razevig, M. Chizh, G. Dong, and B. Hu, "A new method for obtaining radar images of concealed objects in microwave personnel screening systems," *IEEE Transactions on Microwave Theory and Techniques*, vol. 69, no. 1, pp. 357–364, 2021.

[12] Z. Chen, Z. Zeng, D. Fu, Y. Huang, Q. Li, X. Zhang, and J. Wan, "Back-projection imaging for synthetic aperture radar with topography

occlusion," *Remote Sens.*, vol. 15, no. 3, 2023. [Online]. Available: https://www.mdpi.com/2072-4292/15/3/726

[13] L. Pang, H. Liu, Y. Chen, and J. Miao, "Real-time concealed object detection from passive millimeter wave images based on the YOLOv3 algorithm," *Sensors*, vol. 20, no. 6, 2020. [Online]. Available: https://www.mdpi.com/1424-8220/20/6/1678

[14] F. Liang, P. Wang, H. Lv, M. Bai, Q. An, S. Han, Y. Zhang, and J. Wang, "Change detection and enhanced imaging of vital signs based on arc-scanning sar," *IEEE Sensors Journal*, vol. 24, no. 6, pp. 8304–8313, 2024.

[15] A. Y. Owda, M. Owda, and N.-D. Rezgui, "Synthetic aperture radar imaging for burn wounds diagnostics," *Sensors*, vol. 20, no. 3, 2020. [Online]. Available: https://www.mdpi.com/1424-8220/20/3/847

[16] M. Klemm, J. A. Leendertz, D. Gibbins, I. J. Craddock, A. Preece, and R. Benjamin, "Microwave radar-based differential breast cancer imaging: Imaging in homogeneous breast phantoms and low contrast scenarios," *IEEE Transactions on Antennas and Propagation*, vol. 58, no. 7, pp. 2337–2344, 2010.

[17] H. Li, H. Zhang, Y. Kong, and C. Zhou, "Flexible dual-polarized uwb antenna sensors for breast tumor detection," *IEEE Sensors Journal*, vol. 22, no. 13, pp. 13 648–13 658, 2022.

[18] M. Ghamati, M. Taherzadeh, F. Nabki, and M. Popović, "Integrated fast uwb time-domain microwave breast screening," *IEEE Transactions on Instrumentation and Measurement*, vol. 72, pp. 1–12, 2023.

[19] C. Dachena, A. Fedeli, A. Fanti, M. B. Lodi, G. Fumera, A. Randazzo, and M. Pastorino, "Microwave imaging of the neck by means of artificial neural networks for tumor detection," *IEEE Open Journal of Antennas and Propagation*, vol. 2, pp. 1044–1056, 2021.

[20] S. Hosseinzadegan, A. Fhager, M. Persson, S. D. Geimer, and P. M. Meaney, "Discrete dipole approximation-based microwave tomography for fast breast cancer imaging," *IEEE Trans. Microw. Theory Tech.*, vol. 69, no. 5, pp. 2741–2752, 2021.

[21] L. Zhang, Z. Qiao, M.-d. Xing, L. Yang, and Z. Bao, "A robust motion compensation approach for uav sar imagery," *IEEE Transactions on Geoscience and Remote Sensing*, vol. 50, no. 8, pp. 3202–3218, 2012.

[22] F. Zhang, S. Yan, Y. Fu, W. Yang, W. Zhang, and R. Yu, "A novel motion compensation framework for micro uav fmcw sar," in *2023 IEEE 16th International Conference on Electronic Measurement & Instruments (ICEMI)*, 2023, pp. 304–308.

[23] "A new unmanned aerial vehicle synthetic aperture radar for environmental monitoring," *Progress In Electromagnetics Research*, vol. 122, pp. 245–268, 2012.

[24] J. Ding, K. Zhang, X. Huang, and Z. Xu, "High frame-rate imaging using swarm of uav-borne radars," *IEEE Transactions on Geoscience and Remote Sensing*, vol. 62, pp. 1–12, 2024.

[25] F. T. Faul, D. Korthauer, and T. F. Eibert, “Impact of rotor blade rotation of uavs on electromagnetic field measurements,” *IEEE Transactions on Instrumentation and Measurement*, vol. 70, pp. 1–9, 2021.

[26] M. Lyu, Y. Zhao, C. Huang, and H. Huang, “Unmanned aerial vehicles for search and rescue: A survey,” *Remote Sensing*, vol. 15, no. 13, 2023. [Online]. Available: https://www.mdpi.com/2072-4292/15/13/3266

[27] M. Garcia Fernandez, Y. Alvarez Lopez, A. Arboleya Arboleya, B. Gonzalez Valdes, Y. Rodriguez Vaqueiro, F. Las-Heras Andres, and A. Pino Garcia, “Synthetic aperture radar imaging system for landmine detection using a ground penetrating radar on board a unmanned aerial vehicle,” *IEEE Access*, vol. 6, pp. 45 100–45 112, 2018.

[28] Y. A. Lopez, M. Garcia-Fernandez, G. Alvarez-Narciandi, and F. L.-H. Andres, “Unmanned aerial vehicle-based ground-penetrating radar systems: A review,” *IEEE Geoscience and Remote Sensing Magazine*, vol. 10, no. 2, pp. 66–86, 2022.

[29] M. Garcia-Fernandez, G. Alvarez-Narciandi, F. L. Heras, and Y. Alvarez-Lopez, “Comparison of scanning strategies in uav-mounted multichannel gpr-sar systems using antenna arrays,” *IEEE Journal of Selected Topics in Applied Earth Observations and Remote Sensing*, vol. 17, pp. 3571–3586, 2024.

[30] A. Amiri, K. Tong, and K. Chetty, “Feasibility study of multi-frequency ground penetrating radar for rotary uav platforms,” in *IET International Conference on Radar Systems (Radar 2012)*, 2012, pp. 1–6.

[31] M. Weib and J. Ender, “A 3d imaging radar for small unmanned airplanes - artino,” in *European Radar Conference, 2005. EURAD 2005.*, 2005, pp. 209–212.

[32] M. A. Yarleque, S. Alvarez, and H. J. Martinez, “Fmcw gpr radar mounted in a mini-uav for archaeological applications: First analytical and measurement results,” in *2017 International Conference on Electromagnetics in Advanced Applications (ICEAA)*, 2017, pp. 1646–1648.

[33] G. Ludeno, I. Catapano, A. Renga, A. R. Vetrella, G. Fasano, and F. Soldovieri, “Assessment of a micro-uav system for microwave tomography radar imaging,” *Remote Sensing of Environment*, vol. 212, pp. 90–102, 2018. [Online]. Available: https://www.sciencedirect.com/science/article/pii/S0034425718301974

[34] A. Grathwohl, B. Arendt, T. Grebner, and C. Waldschmidt, “Detection of objects below uneven surfaces with a uav-based gpsar,” *IEEE Transactions on Geoscience and Remote Sensing*, vol. 61, pp. 1–13, 2023.

[35] A. Pierce, “Walabot diy can see into walls,” *Ann Arbor: Prakken Publications, Inc*, vol. 76, no. 5, pp. 8–9, 2017. [Online]. Available: https://www.proquest.com/openview/01261a7cf0992e9497a548a2c23d3596/1.pdf?pq-origsite=gscholar&cbl=182

[36] Vayyar imaging - home. [Online]. Available: https://vayyar.com/

[37] The world’s most advanced stud finder. [Online]. Available: https://walabot.com/

[38] N. K. Nikolova, *Introduction to Microwave Imaging*, ser. EuMA High Frequency Technologies Series. Cambridge University Press, 2017.

[39] R. K. Amineh, N. K. Nikolova, and M. Ravan, *Real-Time Three-Dimensional Imaging of Dielectric Bodies Using Microwave/Millimeter Wave Holography.* John Wiley & Sons, 2019.

[40] D. Sheen, D. McMakin, and T. Hall, "Three-dimensional millimeter-wave imaging for concealed weapon detection," *IEEE Trans. Microw. Theory Tech.*, vol. 49, no. 9, pp. 1581–1592, 2001.

[41] C. D. Austin, E. Ertin, and R. L. Moses, "Sparse signal methods for 3-d radar imaging," *IEEE Journal of Selected Topics in Signal Processing*, vol. 5, no. 3, pp. 408–423, 2011.

[42] J. Fessler and B. Sutton, "Nonuniform fast fourier transforms using min-max interpolation," *IEEE Transactions on Signal Processing*, vol. 51, no. 2, pp. 560–574, 2003.

[43] D. Sun, B. Pang, S. Xing, Y. Li, and X. Wang, "Direct 3-d sparse imaging using non-uniform samples without data interpolation," *Electronics*, vol. 9, no. 2, 2020. [Online]. Available: https://www.mdpi.com/2079-9292/9/2/321

[44] J. T. Case, M. T. Ghasr, and R. Zoughi, "Optimum 2-d nonuniform spatial sampling for microwave sar-based nde imaging systems," *IEEE Transactions on Instrumentation and Measurement*, vol. 61, no. 11, pp. 3072–3083, 2012.

[45] F. Marvasti, “Nonuniform sampling theorems for bandpass signals at or below the nyquist density,” *IEEE Transactions on Signal Processing*, vol. 44, no. 3, pp. 572–576, 1996.

[46] ——, “Interpolation of lowpass signals at half the nyquist rate,” in *1995 International Conference on Acoustics, Speech, and Signal Processing*, vol. 2, 1995, pp. 1225–1228 vol.2.

[47] S. Zhou, L. Yang, L. Zhao, and G. Bi, “Forward velocity extraction from uav raw sar data based on adaptive notch filtering,” *IEEE Geoscience and Remote Sensing Letters*, vol. 13, no. 9, pp. 1211–1215, 2016.

[48] M. Farhadi, R. Feger, J. Fink, T. Wagner, and A. Stelzer, “Combining mimo dbf with automotive synthetic aperture radar imaging and phase error correction,” *IEEE Access*, vol. 12, pp. 31 944–31 959, 2024.

[49] M. M. Saurer, B. Hofmann, and T. F. Eibert, “A fully polarimetric multilevel fast spectral domain algorithm for 3-D imaging with irregular sample locations,” *IEEE Trans. Microw. Theory Tech.*, vol. 70, no. 9, pp. 4231–4242, 2022.

[50] A. Yegulalp, “Fast backprojection algorithm for synthetic aperture radar,” in *Proceedings of the 1999 IEEE Radar Conference. Radar into the Next Millennium (Cat. No.99CH36249)*, 1999, pp. 60–65.

[51] A. Moreira and Y. Huang, “Airborne sar processing of highly squinted data using a chirp scaling approach with integrated motion compensation,” *IEEE Transactions on Geoscience and Remote Sensing*, vol. 32, no. 5, pp. 1029–1040, 1994.

[52] L. Zhou, X. Zhang, Y. Wang, L. Li, L. Pu, J. Shi, and S. Wei, "Unambiguous reconstruction for multichannel nonuniform sampling sar signal based on image fusion," *IEEE Access*, vol. 8, pp. 71 558–71 571, 2020.

[53] G. Krieger, N. Gebert, and A. Moreira, "Unambiguous sar signal reconstruction from nonuniform displaced phase center sampling," *IEEE Geoscience and Remote Sensing Letters*, vol. 1, no. 4, pp. 260–264, 2004.

[54] Y. Eldar and A. Oppenheim, "Filterbank reconstruction of bandlimited signals from nonuniform and generalized samples," *IEEE Transactions on Signal Processing*, vol. 48, no. 10, pp. 2864–2875, 2000.

[55] J. Lopez-Sanchez and J. Fortuny-Guasch, "3-d radar imaging using range migration techniques," *IEEE Transactions on Antennas and Propagation*, vol. 48, no. 5, pp. 728–737, 2000.

[56] Y. Gao, M. T. Ghasr, and R. Zoughi, "Effects of and compensation for translational position error in microwave synthetic aperture radar imaging systems," *IEEE Transactions on Instrumentation and Measurement*, vol. 69, no. 4, pp. 1205–1212, 2020.

[57] J. T. Case, M. T. Ghasr, and R. Zoughi, "Nonuniform manual scanning for rapid microwave nondestructive evaluation imaging," *IEEE Transactions on Instrumentation and Measurement*, vol. 62, no. 5, pp. 1250–1258, 2013.

[58] D. Meng, D. Hu, and C. Ding, "Precise focusing of airborne sar data with wide apertures large trajectory deviations: A chirp modulated back-projection

approach," *IEEE Transactions on Geoscience and Remote Sensing*, vol. 53, no. 5, pp. 2510–2519, 2015.

[59] B. Zhang, G. Xu, R. Zhou, H. Zhang, and W. Hong, "Multi-channel back-projection algorithm for mmWave automotive MIMO SAR imaging with Doppler-division multiplexing," *IEEE J. Sel. Top. Signal Process.*, vol. 17, no. 2, pp. 445–457, 2023.

[60] S. Wu, L. Ding, P. Li, Y. Li, L. Chen, and Y. Zhu, "Millimeter-wave sar sparse imaging with 2-d spatially pseudorandom spiral-sampling pattern," *IEEE Transactions on Microwave Theory and Techniques*, vol. 68, no. 11, pp. 4672–4683, 2020.

[61] S. Hu, A. M. Molaei, O. Yurduseven, H. Meng, R. Nilavalan, L. Gan, and X. Chen, "Multistatic mimo sparse imaging based on fft and low-rank matrix recovery techniques," *IEEE Transactions on Microwave Theory and Techniques*, vol. 71, no. 3, pp. 1285–1295, 2023.

[62] T. Zhang, Y. Li, J. Wang, M. Xing, L. Guo, and P. Zhang, "A modified range model and extended omega-k algorithm for high-speed-high-squint sar with curved trajectory," *IEEE Transactions on Geoscience and Remote Sensing*, vol. 61, pp. 1–15, 2023.

[63] Z. Xu, M. Liu, G. Zhou, Z. Wei, B. Zhang, and Y. Wu, "An accurate sparse sar imaging method for enhancing region-based features via nonconvex and tv regularization," *IEEE Journal of Selected Topics in Applied Earth Observations and Remote Sensing*, vol. 14, pp. 350–363, 2021.

[64] M. Liu, J. Pan, J. Zhu, Z. Chen, B. Zhang, and Y. Wu, "A sparse sar imaging method for low-oversampled staggered mode via compound regularization," *Remote Sensing*, vol. 16, no. 8, 2024. [Online]. Available: https://www.mdpi.com/2072-4292/16/8/1459

[65] D. Ao, R. Wang, C. Hu, and Y. Li, "A sparse sar imaging method based on multiple measurement vectors model," *Remote Sensing*, vol. 9, no. 3, 2017. [Online]. Available: https://www.mdpi.com/2072-4292/9/3/297

[66] Y. Wang, Z. He, X. Zhan, Y. Fu, and L. Zhou, "Three-dimensional sparse sar imaging with generalized lq regularization," *Remote Sensing*, vol. 14, no. 2, 2022. [Online]. Available: https://www.mdpi.com/2072-4292/14/2/288

[67] E. J. Candes and M. B. Wakin, "An introduction to compressive sampling," *IEEE Signal Processing Magazine*, vol. 25, no. 2, pp. 21–30, 2008.

[68] T.-H. Pham, K.-H. Kim, and I.-P. Hong, "A study on millimeter wave sar imaging for non-destructive testing of rebar in reinforced concrete," *Sensors*, vol. 22, no. 20, 2022. [Online]. Available: https://www.mdpi.com/1424-8220/22/20/8030

[69] W. Pu, Y. Huang, J. Wu, H. Yang, and J. Yang, "Fast compressive sensing-based sar imaging integrated with motion compensation," *IEEE Access*, vol. 7, pp. 53 284–53 295, 2019.

[70] J. Yang, T. Jin, C. Xiao, and X. Huang, "Compressed sensing radar imaging: Fundamentals, challenges, and advances," *Sensors*, vol. 19, no. 14, 2019. [Online]. Available: https://www.mdpi.com/1424-8220/19/14/3100

[71] M.-S. Kang and J.-M. Baek, "Sar image reconstruction via incremental imaging with compressive sensing," *IEEE Transactions on Aerospace and Electronic Systems*, vol. 59, no. 4, pp. 4450–4463, 2023.

[72] B. Dong, G. Li, and Q. Zhang, "High-resolution and wide-swath imaging of spaceborne sar via random prf variation constrained by the coverage diagram," *IEEE Transactions on Geoscience and Remote Sensing*, vol. 60, pp. 1–16, 2022.

[73] M. M. Abo-Zahhad, A. I. Hussein, and A. M. Mohamed, "Compressive sensing algorithms for signal processing applications: A survey," *International journal of communications, network and system sciences*, vol. 8, no. 6, pp. 197–216, 2015.

[74] S. Bernhardt, R. Boyer, S. Marcos, and P. Larzabal, "Compressed sensing with basis mismatch: Performance bounds and sparse-based estimator," *IEEE Transactions on Signal Processing*, vol. 64, no. 13, pp. 3483–3494, 2016.

[75] S. Tu, J. J. McCombe, D. S. Shumakov, and N. K. Nikolova, "Fast quantitative microwave imaging with resolvent kernel extracted from measurements," *Inverse Problems*, vol. 31, no. 4, p. 045007, mar 2015. [Online]. Available: https://dx.doi.org/10.1088/0266-5611/31/4/045007

[76] D. S. Shumakov and N. K. Nikolova, "Fast quantitative microwave imaging with scattered-power maps," *IEEE Transactions on Microwave Theory and Techniques*, vol. 66, no. 1, pp. 439–449, 2018.

[77] R. Kazemivala, D. Tajik, and N. K. Nikolova, "Simultaneous use of the Born and Rytov approximations in real-time imaging with Fourier-space scattered

power mapping," *IEEE Trans. Microw. Theory Tech.*, vol. 70, no. 5, pp. 2904–2920, 2022.

[78] R. Kazemivala, A. D. Pitcher, J. Nguyen, and N. K. Nikolova, "Real-time millimeter-wave imaging with linear frequency modulation radar and scattered power mapping," *IEEE Transactions on Microwave Theory and Techniques*, pp. 1–14, 2024.

[79] L. Liu, A. C. Trehan, and N. K. Nikolova, "Near-field detection at microwave frequencies based on self-adjoint response sensitivity analysis," *Inverse Problems*, vol. 26, p. 105001, 2010. [Online]. Available: https://api.semanticscholar.org/CorpusID:122866694

[80] C. Liu, M. T. A. Qaseer, and R. Zoughi, "Influence of antenna pattern on synthetic aperture radar resolution for nde applications," *IEEE Transactions on Instrumentation and Measurement*, vol. 70, pp. 1–11, 2021.

[81] R. K. Amineh, J. McCombe, and N. K. Nikolova, "Microwave holographic imaging using the antenna phaseless radiation pattern," *IEEE Antennas Wireless Propag. Lett.*, vol. 11, pp. 1529–1532, Dec. 2012.

[82] Y. Meng, C. Lin, J. Zang, A. Qing, and N. K. Nikolova, "General theory of holographic inversion with linear frequency modulation radar and its application to whole-body security scanning," *IEEE Transactions on Microwave Theory and Techniques*, vol. 68, no. 11, pp. 4694–4705, 2020.

[83] J. Gao, B. Deng, Y. Qin, H. Wang, and X. Li, “An efficient algorithm for mimo cylindrical millimeter-wave holographic 3-d imaging,” *IEEE Transactions on Microwave Theory and Techniques*, vol. 66, no. 11, pp. 5065–5074, 2018.

[84] D. Tajik, R. Kazemivala, J. Nguyen, and N. K. Nikolova, “Accurate range migration for fast quantitative fourier-based image reconstruction with monostatic radar,” *IEEE Transactions on Microwave Theory and Techniques*, vol. 70, no. 9, pp. 4273–4283, 2022.

[85] Q. Cheng, A. Alomainy, and Y. Hao, “Near-field millimeter-wave phased array imaging with compressive sensing,” *IEEE Access*, vol. 5, pp. 18 975–18 986, 2017.

[86] D. Tajik, F. Foroutan, D. S. Shumakov, A. D. Pitcher, and N. K. Nikolova, “Real-time microwave imaging of a compressed breast phantom with planar scanning,” *IEEE J. Electromagn. RF Microw. Med. Biol.*, vol. 2, no. 3, pp. 154–162, 2018.

[87] A. S. Beaverstone, D. S. Shumakov, and N. K. Nikolova, “Frequency-domain integral equations of scattering for complex scalar responses,” *IEEE Trans. Microw. Theory Tech.*, vol. 65, no. 4, pp. 1120–1132, 2017.

[88] D. M. Pozar, *Microwave Engineering*, 4th ed. John Wiley & Sons, 2012.

[89] G. Wang, J.-M. Muñoz-Ferreras, C. Gu, C. Li, and R. Gómez-García, “Application of linear-frequency-modulated continuous-wave (LFMCW) radars for tracking of vital signs,” *IEEE Trans. Microw. Theory Tech.*, vol. 62, no. 6, pp. 1387–1399, 2014.

[90] L. Yi, R. Kaname, R. Mizuno, Y. Li, M. Fujita, H. Ito, and T. Nagatsuma, "Ultra-wideband frequency modulated continuous wave photonic radar system for three-dimensional terahertz synthetic aperture radar imaging," *Journal of Lightwave Technology*, vol. 40, no. 20, pp. 6719–6728, 2022.

[91] C. Ozdemir, S. Demirci, E. Yigit, and B. Yilmaz, "A review on migration methods in b-scan ground penetrating radar imaging," *Mathematical Problems in Engineering*, vol. 2014, no. 1, p. 280738.

[92] R. K. Amineh, A. Khalatpour, H. Xu, Y. Baskharoun, and N. K. Nikolova, "Three-dimensional near-field microwave holography for tissue imaging," *Journal of Biomedical Imaging*, vol. 2012, pp. 5–5, 2012.

[93] R. K. Amineh, J. J. McCombe, A. Khalatpour, and N. K. Nikolova, "Microwave holography using point-spread functions measured with calibration objects," *IEEE Trans. Instrum. Meas.*, vol. 64, no. 2, pp. 403–417, 2015.

[94] Altiar FEKO, Electromagnetic Simulation Software. [Online]. Available: https://altairhyperworks.com/product/FEKO

[95] MATLAB, *ver. R2022b*. Natick, Massachusetts: The MathWorks Inc., 2022.

[96] D. Tajik, R. Kazemivala, J. Nguyen, and N. K. Nikolova, "Accurate range migration for fast quantitative Fourier-based image reconstruction with monostatic radar," *IEEE Trans. Microw. Theory Tech.*, vol. 70, no. 9, pp. 4273–4283, 2022.

[97] C. K. Balanis, *Antenna Theory Analysis and Design*. John Wiley & Sons, Inc., 1997.

[98] N. V. Shahmirzadi, V. Tyagi, J. Nguyen, R. Kazemivala, N. K. Nikolova, and C.-H. Chen, "Planar array of uwb active slot antennas for microwave imaging of the breast," *IEEE Transactions on Antennas and Propagation*, vol. 71, no. 4, pp. 2946–2957, 2023.

[99] D. Tajik, A. D. Pitcher, and N. K. Nikolova, "Comparative study of the Rytov and Born approximations in quantitative microwave holography," *Prog. Electromagn. Res. B*, vol. 79, pp. 1–19, 2017.

[100] *IWR1443BOOST Evaluation Module mmWave Sensing Solution*, Texas Instruments, 2020. [Online]. Available: https://www.ti.com/lit/ug/swru518d/swru518d.pdf?ts=1703684594280

[101] *DCA1000EVM Real-time Data-capture Adapter for Radar Sensing Evaluation Module*, Texas Instruments, 2019.

[102] M. Wen and J. Houlihan, "Application of non-uniform fourier transform to non-uniform sampling fourier transform spectrometers," *arXiv preprint arXiv:2212.04502*, 2022.

[103] M. G. Fernández, Y. Á. López, A. A. Arboleya, B. G. Valdés, Y. R. Vaqueiro, F. L.-H. Andrés, and A. P. García, "Synthetic aperture radar imaging system for landmine detection using a ground penetrating radar on board a unmanned aerial vehicle," *IEEE Access*, vol. 6, pp. 45 100–45 112, 2018.

[104] A. D. Pitcher, C. W. Baard, M. S. Georgiev, and N. K. Nikolova, "Ultra-wideband equivalent-time sampling receiver: limitations and performance analysis," *IEEE Trans. Instrumentation and Measurements*, vol. submitted, 2024.

CHAPTER 5

CONCLUSIONS AND RECOMMENDATIONS FOR FUTURE WORK

5.1 Summary

In this work, new microwave and mmW imaging algorithms are developed and enhanced via: (a) simultaneous use of the Born and Rytov approximations in the data extraction stage to enhance the detection of embedded targets, (b) introducing a method for the fast processing of time-domain signals in microwave and mmW image reconstruction using an SPM approach, and (d) introducing a method for real-time SAR imaging with randomly sampled data on 3D trajectories. All developments are supported by simulated and experimental studies, which is critical for any technology attempting to reach industrial trials. The following discussion highlights future work for each chapter.

5.2 Future Work

(i) Optimization of Data Acquisition

Despite the image reconstruction algorithm being nearly instantaneous, the scan time with the current planar acquisition setup remains several hours long. This issue is especially pronounced in Chapter 3, where experiments conducted in the mmW range with smaller scanning steps result in even longer scan times.

Future efforts should focus on improving the acquisition setup by integrating electronic scanning with antenna arrays that can cover the entire imaging aperture, potentially reducing scan time to just a few minutes.

Moreover, as discussed in Chapter 4, we simulated random acquisition by randomly selecting sampled points from a previously uniformly dense set of measurements. Significant research is still needed to ensure accurate measurement coordinates relative to the imaged object, particularly for handheld and mobile platforms. Enhancing the tolerance of our image reconstruction method to positioning errors is another critical area for future research.

Additionally, reflections from the acquisition setup cause image artifacts, which is another challenge. While filtering techniques reported in several studies can mitigate image clutter to some extent, further improvements in the design of shielding absorbers and non-reflective platforms are necessary.

(ii) Enhanced Image Reconstruction by Use of Iterative Imaging Techniques

Although results in Chapter 2 demonstrate that combining the Born and Rytov approximations can enhance image quality, further research is necessary. The SPM method is a direct inversion algorithm that employs the Born approximation of the total internal field, resulting in a linearized forward model of scattering. This linearization is often problematic in inverse scattering problems, which are inherently nonlinear. While direct inversion algorithms such as SPM and QMH have the advantage of low computational burden, they struggle with strongly heterogeneous targets since they cannot account for multiple-scattering and mutual-coupling effects.

Conversely, iterative algorithms like the Born iterative method [2], the distorted Born iterative method [3], and electromagnetic model-based nonlinear optimization methods [4] can accommodate nonlinear scattering effects. However, these iterative methods are often time-consuming, they are prone to modelling errors and suffer from slow convergence or convergence to a wrong solution.

The algorithm discussed in this thesis, SPM, along with other direct inversion algorithms, can be incorporated in iterative algorithms. By updating the total internal field iteratively rather than relying on linear approximations, the accuracy of the permittivity estimates can be improved. Such an iterative approach could be devised by incorporating a Rytov correction factor for fast, simulation-free updates of the total internal field. Essentially, the iterative process would solve a nonlinear equation, where the initial permittivity distribution obtained from the non-iterative SPM algorithm provides the starting point for the object's permittivity distribution.

Such an iterative approach would leverage the speed of the SPM method, would mitigate the modeling errors associated with electromagnetic solvers, and would address the complex scattering effects in problems where strongly heterogeneous high-contrast objects are imaged.

(iii) Imposing Constraints on Permittivity Values

In the current approach to quantifying the distribution of complex relative permittivity, some non-physical values arise, particularly when using Fourier-based algorithms such as F-SPM. These non-physical values manifest as positive values in the imaginary part of the permittivity and values below 1 in the real part. Physically, this is incorrect, as the media that we image do not exhibit positive imaginary part or real part of permittivity less than one.

To address this issue, an essential modification is to impose constraints within the inversion algorithm that prohibit these non-physical values. By enforcing these constraints, we can eliminate non-physical results and ensure that the estimated permittivity values remain within a physically realistic range. While this adjustment alone does not fully resolve all the complexities introduced by the linearized model of forward scattering, it represents a crucial step toward achieving more accurate and physically meaningful estimations of complex relative permittivity.

(iv) Acquisition of Point Spread Functions

As discussed in Chapters 2, 3, and 4, the SPM direct inversion algorithm can operate with analytical, simulated, or measured PSFs. However, accurate quantitative permittivity values are obtained when using measured PSFs, especially in near-field imaging scenarios. This is because the measured PSF from a point-like scatterer is derived from the same measurement setup as the Object Under Test (OUT), thereby avoiding most of the modeling errors, unlike simulated or analytical PSFs. These modeling errors arise from the inability to predict all influencing factors in the measurement setup, such as fabrication tolerances of the antennas and positioning components, uncertainties in the constitutive parameters of materials (particularly absorbers), aging of materials and connectors, and deformations due to temperature or humidity. Additionally, simulation models often overlook complexities in the cables, connectors, and fine structural components like screws, brackets, and thin supporting plates.

Conversely, as mentioned in Chapter 3, the low signal-to-noise/clutter ratio

(SNCR) of measured data using off-the-shelf LFM radar chips in the mmW frequency range precludes the availability of measured PSFs. Consequently, all experimental reconstructed results provide qualitative estimates of permittivity distribution in terms of normalized reflectivity. To enable far-field quantitative imaging with SPM, future research should focus on improving calibration methods for the PSF to enhance the measurement accuracy. Alternatively, designing a Multiple-Input Multiple-Output (MIMO) radar system would offer a higher SNCR compared to available commercial radars.

Moreover, as mentioned in Chapter 4, the current investigation with mobile platforms assumes that the bore-sight axis of the antennas is fixed along the range direction, i.e., its orientation does not vary even if the platform tilts. While this assumption does not affect analytical PSFs, measured PSFs may differ if the platform tilts. Therefore, a critical future task is to develop system PSFs that account for platform tilt along with the corresponding antenna patterns. This will ensure more accurate and reliable permittivity or reflectivity estimates, especially in mobile and handheld imaging scenarios.

(v) Optimal Choice of Scattering Probe

As discussed in the thesis, the calibration measurement process requires careful consideration of the physical embodiment of a point scatterer (or SP) and the choice of a background medium, which is typically homogeneous within the imaged volume. The precision of the system's PSF, as derived from these measurements, is critically dependent on the characteristics of the selected scattering probe.

Ideally, the size of the SP should be significantly smaller than the shortest wavelength of the employed radiation, adhering to the assumption that the electromagnetic field remains constant within the SP's volume. However, achieving such small sizes can be challenging in practical applications. Metallic SPs, while useful in generating qualitative images, are not suitable when quantitative reconstruction is required. In such cases, dielectric SPs are preferable due to their ability to produce more accurate quantitative data.

For the most precise quantitative estimates, the permittivity of the scattering probe should closely match that of the object intended for detection, especially in regions where the lossy dielectric object's permittivity is similar to that of the SP. This alignment ensures that the measured PSF accurately reflects the object's characteristics. Consequently, the complex relative permittivity of the SP should be chosen to closely resemble that of the target object.

Despite these guidelines, there remains substantial scope for optimizing the choice of SP, particularly in terms of its size and complex permittivity, to achieve the most accurate PSF measurements. The optimal characteristics of the SP may vary significantly depending on the specific application. For example, in the detection of breast malignancies, an SP with permittivity and conductivity properties closely matching those of cancerous breast tissue would be ideal, enhancing the accuracy and reliability of the diagnostic imaging.

(vi) Investigation of Calibration Objects

Calibration objects are essential for accurately characterizing the measurement system in mmWave radar. These objects are specifically designed to produce known and consistent responses to radar signals, enabling precise calibration of the system's parameters. Commonly used calibration objects include flat metal plates, metallic spheres, and corner reflectors, each providing distinct and reliable reference points for evaluating the radar's performance. By employing these calibration objects, engineers can verify that the radar system is accurately measuring critical factors such as distance, angle, velocity, and material properties.

For example, in Chapter 3, we discussed a calibration procedure for the mmWave LFM radar system, where a highly reflective copper plate was used to ensure the reliability of the collected data. It is important to note that these calibration targets differ from the SPs discussed earlier, which are used specifically for enabling quantitative imaging. Investigating the use of various calibration targets, rather than SPs, to characterize each measurement system presents a valuable area for future research. This exploration could lead to more tailored calibration strategies, enhancing the accuracy and reliability of radar systems across different applications.

(vii) Speed Enhancement

As stated in Chapter 4, the proposed SPM imaging technique for random spatial samples can be further improved. Currently, the PSFs for calculating the OUT power map are computed in real space for every imaged pixel and observation point, which is time-consuming. Note that acquiring the measured PSF for every random trajectory of the OUT measurement is in effect not possible. Forming the power maps in Fourier space instead, as discussed in Chapters 2 and 3 with the F-SPM method, could save significant computational time.

One method that could be used with sparse and randomly sampled data is compressed sensing (CS). We could apply the CS pre-processing method on the data, and therefore, compute the OUT power maps in k-space. By integrating CS methods with the proposed SPM method, we would aim to make the process faster.

(viii) Employing Weighting Coefficients

As detailed in Chapter 2, Born's and Rytov's approximations represent two distinct methodologies for extracting scattered data responses in wave propagation. Born's approximation is constrained by both the size and contrast of the scatterers, making it more suitable for scenarios involving smaller scatterers or those with low contrast. In contrast, Rytov's approximation is less restrictive, being primarily limited by the contrast, and is thus more effective in recovering data from larger scatterers. Further, Rytov's approximation is particularly advantageous in cases where transmission coefficients are available, or when the objective is to detect a small scatterer that is encapsulated within a larger object. In the proposed combined Born-Rytov approach, we opted not to apply weighting factors to either of these approximations. This decision was made to maintain simplicity in the initial formulation. However, to further enhance the method's performance, future research could explore the application of different weighting factors tailored to the specific characteristics of the imaged object. Such an approach would allow for a more refined balance between Born's and Rytov's approximations, potentially leading to improved accuracy in scattered data recovery.

Additionally, the principle of applying weighting extends to frequency normalization. At lower frequencies, the increased penetration depth results in slower signal attenuation, thereby yielding a higher SNR. Conversely, higher frequencies, while more prone to attenuation, offer superior image resolution due to their ability to capture finer spatial fluctuations. Typically, a wide-band signal is preferred as it provides a balanced trade-off between penetration depth (and thus SNR) and image quality. However, by employing frequency-specific weighting coefficients, it is possible to further optimize the imaging process. This would ensure that data from frequencies of particular interest are adequately emphasized, thereby enhancing the overall image quality and the reliability of the reconstructed data.

(ix) Synergy of Microwave/mmW Imaging with Deep Learning and Machine Learning Algorithms

Significant advancements in image quality and algorithm speed can be achieved by integrating artificial intelligence (AI) and machine learning (ML) in the development of microwave and mmW imaging systems. Utilizing advanced deep learning (DL) techniques, we can enhance image clarity and detail, which is crucial for medical diagnostics and security screening.

(x) Investigation of Calcification as Indicators of Malignancy

In the current tissue imaging prototype at microwave frequencies, the primary focus has been on detecting variations in water content, as malignant tissues tend to have higher water content compared to benign tissues. This difference in water content has been a key factor in distinguishing between healthy and cancerous tissues using microwave imaging. However, recent studies suggest that the presence and quantity of calcium deposits, or calcifications, surrounding tissues can also serve as important indicators of malignancy.

Given this, an area for future research could involve exploring the feasibility of identifying these calcifications within breast tissue using microwave imaging. Since calcifications are often associated with malignant tumors, detecting them could significantly enhance the accuracy of early breast cancer diagnoses. The first step in this research would be to thoroughly investigate the dielectric properties of calcium across the frequency band of interest in microwave imaging.

Focusing on this aspect could lead to advancements in the accuracy of microwave imaging as a non-invasive, early detection tool, ultimately aiding in the timely diagnosis and treatment of breast cancer.

(xi) Recommendation to Use CT and MRI Images as a Reference

To evaluate the quality of microwave and mmWave images, particularly in terms of their structural accuracy, it is highly recommended to use CT (Computed Tomography) and MRI (Magnetic Resonance Imaging) images as reference standards in biomedical applications. CT and MRI are well-established imaging modalities that provide high-resolution and detailed images of internal structures. These images can serve as benchmarks for assessing the performance of microwave and millimeter-wave imaging systems.

One effective method for this evaluation is the Structural Similarity Index (SSIM), which is a widely used metric for comparing the structural similarity between two images. SSIM considers changes in structural information, and contrast, making it a robust tool for assessing how closely the microwave or millimeter-wave images match the reference images obtained from CT or MRI. Since CT and MRI images are typically qualitative, the microwave/mmWave images obtained from F-SPM method would need to be normalized before comparison. While microwave and millimeter-wave imaging systems may not achieve the same level of detail as CT or MRI, SSIM can still provide valuable insights into the structural accuracy of these images, indicating how well the underlying anatomy or tissue structures are being represented.

BIBLIOGRAPHY

[1] R. Kazemivala, D. Tajik, and N. K. Nikolova, “Simultaneous use of the Born and Rytov approximations in real-time imaging with Fourier-space scattered power mapping,” *IEEE Trans. Microw. Theory Tech.*, vol. 70, no. 5, pp. 2904–2920, 2022.

[2] Y. M. Wang and W. C. Chew, “An iterative solution of the two-dimensional electromagnetic inverse scattering problem,” *International Journal of Imaging Systems and Technology*, vol. 1, no. 1, pp. 100–108, 1989. [Online]. Available: https://onlinelibrary.wiley.com/doi/abs/10.1002/ima.1850010111

[3] W. Chew and Y. Wang, “Reconstruction of two-dimensional permittivity distribution using the distorted born iterative method,” *IEEE Transactions on Medical Imaging*, vol. 9, no. 2, pp. 218–225, 1990.

[4] P. M. Meaney and Q. Fang, *Microwave Imaging: A Model-Based Approach.* Boston, MA: Springer US, 2005, pp. 127–153.

APPENDIX A

COMPLEX LOGARITHM

To clarify the derivation of (2.22), consider the polar form of the complex quantity z, $z = |z| \exp(\mathrm{i}\theta)$, where $\theta = \angle z$. Its complex logarithm can be expressed as

$$\ln(z) = \ln(|z|) + \mathrm{i}\theta \, . \tag{A.1}$$

Accordingly, the logarithm in (2.6) can be reformulated as

$$\ln\left[\frac{S_\zeta^{\mathrm{tot}}(\cdot)}{S_\zeta^{\mathrm{inc}}(\cdot)}\right] = \ln\frac{|S_\zeta^{\mathrm{tot}}(\cdot)|}{|S_\zeta^{\mathrm{inc}}(\cdot)|} + \mathrm{i}\left[\angle S_\zeta^{\mathrm{tot}}(\cdot) - \angle S_\zeta^{\mathrm{inc}}(\cdot)\right] . \tag{A.2}$$

The substitution of (A.2) into (2.6) leads to (2.22).

APPENDIX B

ACQUISITION OF BORN-BASED POWER MAPS

Here, the quantitative Fourier-space SPM equation (C.31) is re-formulated in terms of the FTs of the real and imaginary parts of the contrast as defined in (2.38) and (2.39). To this end, the quantitative real-space SPM equation (2.9) is first expanded into its real part,

$$\begin{aligned}\mathrm{Re}M_{\mathrm{B}}(x', y', z') = \iiint\limits_{z''y''x''} &[\mathrm{Re}\rho(x'', y'', z'') \cdot \\ &\mathrm{Re}\mathcal{M}_{\mathrm{B}}(x' - x'', y' - y'', z', z'') - \mathrm{Im}\rho(x'', y'', z'')\cdot \\ &\mathrm{Im}\mathcal{M}_{\mathrm{B}}(x' - x'', y' - y'', z', z'')]\, dx''dy''dz''\,,\end{aligned} \tag{B.3}$$

and its imaginary part,

$$\begin{aligned}\mathrm{Im}M_{\mathrm{B}}(x', y', z') = \iiint\limits_{z''y''x''} &[\mathrm{Re}\rho(x'', y'', z'') \cdot \\ &\mathrm{Im}\mathcal{M}_{\mathrm{B}}(x' - x'', y' - y'', z'; z'') + \mathrm{Im}\rho(x'', y'', z'')\cdot \\ &\mathrm{Re}\mathcal{M}_{\mathrm{B}}(x' - x'', y' - y'', z'; z'')]\, dx''dy''dz''\,.\end{aligned} \tag{B.4}$$

Here, the subscript "B" indicates that the scattered-power maps M_{B} and $\mathcal{M}_{\mathrm{B}}$ are derived from the Born-approximated scattered-field OUT and PSF responses; see (2.12). The integrals over x'' and y'' in (B.3)–(B.4) are in the form of 2D convolutions, which reduce to multiplications in 2D k-space, leading to:

$$\begin{aligned}\tilde{M}_{\mathrm{B}}^{\mathrm{Re}}(\boldsymbol{\kappa}, z') = \int_{z''} \big[& \tilde{\rho}^{\mathrm{Re}}(\boldsymbol{\kappa}, \boldsymbol{z'}) \cdot \tilde{\mathcal{M}}_{\mathrm{B}}^{\mathrm{Re}}(\boldsymbol{\kappa}, z'; \boldsymbol{z'}) - \\ & \tilde{\rho}^{\mathrm{Im}}(\boldsymbol{\kappa}, \boldsymbol{z'}) \cdot \tilde{\mathcal{M}}_{\mathrm{B}}^{\mathrm{Im}}(\boldsymbol{\kappa}, z'; \boldsymbol{z'}) \big] d\boldsymbol{z'} \,,\end{aligned} \tag{B.5}$$

$$\begin{aligned}\tilde{M}_{\mathrm{B}}^{\mathrm{Im}}(\boldsymbol{\kappa}, z') = \int_{z''} \big[& \tilde{\rho}^{\mathrm{Re}}(\boldsymbol{\kappa}, \boldsymbol{z'}) \cdot \tilde{\mathcal{M}}_{\mathrm{B}}^{\mathrm{Im}}(\boldsymbol{\kappa}, z'; \boldsymbol{z'}) + \\ & \tilde{\rho}^{\mathrm{Im}}(\boldsymbol{\kappa}, \boldsymbol{z'}) \cdot \tilde{\mathcal{M}}_{\mathrm{B}}^{\mathrm{Re}}(\boldsymbol{\kappa}, z'; \boldsymbol{z'}) \big] d\boldsymbol{z'} \,,\end{aligned} \tag{B.6}$$

where $\boldsymbol{\kappa} \equiv (k_x, k_y)$ and

$$\tilde{M}_{\mathrm{B}}^{\mathrm{Re}}(\boldsymbol{\kappa}, z') = \mathrm{FT}_{2\mathrm{D}} \left\{ \mathrm{Re} M_{\mathrm{B}}(x', y', z') \right\}_{(\boldsymbol{\kappa})} \,, \tag{B.7}$$

$$\tilde{M}_{\mathrm{B}}^{\mathrm{Im}}(\boldsymbol{\kappa}, z') = \mathrm{FT}_{2\mathrm{D}} \left\{ \mathrm{Im} M_{\mathrm{B}}(x', y', z') \right\}_{(\boldsymbol{\kappa})} \,, \tag{B.8}$$

$$\tilde{\mathcal{M}}_{\mathrm{B}}^{\mathrm{Re}}(\boldsymbol{\kappa}, z'; \boldsymbol{z'}) = \mathrm{FT}_{2\mathrm{D}} \left\{ \mathrm{Re} \mathcal{M}_{\mathrm{B}}(x', y', z'; \boldsymbol{z'}) \right\}_{(\boldsymbol{\kappa})} \,, \tag{B.9}$$

$$\tilde{\mathcal{M}}_{\mathrm{B}}^{\mathrm{Im}}(\boldsymbol{\kappa}, z'; \boldsymbol{z'}) = \mathrm{FT}_{2\mathrm{D}} \left\{ \mathrm{Im} \mathcal{M}_{\mathrm{B}}(x', y', z'; \boldsymbol{z'}) \right\}_{(\boldsymbol{\kappa})} \,. \tag{B.10}$$

The scattered-power maps defined in (B.7)–(B.10) are all computed directly in k-space for the best computational efficiency. For clarity, let us first consider the OUT map, which, in real space, is computed in accordance with (2.12). Its expansion into real and imaginary parts yields:

$$\begin{aligned}&\mathrm{Re} M_{\mathrm{B}}(x', y', z') = \sum_{m=1}^{N_\omega} \sum_{\zeta=1}^{N_{\mathrm{T}}} \iint_{yx} \big[\mathrm{Re} S_{\zeta,\mathrm{B}}^{\mathrm{sc}}(x, y; \omega_m) \cdot \\ &\mathrm{Re} H_{\zeta,\mathrm{B}}^{\mathrm{sc}}(x - x', y - y'; z'; \omega_m) + \mathrm{Im} S_{\zeta,\mathrm{B}}^{\mathrm{sc}}(x, y; \omega_m) \cdot \\ &\mathrm{Im} H_{\zeta,\mathrm{B}}^{\mathrm{sc}}(x - x', y - y'; z'; \omega_m) \big] \, dx dy \,,\end{aligned} \tag{B.11}$$

and

$$\begin{aligned}
&\mathrm{Im}M_{\mathrm{B}}(x',y',z') = \sum_{m=1}^{N_\omega}\sum_{\zeta=1}^{N_{\mathrm{T}}}\iint\limits_{yx}\Big[\mathrm{Im}S^{\mathrm{sc}}_{\zeta,\mathrm{B}}(x,y;\omega_m)\cdot \\
&\mathrm{Re}H^{\mathrm{sc}}_{\zeta,\mathrm{B}}(x-x',y-y';z';\omega_m) - \mathrm{Re}S^{\mathrm{sc}}_{\zeta,\mathrm{B}}(x,y;\omega_m)\cdot \\
&\ \mathrm{Im}H^{\mathrm{sc}}_{\zeta,\mathrm{B}}(x-x',y-y';z';\omega_m)\Big]\,dxdy\,.
\end{aligned} \tag{B.12}$$

The double integrals in (B.11)–(B.12) are 2D cross-correlations. Hence, the OUT maps in k-space, $\tilde{M}^{\mathrm{Re}}_{\mathrm{B}}(\boldsymbol{\kappa},z')$ and $\tilde{M}^{\mathrm{Im}}_{\mathrm{B}}(\boldsymbol{\kappa},z')$ can be directly computed as:

$$\begin{aligned}
\tilde{M}^{\mathrm{Re}}_{\mathrm{B}}(\boldsymbol{\kappa},z') = \sum_{m=1}^{N_\omega}\sum_{\zeta=1}^{N_{\mathrm{T}}}&\left[\tilde{S}^{\mathrm{Re}}_{\zeta,\mathrm{B}}(\boldsymbol{\kappa};\omega_m)\right]\left[\tilde{H}^{\mathrm{Re}}_{\zeta,\mathrm{B}}(\boldsymbol{\kappa};z';\omega_m)\right]^* \\
&+\left[\tilde{S}^{\mathrm{Im}}_{\zeta,\mathrm{B}}(\boldsymbol{\kappa};\omega_m)\right]\left[\tilde{H}^{\mathrm{Im}}_{\zeta,\mathrm{B}}(\boldsymbol{\kappa};z';\omega_m)\right]^*\,,
\end{aligned} \tag{B.13}$$

$$\begin{aligned}
\tilde{M}^{\mathrm{Im}}_{\mathrm{B}}(\boldsymbol{\kappa},z') = \sum_{m=1}^{N_\omega}\sum_{\zeta=1}^{N_{\mathrm{T}}}&\left[\tilde{S}^{\mathrm{Im}}_{\zeta,\mathrm{B}}(\boldsymbol{\kappa};\omega_m)\right]\left[\tilde{H}^{\mathrm{Re}}_{\zeta,\mathrm{B}}(\boldsymbol{\kappa};z';\omega_m)\right]^* \\
&-\left[\tilde{S}^{\mathrm{Re}}_{\zeta,\mathrm{B}}(\boldsymbol{\kappa};\omega_m)\right]\left[\tilde{H}^{\mathrm{Im}}_{\zeta,\mathrm{B}}(\boldsymbol{\kappa};z';\omega_m)\right]^*\,,
\end{aligned} \tag{B.14}$$

where

$$\tilde{S}^{\mathrm{Re}}_{\zeta,\mathrm{B}}(\boldsymbol{\kappa};\omega_m) = \mathrm{FT}_{\mathrm{2D}}\{\mathrm{Re}S^{\mathrm{sc}}_{\zeta,\mathrm{B}}(x,y;\omega_m)\}_{(\boldsymbol{\kappa})}\,, \tag{B.15}$$

$$\tilde{S}^{\mathrm{Im}}_{\zeta,\mathrm{B}}(\boldsymbol{\kappa};\omega_m) = \mathrm{FT}_{\mathrm{2D}}\{\mathrm{Im}S^{\mathrm{sc}}_{\zeta,\mathrm{B}}(x,y;\omega_m)\}_{(\boldsymbol{\kappa})}\,, \tag{B.16}$$

$$\tilde{H}^{\mathrm{Re}}_{\zeta,\mathrm{B}}(\boldsymbol{\kappa};z';\omega_m) = \mathrm{FT}_{\mathrm{2D}}\{\mathrm{Re}H^{\mathrm{sc}}_{\zeta,\mathrm{B}}(x,y;z';\omega_m)\}_{(\boldsymbol{\kappa})}\,, \tag{B.17}$$

$$\tilde{H}^{\mathrm{Im}}_{\zeta,\mathrm{B}}(\boldsymbol{\kappa};z';\omega_m) = \mathrm{FT}_{\mathrm{2D}}\{\mathrm{Im}H^{\mathrm{sc}}_{\zeta,\mathrm{B}}(x,y;z';\omega_m)\}_{(\boldsymbol{\kappa})}\,. \tag{B.18}$$

Analogously to the OUT scattered-power maps, the SP power maps in k-space are computed as:

$$\begin{aligned} &\tilde{\mathcal{M}}^{\text{Re}}_{\text{B}}(\boldsymbol{\kappa}, z'; z^{\boldsymbol{\prime}}) = \\ &\sum_{m=1}^{N_\omega} \sum_{\zeta=1}^{N_{\text{T}}} \left[\tilde{H}^{\text{Re}}_{\zeta,\text{B}}(\boldsymbol{\kappa}; z^{\boldsymbol{\prime}}; \omega_m)\right] \left[\tilde{H}^{\text{Re}}_{\zeta,\text{B}}(\boldsymbol{\kappa}; z'; \omega_m)\right]^* \\ &\qquad + \left[\tilde{H}^{\text{Im}}_{\zeta,\text{B}}(\boldsymbol{\kappa}; z^{\boldsymbol{\prime}}; \omega_m)\right] \left[\tilde{H}^{\text{Im}}_{\zeta,\text{B}}(\boldsymbol{\kappa}; z'; \omega_m)\right]^* , \end{aligned} \tag{B.19}$$

$$\begin{aligned} &\tilde{\mathcal{M}}^{\text{Im}}_{\text{B}}(\boldsymbol{\kappa}, z'; z^{\boldsymbol{\prime}}) = \\ &\sum_{m=1}^{N_\omega} \sum_{\zeta=1}^{N_{\text{T}}} \left[\tilde{H}^{\text{Im}}_{\zeta,\text{B}}(\boldsymbol{\kappa}; z^{\boldsymbol{\prime}}; \omega_m)\right] \left[\tilde{H}^{\text{Re}}_{\zeta,\text{B}}(\boldsymbol{\kappa}; z'; \omega_m)\right]^* \\ &\qquad - \left[\tilde{H}^{\text{Re}}_{\zeta,\text{B}}(\boldsymbol{\kappa}; z^{\boldsymbol{\prime}}; \omega_m)\right] \left[\tilde{H}^{\text{Im}}_{\zeta,\text{B}}(\boldsymbol{\kappa}; z'; \omega_m)\right]^* . \end{aligned} \tag{B.20}$$

The integrals in the quantitative Born-based equations (B.5)–(B.6) are discretized along $z^{\boldsymbol{\prime}}$ into N_z image slices, similarly to the Rytov-based equation (2.40). The three discretized equations are then put together in the common system (C.32), where the sub-matrices in the system matrix (2.44) are in the form:

$$\begin{aligned} &\tilde{\mathcal{M}}^{\text{Re,Im}}_{\text{B,R}}(\boldsymbol{\kappa}) = \\ &\begin{bmatrix} \tilde{\mathcal{M}}^{\text{Re,Im}}_{\text{B,R}}(\boldsymbol{\kappa}, z_1; z_1) & \cdots & \tilde{\mathcal{M}}^{\text{Re,Im}}_{\text{B,R}}(\boldsymbol{\kappa}, z_1; z_{N_z}) \\ \vdots & \ddots & \vdots \\ \tilde{\mathcal{M}}^{\text{Re,Im}}_{\text{B,R}}(\boldsymbol{\kappa}, z_{N_z}; z_1) & \cdots & \tilde{\mathcal{M}}^{\text{Re,Im}}_{\text{B,R}}(\boldsymbol{\kappa}, z_{N_z}; z_{N_z}) \end{bmatrix} . \end{aligned} \tag{B.21}$$

APPENDIX C

FOURIER-SPACE SCATTERED POWER MAPPING

The F-SPM image-reconstruction method [6,7] has been applied with the well-known forward model of scattering in terms of S-parameters [8]. Its application with the electric-field model follows the same procedure.

Let the data set be composed of the scattered portion of the measured S-parameters, $S_\zeta^{\text{sc}}(\mathbf{r},\omega)$, where $\mathbf{r}$ is the receiver (Rx) position, ω is the frequency, and $\zeta \equiv (i,j)$ denotes the type of response as determined by the receiving (i-th) and transmitting (j-th) antennas. Then, the forward model is stated as:

$$S_\zeta^{\text{sc}}(\mathbf{r},\omega) = c_\zeta \iiint_{V'} \Delta\varepsilon_{\text{r}}(\mathbf{r}')\mathbf{E}_{\zeta,\text{Rx}}^{\text{inc}}(\mathbf{r}',\mathbf{r},\omega) \cdot \mathbf{E}_{\zeta,\text{Tx}}^{\text{tot}}(\mathbf{r}',\mathbf{r}_{\text{Tx}},\omega)d\mathbf{r}' \tag{C.22}$$

where $\mathbf{r}' \in V'$ is a position in the imaged volume V', $\Delta\varepsilon_{\text{r}}(\mathbf{r}')$ is the object's relative-permittivity contrast, $\mathbf{E}_{\zeta,\text{Tx}}^{\text{tot}}$ is the total internal field due to the transmitting (Tx) antenna at position $\mathbf{r}_{\text{Tx}}$, and $\mathbf{E}_{\zeta,\text{Rx}}^{\text{inc}}$ is the background Green function, which is equivalent to the incident field due to the Rx antenna if it were to transmit in the background medium. The relative-permittivity contrast (assumed independent of the frequency and the field polarization) is defined as $\Delta\varepsilon_{\text{r}} = \varepsilon_{\text{r}} - \varepsilon_{\text{r,b}}$, where ε_{r} is the object's relative permittivity whereas $\varepsilon_{\text{r,b}}$ is that of the background. The constant $c_\zeta = \frac{-\text{i}\omega\varepsilon_0}{2a_{\text{Rx}}a_{\text{Tx}}}$ is determined by the root-power waves a_ξ, $\xi = \text{Rx}, \text{Tx}$, incident on the ports of the antennas generating the respective fields. Here, ε_0 is the free-space permittivity.

From (C.22), the system PSF is readily derived as the scattering response due to an electrically small (point-like) scatterer of volume Ω_{sp} and contrast distribution represented by Dirac's δ-function, $\Delta\varepsilon_{\mathrm{r,sp}}\delta(\mathbf{r}' - \mathbf{r}_{\mathrm{sp}})$:

$$H_{\zeta}^{\mathrm{sc}}(\mathbf{r},\omega;\mathbf{r}_{\mathrm{sp}}) = c_{\zeta}\Omega_{\mathrm{sp}}\Delta\varepsilon_{\mathrm{r,sp}}\mathbf{E}_{\zeta,\mathrm{Rx}}^{\mathrm{inc}}(\mathbf{r}_{\mathrm{sp}},\mathbf{r},\omega)\cdot\mathbf{E}_{\zeta,\mathrm{Tx}}^{\mathrm{inc}}(\mathbf{r}_{\mathrm{sp}},\mathbf{r}_{\mathrm{Tx}},\omega)\,. \tag{C.23}$$

Note that (C.23) employs Born's approximation of the total internal field, $\mathbf{E}_{\zeta,\mathrm{Tx}}^{\mathrm{tot}}(\mathbf{r}',\mathbf{r}_{\mathrm{Tx}},\omega) \approx \mathbf{E}_{\zeta,\mathrm{Tx}}^{\mathrm{inc}}(\mathbf{r}',\mathbf{r}_{\mathrm{Tx}},\omega)$, since a point-like scatterer satisfies the assumption of weak scattering. The PSF is the spatial impulse response of the measurement system. Its expression (C.23) provides insight on how to model it analytically or through simulations with account for the field distributions generated by the antennas in the background medium. In close-range imaging, where the scattering from an electrically small probe is sufficiently strong to rise above the measurement noise and uncertainty, the PSF can also be acquired by calibration measurements [6, 9, 10].

In a homogeneous background and with the assumption of weak scattering, the linearized forward model is obtained from (C.22) and (C.23) as [6]:

$$S_{\zeta}^{\mathrm{sc}}(\mathbf{r},\omega) \approx \iiint_{V'} \rho(\mathbf{r}')H_{\zeta}^{\mathrm{sc}}(\mathbf{r}-\mathbf{r}',\omega)d\mathbf{r}' \tag{C.24}$$

where

$$\rho(\mathbf{r}') = \Delta\varepsilon_{\mathrm{r}}(\mathbf{r}')/(\Delta\varepsilon_{\mathrm{r,sp}}\Omega_{\mathrm{sp}}) \tag{C.25}$$

is termed the object's reflectivity function. $H_{\zeta}^{\mathrm{sc}}(\mathbf{r},\omega)$ is the response to a probe at the center of the imaged volume, $\mathbf{r}' = 0$.

With the data, $S_{\zeta}^{\mathrm{sc}}(\mathbf{r},\omega)$, and the PSFs, $H_{\zeta}^{\mathrm{sc}}(\mathbf{r},\omega)$, available, the F-SPM method solves (C.24) for $\rho(\mathbf{r}')$ through a computationally efficient two-stage procedure. The first SPM stage constructs the 3D scattered-power map $M(\mathbf{r}')$ of the OUT as the inner product of the data and the system PSFs. In the case of a planar scan at $z = \bar{z}$, the measurement position is given by $\mathbf{r} = (x, y, \bar{z})$, and the explicit map expression is

$$M(x', y', z') = \sum_{\zeta=1}^{N_{\mathrm{T}}} \int\limits_{\omega} \int\limits_{y} \int\limits_{x} S_{\zeta}^{\mathrm{sc}}(x, y, \omega) \left[H_{\zeta}^{\mathrm{sc}}(x - x', y - y', \omega, z') \right]^* dx dy d\omega \,. \tag{C.26}$$

$M(\mathbf{r}')$ in (C.26) is a 2D cross-correlation in x and y. The most efficient way of computing it is in 2D Fourier space (k_x, k_y), where k_x and k_y are the Fourier variables corresponding to x and y, respectively. For brevity, a point in Fourier (or k) space is denoted as $\boldsymbol{\kappa} = (k_x, k_y)$. The k-space processing requires the FTs of the data at all frequencies,

$$\tilde{S}_{\zeta}^{\mathrm{sc}}(\boldsymbol{\kappa}, \omega_k) = \mathcal{F}_{\mathrm{2D}} \left\{ S_{\zeta}^{\mathrm{sc}}(x, y, \omega_k) \right\} \; \zeta = 1, \ldots, N_{\mathrm{T}} \,, k = 1, \ldots, N_{\omega} \tag{C.27}$$

along with the FTs of the system PSFs at all frequencies and all imaged range slices:

$$\tilde{H}_{\zeta}^{\mathrm{sc}}(\boldsymbol{\kappa}, \omega_k, z_n') = \mathcal{F}_{\mathrm{2D}} \left\{ H_{\zeta}^{\mathrm{sc}}(x, y, \omega_k, z_n') \right\}, \zeta = 1, \ldots, N_{\mathrm{T}} \,, k = 1, \ldots, N_{\omega} \,, n = 1, \ldots, N_z \,. \tag{C.28}$$

Note that the PSFs $H_{\zeta}^{\mathrm{sc}}(x, y, \omega_k, z_n')$ represent the responses acquired with the scattering probe at position $(0, 0, z_n')$, i.e., at the center $(x' = y' = 0)$ of the imaged slice $z_n' = const$. The k-space OUT map is then computed as:

$$\tilde{M}(\boldsymbol{\kappa}, z_n') = \sum_{\zeta=1}^{N_{\mathrm{T}}} \sum_{k=1}^{N_{\omega}} \tilde{S}_{\zeta}^{\mathrm{sc}}(\boldsymbol{\kappa}, \omega_k) \left[\tilde{H}_{\zeta}^{\mathrm{sc}}(\boldsymbol{\kappa}, \omega_k, z_n') \right]^* , n = 1, \ldots, N_z \,. \tag{C.29}$$

The second SPM stage is also performed in k-space [6, 7]. In addition to the OUT map in (C.29), it requires the 2D FTs of the scattering-probe maps. These are obtained analogously to (C.29):

$$\tilde{\mathcal{M}}(\boldsymbol{\kappa}, z'_n; z'_m) = \sum_{\zeta=1}^{N_{\mathrm{T}}} \sum_{k=1}^{N_\omega} \tilde{H}_\zeta^{\mathrm{sc}}(\boldsymbol{\kappa}, \omega_k, z'_m) \left[\tilde{H}_\zeta^{\mathrm{sc}}(\boldsymbol{\kappa}, \omega_k, z'_n)\right]^* n, m = 1, \ldots, N_z \, . \tag{C.30}$$

Here, z'_n indicates an image slice in the scattering-probe map whereas z'_m indicates the slice in which the scattering probe actually resides.

With the OUT and scattering-probe maps available, the 2D FT of the reflectivity function, $\tilde{\rho}(\boldsymbol{\kappa}, z'_n) = \mathcal{F}_{\mathrm{2D}}\left\{\rho(x', y', z'_n)\right\}$, is extracted using the linear map relation [6]:

$$\tilde{M}(\boldsymbol{\kappa}, z'_n) = \sum_{m=1}^{N_z} \tilde{\rho}(\boldsymbol{\kappa}, z'_m) \tilde{\mathcal{M}}(\boldsymbol{\kappa}, z'_n; z'_m) \, , n = 1, ..., N_z \, . \tag{C.31}$$

The N_z equations in (C.31) form a small $N_z \times N_z$ system of equations at each k-space point written as:

$$\tilde{\boldsymbol{\mathcal{M}}}(\boldsymbol{\kappa}) \tilde{\boldsymbol{\rho}}(\boldsymbol{\kappa}) = \tilde{\boldsymbol{m}}(\boldsymbol{\kappa}) \tag{C.32}$$

where

$$\tilde{\boldsymbol{\rho}}(\boldsymbol{\kappa}) = \left[\tilde{\rho}(\boldsymbol{\kappa}, z'_1), \ldots, \tilde{\rho}(\boldsymbol{\kappa}, z'_{N_z})\right]^T , \tag{C.33}$$

$$\tilde{\boldsymbol{m}}(\boldsymbol{\kappa}) = \left[\tilde{M}(\boldsymbol{\kappa}, z'_1), \ldots, \tilde{M}(\boldsymbol{\kappa}, z'_{N_z})\right]^T , \tag{C.34}$$

$$\tilde{\boldsymbol{\mathcal{M}}}(\boldsymbol{\kappa}) = \begin{bmatrix} \tilde{\mathcal{M}}(\boldsymbol{\kappa}, z'_1; z'_1) & \cdots & \tilde{\mathcal{M}}(\boldsymbol{\kappa}, z'_1; z'_{N_z}) \\ \vdots & \ddots & \vdots \\ \tilde{\mathcal{M}}(\boldsymbol{\kappa}, z'_{N_z}; z'_1) & \cdots & \tilde{\mathcal{M}}(\boldsymbol{\kappa}, z'_{N_z}; z'_{N_z}) \end{bmatrix} . \tag{C.35}$$

Since $\tilde{\boldsymbol{\mathcal{M}}}(\boldsymbol{\kappa})$ is a small square matrix, (C.32) can be efficiently solved using LU decomposition.

The real-space reflectivity function $\rho(x', y', z'_n)$ is recovered via the inverse 2D FT of $\tilde{\rho}(\boldsymbol{\kappa}, z_n)$:

$$\rho(x', y', z'_n) = \mathcal{F}_{\rm 2D}^{-1}\left\{\tilde{\rho}(\boldsymbol{\kappa}, z'_n)\right\}\,, n = 1, \ldots, N_z\,. \tag{C.36}$$

The plot of $|\rho(x', y', z'_n)|$ provides a qualitative image of the object's reflectivity. Quantitative image is also possible, provided the system PSFs scale properly with the probe's volume $\Omega_{\rm sp}$ and relative-permittivity contrast $\Delta\varepsilon_{\rm r,sp}$. As per (C.25), the quantitative estimate of the object's relative-permittivity contrast is obtained as:

$$\Delta\varepsilon_{\rm r}(x', y', z'_n) = \Omega_{\rm sp}\Delta\varepsilon_{\rm r,sp}\rho(x', y', z'_n)\,. \tag{C.37}$$

BIBLIOGRAPHY

[1] Altiar FEKO, Electromagnetic Simulation Software. [Online]. Available: https://altairhyperworks.com/product/FEKO

[2] D. Tajik, N. K. Nikolova, and M. D. Noseworthy, "Improving quantitative microwave holography through simultaneous use of the Born and Rytov approximations," in *2019 16th Eur. Radar Conf.*, Oct. 2019, pp. 281–284.

[3] D. Tajik, J. Trac, and N. K. Nikolova, "Quality control of microwave equipment for tissue imaging," *IEEE J. Electromagn. RF Microw. Med. Biol.*, vol. 4, no. 1, pp. 52–60, Mar. 2020.

[4] D. Tajik, R. Kazemivala, and N. K. Nikolova, "Real-time imaging with simultaneous use of born and rytov approximations in quantitative microwave holography," *IEEE Trans. Microw. Theory Techn.*, p. available through early access, Dec. 2021.

[5] *IWR1443BOOST Evaluation Module mmWave Sensing Solution*, Texas Instruments, 2020. [Online]. Available: https://www.ti.com/lit/ug/swru518d/swru518d.pdf?ts=1703684594280

[6] R. Kazemivala, D. Tajik, and N. K. Nikolova, "Simultaneous use of the Born and Rytov approximations in real-time imaging with Fourier-space scattered power mapping," *IEEE Trans. Microw. Theory Tech.*, vol. 70, no. 5, pp. 2904–2920, 2022.

[7] D. S. Shumakov and N. K. Nikolova, "Fast quantitative microwave imaging with scattered-power maps," *IEEE Transactions on Microwave Theory and Techniques*, vol. 66, no. 1, pp. 439–449, 2018.

[8] A. S. Beaverstone, D. S. Shumakov, and N. K. Nikolova, "Frequency-domain integral equations of scattering for complex scalar responses," *IEEE Trans. Microw. Theory Tech.*, vol. 65, no. 4, pp. 1120–1132, 2017.

[9] R. K. Amineh, J. J. McCombe, A. Khalatpour, and N. K. Nikolova, "Microwave holography using point-spread functions measured with calibration objects," *IEEE Trans. Instrum. Meas.*, vol. 64, no. 2, pp. 403–417, 2015.

[10] D. Tajik, A. D. Pitcher, and N. K. Nikolova, "Comparative study of the Rytov and Born approximations in quantitative microwave holography," *Prog. Electromagn. Res. B*, vol. 79, pp. 1–19, 2017.

[11] W. Chew and Y. Wang, "Reconstruction of two-dimensional permittivity distribution using the distorted born iterative method," *IEEE Transactions on Medical Imaging*, vol. 9, no. 2, pp. 218–225, 1990.

[12] Y. M. Wang and W. C. Chew, "An iterative solution of the two-dimensional electromagnetic inverse scattering problem," *International Journal of Imaging Systems and Technology*, vol. 1, no. 1, pp. 100–108, 1989. [Online]. Available: https://onlinelibrary.wiley.com/doi/abs/10.1002/ima.1850010111

[13] P. Meaney, K. Paulsen, B. Pogue, and M. Miga, "Microwave image reconstruction utilizing log-magnitude and unwrapped phase to improve high-contrast

object recovery," *IEEE Transactions on Medical Imaging*, vol. 20, no. 2, pp. 104–116, 2001.

[14] S. Hosseinzadegan, A. Fhager, M. Persson, S. D. Geimer, and P. M. Meaney, "Discrete dipole approximation-based microwave tomography for fast breast cancer imaging," *IEEE Transactions on Microwave Theory and Techniques*, vol. 69, no. 5, pp. 2741–2752, 2021.

[15] P. M. van den Berg and R. E. Kleinman, "A contrast source inversion method," *Inverse Problems*, vol. 13, no. 6, p. 1607, dec 1997. [Online]. Available: https://dx.doi.org/10.1088/0266-5611/13/6/013

[16] P. M. van den Berg, A. Abubakar, and J. T. Fokkema, "Multiplicative regularization for contrast profile inversion," *Radio Science*, vol. 38, no. 2, pp. 23–1–23–10, 2003.

[17] P. Mojabi and J. LoVetri, "Overview and classification of some regularization techniques for the gauss-newton inversion method applied to inverse scattering problems," *IEEE Transactions on Antennas and Propagation*, vol. 57, no. 9, pp. 2658–2665, 2009.

[18] Z. Chen, Z. Zeng, D. Fu, Y. Huang, Q. Li, X. Zhang, and J. Wan, "Back-projection imaging for synthetic aperture radar with topography occlusion," *Remote Sensing*, vol. 15, no. 3, 2023. [Online]. Available: https://www.mdpi.com/2072-4292/15/3/726

[19] X. Hu, B. Wang, M. Xiang, and Z. Wang, "A novel airborne dual-antenna insar calibration method for backprojection imaging model," *IEEE Access*, vol. 9, pp. 43 001–43 012, 2021.

[20] M. E. Yavuz and F. L. Teixeira, "Ultrawideband microwave sensing and imaging using time-reversal techniques: A review," *Remote Sensing*, vol. 1, no. 3, pp. 466–495, 2009. [Online]. Available: https://www.mdpi.com/2072-4292/1/3/466

[21] M. Yousefnia, A. Ebrahimzadeh, M. Dehmollaian, and A. Madannejad, "A time-reversal imaging system for breast screening: Theory and initial phantom results," *IEEE Transactions on Biomedical Engineering*, vol. 65, no. 11, pp. 2542–2551, 2018.

[22] L. Guo, A. S. M. Alqadami, and A. Abbosh, "Stroke diagnosis using microwave techniques: Review of systems and algorithms," *IEEE Journal of Electromagnetics, RF and Microwaves in Medicine and Biology*, vol. 7, no. 2, pp. 122–135, 2023.

[23] W. C. Chew, H. Gan, J. H. Lin, C. C. Lu, G. P. Otto, J. Song, R. L. Wagner, and W. H. Weedon, "Forward and inverse scattering problems in electromagnetic waves," in *National Science Foundation (NSF) Forum on Optical Science and Engineering*, W. H. Carter, Ed., vol. 2524, International Society for Optics and Photonics. SPIE, 1995, pp. 189 – 200. [Online]. Available: https://doi.org/10.1117/12.219573

[24] M. Phaneuf, M. Kelly, and P. Mojabi, "Experimental evaluation of forward and inverse solvers for metasurface design," in *2023 XXXVth General Assembly*

and Scientific Symposium of the International Union of Radio Science (URSI GASS), 2023, pp. 1–4.

[25] R. Harington, *Field Computation by Moment Method.* Krieger Publication, 1982.

[26] A. Taflove and K. Umashankar, "The finite-difference time-domain (fd-td) method for electromagnetic scattering and interaction problems," *Journal of Electromagnetic Waves and Applications*, vol. 1, no. 3, pp. 243–267, 1987. [Online]. Available: https://doi.org/10.1163/156939387X00045

[27] M. Schweiger, S. R. Arridge, M. Hiraoka, and D. T. Delpy, "The finite element method for the propagation of light in scattering media: Boundary and source conditions," *Medical Physics*, vol. 22, no. 11, pp. 1779–1792, 1995. [Online]. Available: https://aapm.onlinelibrary.wiley.com/doi/abs/10.1118/1.597634

[28] P. Mojabi, V. Khoshdel, and J. Lovetri, "Tissue-type classification with uncertainty quantification of microwave and ultrasound breast imaging: A deep learning approach," *IEEE Access*, vol. 8, pp. 182 092–182 104, 2020.

[29] "A review of deep learning approaches for inverse scattering problems (invited review)," *Progress In Electromagnetics Research*, vol. 167, pp. 67–81, 2020.

[30] Z. Wu, Y. Peng, P. Wang, W. Wang, and W. Xiang, "A physics-induced deep learning scheme for electromagnetic inverse scattering," *IEEE Transactions on Microwave Theory and Techniques*, vol. 72, no. 2, pp. 927–947, 2024.

[31] Z. Wei and X. Chen, "Deep-learning schemes for full-wave nonlinear inverse scattering problems," *IEEE Transactions on Geoscience and Remote Sensing*, vol. 57, no. 4, pp. 1849–1860, 2019.

[32] M. Salucci, M. Arrebola, T. Shan, and M. Li, "Artificial intelligence: New frontiers in real-time inverse scattering and electromagnetic imaging," *IEEE Transactions on Antennas and Propagation*, vol. 70, no. 8, pp. 6349–6364, 2022.

[33] H. M. Yao, W. E. I. Sha, and L. Jiang, "Two-step enhanced deep learning approach for electromagnetic inverse scattering problems," *IEEE Antennas and Wireless Propagation Letters*, vol. 18, no. 11, pp. 2254–2258, 2019.

[34] H. H. Zhang, H. M. Yao, L. Jiang, and M. Ng, "Enhanced two-step deep-learning approach for electromagnetic-inverse-scattering problems: Frequency extrapolation and scatterer reconstruction," *IEEE Transactions on Antennas and Propagation*, vol. 71, no. 2, pp. 1662–1672, 2023.

[35] G. Zhang, C. Li, Z. Wang, J. Hu, S. Zheng, X. Liu, and G. Fang, "An efficient spectrum reconstruction algorithm for non-uniformly sampled signals and its application in terahertz sar," *Remote Sensing*, vol. 15, no. 18, 2023. [Online]. Available: https://www.mdpi.com/2072-4292/15/18/4427

[36] S. Hu, A. M. Molaei, O. Yurduseven, H. Meng, R. Nilavalan, L. Gan, and X. Chen, "Multistatic mimo sparse imaging based on fft and low-rank matrix recovery techniques," *IEEE Transactions on Microwave Theory and Techniques*, vol. 71, no. 3, pp. 1285–1295, 2023.

[37] Z. Xu, M. Liu, G. Zhou, Z. Wei, B. Zhang, and Y. Wu, "An accurate sparse sar imaging method for enhancing region-based features via nonconvex and tv regularization," *IEEE Journal of Selected Topics in Applied Earth Observations and Remote Sensing*, vol. 14, pp. 350–363, 2021.

[38] M. Liu, J. Pan, J. Zhu, Z. Chen, B. Zhang, and Y. Wu, "A sparse sar imaging method for low-oversampled staggered mode via compound regularization," *Remote Sensing*, vol. 16, no. 8, 2024. [Online]. Available: https://www.mdpi.com/2072-4292/16/8/1459

[39] S. Bernhardt, R. Boyer, S. Marcos, and P. Larzabal, "Compressed sensing with basis mismatch: Performance bounds and sparse-based estimator," *IEEE Transactions on Signal Processing*, vol. 64, no. 13, pp. 3483–3494, 2016.

[40] D. Tajik, R. Kazemivala, J. Nguyen, and N. K. Nikolova, "Accurate range migration for fast quantitative Fourier-based image reconstruction with monostatic radar," *IEEE Trans. Microw. Theory Tech.*, vol. 70, no. 9, pp. 4273–4283, 2022.

[41] S. Doğu, D. Tajik, M. N. Akıncı, and N. K. Nikolova, "Improving the accuracy of range migration in 3-D near-field microwave imaging," *IEEE Trans. Microw. Theory Tech.*, vol. 71, no. 8, pp. 3540–3551, 2023.

[42] D. Tajik, R. Kazemivala, and N. K. Nikolova, "Real-time imaging with simultaneous use of Born and Rytov approximations in quantitative microwave holography," *IEEE Trans. Microw. Theory Tech.*, vol. 70, no. 3, pp. 1896–1909, 2022.

[43] D. Tajik, F. Foroutan, D. S. Shumakov, A. D. Pitcher, and N. K. Nikolova, "Real-time microwave imaging of a compressed breast phantom with planar scanning," *IEEE J. Electromagn. RF Microw. Med. Biol.*, vol. 2, no. 3, pp. 154–162, 2018.

[44] D. Shumakov, "Development of a near-field microwave imaging system," Ph.D. dissertation, McMaster University, 2017. [Online]. Available: http://hdl.handle.net/11375/22099

[45] R. Kazemivala and N. K. Nikolova, "Real-time synthetic aperture radar imaging with random sampling employing scattered power mapping," *Sensors*, vol. submitted and under revision, 2024.

[46] P. M. Meaney and Q. Fang, *Microwave Imaging: A Model-Based Approach.* Boston, MA: Springer US, 2005, pp. 127–153.

[47] D. O'Loughlin, M. O'Halloran, B. M. Moloney, M. Glavin, E. Jones, and M. A. Elahi, "Microwave breast imaging: Clinical advances and remaining challenges," *IEEE Trans. Biomed. Eng.*, vol. 65, no. 11, pp. 2580–2590, Nov. 2018.

[48] D. M. Sheen, D. L. McMakin, and T. E. Hall, "Three-dimensional millimeter-wave imaging for concealed weapon detection," *IEEE Trans. Microw. Theory Techn.*, vol. 49, no. 9, pp. 1581–1592, Sep. 2001.

[49] D. Byrne, M. Halloran, M. Glavin, and E. Jones, "Data independent radar beamforming algorithms for breast cancer detection," *Prog. Electromagn. Res.*, vol. 107, 2010.

[50] M. Asefi and J. LoVetri, "Use of field-perturbing elements to increase nonredundant data for microwave imaging systems," *IEEE Trans. Microw. Theory Techn.*, vol. 65, no. 9, pp. 3172–3179, Sep. 2017.

[51] M. Hopfer, R. Planas, A. Hamidipour, T. Henriksson, and S. Semenov, "Electromagnetic tomography for detection, differentiation, and monitoring of brain stroke: A virtual data and human head phantom study." *IEEE Antennas Propag. Mag.*, vol. 59, no. 5, pp. 86–97, Oct. 2017.

[52] M. Dehmollaian and K. Sarabandi, "Refocusing through building walls using synthetic aperture radar," *IEEE Trans. Geosci. Remote Sens.*, vol. 46, no. 6, pp. 1589–1599, Jun. 2008.

[53] S. Lambot, E. C. Slob, I. van den Bosch, B. Stockbroeckx, and M. Vanclooster, "Modeling of ground-penetrating radar for accurate characterization of subsurface electric properties," *IEEE Trans. Geosci. Remote Sens.*, vol. 42, no. 11, pp. 2555–2568, Nov. 2004.

[54] M. Benedetti, M. Donelli, and A. Massa, "Multicrack detection in two-dimensional structures by means of GA-based strategies," *IEEE Trans. Antennas Propag.*, vol. 55, no. 1, pp. 205–215, Jan. 2007.

[55] Y. Meng, C. Lin, J. Zang, A. Qing, and N. K. Nikolova, "General theory of holographic inversion with linear frequency modulation radar and its application to whole-body security scanning," *IEEE Trans. Microw. Theory Techn.*, vol. 68, no. 11, pp. 4694–4705, Nov. 2020.

[56] J. R. Gallion and R. Zoughi, "Millimeter-wave imaging of surface-breaking cracks in steel with severe surface corrosion," *IEEE Trans. Instrum. Meas.*, vol. 66, no. 10, pp. 2789–2791, Oct. 2017.

[57] M. Zoofaghari, A. Tavakoli, and M. Dehmollaian, "Reconstruction of concealed objects in a corrugated wall with a smoothly varying roughness using the linear sampling method," *IEEE Trans. Geosci. Remote Sens.*, vol. 54, no. 6, pp. 3589–3598, Jun. 2016.

[58] M. Moallem and K. Sarabandi, "Polarimetric study of MMW imaging radars for indoor navigation and mapping," *IEEE Trans. Antennas Propag.*, vol. 62, no. 1, pp. 500–504, Jan. 2014.

[59] C. A. Schuetz, C. Harrity, G. J. Schneider, J. Murakowski, S. Shi, J. Deroba, and D. W. Prather, "A promising outlook for imaging radar: Imaging flash radar realized using photonic spatial beam processing," *IEEE Microw. Mag.*, vol. 19, no. 3, pp. 91–101, May 2018.

[60] A. Mirbeik-Sabzevari and N. Tavassolian, "Tumor detection using millimeter-wave technology: Differentiating between benign lesions and cancer tissues," *IEEE Microw. Mag.*, vol. 20, no. 8, pp. 30–43, Aug. 2019.

[61] D. O'Loughlin, M. O'Halloran, B. M. Moloney, M. Glavin, E. Jones, and M. A. Elahi, "Microwave breast imaging: Clinical advances and remaining challenges," *IEEE Trans. Biomed. Eng.*, vol. 65, no. 11, pp. 2580–2590, Nov. 2018.

[62] F. Topfer and J. Oberhammer, “Millimeter-wave tissue diagnosis: The most promising fields for medical applications,” *IEEE Microw. Mag.*, vol. 16, no. 4, pp. 97–113, May 2015.

[63] P. M. Meaney, D. Goodwin, A. H. Golnabi, T. Zhou, M. Pallone, S. D. Geimer, G. Burke, and K. D. Paulsen, “Clinical microwave tomographic imaging of the calcaneus: A first-in-human case study of two subjects,” *IEEE Trans. Biomed. Eng.*, vol. 59, no. 12, pp. 3304–3313, Dec. 2012.

[64] R. Scapaticci, L. Di Donato, I. Catapano, and L. Crocco, “A feasibility study on microwave imaging for brain stroke monitoring,” *Prog. Electromagn. Res. B*, vol. 40, Jan. 2012.

[65] A. Fhager, S. Candefjord, M. Elam, and M. Persson, “Microwave diagnostics ahead: Saving time and the lives of trauma and stroke patients,” *IEEE Microw. Mag.*, vol. 19, no. 3, pp. 78–90, May 2018.

[66] D. Ireland, K. Bialkowski, and A. Abbosh, “Microwave imaging for brain stroke detection using Born iterative method,” *IET Microw. Antennas Propag.*, vol. 7, pp. 909–915, Aug. 2013.

[67] E. C. Fear, X. Li, S. C. Hagness, and M. A. Stuchly, “Confocal microwave imaging for breast cancer detection: localization of tumors in three dimensions,” *IEEE Trans. Biomed. Eng.*, vol. 49, no. 8, pp. 812–822, Aug. 2002.

[68] N. K. Nikolova, *Microwave Biomedical Imaging.* American Cancer Society, 2014, pp. 1–22. [Online]. Available: https://onlinelibrary.wiley.com/doi/abs/10.1002/047134608X.W8214

[69] D. W. Winters, B. D. Van Veen, and S. C. Hagness, “A sparsity regularization approach to the electromagnetic inverse scattering problem,” *IEEE Trans. Antennas Propag.*, vol. 58, no. 1, pp. 145–154, Jan. 2010.

[70] T. Rubaek, P. M. Meaney, P. Meincke, and K. D. Paulsen, “Nonlinear microwave imaging for breast-cancer screening using Gauss–Newton’s method and the CGLS inversion algorithm,” *IEEE Trans. Antennas Propag.*, vol. 55, no. 8, pp. 2320–2331, Aug. 2007.

[71] Q. Fang, P. M. Meaney, and K. D. Paulsen, “Viable three-dimensional medical microwave tomography: Theory and numerical experiments,” *IEEE Trans. Antennas Propag.*, vol. 58, no. 2, pp. 449–458, Feb. 2010.

[72] I. Bisio, C. Estatico, A. Fedeli, F. Lavagetto, M. Pastorino, A. Randazzo, and A. Sciarrone, “Brain stroke microwave imaging by means of a Newton-Conjugate-Gradient method in l^p banach spaces,” *IEEE Trans. Microw. Theory Techn.*, vol. 66, no. 8, pp. 3668–3682, Aug. 2018.

[73] P. Tournier, M. Bonazzoli, V. Dolean, F. Rapetti, F. Hecht, F. Nataf, I. Aliferis, I. El Kanfoud, C. Migliaccio, M. de Buhan, M. Darbas, S. Semenov, and C. Pichot, “Numerical modeling and high-speed parallel computing: New perspectives on tomographic microwave imaging for brain stroke detection and monitoring.” *IEEE Antennas Propag. Mag.*, vol. 59, no. 5, pp. 98–110, Oct. 2017.

[74] V. L. Coli, P. Tournier, V. Dolean, I. E. Kanfoud, C. Pichot, C. Migliaccio, and L. Blanc-Féraud, “Detection of simulated brain strokes using microwave

tomography," *IEEE J. Electromagn. RF Microw. Med. Biol.*, vol. 3, no. 4, pp. 254–260, Dec. 2019.

[75] C. Estatico, A. Fedeli, M. Pastorino, and A. Randazzo, "Quantitative microwave imaging method in Lebesgue spaces with nonconstant exponents," *IEEE Trans. Antennas Propag.*, vol. 66, no. 12, pp. 7282–7294, Dec. 2018.

[76] M. Ostadrahimi, P. Mojabi, A. Zakaria, J. LoVetri, and L. Shafai, "Enhancement of Gauss–Newton inversion method for biological tissue imaging," *IEEE Trans. Microw. Theory Techn.*, vol. 61, no. 9, pp. 3424–3434, Sep. 2013.

[77] M. Asefi, A. Baran, and J. LoVetri, "An experimental phantom study for air-based quasi-resonant microwave breast imaging," *IEEE Trans. Microw. Theory Techn.*, vol. 67, no. 9, pp. 3946–3954, Sep. 2019.

[78] N. Abdollahi, I. Jeffrey, and J. LoVetri, "Improved tumor detection via quantitative microwave breast imaging using eigenfunction-based prior," *IEEE Trans. Comput. Imag.*, vol. 6, pp. 1194–1202, Jul. 2020.

[79] D. Smith, O. Yurduseven, B. Livingstone, and V. Schejbal, "Microwave imaging using indirect holographic techniques," *Antennas Propag. Mag.*, vol. 56, no. 1, pp. 104–117, Feb. 2014.

[80] D. Sheen, D. McMakin, and T. Hall, "Near-field three-dimensional radar imaging techniques and applications," *Appl. Opt.*, vol. 49, no. 19, pp. E83–E93, Jul. 2010. [Online]. Available: http://ao.osa.org/abstract.cfm?URI=ao-49-19-E83

[81] R. K. Amineh, A. Khalatpour, and N. K. Nikolova, "Three-dimensional microwave holographic imaging using co- and cross-polarized data," *IEEE Trans. Antennas Propag.*, vol. 60, no. 7, pp. 3526–3531, Jul. 2012.

[82] L. Wang, A. Al-Jumaily, and R. Simpkin, "Investigation of antenna array configurations using far-field holographic microwave imaging technique," *Prog. Electromagn. Res. M*, vol. 42, pp. 1–11, Apr. 2015.

[83] M. Elsdon, D. Smith, M. Leach, and S. J. Foti, "Experimental investigation of breast tumor imaging using indirect microwave holography," *Microw. Opt. Technol. Lett.*, vol. 48, no. 3, pp. 480–482, Mar. 2006. [Online]. Available: https://onlinelibrary.wiley.com/doi/abs/10.1002/mop.21384

[84] J. D. Shea, B. D. Van Veen, and S. C. Hagness, "A TSVD analysis of microwave inverse scattering for breast imaging," *IEEE Trans. Biomed. Eng.*, vol. 59, no. 4, pp. 936–945, Nov. 2012.

[85] Y. Zhang, X. Tuo, Y. Huang, and J. Yang, "A TV forward-looking super-resolution imaging method based on TSVD strategy for scanning radar," *IEEE Trans. Geosci. Remote Sens.*, vol. 58, no. 7, pp. 4517–4528, Jul. 2020.

[86] D. Tajik, A. Pitcher, and N. Nikolova, "Comparative study of the Rytov and Born approximations in quantitative microwave holography," *Prog. Electromagn. Res. B*, vol. 79, pp. 1–19, Jan. 2017.

[87] D. S. Shumakov and N. K. Nikolova, "Fast quantitative microwave imaging with scattered-power maps," *IEEE Trans. Microw. Theory Techn.*, vol. 66, no. 1, pp. 439–449, May 2018.

[88] D. Tajik, F. Foroutan, D. S. Shumakov, A. D. Pitcher, and N. K. Nikolova, "Real-time microwave imaging of a compressed breast phantom with planar scanning," *IEEE J. Electromagn. RF Microw. Med. Biol.*, vol. 2, no. 3, pp. 154–162, May 2018.

[89] S. Tu, J. J. McCombe, D. S. Shumakov, and N. K. Nikolova, "Fast quantitative microwave imaging with resolvent kernel extracted from measurements," *Inverse Problems*, vol. 31, no. 4, p. 045007, Apr. 2015. [Online]. Available: https://doi.org/10.1088/0266-5611/31/4/045007

[90] D. S. Shumakov, D. Tajik, A. S. Beaverstone, and N. K. Nikolova, *Real-Time Quantitative Reconstruction Methods in Microwave Imaging.* Springer International Publishing, 2018, pp. 415–442.

[91] T. Habashy, R. Groom, and B. Spies, "Beyond the Born and Rytov approximations: A nonlinear approach to electromagnetic scattering," *J. Geophys. Res.*, vol. 98, pp. 1759–1775, Feb. 1993.

[92] M. Soumekh, *Synthetic Aperture Radar Signal Processing with MATLAB Algorithms.* Wiley, 1999.

[93] C. Xudong, *Computational Methods for Electromagnetic Inverse Scattering.* Wiley-IEEE, 2018.

[94] M. Pastorino, *Microwave Imaging.* John Wiley & Sons, 2010.

[95] W. C. Chew, *Waves and Fields in Inhomogeneous Media.* Wiley-IEEE Press, 1995.

[96] N. K. Nikolova, *Introduction to Microwave Imaging*, ser. EuMA High Frequency Technologies Series. Cambridge University Press, 2017.

[97] M. Slaney, A. C. Kak, and L. E. Larsen, "Limitations of imaging with first-order diffraction tomography," *IEEE Trans. Microw. Theory Techn.*, vol. 32, no. 8, pp. 860–874, Aug. 1984.

[98] M. Azimi and A. C. Kak, "Distortion in diffraction tomography caused by multiple scattering," *IEEE Trans. Med. Imag.*, vol. 2, no. 4, pp. 176–195, Dec. 1983.

[99] A. S. Beaverstone, D. S. Shumakov, and N. K. Nikolova, "Frequency-domain integral equations of scattering for complex scalar responses," *IEEE Trans. Microw. Theory Techn.*, vol. 65, no. 4, pp. 1120–1132, Jan. 2017.

[100] R. K. Amineh, J. McCombe, and N. K. Nikolova, "Microwave holographic imaging using the antenna phaseless radiation pattern," *IEEE Antennas Wireless Propag. Lett.*, vol. 11, pp. 1529–1532, Dec. 2012.

[101] R. K. Amineh, J. J. McCombe, A. Khalatpour, and N. K. Nikolova, "Microwave holography using point-spread functions measured with calibration objects," *IEEE Trans. Instrum. Meas.*, vol. 64, no. 2, pp. 403–417, 2015.

[102] R. K Amineh, N. Nikolova, and M. Ravan, *Real-Time Three-Dimensional Imaging of Dielectric Bodies Using Microwave/Millimeter-Wave Holography.* Wiley-IEEE Press, 2019.

[103] D. Sundararajan, *Aliasing and Leakage*, Jul. 2018, pp. 159–178.

[104] P. Hopcraft K.I., Smith, *An Introduction to Electromagnetic Inverse Scattering.* Springer, 1992.

[105] D. S. Shumakov, S. Tu, and N. K. Nikolova, "Fast quantitative microwave imaging based on measured point spread functions and inversion in real space," in *2015 IEEE Int. Symp. Antennas Propag. USNC-URSI Radio Sci. Meet. APSURSI 2019 - Proc.*, Jul. 2015, pp. 687–688.

[106] K. Nemez, A. Baran, M. Asefi, and J. LoVetri, "Modeling error and calibration techniques for a faceted metallic chamber for magnetic field microwave imaging," *IEEE Trans. Microw. Theory Techn.*, vol. 65, no. 11, pp. 4347–4356, May 2017.

[107] M. Ostadrahimi, P. Mojabi, C. Gilmore, A. Zakaria, S. Noghanian, S. Pistorius, and J. LoVetri, "Analysis of incident field modeling and incident/scattered field calibration techniques in microwave tomography," *IEEE Antennas Wireless Propag. Lett.*, vol. 10, pp. 900–903, Sep. 2011.

[108] Chao-Hsiung Tseng and Tah-Hsiung Chu, "An effective usage of vector network analyzer for microwave imaging," *IEEE Trans. Microw. Theory Techn.*, vol. 53, no. 9, pp. 2884–2891, Sep. 2005.

[109] O. Yurduseven, J. N. Gollub, K. P. Trofatter, D. L. Marks, A. Rose, and D. R. Smith, "Software calibration of a frequency-diverse, multistatic, computational imaging system," *IEEE Access*, vol. 4, pp. 2488–2497, May 2016.

[110] K. Itoh, "Analysis of the phase unwrapping problem," *Appl. Opt.*, vol. 21, p. 2470, Jul. 1982.

[111] M. O'Halloran, M. Glavin, and E. Jones, "Performance and robustness of a multistatic MIST beamforming algorithm for breast cancer detection," *Prog. Electromagn. Res.*, vol. 105, pp. 403–424, Jan. 2010.

[112] D. M. Pozar, *Microwave Engineering*, 4th ed. John Wiley & Sons, 2012.

[113] W. Xu and I. Cumming, "A region-growing algorithm for InSAR phase unwrapping," *IEEE Trans. Geosci. Remote Sens.*, vol. 37, no. 1, pp. 124–134, Jan. 1999.

[114] FEKO, *Altair FEKO 2020.* Langley Research Park, 144 Research Drive Hampton VA 23666: EM Software & Systems (USA) Inc., 2020.

[115] M. Arevalillo-Herráez, F. R. Villatoro, and M. Gdeisat, "A robust and simple measure for quality-guided 2D phase unwrapping algorithms," *IEEE Trans. Image Process.*, vol. 25, pp. 1–1, Apr. 2016.

[116] J. Strand, T. Taxt, and A. Jain, "Two-dimensional phase unwrapping using a block least-squares method," *IEEE Trans. Image Process.*, vol. 8, no. 3, pp. 375–386, Mar. 1999.

[117] D. Kitahara and I. Yamada, "Algebraic phase unwrapping based on two-dimensional spline smoothing over triangles," *IEEE Trans. Signal Process.*, vol. 64, no. 8, pp. 2103–2118, Apr. 2016.

[118] R. G. McKilliam, B. G. Quinn, I. V. L. Clarkson, B. Moran, and B. N. Vellambi, "Polynomial phase estimation by least squares phase unwrapping," *IEEE Trans. Signal Process.*, vol. 62, no. 8, pp. 1962–1975, Feb. 2014.

[119] D. Tajik, D. S. Shumakov, and N. K. Nikolova, "An experimental comparison between the Born and Rytov approximations in microwave tissue imaging," in *2017 IEEE MTT-S Int. Microw. Symp.*, Oct. 2017, pp. 1391–1393.

[120] R. K. Amineh, A. Trehan, and N. K. Nikolova, "TEM horn antenna for ultra-wide band microwave breast imaging," *Prog. Electromagn. Res. B*, vol. 13, pp. 59–74, Jul. 2009.

[121] G. R. Heidbreder, "Multiple scattering and the method of Rytov," *J. Opt. Soc. Am.*, vol. 57, no. 12, pp. 1477–1479, Dec. 1967.

[122] W. Wang, L. Jing, Z. Li, and R. D. Murch, "Utilizing the Born and Rytov inverse scattering approximations for detecting soft faults in lossless transmission lines," *IEEE Trans. Antennas Propag.*, vol. 65, no. 12, pp. 7233–7243, Dec. 2017.

[123] F. C. Lin and M. A. Fiddy, "The Born–Rytov controversy: I. comparing analytical and approximate expressions for the one-dimensional deterministic case," *J. Opt. Soc. Am. A*, vol. 9, no. 7, pp. 1102–1110, Jul. 1992.

[124] D. Marks, "A family of approximations spanning the Born and Rytov scattering series," *Opt. Express*, vol. 14, pp. 8837–48, Sep. 2006.

[125] G. Tsihrintzis and A. Devaney, "Higher order (nonlinear) diffraction tomography: Inversion of the Rytov series," *IEEE Trans. Inf. Theory*, vol. 46, pp. 1748 – 1761, Aug. 2000.

[126] MATLAB, *version R2019b.* Natick, Massachusetts: The MathWorks Inc., 2019.

[127] M. Wang, R. Scapaticci, M. Cavagnaro, and L. Crocco, "Towards a microwave imaging system for continuous monitoring of liver tumor ablation: Design and in silico validation of an experimental setup," *Diagnostics*, vol. 11, no. 5, May 2021.

[128] R. Scapaticci, L. Di Donato, I. Catapano, and L. Crocco, "A feasibility study on microwave imaging for brain stroke monitoring," *Prog. Electromagn. Res. B*, vol. 40, Jan. 2012.

[129] A. W. Preece, I. Craddock, M. Shere, L. Jones, and H. L. Winton, "MARIA M4: clinical evaluation of a prototype ultrawideband radar scanner for breast cancer detection," *J. Med. Imaging*, vol. 3, no. 3, pp. 1 – 7, Jul. 2016.

[130] A. Fasoula, S. Anwar, Y. Toutain, and L. Duchesne, "Microwave vision: From RF safety to medical imaging," in *2017 11th Eur. Conf. Antennas Propag. EUCAP*, Mar. 2017, pp. 2746–2750.

[131] S. Poltschak, M. Freilinger, R. Feger, A. Stelzer, A. Hamidipour, T. Henriksson, M. Hopfer, R. Planas, and S. Semenov, "High precision realtime RF-measurement system for imaging of stroke," in *2017 47th Eur. Microw. Conf. EuMC*, Oct. 2017, pp. 864–867.

[132] T. Grzegorczyk, P. Meaney, S. Jeon, S. Geimer, and K. Paulsen, "Importance of phase unwrapping for the reconstruction of microwave tomographic images," *Biomed. Opt. Express*, vol. 2, pp. 315–30, Feb. 2011.

[133] J. Szumowski, W. R. Coshow, F. Li, and S. F. Quinn, "Phase unwrapping in the three-point dixon method for fat suppression mr imaging," *Radiology*, vol. 192, no. 2, pp. 555–561, Aug. 1994, pMID: 8029431.

[134] P. M. Meaney, S. D. Geimer, and K. D. Paulsen, "Two-step inversion with a logarithmic transformation for microwave breast imaging," *Med. Phys.*, vol. 44, p. 4239–4251, Jul. 2017.

[135] P. Meaney, A. Hartov, S. Bulumulla, T. Raynolds, C. Davis, F. Schoenberger, S. Richter, and K. Paulsen, "A 4-channel, vector network analyzer microwave imaging prototype based on software defined radio technology," *Rev. Sci. Instrum.*, vol. 90, p. 044708, Apr. 2019.

[136] G. E. P. Box and D. R. Cox, "An analysis of transformations," *J. R. Stat. Soc. Series B Stat. Methodol.*, vol. 26, no. 2, pp. 211–252, Apr. 1964.

[137] *NIST/SEMATECH e-Handbook of Statistical Methods*, Apr. 2012. [Online]. Available: http://www.itl.nist.gov/div898/handbook/

[138] *Limits of human exposure to radiofrequency electromagnetic energy in the frequency range from 3 KHz to 300 GHz.* Health Canada, 2015. [Online]. Available: https://www.canada.ca/en/health-canada/services/publications/health-risks-safety/limits-human-exposure-radiofrequency-electromagnetic-energy-range-3-300.html

[139] D. C. Ghiglia and L. A. Romero, "Robust two-dimensional weighted and unweighted phase unwrapping that uses fast transforms and iterative

methods," *J. Opt. Soc. Am. A*, vol. 11, no. 1, pp. 107–117, Jan. 1994. [Online]. Available: http://opg.optica.org/josaa/abstract.cfm?URI=josaa-11-1-107

[140] M. Arevalillo-Herráez, D. Burton, M. Lalor, and M. Gdeisat, "Fast two-dimensional phase-unwrapping algorithm based on sorting by reliability following a noncontinuous path," *Appl. Opt.*, vol. 41, pp. 7437–44, Jan. 2003.

[141] J. W. Goodman, *Speckle Phenomena in Optics: Theory and Applications*, 2nd ed. SPIE, 2020.

[142] Q. Zhang, Y. Han, and Y. Wu, "Comparison and combination of three spatial phase unwrapping algorithms," *Opt. Rev.*, vol. 26, pp. 380—-390, Aug. 2019.

[143] S. Hamidi and S. S. Naeini, "Millimeter-wave circular synthetic aperture radar imaging," in *2021 IEEE Canadian Conference on Electrical and Computer Engineering (CCECE)*, 2021, pp. 1–6.

[144] M. Soumekh, "Range stacking: an interpolation-free SAR reconstruction algorithm," in *Algorithms for Synthetic Aperture Radar Imagery V*, E. G. Zelnio, Ed., vol. 3370, International Society for Optics and Photonics. SPIE, 1998, pp. 13 – 24. [Online]. Available: https://doi.org/10.1117/12.321823

[145] D. M. Sheen, D. L. McMakin, and T. E. Hall, "Cylindrical millimeter-wave imaging technique for concealed weapon detection," in *26th AIPR Workshop: Exploiting New Image Sources and Sensors*, J. M. Selander, Ed., vol. 3240, International Society for Optics and Photonics. SPIE, 1998, pp. 242 – 250. [Online]. Available: https://doi.org/10.1117/12.300061

[146] L. Junhui, W. Hong, W. Xuegang, Y. Yang, and H. Donglin, “Comparative study on stepped frequency, pulsed and continuous wave SARs,” 2016. [Online]. Available: https://api.semanticscholar.org/CorpusID:117345140

[147] D. Sheen, D. McMakin, and T. Hall, “Three-dimensional millimeter-wave imaging for concealed weapon detection,” *IEEE Trans. Microw. Theory Tech.*, vol. 49, no. 9, pp. 1581–1592, 2001.

[148] ——, “Near-field three-dimensional radar imaging techniques and applications,” *Appl. Opt.*, vol. 49, no. 19, pp. E83–E93, July 2010. [Online]. Available: https://opg.optica.org/ao/abstract.cfm?URI=ao-49-19-E83

[149] X. Zhuge and A. G. Yarovoy, “Three-dimensional near-field MIMO array imaging using range migration techniques,” *IEEE Trans. Image Process.*, vol. 21, no. 6, pp. 3026–3033, 2012.

[150] S. Kharkovsky and R. Zoughi, “Microwave and millimeter wave nondestructive testing and evaluation - overview and recent advances,” *IEEE Instrum. Meas. Mag.*, vol. 10, no. 2, pp. 26–38, 2007.

[151] C. Feng, X. Jiang, M.-G. Jeong, H. Hong, C.-H. Fu, X. Yang, E. Wang, X. Zhu, and X. Liu, “Multitarget vital signs measurement with chest motion imaging based on mimo radar,” *IEEE Trans. Microw. Theory Tech.*, vol. 69, no. 11, pp. 4735–4747, 2021.

[152] Y. Song, T. Jin, Y. Dai, and X. Zhou, “Efficient through-wall human pose reconstruction using UWB MIMO radar,” *IEEE Antennas Wirel. Propag. Lett.*, vol. 21, no. 3, pp. 571–575, 2022.

[153] A. Mostajeran, A. Cathelin, and E. Afshari, “A 170-GHz fully integrated single-chip FMCW imaging radar with 3-D imaging capability,” *IEEE J. Solid-State Circuits*, vol. 52, no. 10, pp. 2721–2734, 2017.

[154] C. Li, Z. Peng, T.-Y. Huang, T. Fan, F.-K. Wang, T.-S. Horng, J.-M. Muñoz-Ferreras, R. Gómez-García, L. Ran, and J. Lin, “A review on recent progress of portable short-range noncontact microwave radar systems,” *IEEE Trans. Microw. Theory Tech.*, vol. 65, no. 5, pp. 1692–1706, 2017.

[155] Z. Briqech, S. Gupta, A.-A. Beltay, A. Elboushi, A.-R. Sebak, and T. A. Denidni, “57–64 GHz imaging/detection sensor—part II: Experiments on concealed weapons and threatening materials detection,” *IEEE Sens. J.*, vol. 20, no. 18, pp. 10 833–10 840, 2020.

[156] L. Pang, H. Liu, Y. Chen, and J. Miao, “Real-time concealed object detection from passive millimeter wave images based on the YOLOv3 algorithm,” *Sensors*, vol. 20, no. 6, 2020. [Online]. Available: https://www.mdpi.com/1424-8220/20/6/1678

[157] C. J. Li, S.-T. Yang, and H. Ling, “In-situ ISAR imaging of wind turbines,” *IEEE Trans. Antennas Propag.*, vol. 64, no. 8, pp. 3587–3596, 2016.

[158] J. Chen, Y. Zhang, S. Guo, G. Cui, P. Wu, C. Jia, and L. Kong, “Joint estimation of NLOS building layout and targets via sparsity-driven approach,” *IEEE Trans. Geosci. Remote Sens.*, vol. 60, pp. 1–13, 2022.

[159] H. Karami, H. Tabarsa, G. B. Gharehpetian, Y. Norouzi, and M. A. Hejazi, “Feasibility study on simultaneous detection of partial discharge and axial

displacement of HV transformer winding using electromagnetic waves," *IEEE Trans. Ind. Inform.*, vol. 16, no. 1, pp. 67–76, 2020.

[160] H. Rahbarimagham, H. K. Porzani, M. S. A. Hejazi, M. S. Naderi, and G. B. Gharehpetian, "Determination of transformer winding radial deformation using UWB system and hyperboloid method," *IEEE Sens. J.*, vol. 15, no. 8, pp. 4194–4202, 2015.

[161] J. Jebramcik, I. Rolfes, N. Pohl, and J. Barowski, "Millimeterwave radar systems for in-line thickness monitoring in pipe extrusion production lines," *IEEE Sens. Lett.*, vol. 4, no. 5, pp. 1–4, 2020.

[162] Y. Song, J. Hu, N. Chu, T. Jin, J. Zhang, and Z. Zhou, "Building layout reconstruction in concealed human target sensing via UWB MIMO through-wall imaging radar," *IEEE Geosci. Remote Sens. Lett.*, vol. 15, no. 8, pp. 1199–1203, 2018.

[163] M. M. Saurer, B. Hofmann, and T. F. Eibert, "A fully polarimetric multilevel fast spectral domain algorithm for 3-D imaging with irregular sample locations," *IEEE Trans. Microw. Theory Tech.*, vol. 70, no. 9, pp. 4231–4242, 2022.

[164] F. Gumbmann and A. Schiessl, "Short-range imaging system with a nonuniform SFCW approach," *IEEE Trans. Microw. Theory Tech.*, vol. 65, no. 4, pp. 1345–1354, 2017.

[165] Y. Meng, C. Lin, J. Zang, A. Qing, and N. K. Nikolova, "General theory of holographic inversion with linear frequency modulation radar and its application

to whole-body security scanning," *IEEE Trans. Microw. Theory Tech.*, vol. 68, no. 11, pp. 4694–4705, 2020.

[166] Y. Meng, C. Lin, A. Qing, and N. K. Nikolova, "Accelerated holographic imaging with range stacking for linear frequency modulation radar," *IEEE Trans. Microw. Theory Tech.*, vol. 70, no. 3, pp. 1630–1638, 2022.

[167] J. Moll, P. Schops, and V. Krozer, "Towards three-dimensional millimeter-wave radar with the bistatic fast-factorized back-projection algorithm—potential and limitations," *IEEE Trans. Terahertz Sci. Technol.*, vol. 2, no. 4, pp. 432–440, 2012.

[168] T. Kitamura and K. Suwa, "Doppler division multiplexed multiple-input–multiple-output imaging using cascaded millimeter-wave radars," *IEEE Trans. Microw. Theory Tech.*, vol. 70, no. 3, pp. 1571–1581, 2022.

[169] B. Zhang, G. Xu, R. Zhou, H. Zhang, and W. Hong, "Multi-channel back-projection algorithm for mmWave automotive MIMO SAR imaging with Doppler-division multiplexing," *IEEE J. Sel. Top. Signal Process.*, vol. 17, no. 2, pp. 445–457, 2023.

[170] J.-W. Ting, D. Oloumi, and K. Rambabu, "FMCW SAR system for near-distance imaging applications—practical considerations and calibrations," *IEEE Trans. Microw. Theory Tech.*, vol. 66, no. 1, pp. 450–461, 2018.

[171] S. Li, G. Zhao, H. Sun, and M. Amin, "Compressive sensing imaging of 3-D object by a holographic algorithm," *IEEE Trans. Antennas Propag.*, vol. 66, no. 12, pp. 7295–7304, 2018.

[172] G. Wang, F. Qi, Z. Liu, C. Liu, C. Xing, and W. Ning, "Comparison between back projection algorithm and range migration algorithm in terahertz imaging," *IEEE Access*, vol. 8, pp. 18 772–18 777, 2020.

[173] D. Bleh, M. Rösch, M. Kuri, A. Dyck, A. Tessmann, A. Leuther, S. Wagner, B. Weismann-Thaden, H.-P. Stulz, M. Zink, M. Rießle, R. Sommer, J. Wilcke, M. Schlechtweg, B. Yang, and O. Ambacher, "W -band time-domain multiplexing FMCW MIMO radar for far-field 3-D imaging," *IEEE Trans. Microw. Theory Tech.*, vol. 65, no. 9, pp. 3474–3484, 2017.

[174] R. K. Amineh, M. Ravan, and R. Sharma, "Nondestructive testing of nonmetallic pipes using wideband microwave measurements," *IEEE Trans. Microw. Theory Tech.*, vol. 68, no. 5, pp. 1763–1772, 2020.

[175] M. B. Shah, Y. Gao, M. Ravan, and R. K. Amineh, "Quantitative defect size evaluation in fluid-carrying nonmetallic pipes," *IEEE Trans. Microw. Theory Tech.*, vol. 70, no. 8, pp. 4071–4081, 2022.

[176] J. Gao, B. Deng, Y. Qin, H. Wang, and X. Li, "An efficient algorithm for MIMO cylindrical millimeter-wave holographic 3-D imaging," *IEEE Trans. Microw. Theory Tech.*, vol. 66, no. 11, pp. 5065–5074, 2018.

[177] B. Yektakhah and K. Sarabandi, "All-directions through-the-wall imaging using a small number of moving omnidirectional bi-static FMCW transceivers," *IEEE Trans. Geosci. Remote Sens.*, vol. 57, no. 5, pp. 2618–2627, 2019.

[178] A. Randazzo, C. Ponti, A. Fedeli, C. Estatico, P. D'Atanasio, M. Pastorino, and G. Schettini, "A two-step inverse-scattering technique in variable-exponent

Lebesgue spaces for through-the-wall microwave imaging: Experimental results," *IEEE Trans. Geosci. Remote Sens.*, vol. 59, no. 9, pp. 7189–7200, 2021.

[179] C. Q. Mayoral, C. García González, J. C. I. Galarregui, D. Marín, D. Gastón, C. Miranda, R. Gonzalo, I. Maestrojuán, L. G. Santesteban, and I. Ederra, "Water content continuous monitoring of grapevine xylem tissue using a portable low-power cost-effective FMCW radar," *IEEE Trans. Geosci. Remote Sens.*, vol. 57, no. 8, pp. 5595–5605, 2019.

[180] Y. Nan, X. Huang, and Y. J. Guo, "A millimeter-wave GCW-SAR based on deramp-on-receive and piecewise constant Doppler imaging," *IEEE Trans. Geosci. Remote Sens.*, vol. 58, no. 1, pp. 680–690, 2020.

[181] Y. K. Chan and V. Koo, "An introduction to synthetic aperture radar (SAR)," *Prog. Electromagn. Res. B*, vol. 2, pp. 27–60, 2008.

[182] Z. Cui, J. Ren, L. Li, J. Gu, and J. Zhang, "Defocusing recovery technology of terahertz image based on 3-D psf simulations," *IEEE Trans. Instrum. Meas.*, vol. 72, pp. 1–10, 2023.

[183] W. Ning, F. Qi, Z. Liu, Y. Wang, H. Wu, and J. Wang, "Resolution enhancement in terahertz imaging via deconvolution," *IEEE Access*, vol. 7, pp. 65 116–65 121, 2019.

[184] S. Tu, J. McCombe, D. Shumakov, and N. Nikolova, "Fast quantitative microwave imaging with resolvent kernel extracted from measurements," *Inverse Probl.*, vol. 31, no. 4, p. 045007, 2015.

[185] Q. Mao, J. Liu, Y. Zhu, C. Lv, Y. Lu, D. Wei, S. Yan, S. Ding, and D. Ling, "Developing industry-level terahertz imaging resolution using mathematical model," *IEEE Trans. Terahertz Sci. Technol.*, vol. 11, no. 5, pp. 583–590, 2021.

[186] S. Gu, C. Li, X. Gao, Z. Sun, and G. Fang, "Three-dimensional image reconstruction of targets under the illumination of terahertz gaussian beam—theory and experiment," *IEEE Trans. Geosci. Remote Sens.*, vol. 51, no. 4, pp. 2241–2249, 2013.

[187] G. Wang, J.-M. Muñoz-Ferreras, C. Gu, C. Li, and R. Gómez-García, "Application of linear-frequency-modulated continuous-wave (LFMCW) radars for tracking of vital signs," *IEEE Trans. Microw. Theory Tech.*, vol. 62, no. 6, pp. 1387–1399, 2014.

[188] Z. Peng, J. M. Muñoz-Ferreras, Y. Tang, C. Liu, R. Gómez-García, L. Ran, and C. Li, "A portable FMCW interferometry radar with programmable low-IF architecture for localization, ISAR imaging, and vital sign tracking," *IEEE Trans. Microw. Theory Tech.*, vol. 65, no. 4, pp. 1334–1344, 2017.

[189] S. Hosseinzadegan, A. Fhager, M. Persson, S. D. Geimer, and P. M. Meaney, "Discrete dipole approximation-based microwave tomography for fast breast cancer imaging," *IEEE Trans. Microw. Theory Tech.*, vol. 69, no. 5, pp. 2741–2752, 2021.

[190] D. J. Kurrant, M. Omer, and E. C. Fear, "Automated workflow for evaluating microwave and multi-modality breast images," *IEEE J. Electromagn. RF Microw. Med. Biol.*, vol. 7, no. 3, pp. 290–300, 2023.

[191] M. Ghamati, M. Taherzadeh, F. Nabki, and M. Popović, "Integrated fast UWB time-domain microwave breast screening," *IEEE Trans. Instrum. Meas.*, vol. 72, pp. 1–12, 2023.

[192] D. O. Rodriguez-Duarte, J. A. T. Vasquez, R. Scapaticci, L. Crocco, and F. Vipiana, "Assessing a microwave imaging system for brain stroke monitoring via high fidelity numerical modelling," *IEEE J. Electromagn. RF Microw. Med. Biol.*, vol. 5, no. 3, pp. 238–245, 2021.

[193] Y. Fang, K. Bakian-Dogaheh, and M. Moghaddam, "Real-time 3D microwave medical imaging with enhanced variational Born iterative method," *IEEE Trans. Med. Imaging*, vol. 42, no. 1, pp. 268–280, 2023.

[194] A. Ribalta, "Time-domain reconstruction algorithms for FMCW-SAR," *IEEE Geosci. Remote. Sens. Lett.*, vol. 8, no. 3, pp. 396–400, 2011.

[195] B. Yektakhah and K. Sarabandi, "All-directions through-the-wall imaging using a small number of moving omnidirectional bi-static FMCW transceivers," *IEEE Trans. Geosci. Remote Sens.*, vol. 57, no. 5, pp. 2618–2627, 2019.

[196] Z. Chen, Z. Zeng, D. Fu, Y. Huang, Q. Li, X. Zhang, and J. Wan, "Back-projection imaging for synthetic aperture radar with topography occlusion," *Remote Sens.*, vol. 15, no. 3, 2023. [Online]. Available: https://www.mdpi.com/2072-4292/15/3/726

[197] A. Zhuravlev, V. Razevig, A. Rogozin, and M. Chizh, "Microwave imaging of concealed objects with linear antenna array and optical tracking of the target

for high-performance security screening systems," *IEEE Trans. Microw. Theory Tech.*, vol. 71, no. 3, pp. 1326–1336, 2023.

[198] N. J. Kinzie, "Ultra-wideband pulse Doppler radar for short-range targets," Ph.D. dissertation, University of Colorado at Boulder, 2011.

[199] Z. Wang, A. Bovik, H. Sheikh, and E. Simoncelli, "Image quality assessment: from error visibility to structural similarity," *IEEE Trans. Image Processing*, vol. 13, no. 4, pp. 600–612, 2004.

[200] M. Kazemi, Z. Kavehvash, and M. Shabany, "K-space aware multi-static millimeter-wave imaging," *IEEE Trans. Image Processing*, vol. 28, no. 7, pp. 3613–3623, 2019.

[201] "Ieee standard definitions of terms for radio wave propagation," *IEEE Std 211-1997*, pp. 1–44, 1997.

[202] R. K. Amineh, N. K. Nikolova, and M. Ravan, *Real-Time Three-Dimensional Imaging of Dielectric Bodies Using Microwave/Millimeter Wave Holography.* John Wiley & Sons, 2019.

[203] E. D. Jansing, *Introduction to Synthetic Aperture Radar.* McGraw Hill, 2021.

[204] MATLAB, *ver. R2022b.* Natick, Massachusetts: The MathWorks Inc., 2022.

[205] G. Golub and C. Van Loan, *Matrix Computations*, 3rd ed. Baltimore: John Hopkins University Press, 1996.

[206] *DCA1000EVM Real-time Data-capture Adapter for Radar Sensing Evaluation Module*, Texas Instruments, 2019.

[207] E. J. Feleppa, "Holography and medicine," *IEEE Trans. Biomed. Eng.*, no. 3, pp. 194–205, 1972.

[208] D. Smith, O. Yurduseven, B. Livingstone, and V. Schejbal, "Microwave imaging using indirect holographic techniques," *IEEE Antennas and Propagation Mag.*, vol. 56, no. 1, pp. 104–117, 2014.

[209] M. Dvorsky, S. Y. Sim, D. T. Motes, T. Watt, A. Shah, M. T. A. Qaseer, and R. Zoughi, "Multistatic ka-band (26.5–40 ghz) millimeter-wave 3-d imaging system," *IEEE Transactions on Instrumentation and Measurement*, vol. 72, pp. 1–14, 2023.

[210] R. K. Amineh, A. Khalatpour, H. Xu, Y. Baskharoun, and N. K. Nikolova, "Three-dimensional near-field microwave holography for tissue imaging," *Journal of Biomedical Imaging*, vol. 2012, pp. 5–5, 2012.

[211] M. J. Horst, M. T. Ghasr, and R. Zoughi, "A compact microwave camera based on chaotic excitation synthetic-aperture radar," *IEEE Transactions on Antennas and Propagation*, vol. 67, no. 6, pp. 4148–4161, 2019.

[212] T. Truong, A. Dinh, and K. Wahid, "An ultra-wideband frequency system for non-destructive root imaging," *Sensors*, vol. 18, no. 8, 2018. [Online]. Available: https://www.mdpi.com/1424-8220/18/8/2438

[213] S. Gui, J. Li, Y. Yang, F. Zuo, and Y. Pi, "A sar imaging method for walking human based on mωka-FrFT-mmGLRT," *IEEE Transactions on Geoscience and Remote Sensing*, vol. 60, pp. 1–12, 2022.

[214] S. Gui, Y. Yang, J. Li, F. Zuo, and Y. Pi, "Thz radar security screening method for walking human torso with multi-angle synthetic aperture," *IEEE Sensors Journal*, vol. 21, no. 16, pp. 17 962–17 972, 2021.

[215] A. Zhuravlev, V. Razevig, M. Chizh, G. Dong, and B. Hu, "A new method for obtaining radar images of concealed objects in microwave personnel screening systems," *IEEE Transactions on Microwave Theory and Techniques*, vol. 69, no. 1, pp. 357–364, 2021.

[216] F. Liang, P. Wang, H. Lv, M. Bai, Q. An, S. Han, Y. Zhang, and J. Wang, "Change detection and enhanced imaging of vital signs based on arc-scanning sar," *IEEE Sensors Journal*, vol. 24, no. 6, pp. 8304–8313, 2024.

[217] A. Moreira and Y. Huang, "Airborne sar processing of highly squinted data using a chirp scaling approach with integrated motion compensation," *IEEE Transactions on Geoscience and Remote Sensing*, vol. 32, no. 5, pp. 1029–1040, 1994.

[218] L. Zhou, X. Zhang, Y. Wang, L. Li, L. Pu, J. Shi, and S. Wei, "Unambiguous reconstruction for multichannel nonuniform sampling sar signal based on image fusion," *IEEE Access*, vol. 8, pp. 71 558–71 571, 2020.

[219] G. Krieger, N. Gebert, and A. Moreira, "Unambiguous sar signal reconstruction from nonuniform displaced phase center sampling," *IEEE Geoscience and Remote Sensing Letters*, vol. 1, no. 4, pp. 260–264, 2004.

[220] Y. Eldar and A. Oppenheim, “Filterbank reconstruction of bandlimited signals from nonuniform and generalized samples,” *IEEE Transactions on Signal Processing*, vol. 48, no. 10, pp. 2864–2875, 2000.

[221] S. Zhao, R. Wang, Y. Deng, Z. Zhang, N. Li, L. Guo, and W. Wang, “Modifications on multichannel reconstruction algorithm for sar processing based on periodic nonuniform sampling theory and nonuniform fast fourier transform,” *IEEE Journal of Selected Topics in Applied Earth Observations and Remote Sensing*, vol. 8, no. 11, pp. 4998–5006, 2015.

[222] J. Fessler and B. Sutton, “Nonuniform fast fourier transforms using min-max interpolation,” *IEEE Transactions on Signal Processing*, vol. 51, no. 2, pp. 560–574, 2003.

[223] J. Lopez-Sanchez and J. Fortuny-Guasch, “3-d radar imaging using range migration techniques,” *IEEE Transactions on Antennas and Propagation*, vol. 48, no. 5, pp. 728–737, 2000.

[224] X. Tian, T. Chang, and H.-L. Cui, “Short-range millimeter-wave imaging in the presence of array element position deviation,” *IEEE Transactions on Microwave Theory and Techniques*, vol. 70, no. 3, pp. 1910–1919, 2022.

[225] Y. Gao, M. T. Ghasr, and R. Zoughi, “Effects of and compensation for translational position error in microwave synthetic aperture radar imaging systems,” *IEEE Transactions on Instrumentation and Measurement*, vol. 69, no. 4, pp. 1205–1212, 2020.

[226] J. T. Case, M. T. Ghasr, and R. Zoughi, “Nonuniform manual scanning for rapid microwave nondestructive evaluation imaging,” *IEEE Transactions on Instrumentation and Measurement*, vol. 62, no. 5, pp. 1250–1258, 2013.

[227] M. Garcia Fernandez, Y. Alvarez Lopez, A. Arboleya Arboleya, B. Gonzalez Valdes, Y. Rodriguez Vaqueiro, F. Las-Heras Andres, and A. Pino Garcia, “Synthetic aperture radar imaging system for landmine detection using a ground penetrating radar on board a unmanned aerial vehicle,” *IEEE Access*, vol. 6, pp. 45 100–45 112, 2018.

[228] D. Meng, D. Hu, and C. Ding, “Precise focusing of airborne sar data with wide apertures large trajectory deviations: A chirp modulated back-projection approach,” *IEEE Transactions on Geoscience and Remote Sensing*, vol. 53, no. 5, pp. 2510–2519, 2015.

[229] S. Zhou, L. Yang, L. Zhao, and G. Bi, “Forward velocity extraction from uav raw sar data based on adaptive notch filtering,” *IEEE Geoscience and Remote Sensing Letters*, vol. 13, no. 9, pp. 1211–1215, 2016.

[230] S. Wu, L. Ding, P. Li, Y. Li, L. Chen, and Y. Zhu, “Millimeter-wave sar sparse imaging with 2-d spatially pseudorandom spiral-sampling pattern,” *IEEE Transactions on Microwave Theory and Techniques*, vol. 68, no. 11, pp. 4672–4683, 2020.

[231] D. Ao, R. Wang, C. Hu, and Y. Li, “A sparse sar imaging method based on multiple measurement vectors model,” *Remote Sensing*, vol. 9, no. 3, 2017. [Online]. Available: https://www.mdpi.com/2072-4292/9/3/297

[232] Y. Wang, Z. He, X. Zhan, Y. Fu, and L. Zhou, “Three-dimensional sparse sar imaging with generalized lq regularization,” *Remote Sensing*, vol. 14, no. 2, 2022. [Online]. Available: https://www.mdpi.com/2072-4292/14/2/288

[233] S. Hu, A. M. Molaei, O. Yurduseven, H. Meng, R. Nilavalan, L. Gan, and X. Chen, “Multistatic mimo sparse imaging based on fft and low-rank matrix recovery techniques,” *IEEE Transactions on Microwave Theory and Techniques*, vol. 71, no. 3, pp. 1285–1295, 2023.

[234] S. Tu, J. J. McCombe, D. S. Shumakov, and N. K. Nikolova, “Fast quantitative microwave imaging with resolvent kernel extracted from measurements,” *Inverse Problems*, vol. 31, no. 4, p. 045007, mar 2015. [Online]. Available: https://dx.doi.org/10.1088/0266-5611/31/4/045007

[235] R. Kazemivala, A. D. Pitcher, J. Nguyen, and N. K. Nikolova, “Real-time millimeter-wave imaging with linear frequency modulation radar and scattered power mapping,” *IEEE Transactions on Microwave Theory and Techniques*, pp. 1–14, 2024.

[236] S. Kharkovsky, J. Case, M. Abou-Khousa, R. Zoughi, and F. Hepburn, “Millimeter-wave detection of localized anomalies in the space shuttle external fuel tank insulating foam,” *IEEE Transactions on Instrumentation and Measurement*, vol. 55, no. 4, pp. 1250–1257, 2006.

[237] M. M. Abo-Zahhad, A. I. Hussein, and A. M. Mohamed, “Compressive sensing algorithms for signal processing applications: A survey,” *International journal of communications, network and system sciences*, vol. 8, no. 6, pp. 197–216, 2015.

[238] A. Y. Owda, M. Owda, and N.-D. Rezgui, "Synthetic aperture radar imaging for burn wounds diagnostics," *Sensors*, vol. 20, no. 3, 2020. [Online]. Available: https://www.mdpi.com/1424-8220/20/3/847

[239] M. Klemm, J. A. Leendertz, D. Gibbins, I. J. Craddock, A. Preece, and R. Benjamin, "Microwave radar-based differential breast cancer imaging: Imaging in homogeneous breast phantoms and low contrast scenarios," *IEEE Transactions on Antennas and Propagation*, vol. 58, no. 7, pp. 2337–2344, 2010.

[240] H. Li, H. Zhang, Y. Kong, and C. Zhou, "Flexible dual-polarized uwb antenna sensors for breast tumor detection," *IEEE Sensors Journal*, vol. 22, no. 13, pp. 13 648–13 658, 2022.

[241] M. Ghamati, M. Taherzadeh, F. Nabki, and M. Popović, "Integrated fast uwb time-domain microwave breast screening," *IEEE Transactions on Instrumentation and Measurement*, vol. 72, pp. 1–12, 2023.

[242] C. Dachena, A. Fedeli, A. Fanti, M. B. Lodi, G. Fumera, A. Randazzo, and M. Pastorino, "Microwave imaging of the neck by means of artificial neural networks for tumor detection," *IEEE Open Journal of Antennas and Propagation*, vol. 2, pp. 1044–1056, 2021.

[243] L. Zhang, Z. Qiao, M.-d. Xing, L. Yang, and Z. Bao, "A robust motion compensation approach for uav sar imagery," *IEEE Transactions on Geoscience and Remote Sensing*, vol. 50, no. 8, pp. 3202–3218, 2012.

[244] T. Zhang, Y. Li, J. Wang, M. Xing, L. Guo, and P. Zhang, "A modified range model and extended omega-k algorithm for high-speed-high-squint sar

with curved trajectory," *IEEE Transactions on Geoscience and Remote Sensing*, vol. 61, pp. 1–15, 2023.

[245] F. Zhang, S. Yan, Y. Fu, W. Yang, W. Zhang, and R. Yu, "A novel motion compensation framework for micro uav fmcw sar," in *2023 IEEE 16th International Conference on Electronic Measurement & Instruments (ICEMI)*, 2023, pp. 304–308.

[246] "A new unmanned aerial vehicle synthetic aperture radar for environmental monitoring," *Progress In Electromagnetics Research*, vol. 122, pp. 245–268, 2012.

[247] M. Farhadi, R. Feger, J. Fink, T. Wagner, and A. Stelzer, "Combining mimo dbf with automotive synthetic aperture radar imaging and phase error correction," *IEEE Access*, vol. 12, pp. 31 944–31 959, 2024.

[248] J. Ding, K. Zhang, X. Huang, and Z. Xu, "High frame-rate imaging using swarm of uav-borne radars," *IEEE Transactions on Geoscience and Remote Sensing*, vol. 62, pp. 1–12, 2024.

[249] Y. A. Lopez, M. Garcia-Fernandez, G. Alvarez-Narciandi, and F. L.-H. Andres, "Unmanned aerial vehicle-based ground-penetrating radar systems: A review," *IEEE Geoscience and Remote Sensing Magazine*, vol. 10, no. 2, pp. 66–86, 2022.

[250] M. Garcia-Fernandez, G. Alvarez-Narciandi, F. L. Heras, and Y. Alvarez-Lopez, "Comparison of scanning strategies in uav-mounted multichannel gpr-sar systems using antenna arrays," *IEEE Journal of Selected Topics in Applied Earth Observations and Remote Sensing*, vol. 17, pp. 3571–3586, 2024.

[251] J. T. Case, M. T. Ghasr, and R. Zoughi, "Optimum 2-d nonuniform spatial sampling for microwave sar-based nde imaging systems," *IEEE Transactions on Instrumentation and Measurement*, vol. 61, no. 11, pp. 3072–3083, 2012.

[252] F. Marvasti, "Nonuniform sampling theorems for bandpass signals at or below the nyquist density," *IEEE Transactions on Signal Processing*, vol. 44, no. 3, pp. 572–576, 1996.

[253] ——, "Interpolation of lowpass signals at half the nyquist rate," in *1995 International Conference on Acoustics, Speech, and Signal Processing*, vol. 2, 1995, pp. 1225–1228 vol.2.

[254] F. T. Faul, D. Korthauer, and T. F. Eibert, "Impact of rotor blade rotation of uavs on electromagnetic field measurements," *IEEE Transactions on Instrumentation and Measurement*, vol. 70, pp. 1–9, 2021.

[255] E. J. Candes and M. B. Wakin, "An introduction to compressive sampling," *IEEE Signal Processing Magazine*, vol. 25, no. 2, pp. 21–30, 2008.

[256] G. Agresti and S. Milani, "Material identification using rf sensors and convolutional neural networks," in *ICASSP 2019 - 2019 IEEE International Conference on Acoustics, Speech and Signal Processing (ICASSP)*, 2019, pp. 3662–3666.

[257] A. Pierce, "Walabot diy can see into walls," *Ann Arbor: Prakken Publications, Inc*, vol. 76, no. 5, pp. 8–9, 2017. [Online]. Available: https://www.proquest.com/openview/01261a7cf0992e9497a548a2c23d3596/1.pdf?pq-origsite=gscholar&cbl=182

[258] "Investigation of antenna array configurations using far-field holographic microwave imaging technique," *Progress In Electromagnetics Research M*, vol. 42, pp. 1–11, 2015.

[259] Vayyar imaging - home. [Online]. Available: https://vayyar.com/

[260] The world's most advanced stud finder. [Online]. Available: https://walabot.com/

[261] A. Amiri, K. Tong, and K. Chetty, "Feasibility study of multi-frequency ground penetrating radar for rotary uav platforms," in *IET International Conference on Radar Systems (Radar 2012)*, 2012, pp. 1–6.

[262] M. Weib and J. Ender, "A 3d imaging radar for small unmanned airplanes - artino," in *European Radar Conference, 2005. EURAD 2005.*, 2005, pp. 209–212.

[263] M. A. Yarleque, S. Alvarez, and H. J. Martinez, "Fmcw gpr radar mounted in a mini-uav for archaeological applications: First analytical and measurement results," in *2017 International Conference on Electromagnetics in Advanced Applications (ICEAA)*, 2017, pp. 1646–1648.

[264] G. Ludeno, I. Catapano, A. Renga, A. R. Vetrella, G. Fasano, and F. Soldovieri, "Assessment of a micro-uav system for microwave tomography radar imaging," *Remote Sensing of Environment*, vol. 212, pp. 90–102, 2018. [Online]. Available: https://www.sciencedirect.com/science/article/pii/S0034425718301974

[265] A. Grathwohl, B. Arendt, T. Grebner, and C. Waldschmidt, "Detection of objects below uneven surfaces with a uav-based gpsar," *IEEE Transactions on Geoscience and Remote Sensing*, vol. 61, pp. 1–13, 2023.

[266] G. Li, J. Xu, Y.-n. Peng, and X.-g. Xia, "Location and imaging of moving targets using nonuniform linear antenna array sar," *IEEE Transactions on Aerospace and Electronic Systems*, vol. 43, no. 3, pp. 1214–1220, 2007.

[267] P. Huang, X.-G. Xia, Y. Gao, X. Liu, G. Liao, and X. Jiang, "Ground moving target refocusing in sar imagery based on rfrt-frft," *IEEE Transactions on Geoscience and Remote Sensing*, vol. 57, no. 8, pp. 5476–5492, 2019.

[268] Z. Pan, H. Fan, and Z. Zhang, "Nonuniformly-rotating ship refocusing in sar imagery based on the bilinear extended fractional fourier transform," *Sensors*, vol. 20, no. 2, 2020. [Online]. Available: https://www.mdpi.com/1424-8220/20/2/550

[269] F. B. A. B. E. D. M. M. Martorella, E. Giusti, "Isar based technique for refocusing non-cooperative targets in sar images," *IET Radar, Sonar Navigation*, vol. 6, pp. 332–340(8), June 2012. [Online]. Available: https://digital-library.theiet.org/content/journals/10.1049/iet-rsn.2011.0310

[270] D. Sun, B. Pang, S. Xing, Y. Li, and X. Wang, "Direct 3-d sparse imaging using non-uniform samples without data interpolation," *Electronics*, vol. 9, no. 2, 2020. [Online]. Available: https://www.mdpi.com/2079-9292/9/2/321

[271] C. D. Austin, E. Ertin, and R. L. Moses, "Sparse signal methods for 3-d radar imaging," *IEEE Journal of Selected Topics in Signal Processing*, vol. 5, no. 3, pp. 408–423, 2011.

[272] A. Yegulalp, "Fast backprojection algorithm for synthetic aperture radar," in *Proceedings of the 1999 IEEE Radar Conference. Radar into the Next Millennium (Cat. No.99CH36249)*, 1999, pp. 60–65.

[273] N. V. Shahmirzadi, V. Tyagi, J. Nguyen, R. Kazemivala, N. K. Nikolova, and C.-H. Chen, "Planar array of uwb active slot antennas for microwave imaging of the breast," *IEEE Transactions on Antennas and Propagation*, vol. 71, no. 4, pp. 2946–2957, 2023.

[274] T.-H. Pham, K.-H. Kim, and I.-P. Hong, "A study on millimeter wave sar imaging for non-destructive testing of rebar in reinforced concrete," *Sensors*, vol. 22, no. 20, 2022. [Online]. Available: https://www.mdpi.com/1424-8220/22/20/8030

[275] M. A. Abou-Khousa, M. S. U. Rahman, K. M. Donnell, and M. T. A. Qaseer, "Detection of surface cracks in metals using microwave and millimeter-wave nondestructive testing techniques—a review," *IEEE Transactions on Instrumentation and Measurement*, vol. 72, pp. 1–18, 2023.

[276] C. Liu and R. Zoughi, "Adaptive synthetic aperture radar (sar) imaging for optimal cross-range resolution and image quality in nde applications," *IEEE Transactions on Instrumentation and Measurement*, vol. 70, pp. 1–7, 2021.

[277] W. Pu, Y. Huang, J. Wu, H. Yang, and J. Yang, "Fast compressive sensing-based sar imaging integrated with motion compensation," *IEEE Access*, vol. 7, pp. 53 284–53 295, 2019.

[278] J. Yang, T. Jin, C. Xiao, and X. Huang, "Compressed sensing radar imaging: Fundamentals, challenges, and advances," *Sensors*, vol. 19, no. 14, 2019. [Online]. Available: https://www.mdpi.com/1424-8220/19/14/3100

[279] M. Lyu, Y. Zhao, C. Huang, and H. Huang, "Unmanned aerial vehicles for search and rescue: A survey," *Remote Sensing*, vol. 15, no. 13, 2023. [Online]. Available: https://www.mdpi.com/2072-4292/15/13/3266

[280] M.-S. Kang and J.-M. Baek, "Sar image reconstruction via incremental imaging with compressive sensing," *IEEE Transactions on Aerospace and Electronic Systems*, vol. 59, no. 4, pp. 4450–4463, 2023.

[281] B. Dong, G. Li, and Q. Zhang, "High-resolution and wide-swath imaging of spaceborne sar via random prf variation constrained by the coverage diagram," *IEEE Transactions on Geoscience and Remote Sensing*, vol. 60, pp. 1–16, 2022.

[282] Z. Xu, M. Liu, G. Zhou, Z. Wei, B. Zhang, and Y. Wu, "An accurate sparse sar imaging method for enhancing region-based features via nonconvex and tv regularization," *IEEE Journal of Selected Topics in Applied Earth Observations and Remote Sensing*, vol. 14, pp. 350–363, 2021.

[283] M. Liu, J. Pan, J. Zhu, Z. Chen, B. Zhang, and Y. Wu, "A sparse sar imaging method for low-oversampled staggered mode via compound

regularization," *Remote Sensing*, vol. 16, no. 8, 2024. [Online]. Available: https://www.mdpi.com/2072-4292/16/8/1459

[284] M. Paun, "Through-wall imaging using low-cost frequency-modulated continuous wave radar sensors," *Remote Sensing*, vol. 16, no. 8, 2024. [Online]. Available: https://www.mdpi.com/2072-4292/16/8/1426

[285] M. G. Fernández, Y. Á. López, A. A. Arboleya, B. G. Valdés, Y. R. Vaqueiro, F. L.-H. Andrés, and A. P. García, "Synthetic aperture radar imaging system for landmine detection using a ground penetrating radar on board a unmanned aerial vehicle," *IEEE Access*, vol. 6, pp. 45 100–45 112, 2018.

[286] A. D. Pitcher, C. W. Baard, M. S. Georgiev, and N. K. Nikolova, "Ultra-wideband equivalent-time sampling receiver: limitations and performance analysis," *IEEE Trans. Instrumentation and Measurements*, vol. submitted, 2024.

[287] D. M. Pozar, *Microwave Engineering*, 4th ed. John Wiley & Sons, 2012.

[288] J. Gao, B. Deng, Y. Qin, H. Wang, and X. Li, "An efficient algorithm for mimo cylindrical millimeter-wave holographic 3-d imaging," *IEEE Transactions on Microwave Theory and Techniques*, vol. 66, no. 11, pp. 5065–5074, 2018.

[289] M. Wen and J. Houlihan, "Application of non-uniform fourier transform to non-uniform sampling fourier transform spectrometers," *arXiv preprint arXiv:2212.04502*, 2022.

[290] L. Liu, A. C. Trehan, and N. K. Nikolova, "Near-field detection at microwave frequencies based on self-adjoint response sensitivity analysis,"

Inverse Problems, vol. 26, p. 105001, 2010. [Online]. Available: https://api.semanticscholar.org/CorpusID:122866694

[291] C. K. Balanis, *Antenna Theory Analysis and Design.* John Wiley & Sons, Inc., 1997.

[292] C. Liu, M. T. A. Qaseer, and R. Zoughi, "Influence of antenna pattern on synthetic aperture radar resolution for nde applications," *IEEE Transactions on Instrumentation and Measurement*, vol. 70, pp. 1–11, 2021.

[293] Y. Meng, C. Lin, J. Zang, A. Qing, and N. K. Nikolova, "General theory of holographic inversion with linear frequency modulation radar and its application to whole-body security scanning," *IEEE Transactions on Microwave Theory and Techniques*, vol. 68, no. 11, pp. 4694–4705, 2020.

[294] D. Tajik, R. Kazemivala, J. Nguyen, and N. K. Nikolova, "Accurate range migration for fast quantitative fourier-based image reconstruction with monostatic radar," *IEEE Transactions on Microwave Theory and Techniques*, vol. 70, no. 9, pp. 4273–4283, 2022.

[295] Q. Cheng, A. Alomainy, and Y. Hao, "Near-field millimeter-wave phased array imaging with compressive sensing," *IEEE Access*, vol. 5, pp. 18 975–18 986, 2017.

[296] L. Yi, R. Kaname, R. Mizuno, Y. Li, M. Fujita, H. Ito, and T. Nagatsuma, "Ultra-wideband frequency modulated continuous wave photonic radar system for three-dimensional terahertz synthetic aperture radar imaging," *Journal of Lightwave Technology*, vol. 40, no. 20, pp. 6719–6728, 2022.

[297] C. Ozdemir, S. Demirci, E. Yigit, and B. Yilmaz, “A review on migration methods in b-scan ground penetrating radar imaging,” *Mathematical Problems in Engineering*, vol. 2014, no. 1, p. 280738.